

LNF-06/ 23 (P)  
7 September 2006

## **Papers presented at EPAC 2006**

Accelerator Division

*Contributions to the  
10<sup>th</sup> European Particle Accelerator Conference (EPAC 2006)  
26-30 June, Edinburgh, UK*



## CONTENTS

### *Invited Oral*

#### **Damping Rings towards Ultra-low Emittances**

Susanna Guiducci (INFN/LNF, Frascati) ..... 9

#### **CLIC Feasibility Study in CTF3**

Andrea Ghigo (INFN/LNF, Frascati) ..... 14

#### **Overview of FEL Injectors**

Massimo Ferrario (INFN/LNF, Frascati) ..... 19

### *Contributed Oral*

#### **DAFNE Experience with Negative Momentum Compaction**

M. Zobov, D. Alesini, M.E. Biagini, A. Drago, A. Gallo, C. Milardi,  
P. Raimondi, B. Spataro, A. Stella (INFN/LNF, Frascati) ..... 24

#### **Beam Dynamics Simulation in e- Rings in SRFF Regim**

L. Falbo, D. Alesini, M. Migliorati (INFN/LNF, Frascati) ..... 27

### *Contributed Posters*

#### **Future Seeding Experiments at SPARC**

L. Giannessi, S. Ambrogio, F. Ciocci, G. Dattoli, A. Doria, G.P. Gallerano, E. Giovenale,  
M. Quattromini, A. Renieri, C. Ronsivalle, I.P. Spassovsky (ENEA-Frascati),  
M. Bougeard, B. Carré, D. Garzella, M. Labat, G. Lambert, H. Merdji, P. Salieres,  
O. Tcherbakoff (CEA, Gif-sur-Yvette), A. Dipace, E. Sabia (ENEA-Napoli), L. Serafini  
(INFN-Milano), D. Alesini, M.E. Biagini, R. Boni, M. Castellano, A. Clozza, A. Drago,  
M. Ferrario, V. Fusco, A. Gallo, A. Ghigo, M. Migliorati, L. Palumbo, C. Sanelli,  
F. Sgamma, B. Spataro, S. Tomassini, C. Vaccarezza, C. Vicario (INFN-LNF, Frascati),  
S. de Silvestri, M. Nisoli, G. Sansone, S. Stagira (Politecnico-Milano), M.-E. Couprie  
(SOLEIL, Gif-sur-Yvette), L. Poletto, G. Tondello (Università di Padova), M. Mattioli,  
P. Musumeci, M. Petrarca (Università di Roma 1) ..... 30

#### **Laser Comb: Simulations of Pre-modulated E- Beams at the Photocathode of a High Brightness RF Photoinjector**

M. Boscolo, M. Ferrario, C. Vaccarezza (INFN/LNF, Frascati), I. Boscolo, F. Castelli,  
S. Cialdi (INFN-Milano), P. Musumeci (INFN-Roma 1)..... 33

### **A Biperiodic X-band RF Cavity for SPARC**

- L. Ficcadenti, M. Esposito, A. Mostacci, L. Palumbo (Università di Roma 1),  
A. Bacci (INFN-Milano.), D. Alesini, B. Spataro (INFN-LNF, Frascati) ..... 36

### **Metal Film Photocathodes for High Brightness Electron Injectors**

- G. Gatti, L. Cultrera, F. Tazzioli, C. Vicario (INFN-LNF, Frascati), C. Ristoscu (INFLPR, Bucharest), A. Perrone (Lecce University; INFN-Lecce), J. Langner, M. Sadowski, P. Strzyzewski (The Andrzej Soltan Institute for Nuclear Studies, Swierk/Otwock), A. Fiori, S. Orlanducci (Università di Roma 2)..... 39

### **Status of the SPARX FEL Project**

- C. Vaccarezza, D. Alesini, M. Bellaveglia, S. Bertolucci, M.E. Biagini, R. Boni, M. Boscolo, M. Castellano, A. Clozza, L. Cultrera, G. Di Pirro, A. Drago, A. Esposito, M. Ferrario, D. Filippetto, V. Fusco, A. Gallo, A. Ghigo, S. Guiducci, M. Migliorati, L. Palumbo, L. Pellegrino, M.A. Preger, C. Sanelli, M. Serio, F. Sgamma, B. Spataro, A. Stella, F. Tazzioli, M. Vescovi, C. Vicario (INFN/LNF, Frascati), F. Ciocci, G. Dattoli, A. Doria, F. Flora, G.P. Gallerano, L. Giannessi, E. Giovenale, G. Messina, P.L. Ottaviani, G. Parisi, L. Picardi, M. Quattromini, A. Renieri, C. Ronsivalle (ENEA-Frascati), S. Cialdi, C. Maroli, V. Petrillo, M. Rome, L. Serafini (INFN-Milano), L. Catani, E. Chiadroni, A. Cianchi, C. Schaerf (INFN-Roma 2), P. Musumeci (INFN-Roma 1), F. Alessandria, A. Bacci, F. Broggi, C. De Martinis, D. Giove, M. Mauri (INFN/LASA, Milano), L. Ficcadenti, M. Mattioli, A. Mostacci (Università di Roma 1), P. Emma (SLAC, Menlo Park), S. Reiche, J. Rosenzweig (UCLA, Los Angeles)..... 42

### **Status of the SPARC Project**

- P. Musumeci, D. Levi, M. Mattioli, G. Medici, D. Pelliccia, M. Petrarca (Università di Roma 1), F. Ciocci, G. Dattoli, A. Dipace, A. Doria, G.P. Gallerano, L. Giannessi, E. Giovenale, G. Messina, P.L. Ottaviani, S. Pagnutti, L. Picardi, M. Quattromini, A. Renieri, G. Ronci, C. Ronsivalle, M. Rosetti, E. Sabia, M. Sassi, A. Torre, A. Zucchini (ENEA-Frascati), A. Perrone (INFN-Lecce), F. Alessandria, A. Bacci, I. Boscolo, F. Broggi, S. Cialdi, C. De Martinis, D. Giove, C. Maroli, M. Mauri, V. Petrillo, M. Rome, A.R. Rossi, L. Serafini (INFN-Milano), L. Catani, E. Chiadroni, A. Cianchi, E. Gabrielli, S. Tazzari (INFN-Roma 2), D. Alesini, M. Bellaveglia, S. Bertolucci, R. Boni, M. Boscolo, M. Castellano, A. Clozza, L. Cultrera, G. Di Pirro, A. Drago, A. Esposito, M. Ferrario, L. Ficcadenti, D. Filippetto, V. Fusco, A. Gallo, G. Gatti, A. Ghigo, M. Incurvati, C. Ligi, F. Marcellini, M. Migliorati, A. Mostacci, L. Palumbo, L. Pellegrino, M.A. Preger, R. Ricci, C. Sanelli, M. Serio, F. Sgamma, B. Spataro, A. Stecchi, A. Stella, F. Tazzioli, C. Vaccarezza, M. Vescovi, C. Vicario (INFN/LNF, Frascati), S. Reiche, J. Rosenzweig, G. Travish (UCLA, Los Angeles) ..... 45

### **Production of Coherent X-rays with a Free Electron Laser Based on an Optical Wiggler**

- V. Petrillo, A. Colzato (Università degli Studi di Milano), A. Bacci, C. Maroli, L. Serafini (INFN-Milano), M. Ferrario (INFN/LNF, Frascati) ..... 48

### **Progress on the Pi-mode X-band RF Cavity for SPARC**

- L. Ficcadenti, M. Esposito, A. Mostacci, L. Palumbo (Università di Roma 1),  
A. Bacci (INFN-Milano), D. Alesini, B. Spataro (INFN/LNF, Frascati)..... 51

<b>LHC IR Upgrade: A Dipole First Option with Local Chromaticity Correction</b>	
R. de Maria, O.S. Brüning (CERN, Geneva), P. Raimondi (INFN/LNF, Frascati).....	54
<b>Beam-beam Simulations for a Single Pass SuperB-factory</b>	
M.E. Biagini (INFN/LNF, Frascati), D. Schulte (CERN, Geneva), P. Raimondi, J. Seeman (SLAC, Menlo Park).....	57
<b>DAFNE Status Report</b>	
A. Gallo, D. Alesini, M.E. Biagini, C. Biscari, R. Boni, M. Boscolo, B. Buonomo, A. Clozza, G. Delle Monache, E. Di Pasquale, G. Di Pirro, A. Drago, A. Ghigo, S. Guiducci, M. Incurvati, P. Iorio, C. Ligi, F. Marcellini, C. Marchetti, G. Mazzitelli, C. Milardi, L. Pellegrino, M.A. Preger, L. Quintieri, R. Ricci, U. Rotundo, C. Sanelli, M. Serio, F. Sgamma, B. Spataro, A. Stecchi, A. Stella, S. Tomassini, C. Vaccarezza, M. Vescovi, M. Zobov (INFN/LNF, Frascati), E. Levichev, S. Nikitin, P. Piminov, D. Shatilov (BINP SB RAS, Novosibirsk), G. Benedetti (CELLS, Bellaterra), L. Falbo (INFN-Pisa), J. Fox, P. Raimondi, D. Teytelman (SLAC, Menlo Park).....	60
<b>Preliminary Study of a Crab Crossing System for DAFNE</b>	
A. Gallo, D. Alesini, F. Marcellini, P. Raimondi, M. Zobov (INFN/LNF, Frascati) .....	63
<b>MAD-X/PTC Lattice Design for DAFNE at Frascati</b>	
F. Schmidt (CERN, Geneva), C. Milardi (INFN/LNF, Frascati), E. Forest (KEK, Ibaraki).....	66
<b>Achieving a Luminosity of <math>10^{34}</math> cm<sup>2</sup> s in the PEP-II B-factory</b>	
J. Seeman, M. Browne, Y. Cai, W. Colocho, F.-J. Decker, M. Donald, S. Ecklund, R. Erickson, A.S. Fisher, J. Fox, S. Heifets, R. Iverson, A. Kulikov, A. Novokhatski, V. Pacak, M.T.F. Pivi, C.H. Rivetta, M. Ross, P. Schuh, K.G. Sonnad, M. Stanek, M.K. Sullivan, P. Tenenbaum, D. Teytelman, J.L. Turner, D. Van Winkle, M. Weaver, U. Wienands, W. Wittmer, M. Woodley, Y.T. Yan, G.S. Yocky (SLAC, Menlo Park), W. Kozanecki (CEA, Gif-sur-Yvette), M.E. Biagini (INFN/LNF, Frascati).....	69
<b>Design of an Asymmetric Super-B Factory</b>	
J. Seeman, Y. Cai, A. Novokhatski, A. Seryi, M.K. Sullivan, U. Wienands (SLAC, Menlo Park), M.E. Biagini, P. Raimondi (INFN/LNF, Frascati) .....	72
<b>Design of a Strip-line Extraction Kicker for CTF3 Combiner Ring</b>	
R. Corsini, S. Doebert, F. Tecker, P. Urschütz (CERN, Geneva), D. Alesini, C. Biscari, B. Buonomo, A. Ghigo, F. Marcellini, B. Preger, M. Serio, A. Stella (INFN/LNF, Frascati) .....	75
<b>Commissioning Status of the CTF3 Delay Loop</b>	
I. Rodriguez, F. Toral (CIEMAT, Madrid), L. García-Tabarés (CEDEX, Madrid), A. Ghigo, F. Marcellini (INFN/LNF, Frascati).....	78
<b>The DAFNE Beam Test Facility: from 1 to 10 Billiards of Particles</b>	
G. Mazzitelli, B. Buonomo, L. Quintieri (INFN/LNF, Frascati), P. Valente (INFN-Roma 1).....	81

**Choosing a Baseline Configuration for the ILC Damping Rings**

A. Wolski (Liverpool University), J. Gao (IHEP Beijing),  
S. Guiducci (INFN/LNF, Frascati) ..... 84

**Turn by Turn Measurements at DAFNE Based on the Libera Beam Position Processor**

A. Stella, M. Serio (INFN/LNF, Frascati) ..... 87

**Design and Tests of New Fast Kickers for the DAFNE Collider and the ILC Damping Rings**

D. Alesini, S. Guiducci, F. Marcellini, P. Raimondi (INFN/LNF, Frascati) ..... 90

**Study of the Effect of Multipolar Components in the SPARC Emittance Compensation Gun Solenoid**

C. Ronsivalle, G. Dattoli, L. Picardi, M. Quattromini (ENEA-Frascati),  
G. Bazzano (CNAO Foundation, Milan), P. Musumeci (INFN-Roma 1),  
M. Ferrario, M. Migliorati, L. Palumbo, M.A. Preger, C. Sanelli (INFN/LNF,  
Frascati), J. Rosenzweig (UCLA, Los Angeles) ..... 93

**Analysis of Radiative Effects in the Electron Emission from the Photocathode and in the Acceleration inside the RF Cavity of a Photoinjector using the 3D Numerical Code RETAR**

V. Petrillo, C. Maroli (Università degli Studi di Milano), A. Bacci, A.R. Rossi,  
L. Serafini (INFN-Milano), M. F. (INFN/LNF, Frascati),  
G. Alberti (Università degli Studi di Milano) ..... 96

**The RF Deflector for the CTF3 Delay Loop**

F. Marcellini, D. Alesini (INFN/LNF, Frascati) ..... 99

**The PLASMONX Project for Advanced Beam Physics Experiments**

L. Serafini, A. Bacci, R. Bonifacio, M. Cola, C. Maroli, V. Petrillo, N. Piovella,  
R. Pozzoli, M. Rome, A.R. Rossi, L.a Volpe (INFN-Milano), W. Baldeschi, A. Barbini,  
M. Galimberti, A. Giulietti, L.A. Gizzi, P. Koester, L. Labate, S. Laville, A. Rossi,  
P. Tomassini (CNR/IPP, Pisa), U. Bottigli, B. Golosio, P.N. Oliva, A. Poggiu,  
S. Stumbo (INFN-Cagliari), P. Musumeci (INFN-Roma 1), F. Alessandria, F. Broggi,  
C. De Martinis, D. Giove, M. Mauri (INFN/LASA-Milano), D. Alesini, M. Bellaveglia,  
S. Bertolucci, R. Boni, M. Boscolo, M. Castellano, A. Clozza, G. Di Pirro, A. Drago,  
A. Esposito, M. Ferrario, L. Ficcadenti, D. Filippetto, V. Fusco, A. Gallo, G. Gatti,  
A. Ghigo, M. Incurvati, C. Ligi, F. Marcellini, M. Migliorati, A. Mostacci, L. Palumbo,  
L. Pellegrino, M.A. Preger, R. Ricci, C. Sanelli, M. Serio, F. Sgamma, B. Spataro,  
A. Stecchi, A. Stella, F. Tazzioli, C. Vaccarezza, M. Vescovi, C. Vicario (INFN/LNF,  
Frascati), C.A. Cecchetti, D. Giulietti (Università di Pisa), D. Levi, M. Mattioli,  
G. Medici, D. Pelliccia, M. Petrarca (Università di Roma 1) ..... 102

**The Design of a Hybrid Photoinjector for High Brightness Beam Applications**

D. Alesini, M. Ferrario, V. Fusco, B. Spataro (INFN/LNF, Frascati), L. Ficcadenti,  
A. Mostacci, L. Palumbo (Università di Roma 1), B. O'Shea, J. Rosenzweig,  
G. Travish (UCLA, Los Angeles) ..... 105

**CLIC Polarized Positron Source Based on Laser Compton Scattering**

F. Zimmermann, H.-H. Braun, M. Korostelev, L. Rinolfi, D. Schulte (CERN, Geneva),  
 V. Strakhovenko (BINP SB RAS, Novosibirsk), K. Moenig (DESY, Zeuthen),  
 H.D. Sato (HU/AdSM, Higashi-Hiroshima), T. Takahashi (Hiroshima University,  
 Higashi-Hiroshima), J. Gao (IHEP, Beijing), X. Artru, R. Chehab, M. Chevallier  
 (IN2P3 IPNL, Villeurbanne), S. Guiducci, P. Raimondi (INFN/LNF, Frascati),  
 S. Araki, Y. Higashi, Y. Honda, Y. Kurihara, M. Kuriki, T. Okugi, T. Omori,  
 T. Taniguchi, N. Terunuma, J. Urakawa (KEK, Ibaraki), A. Variola, F. Zomer  
 (LAL, Orsay), V. Soskov (LPI, Moscow), M. Fukuda, K. Hirano, M. Takano  
 (NIRS, Chiba-shi), E.V. Bulyak, P. Gladkikh (NSC/KIPT, Kharkov), T. Hirose,  
 K. Sakaue, M. Washio (RISE, Tokyo), A. Tsunemi (SHI, Tokyo) ..... 108

**CNAO Resonance Sextupole Magnet Power Converters**

M. Farioli, F. Burini, S. Carrozza, M. Cavazza, S. Minisgallo, M. Pretelli, G. Taddia  
 (O.C.E.M. S.p.A., Bologna), D. Bagnara, M. Spera, A. Tilli, M. Toniato  
 (CASY, Bologna), I. De Cesaris (CNAO Foundation, Milan), M. Incurvati, C. Sanelli  
 (INFN/LNF, Frascati) ..... 111

**CNAO Storage Ring Dipole Magnet Power Converter 3000A / ±1600V**

M. Pretelli, F. Burini, S. Carrozza, M. Cavazza, M. Farioli, S. Minisgallo, G. Taddia  
 (O.C.E.M. S.p.A., Bologna), F. Ronchi, C. Rossi, M. Spera, M. Toniato (CASY,  
 Bologna), I. De Cesaris (CNAO Foundation, Milan), M. Incurvati, C. Sanelli  
 (INFN/LNF, Frascati) ..... 114

**The Italian Hadrontherapy Center (CNAO): A Review of the Power Supply System  
 for Conventional Magnets**

M. Incurvati, C. Sanelli (INFN/LNF, Frascati), I. De Cesaris (CNAO Foundation, Milan),  
 L. Balbo, N. Balbo, A. Tescari (EEI, Vicenza), F. Burini, S. Carrozza, M. Cavazza,  
 M. Farioli, S. Minisgallo, M. Pretelli, G. Taddia (O.C.E.M. S.p.A., Bologna) ..... 117

**Electron Beam-laser Interaction near the Cathode in a High Brightness Photoinjector**

M. Ferrario, G. Gatti (INFN/LNF, Frascati), L. Serafini (INFN-Milano),  
 J. Rosenzweig (UCLA, Los Angeles) ..... 120

**Wire Compensation of Parasitic Crossings in DAFNE**

M. Zobov, D. Alesini, C. Milardi, M.A. Preger, P. Raimondi (INFN/LNF, Frascati),  
 D. Shatilov (BINP SB RAS, Novosibirsk) ..... 123

**The Fast Vertical Single-bunch Instability after Injection into the CERN Super Proton  
 Synchrotron**

E. Métral, G. Arduini, T. Bohl, H. Burkhardt, G. Rumolo (CERN, Geneva),  
 B. Spataro (INFN/LNF, Frascati) ..... 126

**Design and Testing of Gproto Bunch-by-bunch Signal Processor**

D. Teytelman, R. Akre, J. Fox, A.K. Krasnykh, C.H. Rivetta, D. Van Winkle (SLAC,  
 Menlo Park), A. Drago (INFN/LNF, Frascati), J.W. Flanagan, T. Naito, M. Tobiyama  
 (KEK, Ibaraki) ..... 129

**Commissioning of the Laser System for SPARC Photoinjector**

C. Vicario, M. Bellaveglia, D. Filippetto, A. Gallo, G. Gatti, A. Ghigo  
(INFN/LNF, Frascati), P. Musumeci, M. Petrarca (INFN-Roma 1) ..... 132

**Production of Temporally Flat Top UV Laser Pulses for SPARC Photoinjector**

M. Petrarca, P. Musumeci (INFN-Roma 1), I. Boscolo, S. Cialdi (INFN-Milano),  
G. Gatti, A. Ghigo, C. Vicario (INFN/LNF, Frascati),  
M. Mattioli (Università di Roma 1) ..... 135

**Nb-Pb Superconducting RF-Gun**

J. Sekutowicz, J. Iversen, D. Klinke, D. Kostin, W.-D. Möller (DESY, Hamburg),  
I. Ben-Zvi, A. Burrill, T. Rao, J. Smedley (BNL, Brookhaven), M. Ferrario  
(INFN/LNF, Frascati), P. Kneisel (Jefferson Lab, Newport News), R. Lefferts,  
A. Lipski (SBUNSL, Stony Brook, New York), Kwok Ko, Liling Xiao (SLAC,  
Menlo Park), J. Langner, P. Strzyzewski (The Andrzej Soltan Institute for Nuclear  
Studies, Swierk/Otwock), J. Rosenzweig (UCLA, Los Angeles), K. Szalowski  
(University of Lodz) ..... 138

**Characterization of the SPARC Photo-injector with the Movable Emittance Meter**

A. Cianchi, L. Catani, E. Chiadroni (INFN-Roma 2), P. Musumeci (INFN-Roma 1),  
M. Boscolo, M. Castellano, G. Di Pirro, M. Ferrario, D. Filippetto, V. Fusco,  
L. Palumbo, C. Vaccarezza (INFN/LNF, Frascati) ..... 141

# DAMPING RINGS TOWARDS ULTRA-LOW EMITTANCES\*

Susanna Guiducci, INFN-LNF, Frascati, Italy

## Abstract

Damping Rings (DR) designs to achieve ultra-low emittance beams in Linear Colliders (ILC and CLIC) will be reviewed pointing out the major issues both from the beam dynamics and the technological point of view and comparing the required performances with the one achieved at SLC. The design, beam simulations, benchmarking and performances already achieved in test facilities, especially the KEK-ATF1 facility, will be presented. Finally, future R&D plans and schedule in terms of beam performances, beam stability and technological development as well as the world-wide organization to achieve them will be discussed.

## INTRODUCTION

Parameters of ILC and CLIC Damping Rings (DR) are listed in Table 1 compared with those for SLC DR. DR parameters for high energy colliders ILC and CLIC are quite different from SLC ones in terms of lower emittance, higher current, higher number of bunches and shorter bunch distance. SLC has been operated between 1986 and 1998, since then progress has been achieved both in storing high currents ( $\Phi$  and B-Factories), very low emittances (ATF, 3rd generation synchrotron light sources), and in stabilizing the beams. The main difference in the present DR designs is that they all are wigglers dominated rings, to increase radiation damping and reduce emittance.

Table 1: SLC, ILC and CLIC DR Parameters

	SLC	ILC	CLIC
Energy (GeV)	1.19	5	2.4
C (m)	35	6695	360
N bunches	1	2767	1554
N part./bunch	$4 \times 10^{10}$	$2 \times 10^{10}$	$2 \times 10^9$
$\tau_{x,y}$ (ms)	3.5	25	2.8
$\gamma \epsilon_x$ (nm)	$3 \times 10^4$	5600	550
$\gamma \epsilon_y$ (nm)	$1.7 \times 10^4$	20	3.3
Mom. comp.	$1.5 \times 10^{-2}$	$4.1 \times 10^{-4}$	$0.81 \times 10^{-4}$
$U_0$ (MeV)	0.080	8.7	2.1
Energy spread	$0.77 \times 10^{-3}$	$1.29 \times 10^{-3}$	$1.26 \times 10^{-3}$
$\sigma_l$ (mm)	5	6.0	1.55
RF volt.(MV)	0.8	46.6	2.4
RFfreq.(MHz)	714	650	1875

## SLC EXPERIENCE

SLC experience has demonstrated the importance of the DR in order to achieve the proper beam sizes and beam stability at the IP [1].

\* This work is supported by the Commission of the European Communities under the 6th Framework Programme "Structuring the European Research Area", contract number RIDS-011899.

The Final Focus Test Beam (FFTB) at SLAC demonstrated the possibility of focused beam sizes in the nanometer ranges, achieving 50nm vertical beam size.

Soon after SLC commissioning it was realized that the longitudinal microwave instability threshold current (single bunch) was very low in the DR [2]. Above threshold there was small pulse-to-pulse variation in bunch length and longitudinal phase of the extracted beam, that was amplified in the linac, and that made it almost impossible to operate the collider. When the microwave instability was recognized as a limiting performance (in the late 1980's), the bellows were sleeved; in 1994 the entire chamber in both rings was removed, and a new, low impedance vacuum chamber was installed.

When the "new" DRs were turned on, it was found that bunch lengthening was indeed reduced; the threshold, however, also went down. This was due to a new "weak" instability, which triggered theoretical work, and was, in the end, rather well understood. It was then possible to routinely run the Drs at more than twice the threshold, increasing the number of particles per bunch by a factor  $\sim 1.5$  with respect to the old ring.

## CLIC DAMPING RING

The emittance requirements for the CLIC DR are very demanding due to the extremely small beam sizes at the IP needed to get high luminosity at the multi-TeV energies. The bunch structure and damping time are given by the time pulse structure of the CLIC linac [30]. A very short bunch distance and high RF frequency, unusual in storage rings, are needed and the ring circumference remains comparatively small.

The CLIC DRs aim at unprecedented small normalized equilibrium emittances of 3.3 nm vertical and 550 nm horizontal, for a bunch charge of  $2.6 \cdot 10^9$  particles at 2.4 GeV [4]. In this parameter regime the dominant emittance growth mechanism is Intra-Beam Scattering (IBS).

Intense synchrotron radiation damping from wigglers is required to counteract IBS effect. The ring is based on a racetrack shape with two  $180^\circ$  arcs made from 48 TME cells each and long straight sections to accommodate a total wiggler length of 152 m. Although dynamic aperture and tolerances of this design remain challenging, benefits are obtained from the strong damping.

Most of the beam dynamics issues related to high currents are similar to that for the ILC DR, in fact the charge per bunch is 10 times lower but the bunch spacing is  $\sim 10$  times shorter and the total current is nearly the same. The most challenging technical issues are related to the wiggler design and to problems of wiggler radiation absorption.

## ILC DAMPING RING

The Baseline Configuration (BC) for the ILC DR was chosen in November 2005 by a working group of nearly 50 researchers that have performed comparative studies of different options based on seven different lattices with circumferences ranging from 17 to 3 km. A description of the process and of the principle considerations leading to the choices of the baseline DR configuration is given in [5] and the supporting studies are documented in [6].

Here we summarize the recommendation for the choice of the circumference and layout. The positron damping ring should consist of two (roughly circular) rings of approximately 6 km circumference in a single tunnel. For the electrons the configuration consists of a single 6 km ring. The main issues for the circumference choice were acceptance, collective effects and kickers. Achieving the required acceptance is easier in a large, nearly periodic, 6 km ring than in a “dogbone ring”, like the TESLA one, or in a compact 3 km ring. Some of the beam dynamics issues, in particular fast-ion instability and electron cloud, favor a larger circumference, while others as space-charge favor a smaller circumference.

The choice of having two rings for positrons is mainly due to electron-cloud effects that make a single ring of circumference 6 km or lower unattractive, unless significant progress can be made with mitigation techniques. Space-charge effects will be less problematic in a 6 km than in a 17 km ring. The injection/extraction kickers are more difficult in a shorter ring; at present the kickers for a 6 km ring are considered feasible even though more R&D is required to fulfil all the specifications.

The parameters in Table 1 refer to the BC that will be used for the Reference Design Report and the cost estimate to be completed by the end of this year. All the specifications should be satisfied also for the “low charge” parameter set, which foresees twice the number of bunches with half the charge.

The ring (OCS) has a 10-fold symmetry and incorporates 10 straight sections, of which 4 dedicated to RF and wigglers and 2 for injection/extraction lines and tune adjustment [7]. Each of the 10 arcs is made of 7 TME cells plus dispersion suppressor. A lattice design based on FODO cells is also under study to compare the performances [8, 9].

## BEAM DYNAMICS ISSUES

### Acceptance

A large acceptance is needed to inject the high emittance positron beam with high efficiency.

Extensive dynamic aperture studies on reference lattices proposed for the BC have been performed applying different techniques [6]. For comparison the calculations have been performed with different wiggler models and different codes, finding a good agreement. In Fig.1 is shown dynamic aperture in the OCS lattice with a realistic wiggler model, based on the CESRc wiggler, and with multipole errors included. The aperture required for

injection is  $3\sigma_x$  and the dynamic aperture is greater than  $5\sigma_x$  even for 1% energy deviation.

The injection efficiency of the reference lattices has been estimated using a simulated distribution of injected positrons: the OCS lattice achieves 100% injection efficiency with a good safety margin.

Finally, tracking studies were done to determine the effects of the physical aperture in the wiggler, which is expected to be the limiting aperture [10].

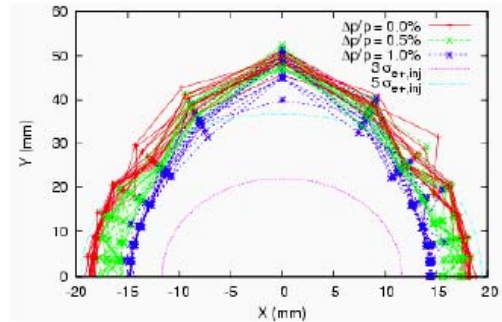


Figure 1: Dynamic aperture in the OCS lattice with modified CESRc wiggler model and multipole errors.

### Low Emittance

The achievement of ultra low vertical emittance is one of the challenges of DR. This requires very good alignment tolerances, lattices with low sensitivity to alignment errors, beam based alignment techniques, efficient coupling and dispersion correction algorithms, and high resolution beam position monitors [11].

Simulations show that, assuming the alignment errors of the KEK ATF ring, the design vertical emittance of 2 pm could be achieved in the OCS ring. Anyway an experimental demonstration of such a low emittance is still expected.

Intensive studying on the feasibility of an even smaller vertical emittance are performed for the CLIC DR [12].

### E-cloud

Electron cloud effects were one of the crucial issues in the choice of the circumference for the ILC baseline configuration. Studies to benchmark the simulation codes against experimental data are ongoing at the CERN SPS, DAΦNE, the PSR, PEP-II and KEKB; so far, the results of the simulation codes are generally supported by experimental data.

The build-up of the electron cloud is strongly dependent on the bunch separation, which decreases with the damping ring circumference; therefore reducing the circumference can make electron cloud effects more severe. Electron cloud can be difficult to suppress in the dipole and wiggler regions where it is expected to be most severe. Careful estimates were made of the secondary electron yield threshold for electron cloud build-up, and the related single- and coupled-bunch instabilities, as a function of beam current and surface properties for a variety of optics designs [13]. On the basis of this work, the baseline configuration currently specifies a pair of

6 km damping rings for the positron beam. It would be highly desirable to find possible solutions to mitigate the effects of the electron cloud in order to achieve the nominal design parameters in a single 6 km ring.

### *Fast Ion Instabilities*

Due to high bunch density and short bunch spacing fast ion instabilities could be a serious problem for electron DR. Gaps in the bunch fill pattern can reduce the ion density by a factor 100 and even more. Feedback system can suppress the instability in the ILC DR, even for 3ns bunch spacing, if there is sufficient gap between the trains. This argument is treated in many papers at this conference [14, 15, 16, 17, 18].

### *Other Collective Instabilities*

In the absence of a detailed design of the vacuum components, a preliminary estimate of the ILC DR broadband impedance has been performed scaling from PEP-II-LER. To mitigate the risk of operating above the microwave instability threshold the present version of the OCS lattice has a higher momentum compaction and therefore a high RF voltage, which drives a cost increase. Possible solutions have been considered: first of all the design of a low impedance vacuum chamber; as an alternative the use of a high harmonic RF cavity to shorten the bunch or a negative momentum compaction lattice that could allow a shorter bunch length, as shown by recent measurements at DAFNE, and could allow to operate with negative chromaticity at reduced sextupole strengths [19].

Other collective effects are Intrabeam Scattering (IBS) [20] and space charge effect [21]. The first is extremely important for the CLIC DR [4], the second is important only for very long DR, as the TESLA DR, but should not be a concern for the OCS ring.

## TECHNOLOGICAL ISSUES

### *Fast Kickers*

The injection and extraction kickers are one of the most critical issues since the bunch distance in the ring, and therefore the choice of the ring circumference, are related to the kicker pulse duration; moreover the stability of the beam position at the IP depends also on the kicker pulse stability. R&D programs are in progress in different laboratories at a global level both on the fast pulsers and on the stripline electrodes.

The injection and extraction kickers for the positron should satisfy the following requirements: ultra short rise and fall time (total pulse duration  $< 12.4$  ns for  $e^+$ ,  $< 6.2$  ns for  $e^-$ ); good uniformity; low impedance; 3 Mhz for  $e^+$  (6 Mhz for  $e^-$ ) repetition rate.

Stripline kickers studied for the ILC positron DR can be used for an upgrade of the DAΦNE injection system (see Fig. 2). This will allow to test with beam measurements the achievement of the kicker performances and

possibly to test new fast pulsers. High voltage test on a prototype have been successfully made [22].

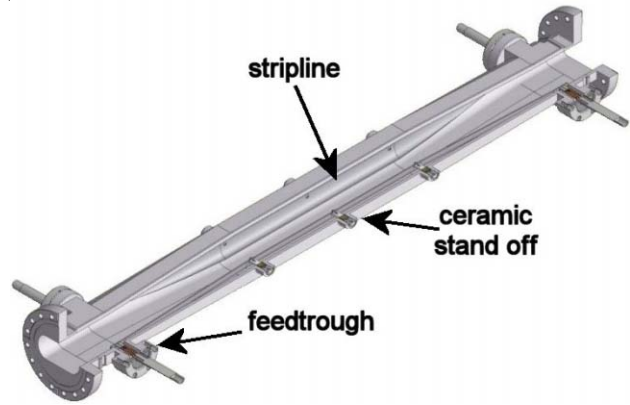


Figure 2: Mechanical drawing of the kicker.

The striplines, 327 mm long, producing beam deflection of 0.1 mrad with 7 kV voltage pulses at 1.28 GeV installed at the KEK-ATF were used to test pulsers with beam. A total width of the main pulse around 5 ns has been achieved, with a small pulse ahead of the main pulse, and a tail of more than 5 ns. Tests to correct these effects have been done connecting two pulsers with opposite polarity and achieving a sharp edge with 2.2 ns rise time [23].

Although results so far indicate the feasibility of kickers with rise/fall times sufficient to allow bunch separations as short as 3 ns, the full specifications have not yet been achieved. Pulse repetition rates of 3 Mhz have been demonstrated, but the specifications for the pulse amplitude stability look still to be very challenging.

There is a fruitful collaboration between many laboratories on the kickers and pulsers R&D [24, 25], and the performances achieved are rapidly improving.

### *Wigglers*

A high quality field is needed to achieve the dynamic aperture necessary for good injection efficiency. A large gap is needed to achieve the necessary acceptance for the large injected positron beam: a full aperture of at least 32 mm is highly desirable for injection efficiency.

Wiggler technology Baseline: The CESR-c SC wigglers have demonstrated the basic requirements for the ILC damping ring wigglers and have been chosen as baseline, since they allow for a very good field uniformity in a large aperture [26].

Alternatives are Hybrid PM wigglers [27] that have the advantage of not requiring power supplies, cabling, cooling and cryogenics. A design with acceptable costs for hybrid wigglers, meeting specifications for aperture and field quality, steel needs to be developed.

New wigglers for CLIC based both on SC and PM technology have been proposed. In this case the challenges are in the achievement of the highest field with the lowest period length and the handling of the heating due to the synchrotron radiation [4].

## Feedbacks

A digital feedback system of the type used at DAΦNE, PEP-II and KEKB is certainly recommended for the DR: in a digital system the feedback gain can be increased without increasing the noise. A stripline electrode can be used as kicker in the transverse plane and an overdamped cavity (DAΦNE type) in the longitudinal plane. The minimum feedback damping time measured at DAΦNE is 6 ms, corresponding to 20 turns with a 500 W power amplifier.

Tests of an FPGA based feedback system were recently made by an international collaboration at KEKB and ATF [28].

## TEST FACILITIES

### Accelerator Test Facility ATF

The KEK Accelerator Test Facility (ATF) is a 1.3GeV storage ring capable of producing ultra-low emittance electron beams and has a beam extraction line for ILC R&D [29]. The ATF has proven to be an ideal place for researches with small, stable beams:  $2 \times 10^{10}$  single bunch and low current 20 bunch-train with 2.8nsec bunch spacing have been extracted.

The DR is used by an international collaboration for beam dynamics studies, as fast ion instability, micro-wave instability, damping wigglers, and for developing specific DR instrumentation, as pulsed laser wire monitor, X-ray SR monitor, very fast kicker with about 1nsec rise/fall time.

The smallest vertical emittance has been achieved in single-bunch-mode operation at ATF. The emittances were measured with a laser-wire beam-profile monitor installed in the DR. The bunch length and the momentum spread of the beam were also recorded under the same conditions. The smallest vertical rms emittance measured is 4 pm in the limit of zero current. It increases by a factor of 1.5 for a bunch intensity of  $10^{10}$  electrons. There are no discrepancies between the measured data and the calculations of intra-beam scattering.

The ATF2 proposal aims to create a final focus test facility that, using a low emittance ILC-like bunch train extracted from ATF1 and compact final focus optics, would be capable of achieving 37 nm beam size with a beam centroid stability within a few nm.

### New Proposals

CESR-c as DR test facility. In 2008 it will be possible to reconfigure CESR as a damping ring test facility, CesrTF, for the ILC project. With its complement of 12 damping wigglers that meet or exceed all ILC damping ring requirements, CesrTF will offer horizontal emittances in the few nanometer range and the ability to operate with positrons or electrons [30].

The HERA electron ring, which ends operation mid 2007, matches almost perfectly the major DR design parameters; therefore it has been proposed to use it for the ILC DR [31].

## R&D PLANS

R&D plans are in progress at a worldwide level. The ILC activity is leaded by GDE, which has a dedicated R&D board to coordinate the activity for the whole project. For the damping ring an international working group on voluntary base has been set-up. The activity of this group is coordinated by the 4 DR Area Leaders and is focused on tasks, with a task coordinator, dedicated to the major issues. Regional organizations and funding, as EUROTeV in Europe, are present. There is a strict collaboration with the CLIC DR activity in the tasks dedicated to common issues, the most important are e-cloud and fast ion instabilities.

The ongoing activity is well represented by the many papers presented at this conference on DR issues. Based on the proposal of the research groups a list of R&D activities for the DR has been compiled and will be discussed at the next GDE meeting at Vancouver.

### Beam Dynamics Single Particle

Lattice design activities will continue in order to optimize the performance, improving dynamic aperture, reducing sensitivities to errors and misalignments and to different instabilities and at the same time setting the specifications for the technical systems.

### Beam Dynamics Multi Particle

R&D efforts are in progress worldwide to improve simulation codes benchmarking at existing facilities in order to fully characterize e-cloud instability and to find cures to mitigate it.

Between the possible solutions vacuum chamber coatings with low SEY materials, and grooves in the chamber have been proposed. At present a very promising solution is the use of clearing electrodes [32], which, should strongly reduce the electron density in the beam region. Further study and experimental demonstration are needed.

Characterize the fast ion instability and define the requirements for vacuum chamber pressure, gaps in the fill pattern and feedback systems in the electron DR.

Develop impedance models, and calculate short and long-range wakefields and single-bunch instability thresholds to characterize single and multi-bunch instabilities.

Characterize space-charge effects, estimate emittance growth from IBS, estimate the impact from coherent synchrotron radiation (CSR), injection and extraction transients, Touschek lifetime.

### Technical Subsystems

Optimize designs of vacuum system components in order to minimize single and multi bunch instabilities, handle the high synchrotron radiation power in the wiggler sections and mitigate effects of e-cloud and fast ion instability.

Develop design of wigglers satisfying DR requirements for aperture and field quality, peak field and period length

and synchrotron radiation power handling and e-cloud mitigation.

Develop stripline electrode design and high power pulser for fast injection/extraction kickers.

Develop dedicated diagnostics as high resolution bpms, precision bunch-by-bunch beam size monitor, instrumentation for monitoring emittance damping, fast dispersion measurements.

Design low noise, fast damping time transverse and longitudinal feedback systems.

### Tests

The most important tests to demonstrate DR performance are the measurement of a vertical emittance lower than 2 pm, the effectiveness of cures for e-cloud instability and the beam tests of fast injection/extraction kickers.

## REFERENCES

- [1] P. Raimondi et al., “Luminosity Upgrades For The SLC”, PAC99, New York, 1999.
- [2] K. L.F. Bane et al, “Impedance Calculation and verification in storage Rings”, SLAC-PUB-11007, January 2005.
- [3] H. Braun, “CLIC Progress Towards Multi-TeV Linear Colliders”, PAC05, Knoxville, 2005.
- [4] H. Braun et al, “Minimizing Emittance for the CLIC Damping Ring”, these Proceedings.
- [5] A. Wolski, J. Gao, S. Guiducci, “Choosing a Baseline Configuration for the ILC Damping Rings”, these Proceedings.
- [6] A. Wolski, J. Gao, S. Guiducci, “Configuration Studies and Recommendations for the ILC Damping Rings”, LBNL-59449 (February 2006).
- [7] A. Xiao, “Damping Rings lattice design”, [http://www.desy.de/~awolski/ILCDR/USTeleconference\\_files/2006-03-01/ILC1.pdf](http://www.desy.de/~awolski/ILCDR/USTeleconference_files/2006-03-01/ILC1.pdf)
- [8] Y. Sun, “Optimization of ILC Damping Rings Lattice”, these Proceedings.
- [9] E. Kim, “Lattice Design of a 6 km Electron Damping Ring for International Linear Collider”, these Proceedings.
- [10] I. Reichel, A. Wolski, “Tracking Studies to Determine the Required Wiggler Aperture for the ILC Damping Rings”, these Proceedings.
- [11] J. Jones, “Tuning Algorithms for the ILC Damping Rings”, these Proceedings.
- [12] M. Korostelev et al, ”Correction of Vertical Dispersion and Betatron Coupling for the CLIC Damping”, these Proceedings.
- [13] M.T.F. Pivi et al, “Simulation of the Electron Cloud for Various Configurations of a Damping Ring for the ILC”, these Proceedings.
- [14] G. Xia, “Preliminary Studies of Ion Effects in ILC Damping Rings”, these Proceedings.
- [15] F. Zimmermann et al, “Ion Effects in the Damping Rings of ILC and CLIC”, these Proceedings.
- [16] L. Wang et al, “Ion Effects in the Electron Damping Ring of the International Linear Collider”, these Proceedings.
- [17] E. Kim, K. Ohmi, “Simulations on Fast-ion Instabilities in the ILC Damping Rings”, these Proceedings.
- [18] L. Wang et al, “Ion Effects in the Electron Damping Ring of the International Linear Collider”, these Proceedings.
- [19] M. Zobov et al., “DAFNE with negative momentum compaction”, these Proceedings.
- [20] I. Reichel, A. Wolski, “Intrabeam Scattering Studies for the ILC Damping Rings Using a New Matlab Code”, these Proceedings.
- [21] M. Venturini, A. Wolski, “Space Charge and Equilibrium Emittances in Damping Rings”, these Proceedings.
- [22] D. Alesini et al, “Design and Tests of New Fast Kickers for the DAFNE Collider and the ILC Damping Rings”, these Proceedings.
- [23] J. Urakawa, “New Results in Kicker Studies and Instrumentation”, GDE meeting, Bangalore, March 2006.
- [24] S. De Santis et al, “Design of a Fast Extraction Kicker for the Advanced Test Facility”, these Proceedings.
- [25] M.A. Palmer et al, “Tests of a High Voltage Pulser for ILC Damping Ring Kickers”, these Proceedings.
- [26] M.A. Palmer et al, “Optimization of CESR-c Superferric Wiggler for the International Linear Collider Damping Rings”, these Proceedings.
- [27] A. Babayan, et al., “Wiggler Magnet Optimization for Linear Collider Damping Ring”, EUROTeV-Report-2006-011.
- [28] D. Teytelman et al., “Design and Testing of Gproto Bunch-by-bunch Signal Processor”, These Proceedings.
- [29] J. Urakawa, “Results From DR and Instrumentation Test Facilities”, PAC05, Knoxville, 2005.
- [30] M. A. Palmer et al, “The Proposed Conversion of CESR to an ILC Damping Ring Test Facility”, these Proceedings.
- [31] F. Willeke, “The use of the HERA Electron Ring in Conjunction with ILC Damping Rings”, <http://events.lal.in2p3.fr/conferences/eaef/>
- [32] H. Fukuma, et al., “A Perfect Electrode to Suppress Secondary Electrons inside Various Magnets”, these Proceedings.

# CLIC FEASIBILITY STUDY IN CTF3

A. Ghigo for the CLIC Collaboration, INFN/LNF, Frascati (Roma), Italy

## Abstract

The CLIC Test Facility, (CTF3), under construction and test at CERN is the product of a multilateral international collaboration to address all the key issues of the CLIC technology. The presentation, after the description of the CLIC scheme towards multi-TeV Linear Collider and of the main advantage of the two beams accelerator scheme, will focus on the status of the CTF3 project and of the technological developments; in particular the performances already achieved in the high field accelerating structures and in the RF power production. The results of the recombination process for the drive beam as well as the plans and schedule for the future are reported.

## INTRODUCTION

The High Energy Physics experiments, after exploration of the 100 GeV (center of mass c.m.) energy range by the hadrons colliders at CERN and Fermilab and by the electron-positron colliders LEP and SLC, are moving in these years in the range of TeV scale that will be first investigated at CERN by the Large Hadrons Collider (LHC).

New generation of  $e^+e^-$  colliders, with luminosity values larger than  $10^{34} \text{ cm}^{-2}\text{s}^{-1}$ , will be needed to make the complementary precision measurements, as happened in the past, in the same energy range because of the cleanliness of the events. The  $e^+e^-$  accelerator candidate for TeV energy ranges, at the moment the only one, is the linear collider. Several projects have been proposed for different energy ranges. The effort in these years is converging on a worldwide project: the International Linear Collider (ILC) that has the goal to investigate with high luminosity the c.m. energy range of 500 GeV with the possibility to increase energy up to 1 TeV [1]. The ILC program foresees a technical design report for the construction of the collider using superconducting accelerating structures ready for the end of 2009.

Several theories beyond the Standard Model, that foresees supersymmetry, extra dimensions or new strong interactions, predict new dynamics at the TeV scale. Supersymmetry with relative sparticle production as well as heavy mass Higgs bosons can be studied by raising the energy up to 5 TeV [2].

The Compact Linear Collider (CLIC) can cover the c.m. energy range for  $e^+e^-$  collisions between 0.5 - 5 TeV adopting an unconventional technique to accelerate the beams limiting the overall length of the accelerator.

## CLIC

CLIC is based on two-beam acceleration method in which the RF power for the main linac sections is produced by a high intensity, low energy electron beam, called drive beam, running parallel to the main linac [3, 4]. The power is extracted by decelerating the

drive beam by special Power Extraction and Transfer Structures (PETS).

Increasing the accelerating gradient limits the length of the collider: this is possible using high frequency, normal conducting, and travelling wave accelerating structures.

The electron and positron beams are accelerated in 30 GHz RF cavities with a loaded accelerating gradient of 150 MV/m on 70 ns pulse length. The design and fabrication of the structures call for perfect structure straightness tight, alignment tolerance and long-range wake field suppression to preserve the beam emittance.

The CLIC parameters optimised at c.m. energy of 3 TeV are shown in Table 1. Figure 1 shows the layout of the accelerator complex.

The drive beam linear accelerator produces 94  $\mu\text{s}$  long electron pulses at the energy of 2.4 GeV using RF power from 350 klystrons with a power of 40 MW each. The compressor system formed by three recombination rings provides a series of pulses 70 ns long with a current of 180 A. These pulses pump 21 decelerator sectors 669 m long where the power is extracted and transferred to the 30 GHz accelerating structures. The main beams are generated in the 2.4 GeV pre-injectors, reduced in emittance in the damping rings, accelerated in a linac booster to 9 GeV, recombined reducing the bunch spacing to 8 cm and finally injected in the main linac to increase the energy up to 3 TeV.

Table 1: CLIC parameters

Parameter	Unit	
Energy (center of mass)	TeV	3
Total length	km	33.6
Luminosity	$\text{cm}^{-2}\text{s}^{-1}$	$6.5 \times 10^{34}$
Luminosity (in 1% energy)	$\text{cm}^{-2}\text{s}^{-1}$	$3.3 \times 10^{34}$
Beamstrahlung mom. spread	%	16
Main Linac RF frequency	GHz	30
Gradient loaded/unloaded	MV/m	172 / 150
Linac repetition rate	Hz	150
No. of particle / bunch		$2.5 \times 10^9$
No. of bunch / pulse		220
Bunch separation	ns	0.267
Bunch train length	ns	58.4
$\sigma_H^* / \sigma_V^*$ before pinch	nm	60 / 0.7
Total site AC power	MW	418
Efficiency AC to Main beam	%	12.5

The foreseen luminosity value for CLIC is  $6.5 \times 10^{34} \text{ cm}^{-2}\text{s}^{-1}$  ( $3.3 \times 10^{34}$  in a 1% energy bin).

To obtain such high luminosity the beam size at the interaction point must be in nanometer range; this is a characteristic of the high frequency linac; in fact it is possible to reduce the bunch length and focus the beam with optical functions of the order of millimeters.

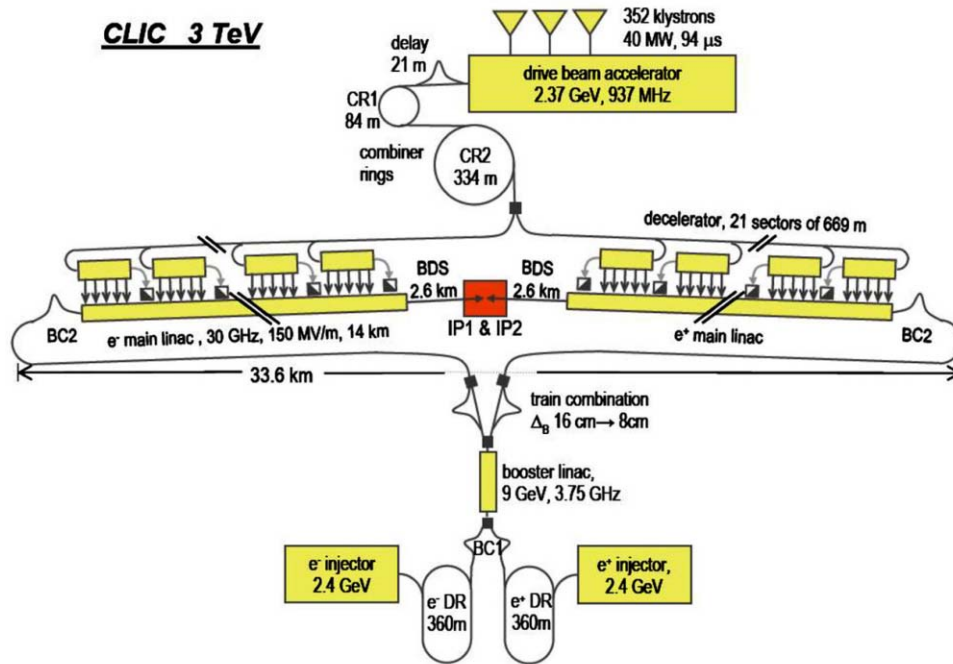


Figure 1: Layout of CLIC at 3 TeV.

In order to maintain the luminosity constant the beam delivery system has to be stabilized in the nm range. An R&D program dedicated to this important issue started at CERN using ultra stabilized optical bench and active feedbacks on mechanical positioning. Long term stability of quadrupole position within 0.5 nm has been demonstrated.

### CLIC TEST FACILITIES

The CLIC Test Facility programme addresses all the key issues of the CLIC technology.

The CLIC Study Group, in agreement with the recommendation of the International Linear Collider Review Committee (ILC-TRC), decided to focus the CTF3 activities on the R&D, test and validation of key feasibility issues [5]:

- Damped accelerating structure at designed gradient and pulse length.
- Drive beam generation with fully loaded linac.
- Power extraction and transfer structure (PETS).
- Structure with hard-breaking material (W, Mo).
- Stability and losses of drive beam decelerator.
- Linac sub-unit with the beam.

#### CTF1 and CTF2

CTF3 is not the first test machine for CLIC: in CTF1 and CTF2 the proof of principle of the dual beam acceleration was tested for short train of bunches [6]. A photoinjector was used to produce the electron beam that was accelerated by 3 GHz conventional linac sections. The beam was then decelerated by 30 GHz RF structure and the extracted power was sent to the input port of 30 GHz accelerating structures. A probe beam was accelerated demonstrating the two-beams accelerator scheme.

In CTF2 the possibility to achieve 190 MV/m accelerating gradient in a short pulse train was also demonstrated. This result was achieved after R&D activity on the 30 GHz RF accelerating structures; in particular, by changing the iris material to increase the damage threshold.

The accelerating gradient values achieved were 120, 150, 190 MV/m for copper, tungsten, molybdenum iris respectively.

#### CTF3 Preliminary Phase

The pre-injector of the Large Electron Positron collider (LEP) at CERN, composed by a 500 MeV linac and an accumulator ring (EPA) approximately 100 m long, will be not used in the new Large Hadron Collider (LHC). The complex became available after LEP decommissioning. The proposal to reuse the building, the infrastructures and the equipments to build a facility to test the CLIC components and validate the machine parameters was accepted.

The CLIC Test Facility 3 project started with a preliminary phase in which short trains of bunches (16 ns) were injected and recombined with interleaving technique in the slightly modified EPA ring [7].

The existing LIL Linac has been shortened to leave the first part of the linac tunnel free to install the new gun realized for CTF3 nominal phase.

CTF3 preliminary phase proved that it is possible to interleave up to five trains of bunches one inside the other. The beam is injected selectively by two 3 GHz RF deflectors used as injection kickers after fine tuning of the ring length and of the RF signal phase [8]. Reducing the bunch distance and the total pulse length the pulse current has been increased by a factor of five and the bunch frequency of 15 GHz has been obtained.

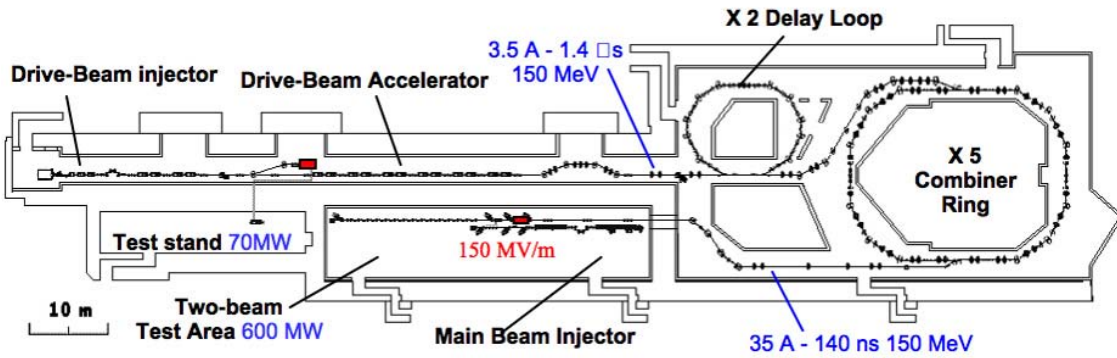


Figure 2: Layout of CTF3 Complex.

### CTF3

CTF3 must produce the drive beam with the characteristics necessary to test the CLIC components at the nominal parameters value.

In January 2002 the conceptual design report for the construction of CTF3 was ready [9] and the realization of the components started with contribution of the collaborating institutes (see Table 2).

The drive beam system is composed by a linac and a recombination system formed by two rings: the Delay Loop (DL) that provides a current/frequency multiplication by a factor of two and the Combiner Ring (CR) that allows multiplication by another factor of five [10]. The CLIC experimental area (CLEX) dedicated to the deceleration and acceleration test using the drive beam is now under construction (see Fig. 2).

#### Linac

The construction of the CTF3 complex started in 2003 with the installation of the injector in part of the LIL linac tunnel. This equipment has soon delivered full current of nominal pulse length.

In 2004 half of the 16 full loading sections of the linac and the transfer line, including a magnetic chicane and the beam measurement section have been installed.

The CTF3 3GHz fully loaded Linac produces a  $1.5 \mu\text{s}$  long train of bunches at 1.5GHz repetition rate with an average current along the train of 3.5 A. A sub-harmonic bunching system (bunch coding) permits to change the bunch phase along the train creating series of bunch sub-trains 140 ns long with  $180^\circ$  phase difference [11]. This system is necessary to double the frequency and the pulse current using the Delay Loop ring, and to create a series of 140 ns long bunch trains and empty gaps along the  $1.5 \mu\text{s}$  train necessary for the recombination procedure in the Combiner Ring.

The fully beam-loaded operation of the travelling wave section of the Drive Beam Accelerator (DBA) has been successfully tested by reusing all existing 3 GHz klystrons and modulators. The developed DBA sections are composed by 34 cells (2 with couplers); to reduce the dangerous High Order Mode excited by the beam, radial slots are machined in the iris creating four wave guides with cut-off frequency above the fundamental. The HOM

power is dissipated in wide band Silicon Carbide loads placed inside the waveguides [12].

The linac was commissioned and transfer efficiency from the RF power to the electron beam of 95% has been measured without any beam break-up observation.

In 2005 the rest of the linac sections have been installed and successfully commissioned.

#### Power Production Station and Test Stand

To continue the R&D work during the installation of the pulse compressor system (DL & CR), a 30 GHz power production station has been installed parallel to the linac in the tunnel. A dogleg line joins the PETS to the linac to allow fast switch between 30 GHz RF power production and operation mode and the commissioning of the rest of the CTF3 complex. Using approximately one third of the linac length, the electron beam at the power station has an energy of 70 MeV, current of 6.4 A, bunch length of 1 mm and 3 GHz of bunch frequency [13]. The power extracted is transferred by means of a 17 m long waveguide to a neighbouring laboratory, the old CTF2 tunnel, where the 30 GHz accelerating structures are tested.

The power production station has been continuously operated for the conditioning and test of the accelerating structure. More than 100 MW of RF power at 30 GHz has been extracted by PETS in 70 ns long pulse, and transferred with 75% efficiency to the test stand [14].

The accelerating gradient of 140 MV/m at 70 ns pulse length has been routinely achieved.

Breakdown probabilities of different cavity configuration versus the peak gradient and peak gradient versus pulse length have been measured. The 30 GHz accelerating structures, 500 mm long, have been produced brazing 150 disks. In each disk, half cavity and HOM absorber aperture have been machined. A new fabrication method has been adopted in which the entire structure is longitudinally divided into quadrants. All the quadrant cavities are machined by single metal blocks including the cooling and vacuum channels. The quarter sections are then longitudinally brazed. Advantages in terms of electrical conductance and vacuum quality to lower the breakdown rate, employing this method are expected together with reduction of the production cost. The first accelerating section produced with this method is now under test.

Table 2: CLIC / CTF3 collaborating Institutes and their contribution

Ankara University (Turkey)	CTF3 beam studies & operation
Berlin Tech. University (Germany)	Structure simulations
BINP (Russia)	CTF3 magnet development and construction
CCLRC / RAL (England)	Laser for CTF3 and CLIC photo-injector
CERN	Study coordination, Structures R&D, CTF3 construction and commissioning
CIEMAT (Spain)	CTF3 septa and kicker, correctors, PETS
DAPNIA / Saclay (France)	CTF3 probe beam injector
Finnish Industry (Finland)	Sponsorship of mechanical engineer
INFN / LNF (Italy)	CTF3 Delay Loop, transfer lines & RF deflectors, ring vacuum chambers
JINR & IAP (Russia)	Surface heating tests of 30 GHz structures
KEK (Japan)	Low emittance beams in ATF
LAL / Orsay (France)	CTF3 Electron guns and pre-buncher cavities
LAP / ESIA (France)	CTF3 beam position monitor electronics, stabilization studies
LLBL / LBL (USA)	Laser wire studies
North-West University Illinois (USA)	Beam loss studies & CTF3 equipment
SLAC (USA)	CTF3 injector, high gradient structures design & test
Uppsala Univ. (Sweden)	CTF3 high frequency beam monitoring system

### *Transfer Line and Magnetic Chicane*

The first part of the transfer line between the linac and the Delay Loop has been also installed in 2004 including a magnetic chicane and beam measurement station.

In particular the magnetic chicane is used to control the bunch length by changing the optical functions (R56 parameter), to avoid the beam degradation due to the coherent synchrotron radiation [15].

The measurement line is composed by a magnetic spectrometer to measure the energy and energy spread, an Optical Transition Radiation station to measure the beam transverse distributions and the emittance in conjunction with the upstream quadrupoles. An optical line that transfers the OTR light to an external laboratory equipped with a streak camera for the bunch length measurement has been also installed.

An alternative method to measure the bunch length with a resolution better than the 2 ps of the existing streak camera is the use of the RF deflector, already realized for CTF3, in the zero crossing mode. The bunch particles, passing through this RF structure, are differently deflected depending on their longitudinal position; the OTR monitor is used to detect the transverse distribution to deduce, after accurate calibration, the longitudinal one. The resolution obtained was better than 0.7 ps and a minimum bunch length of 0.5mm has been obtained setting the chicane in the bunch compression mode [16].

### *Recombination System*

The pulse recombination system is composed by two rings: the Delay Loop and the Combiner Ring. To obtain the maximum power extraction efficiency the drive beam must have short bunches equally spaced. Design criteria of these rings are dictated in order to fulfil these requirements; the energy spread should be as small as possible and the machine lattice has to be isochronous in

order to avoid lengthening of bunches. Also the energy loss must be small to avoid that the bunches of different trains, performing a different number of turns in the ring, have different spacing.

All the vacuum chamber components are designed with very low coupling impedance to minimize the energy loss and energy spread in the beam. A simulation study of the coherent synchrotron radiation (CSR) has shown that the bunch length should be increased, through the chicane, in all bunches up to the limit in which the energy spread due to the CSR becomes acceptable.

The Delay Loop has been installed in 2005 sharing the time with the linac operation. The commissioning started at the end of the year showing good transmission efficiency between the injection/extraction by means of innovative 1.5 GHz RF deflector [17]. In April and May this year the recombination process has been successfully proved switching on the bunch coding system and setting the nominal isochronous optic for the Delay Loop.

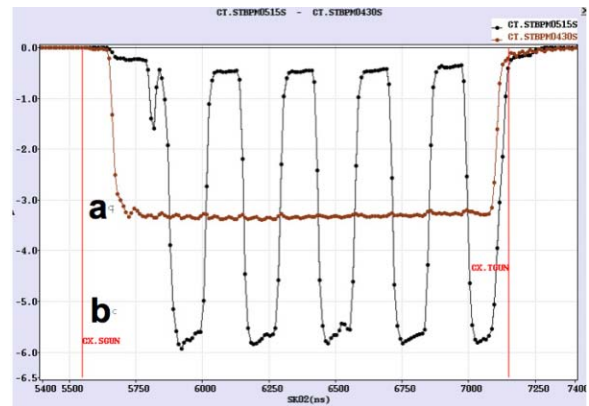


Figure 3: bunch trains recombination in the Delay Loop: a) train of bunches at the Linac end, b) bunch trains after Delay Loop.

In Fig. 3 the beam position monitor (BPM) signals are summed in order to give a total current measurement: trace a) shows the current distribution along the 1.5  $\mu$ s long train (the 1.5 GHz fine structure is not detected because of the low frequency response of the monitor. Trace b) shows the BPM signal after the Delay Loop in which the trains with opposite phase have been recombined doubling the current of the incoming beam up to 6 A on the five pulses with the nominal pulse duration of 140 ns [18].

### *Future Program*

In order to complete the CTF3 program within 2010 a new work program has been launched in 2004 organizing the project with a more extended collaboration as shown in Table 2.

The Combiner Ring design is accomplished and the layout frozen. The magnet positioning and the vacuum chamber realization have started with the target to complete the installation of the ring and the transfer line that joins the two rings by the end of the year. The commissioning activity is foreseen for the early 2007.

In the same period the realization the CLIC experimental area (CLEX) building will be completed. The building, placed parallel to the CTF3 drive beam linac tunnel, will host the injector that provides the probe beam that will be accelerated in the dual beam acceleration scheme. This injector will be used to test the acceleration in the 30 GHz structures, the effects of RF breakdown, wakefield and beam loading in the two beam test stand. Using an RF photoinjector and a velocity bunching system, also short bunches ( $\sigma_t < 0.8$  ps) with low emittance will be produced to test the high resolution diagnostic systems.

The Test Beam Line (TBL) is a scaled version of the CLIC decelerator sector. It is composed by 14 PETS structures; this will be used to extract the power from the drive beam. It will be used to validate beam stability in the drive-beam decelerator [19].

A Joint Research Activity to develop the high charge long pulse photoinjector for the CTF3 and CLIC drive beam has been founded by EU Commission in the FP6 program. The realization phase is well advanced; The first test with beam is foreseen next year [20].

## CONCLUSIONS

CLIC technology is not completely mature and it still requires challenging R&D. In CTF1, CTF2 and in the first step of new CTF3 many promising results have been obtained.

The CLIC Test facility 3 is in the installation phase by an international collaboration to demonstrate the CLIC feasibility before 2010. The construction of the CTF3 complex has been advanced in stages and so far the installed parts have been successfully commissioned.

## REFERENCES

- [1] <http://www.linearcollider.org/cms/>
- [2] M. Battaglia, A. De Roeck, J. Ellis, D. Shulte (eds.), "Physics at the CLIC multi TeV Linear Collider", CERN Reports Physics Dept. CERN-2004-005.
- [3] J.P.Delahaye for CLIC team, "The CLIC study of a multi-TeV  $e^+e^-$  linear colliders", Proc. PAC99 New York, USA.
- [4] G.Guignard (ed.), "A 3 TeV  $e^+e^-$  linear collider based on CLIC technology", CERN 2000-008 and R.Corsini (ed.) "The CLIC power source" CERN Yellow Report 99-06.
- [5] H.H. Braun for CLIC team "CLIC progress towards multi-TeV linear colliders", Proceedings of PAC 2005, Knoxville.
- [6] H.H. Braun "CTF2 description and performances", Proceedings of VIII International Workshop on Linear Collider, LC 1999, Frascati, Italy.
- [7] D.Allard et al., "CTF3 design report – Preliminary phase", CERN/PS, 2001-072 (RF).
- [8] D. Alesini et al. "RF beam deflector for CTF3 combiner ring", Proceedings of EPAC 2002, Paris, France.
- [9] G.Geschonke, A.Ghigo (ed.), "CTF3 Design Report", CERN/PS 2002-008(RF), LNF-02/008 (IR).
- [10] D.Alesini et al., "CTF3 compressor system", Proceedings of EPAC 2002, Paris, France.
- [11] G.Carron et al., "Beam dynamics and first operation of the sub-harmonic bunching system in CTF3 injector", these Proceedings.
- [12] G. Carron et al., "Design of a 3 GHz accelerator structure for the CLIC test facility (CTF3) drive beam", Proceedings of the XX International Linac Conference, Monterey 2000, California
- [13] C. Achard et al., "30 GHz power production in CTF3", Proceedings of PAC 2005, Knoxville, USA.
- [14] W. Wuensch et al., "A high-gradient test of a 30 GHz Molybdenum-iris structure", these Proceedings.
- [15] A. Ghigo et al., "Commissioning and First Measurements on the CTF3 Chicane", Proceedings of PAC 2005, Knoxville.
- [16] D. Alesini et al. "Longitudinal phase space characterization of the CTF3 beam with the RF deflector", Proceedings of PAC 2005, Knoxville.
- [17] F. Marcellini et al., "The RF deflector for the CTF3 Delay Loop" these Proceedings
- [18] C. Biscari et al., "Commissioning status of the CTF3 Delay Loop", these Proceedings.
- [19] E. Adli et al., "Progress on CF3-TBL", these proceedings.
- [20] G. Bienvenu et al., "The PHIN photoinjector for the CTF3 drive beam" these Proceedings.

## OVERVIEW OF FEL INJECTORS

M. Ferrario, INFN-LNF, Frascati, Italy

### Abstract

Future light sources based on high gain free electron lasers, require the production, acceleration and transport up to the undulator entrance of high brightness (low emittance, high peak current) electron bunches. Wake fields effects in accelerating sections and in magnetic bunch compressors typically contribute to emittance degradation, hence the injector design and its operation is the leading edge for high quality beam production and for the success of the future light sources. DC and RF guns, photo-cathode materials, laser pulse shaping and sub-ps synchronization systems are evolving towards a mature technology to produce high quality and stable beams. Nevertheless reduction of thermal emittance, damping of emittance oscillations and bunch compression are still the main issues and challenges for injector designs. With the advent of Energy Recovery Linacs, superconducting RF guns have been also considered in many new projects as a possible electron source operating in CW mode. An overview of recent advancements and future perspectives in FEL injectors will be illustrated in this talk.

### INTRODUCTION

After the successful demonstration of exponential gain in a Self Amplified Spontaneous Emission Free Electron Laser (SASE-FEL) at UCLA and LANL and the operation up to saturation with the LEUTL (500 nm), TTF\_II (93 nm) and VISA (800 nm) experiments, including harmonic generation at HGHG, a number of short wavelength SASE-FEL projects have been funded or proposed world wide, oriented as user facilities. The choice of FEL radiation wavelength ranges from 100 nm down to 1 Angstrom (LCLS and XFEL) and the adopted linac technology is based on normal conducting (S-band or C-band) or superconducting accelerating structures (L-band), see Fig. 1.

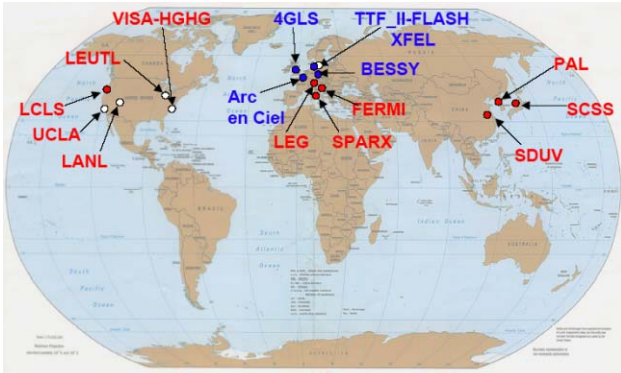


Figure 1: IV generation synchrotron light sources based on short wavelength FEL world distribution. Red and blue labels: FEL projects based on normal conducting or superconducting technology respectively. White circles: first SASE demonstrative experiments.

The optimization of the FEL parameters is quite a complicated task [1] but the main requirement for the electron beam in order to achieve short wavelength radiation in a reasonable long undulator (30-100 m) is clear: high transverse brightness and low energy spread ( $\sim 0.1\%$ ). Transverse beam brightness is defined hereafter with the approximated [2] expression:

$$B_{\perp} \approx \frac{2I}{\varepsilon_{n,x}\varepsilon_{n,y}}$$

where  $I$  is the bunch peak current and  $\varepsilon_n$  is the bunch transverse normalised emittance. The expected transverse brightness for electron beams driving short wavelength SASE FEL facilities is of the order of  $10^{15} - 10^{16}$  A/m<sup>2</sup>. High brightness beam essentially means high bunch charge density (with peak currents of several kA) and low emittance ( $\sim 1$   $\mu\text{m}$ ). The difficulties to achieve such a high quality beam are partially mitigated by the fact that the FEL resonance condition implies that electrons slips back in phase with respect to photons by one radiation wavelength  $\lambda_r$  per undulator period  $\lambda_u$ . Hence radiation amplification occurs on a scale length of the slippage length  $L_s = N_u \lambda_r$ , where  $N_u$  is the number of undulator periods, typically much shorter than the bunch length so that bunch slice parameters are important. Wake fields effects in accelerating sections and in magnetic bunch compressors typically contribute to emittance degradation, hence the injector design and its operation is the leading edge for high quality beam production and for the success of the future light sources. DC and RF guns, photo-cathode materials, laser pulse shaping and sub-ps synchronization systems are evolving towards a mature technology to produce high quality and stable beams. In particular the technique termed “emittance compensation” [3] has been experimentally verified in many laboratories and theoretically well understood [4]. It is important to emphasize that high charge density beams experience two distinct regimes along the accelerator, depending on the laminarity parameter  $\rho$  defined as the ratio between the space charge and the thermal emittance  $\varepsilon_{th}$  terms in the transverse envelope equation:

$$\rho = \left( \frac{I}{\gamma\gamma' I_A \varepsilon_{th}} \right)^2$$

where  $I_A$  is the Alfvén current, and  $\gamma' \sim 2E_{acc}$  [MeV] is the normalised gradient. When  $\rho \gg 1$  the transverse beam dynamics is dominated by space charge effects, the typical injector regime. Correlated emittance oscillations are observed in this regime [4], caused by the different local current along the bunch and by finite bunch length effects. In this case special matching condition should be adopted (invariant envelope [4]) to properly damp the

residual correlated emittance oscillations. By accelerating the beam, a transition occurs to the so-called emittance dominated regime, when  $\rho \ll 1$ , in this case the transverse beam dynamics is dominated by the emittance and correlated effects are not anymore observed. In case of bunch compressor systems are foreseen along the linac space charge effects might become important again and the transition from space charge to emittance dominated regime shift at higher energy, see Fig. 2. In this case the whole linac behaves like a long injector [5] and the same matching techniques [4,5] should be adopted also at higher energy.

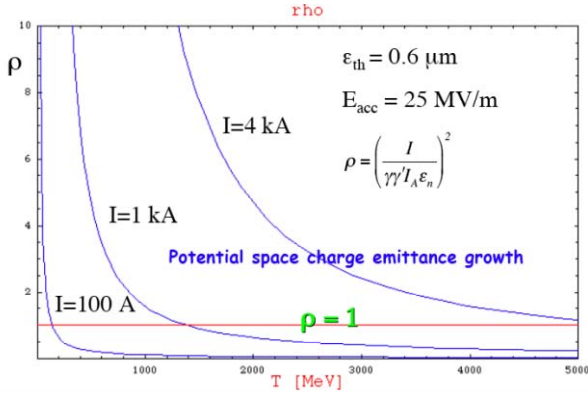


Figure 2: Laminarity parameter  $\rho$  versus beam energy  $T$  for different beam currents. Notice for example that a 1 kA beam is space charge dominated up to 1 GeV.

In the next sections the state of the art of normal conducting and superconducting injectors will be briefly discussed taking some representative case as examples. For a more detailed and systematic analysis, not limited by conference proceeding requirements, see [6] and [7].

## HIGH PEAK BRIGHTNESS INJECTORS

As shown in Fig. 3 the brightness achieved so far by the operating injectors is not sufficient to drive short wavelength SASE FEL experiments, thus requiring additional bunch compression schemes downstream the injector in order to reach the  $10^{15}$  A/m<sup>2</sup> threshold.

As one can notice from the plot, the brightness increases with the gun operating frequency, with a record well in excess of  $10^{14}$  A/m<sup>2</sup> achieved at ATF [8], obtained with an 1.6 cells S-band photo-injector, a widely used RF gun design shown in Fig. 4. In a RF photo-injector in fact, electrons are emitted by a photo-cathode located inside an RF cavity that is illuminated by a laser pulse, so that the bunch length and shape can be controlled on a picosecond time scale via the properties of the laser pulse. The emitted electrons are rapidly accelerated to relativistic energies, thus partially mitigating the emittance growth due to space charge force effects. Operation at higher frequency allows higher peak field in the RF cavity as it is desirable. The ATF results confirm the expected performance of a photoinjector after a long operating experience and improvements of the facility like the use of Mg cathode with QE=0.25 % to reduce the laser load

compared to the Cu cathodes with typical QE<0.1 %, high gradient in the cavity (> 130 MV/m), good alignment and stability of the driving laser and RF system.

Sumitomo Heavy Industries SHI results [9] are very important since they have demonstrated the advantages of using laser pulse shaping to reduce non-linear space charge effects in the beam. With a 10 ps flat top laser pulse with rising time shorter than 1.5 ps, produced by a femtosecond Ti:Sa laser system equipped with a liquid crystal spatial light modulator pulse shaper (LCM), they have measured at 14 MeV an emittance of 1.3  $\mu$ m at 1 nC charge, a reduction of a factor 2 with respect to a Gaussian electron distribution.

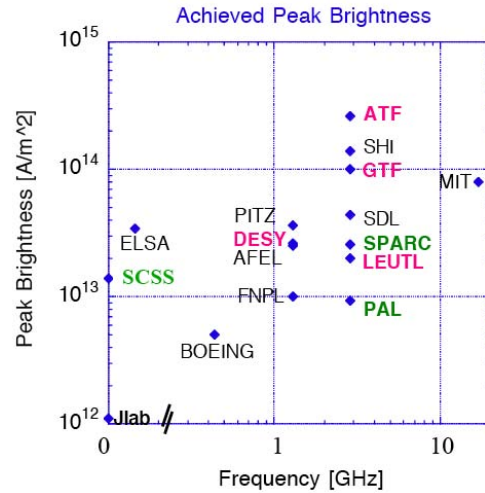


Figure 3: Achieved peak brightness versus gun frequency. Red labels: results achieved with  $\rho < 1$ , black labels: measurements performed at low energy  $\rho > 1$ , green labels: preliminary results of new facilities. DC guns are indicated as 0 frequency.

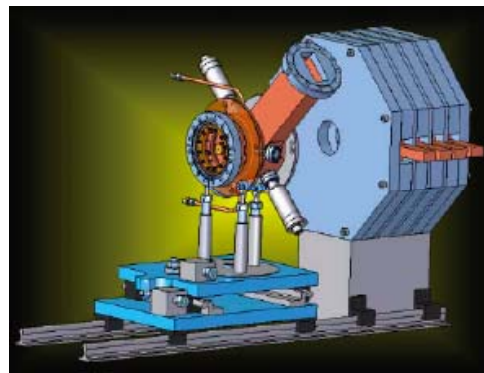


Figure 4: 1.6 cells S-band gun cavity of the BNL/SLAC/UCLA design with solenoid.

A 1.6 cells S-band gun design is foreseen also for the LCLS experiment [10], the first X-ray SASE FEL, whose commissioning will begin in January 2007 and whose expected brightness is  $2 \times 10^{14}$  A/m<sup>2</sup> at 135 MeV. The LCLS gun test facility GTF despite operating in a not fully optimised layout, has demonstrated the possibility to achieve the LCLS required brightness, at least in the low

charge (0.2 nC) operating mode. Several modification has been adopted for the final LCLS photoinjector [11], including laser pulse shaping and axial injection, increased mode separation, suppression of RF dipole and solenoid quadrupole field components.

A very similar photoinjector has began in March 2006 its commissioning stage: the SPARC project at INFN Frascati [12,13].



Figure 5: 1.6 cells S-band gun cavity with solenoid and movable emittance meter installed in the SPARC hall.

The peculiarity of this project is the possibility to test different laser pulse shaping techniques (based on DAZZLER and LCM) with an advanced diagnostic techniques, the so called movable emittance meter device [14], that gives the possibility to investigate the emittance compensation process along the 2 m long drift at the exit of the RF gun. One of the goal of the SPARC experiment is to confirm the theoretical prediction of a new working point for an optimal matching with the subsequent booster [15]. Preliminary results obtained so far with a not yet optimized machine operation, in particular without pulse shaping, are very encouraging showing the possibility to achieve a brightness of  $4 \times 10^{13}$  A/m<sup>2</sup> at 5.5 MeV. The possibility to compare simulations with experimental data [14] as a function of the beam position in the drift have also shown that when the beam waist is obtained at 1.5 m, where the booster will be located, the emittance minimum is found at 1.8 m as expected from the optimal working point. Operation with laser pulse shaping is foreseen in July.

L-band photoinjectors despite the lower peak field achievable (< 60 MV/m) and hence a lower expected peak brightness are able to generate long electron bunch trains (~ 800  $\mu$ s with MHz repetition rate) in long RF pulses with low emittance, as required to drive pulsed (10 Hz) superconducting RF linac. In addition high QE cathodes like Cs<sub>2</sub>Te (very sensitive to high peak field) can be used in this case, thus reducing the required laser pulse energy. The DESY injector is now routinely able to produce 20 ps long bunches with 1 nC Gaussian charge distribution and emittance of 2.1  $\mu$ m at 100 MeV. The high injector stability (certainly more important than unstable peak performances) achieved at DESY allowed the successful operation of the 13 nm SASE FEL experiment FLASH, a very remarkable and unique result.

At the PITZ gun test facility even better performances have been obtained (emittance ~ 1.1  $\mu$ m) with a flat top longitudinal profile, very close to meet the requirements for the X-FEL user facility.

In the early stage of the commissioning a photoinjector can be affected by many problems since its performances are strongly dependent on the uniformity and pointing stability of the laser beam, the Quantum Efficiency (QE) of the cathode, the dark currents when peak field exceeds 100 MV/m and in some case RF breakdown. For the reasons listed above a completely different and more conventional choice has been done for the SCSs injector that is recently entered in the commissioning stage with very interesting results [16]. A single crystal CeB<sub>6</sub> thermionic cathode inserted in a high voltage (500 kV) pulsed gap has been adopted as electron source. The advantage of this choice is the possibility to generate a stable beam in terms of charge, energy and pointing stability with uniform current distribution. The drawback is that only a 10 MV/m accelerating field can be generated in the 5 cm long gap, thus allowing only a low charge density beam generation in along pulse. Further manipulation of the beam is then necessary in order to achieve the required brightness by means of a sub-harmonic buncher, a chopper and a booster cavity before injecting the beam in S-band capture sections followed by a C-band linac, as shown in Fig. 6.

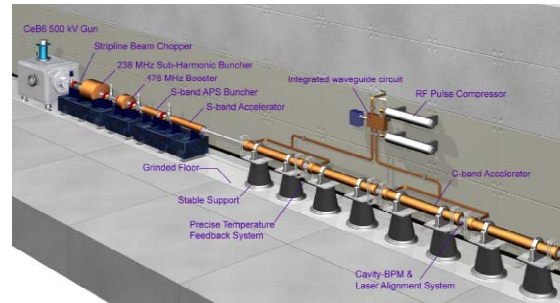


Figure 6: Layout of the SCSs thermionic injector.

Nevertheless, as reported in [16], with this injector the SCSs group has been able to reach very competitive results at 50 MeV: 110 A peak current with rms normalised emittance of 3  $\mu$ m (slice emittance < 2  $\mu$ m) corresponding to an achieved brightness of ~ 3  $10^{13}$  A/m<sup>2</sup>. The exponential gain at 50 nm observed in the SCSs undulator means also that at least one slice of the bunch has even better brightness. The SCSs is the first SASE FEL driven by a thermionic injector.

Another alternative design is subject of investigation at the Low Emittance Gun Project LEG at PSI [17]. The idea in this case is to generate an ultra-low thermal emittance beam (~ 0.05  $\mu$ m) by means of cathode field emission process and to prevent space charge induced emittance growth with a strong acceleration immediately after the emitters with a high voltage pulsed diode, followed by a 1.6 cells cavity and a linac. Preliminary simulations [18] show that with a careful beam matching to the subsequent accelerating structure an emittance

lower than 1  $\mu\text{m}$  can be obtained at 200 MeV. Two possible choices for this cathodes are under investigation: field emitter arrays (FEA) and single needle cathode electron sources. FEA can give a high current density ( $\sim 10^{12}$  A/mm<sup>2</sup>) while a needle cathode (ZrC, HfC) would have the possibility to temporally modulate the electron beam through laser pulse assisted emission. To overcome the main observed drawbacks: non-uniform emission and arc breakdown, a conditioning process on FEA has been developed at PSI and tests are under way.

## VELOCITY BUNCHING

Since the impact of magnetic compressors on the beam quality is a relevant and compelling topic, with the tendency to have serious emittance growth due to coherent synchrotron radiation effects in bends, a new method able to compress the bunch at moderate energies (tens of MeV), using rectilinear trajectories, and integrated in the emittance compensation process, has been proposed [19]. This scheme, named *velocity bunching*, has the following characteristics: although the phase space rotation in this process is still based on a correlated velocity chirp in the electron bunch, in such a way that electrons on the tail of the bunch are faster (more energetic) than electrons in the bunch head, this rotation does not happen in free space but inside the longitudinal potential of a traveling RF wave which accelerates the beam inside a long multi-cell traveling wave (TW) RF structure, applying at the same time an off crest energy chirp to the injected beam. This is possible if the injected beam is slightly slower than the phase velocity of the RF wave so that, when injected at the crossing field phase (no field applied), it will slip back to phases where the field is accelerating, but at the same time it will be chirped and compressed. The key point is that compression and acceleration take place at the same time within the same linac section, actually the first section following the gun, that typically accelerates the beam, under these conditions, from a few MeV ( $> 4$ ) up to 25-35 MeV.

Table 1: Velocity bunching experiments

	BNL	UCLA	DUV-FEL	UTNL	LLNL
Charge [nC]	0.04	0.2	0.2	1	0.2
Length [ps]	0.37	0.39	0.5	0.5	<0.3
Compression Ratio	6	15	>3	>13	10
Reference	[20]	[21]	[22]	[23]	[21]

A fully optimized dedicated photo-injector for application of the velocity bunching technique still does not exist: one of the missions of the SPARC project is indeed to design and commission such a system.

## HIGH AVERAGE BRIGHTNESS INJECTORS

With the advent of proposed superconducting energy recovery linacs (ERL) dedicated to production of

radiation [24] that operate at high average current (high duty factor), the demand for high peak and high average brightness, pushes the injector community to consider also the possibility of using a superconducting RF photoinjector. In the past, for an implementation of SRF guns it was always assumed that one needs strong focusing inside the gun, near the photocathode. This assumption has been partially driven by relatively low achievable gradient in SRF guns. A solution which avoids use of solenoid fields in transverse beam control near the cathode, has been proposed in [25] using recessed cathode to enhance transverse RF component on the cathode surface. Experimental test have demonstrated that this solution is not enough to prevent space charge emittance growth downstream the gun exit. The improvement in superconducting cavity fabrication allows today accelerating gradient higher than 30 MV/m, corresponding to peak field of 60 MV/m [26]. An alternative scheme in which rf focusing is not required can today be considered. A very attractive approach has been proposed at BNL [27]. The basic idea is to illuminate with UV laser the back wall of the superconducting Nb cavity accelerating in this way photo-emitted electrons. An optimized configuration has been proposed in [28], in which the working point described in [15] has been scaled to an L-band SC gun design.

Another proposed scheme is to excite a TE magnetic mode inside the cavity, as shown in Fig. 7, that focuses the electron beam and prevents the increase of the transverse emittance [29].

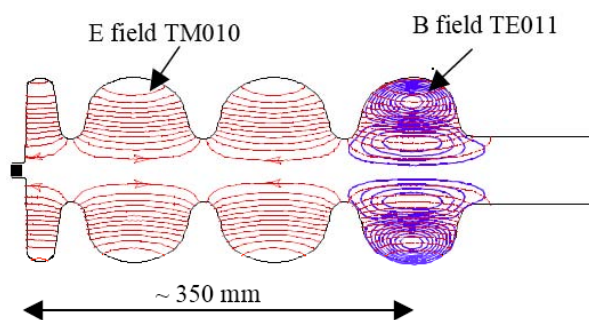


Figure 7: Electric field of the accelerating TM010 mode (red lines) and magnetic flux of the solenoidal TE011 mode in 3.5-cell L-band superconducting FZR cavity.

Operation with high average beam current requires photocathodes having enhanced quantum efficiency. When superconductor is used as a photoemitter, high QE minimizes the thermal load on the superconducting surface. More generally, high QE implies that one may keep the size and cost of the high duty cycle laser system used to illuminate the photocathode within reasonable limits. It has been recently proposed to use lead as a photocathode deposited on the back wall of the gun cavity. Preliminary measurements [30] show a  $\text{QE} = 1.7 \cdot 10^{-3}$  for a lead cathode illuminated by a 213 nm laser.

The extreme case of ampere class superconducting guns is discussed in [31]. These devices require careful control of the higher order mode trapping and are specifically designed with wide beam tubes so to facilitate damping of unwanted trapped HOM.

## ACKNOWLEDGEMENTS

The author would like to thank all the colleagues that have promptly provided material and information during the preparation of this work. A particular thanks is addressed to F. Stephan and J. Sekutowicz, authors of previous injectors overview [6,7], for the many helpful and useful suggestions.

This work has been partially supported by the EU Commission in the sixth framework programme, contract no. 011935 EUROFEL.

## REFERENCES

- [1] M. Xie, “Design Optimization for an X-ray FEL driven by SLAC linac”, Proc. of PAC Conference, 1995.
- [2] C. A. Brau, “What brightness means”, Proc. of the ICFA workshop on “The physics and applications of high brightness beams”, Sardinia, July 2002, World Scientific.
- [3] B. E. Carlsten, Nucl. Instrum. Methods A **285**, 313 (1989).
- [4] L. Serafini, J. B. Rosenzweig, Phys. Rev. E **55** (1997) 7565.
- [5] V. Fusco et al., “Beam dynamics studies for the sparxino linac”, Proc. of FEL Conference, Stanford, 2005.
- [6] F. Stephan, “Status and perspectives of photo injector developments for high brightness beams”, Proc. of the ICFA workshop on “The physics and applications of high brightness beams”, Erice, October 2005, World Scientific.
- [7] J. Sekutowicz, “Superconducting rf photoinjectors: an overview”, beams”, Proc. of the ICFA workshop on “The physics and applications of high brightness beams”, Erice, October 2005, World Scientific.
- [8] V. Yakimenko, “Optimization of the beam brightness generated by the 1.6 cell gun with asymmetric tuning”, Proc. of the ICFA workshop on “The physics and applications of high brightness beams”, Erice, October 2005, World Scientific.
- [9] J. Yang et al., Journal of Applied Physics, V. 92, n, 3, 2002.
- [10] Linac Coherent Light Source (LCLS) Conceptual Design Report, SLAC-R-593 (2002).
- [11] C.Limborg-Deprey, D.Dowell, J.Schmerge and Z.Li, L.Xiao, LCLS-TN-05-3.
- [12] D. Alesini et al., “Status of the SPARC project”, Proc. of EPAC Conference, Edinburgh, 2006.
- [13] G. Bazzano et al., “Study of the effect of multipolar components in the SPARC emittance compensation gun solenoid”, Proc. of EPAC Conference, Edinburgh, 2006.
- [14] A. Cianchi et al., “Characterization of the SPARC photo-injector with the movable emittance meter”, Proc. of EPAC Conference, Edinburgh, 2006.
- [15] M. Ferrario et al., SLAC-PUB-8400.
- [16] T. Shintake, “Status of the SCSS test accelerator and XFEL project in Japan”, Proc. of EPAC Conference, Edinburgh, 2006.
- [17] M R. Ganter, “Low emittance gun concept”, Proc. of the ICFA workshop on “The physics and applications of high brightness beams”, Erice, October 2005, World Scientific.
- [18] M. Pedrozzi, “Post acceleration concept for the LEG project”, Proc. of the ICFA workshop on “The physics and applications of high brightness beams”, Erice, October 2005, World Scientific.
- [19] L. Serafini, M. Ferrario, “Velocity Bunching in PhotoInjectors”, AIP CP 581, 2001, pag.87.
- [20] X.J. Wang et al, Phys. Rev. E 54, R3121 (1996).
- [21] S. G. Anderson et al., “Velocity bunching of high-brightness electron beams”, Phys. Rev. ST-AB, **8**, 014401 (2005).
- [22] P. Piot, et al., “Subpicosecond compression by velocity bunching in a photoinjector”, Phys. Rev. ST-AB, **6**, 033503 (2003).
- [23] H. Iijima et al., “Experimental Verification of Velocity Bunching via Shot-by-Shot Measurement at S-Band Photoinjector and Linac, submitted to Japanese Journal of Applied Physics.
- [24] L. Merminga, “Technical approaches for high-average-power free-electron lasers”, Rev. Modern Phys., **74**, (2002).
- [25] D. Janssen, V. Volkov, Nucl. Instr. and Meth. A 452 (2000), 34.
- [26] L. Lilje, “Achievement of 35 MV/m in the TESLA Superconducting Cavities Using Electropolishing as a Surface Treatment”, Proc. of EPAC 2004.
- [27] T. Srinivasan-Rao et al., “Design, Construction and Status of All Niobium Superconducting Photoinjector at BNL”, PAC03, Portland 2003, USA.
- [28] J. Sekutowicz et al., “Proposed Continuous Wave Energy Recovery Operation of an XFEL”, Phys. Rev. ST-AB, **8**, 010701 (2005).
- [29] K. Floettman et al., “Emittance compensation in a superconducting rf gun with a magnetic mode”, Phys. Rev. ST-AB, **7**, 090702 (2004).
- [30] J. Smedley, “Progress on Lead Photocathodes for Superconducting Injectors”, PAC05, Knoxville 2003, USA.
- [31] I. Ben-Zvi et al., “Ampere Average Current Photoinjector and Energy Recovery Linac”, Proc of FEL 2004.

# DAΦNE EXPERIENCE WITH NEGATIVE MOMENTUM COMPACTION

M. Zobov, D. Alesini, M.E. Biagini, A. Drago, A. Gallo, C. Milardi, P. Raimondi,  
B. Spataro, A. Stella, LNF-INFN, Frascati, Italy

## Abstract

There are several potential advantages for a collider operation with a lattice with negative momentum compaction factor (alfa,  $\alpha_c$ ). Since the lattice of the Frascati e+e-  $\Phi$ -factory DAΦNE is flexible enough to provide collider operation even with  $\alpha_c < 0$ , we have exploited this possibility for an experimental study of the beam dynamics. The negative momentum compaction lattices have been successfully implemented and stable 1 A currents have been stored in both electron and positron rings without any problem for RF cavities and feedback systems operation. First collisions have been tested at low currents. In this paper we describe the experimental results and compare them with expectations and numerical simulations. Present limitations to DAΦNE operation with  $\alpha_c < 0$  and ways to overcome them are also discussed.

## INTRODUCTION

The e+e- collider DAΦNE, the 1.02 GeV c.m. Frascati  $\Phi$ -factory [1], has reached a peak luminosity of about  $1.5 \times 10^{32} \text{cm}^{-2} \text{s}^{-1}$  and a daily integrated luminosity of  $10 \text{pb}^{-1}$  [2]. At present the DAΦNE Team is discussing several scenarios for future upgrades [3] and different ideas aimed at increasing the luminosity are being studied theoretically and tested experimentally. One of such ideas which does not require additional costs since it relies only on the flexibility of the lattice is to realize an optical structure with a negative momentum compaction factor.

There are several potential advantages for beam dynamics and luminosity performance of a collider with a negative momentum compaction factor:

- The bunch length is shorter since the wake potential is focusing. A shorter bunch is preferable for both peak luminosity and beam-beam lifetime improvement since the transverse beta functions at the interaction point (IP) can be reduced proportionally to the bunch length. Moreover, the Piwinski angle becomes lower in collisions with a crossing angle, as in the case of DAΦNE.
- Qualitative considerations confirmed by numerical simulations have shown that a lattice with negative momentum compaction can make the longitudinal beam-beam effects less harmful [4], improving beam lifetime and decreasing transverse beam size blow up. Moreover,  $\alpha_c < 0$  avoids coherent and incoherent instabilities arising when the longitudinal beam-beam kick gets comparable with the RF voltage [5].
- It has been shown that for certain vacuum chamber coupling impedances the microwave instability threshold can be higher with negative  $\alpha_c$  [6]. This, however, has not been confirmed in few dedicated

experiments [7, 8, and 9] and must be checked for the DAΦNE impedance.

- The single bunch head-tail instability with negative momentum compaction takes place with positive chromaticity. This means that one can operate a storage ring with a ‘natural’ negative chromaticity without correcting sextupoles.

Thus, a dedicated machine experiment aimed at studying DAΦNE performance with  $\alpha_c < 0$  was scheduled and then performed with the following principal goals:

- to check the reliability of the lattice model by varying the momentum compaction in a wide range,
- to prove bunch shortening with the wake fields in DAΦNE and to study the microwave instability,
- to study RF cavities and feedbacks performance and to investigate the high current multibunch dynamics,
- to perform beam-beam collisions with negative  $\alpha_c$ .

This paper describes the obtained results and analyzes the experimental data comparing them with expectations and numerical simulations. Present limitations to DAΦNE operation with negative momentum compaction and possible ways to overcome them are also discussed.

## LATTICE MODIFICATION

DAΦNE is a double ring collider sharing two interaction regions; each ring consists of a long external arc and a short internal one based on a quasi-achromatic cell built using a bending-wiggler-bending sequence. The presence of the wiggler in the region of maximum dispersion doubles the radiation emitted in the dipoles reducing damping times. Moreover the optics flexibility (all quadrupoles are independently powered) makes it possible to tune the beam emittance by varying the dispersion in the wiggler at constant field.

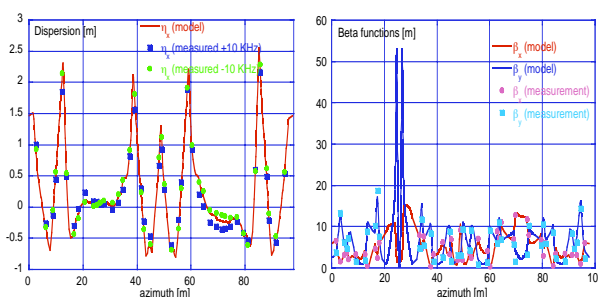


Figure 1: Optical functions of the positron ring with  $\alpha_c = -0.019$  (solid lines: modeling; dots: measurements).

The behaviour of the dispersion function in the arcs determines also the value of the momentum compaction factor  $\alpha_c$ . In the nominal working conditions  $\alpha_c = 0.02-0.024$ , but this parameter can be easily moved toward negative values by making the dispersion function

negative alternatively at the entrance and at the exit of the arcs along the beam direction. The dispersion adjustments should preserve the transverse betatron functions and the relative betatron phase advances in the two interaction regions and minimize their variation along the rings. This requires a general reconfiguration of the currents in all quadrupoles. During a short period devoted to machine studies two different value of  $\alpha_c$  have been investigated:  $\alpha_c = -.02$  (in both rings) and  $\alpha_c = -.036$  (only in the electron ring). After applying the new optics with negative momentum compaction and slight lattice optimization the ring has been completely characterized by measuring betatron functions, first and second order dispersion, chromaticity with and without sextupoles and the synchrotron frequency before starting systematic bunch length measurements. The optics implementation and measurements required less than one day per ring. In both rings the experimental data are in a good agreement with the optics model both for the linear and non-linear parts [10]. As an example, the transverse betatron functions and the dispersion measured in the positron ring are compared with the computed ones in Fig. 1.

## BEAM DYNAMICS

Many beam dynamics experiments, including bunch length measurements, study of high current multibunch operation and first beam-beam collisions, were performed with  $\alpha_c = -0.019$  in the positron ring and  $\alpha_c = -0.021$  in the electron one. The absolute values of the negative  $\alpha_c$  were chosen to be as close as possible to the positive one in the normal collider operating conditions.

### Bunch Shortening

Impedances and wake fields are well known for both the positron [11] and the electron [12] ring. Numerical simulations based on the wake fields reproduce well bunch length, charge distribution inside the bunch and the microwave instability threshold with positive momentum compaction. These wakes have been also used to simulate bunch shortening with negative alfa [13]. According to the predictions the bunch length should be shorter by 50÷70% than in nominal operating conditions.

In order to confirm these predictions the bunch length in both rings has been measured by means of a streak camera. The measurement set up is discussed elsewhere [14]. The results are shown in Fig. 2 comparing bunch length for positive and negative  $\alpha_c$ . It can be observed that the bunch is substantially shorter with  $\alpha_c < 0$ , it shortens up to the microwave threshold and then starts growing. As predicted by simulations, for the positron ring the microwave instability threshold is only slightly lower than with the positive alfa: it is shifted from 9÷10 mA down to 7 mA. No instability sidebands have been observed up to 16 mA/bunch which is higher than in the present working conditions. No intensity loss due to the head-tail instability has been detected for positron bunch currents as high as 40 mA with high negative chromaticities.

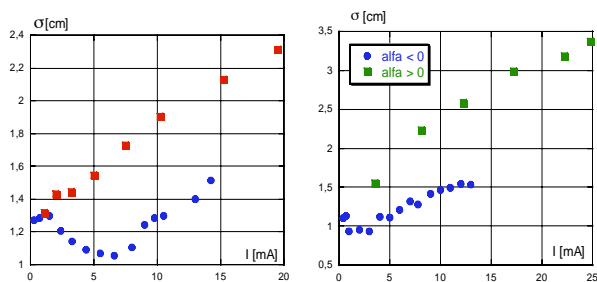


Figure 2: Bunch length as a function of bunch current in positron (left) and electron (right) rings (squares: positive alfa; circles: negative alfa).

In the electron ring the bunch length is also shorter with the negative momentum compaction, but the microwave instability threshold is significantly lower than in the positron ring. This is explained by the larger coupling impedance of the electron ring (by about a factor 2) [12].

### Multibunch Operation

The RF cavity operation with negative momentum compaction factor required only:

- change of the RF phase by about 170 degree (1.3 ns in time units) with respect to the injection complex, since the synchronous phase in this case is on the positive slope of the RF voltage;
- re-adjustment of the tuning loop to get a certain positive detuning of the accelerating mode frequency, i.e. to provide some Robinson damping already at low current.

High current operation in both rings has been tested by injecting 100 consecutive bunches (out of a maximum of 120). No particular problem has been detected in managing the multibunch dynamics. Surprisingly, feedbacks were not necessary to store 400 mA in the electron ring. In order to obtain about 1 A of stable currents in both electron and positron beams the following procedures and set ups of the feedback systems have been applied:

- Longitudinal feedback: ‘standard’ FIR filter (broad-band, ‘low gain’), front-end and back-end retiming in both rings.
- Vertical feedback: only back-end and front-end retiming in both rings.
- Horizontal feedback: back-end and front-end retiming only in the positron ring; no horizontal motion in the electron ring till about 1A.

The maximum storable currents at the level of 1 A were limited by injection saturation. Further current increase would require careful adjustment of injection closed bumps and dynamic aperture optimization.

### First Beam-Beam Collisions

Optimization of beam-beam collisions has been carried out at low beam currents (less than 100 mA/beam) by measuring the luminosity as a function of calibrated vertical and horizontal bumps at the interaction point (IP). The average geometric rms beam sizes ( $\Sigma_{x,y}$ ) at IP, extracted from these measurements, have been minimized by adjusting collider parameters such as tunes, coupling,

beams overlap etc. After tuning we managed to reduce the vertical capital sigma  $\Sigma_y$  down to 8.2  $\mu\text{m}$  and the horizontal one to 1 mm. These  $\Sigma_{x,y}$  are comparable with the best values obtained in DAΦNE with positive momentum compaction.

By increasing the beam currents in collision the best obtained luminosity was  $2.5 \times 10^{31} \text{cm}^{-2} \text{s}^{-1}$  while colliding 300 mA electrons against 300 mA positrons. This result corresponds to a specific luminosity of  $2.5 \times 10^{28} \text{cm}^{-2} \text{s}^{-1} \text{mA}^{-2}$  defined as the single bunch luminosity divided by the product of colliding bunch currents. One can compare this number with the typical specific luminosity in high current collisions in DAΦNE with  $\alpha_c > 0$  which ranges between 1 and 1.5 in units of  $10^{28} \text{cm}^{-2} \text{s}^{-1} \text{mA}^{-2}$ . However, such comparison is not conclusive since so far with  $\alpha_c < 0$  we did not collide as high currents as they are in routine DAΦNE operation with  $\alpha_c > 0$ .

### LIMITATIONS AND CURES

The principal limitation that forced us to suspend high current beam-beam collisions was a very fast growth of the electron vertical beam size above a threshold of 3-4 mA per bunch. A strong correlation between the longitudinal microwave instability and the vertical size blow up has been found. As can be seen in Fig.3, the single bunch longitudinal instability threshold at about 3 mA (a) corresponds to a vertical size blow up threshold at 300 mA (b) for an electron beam of 90 bunches.

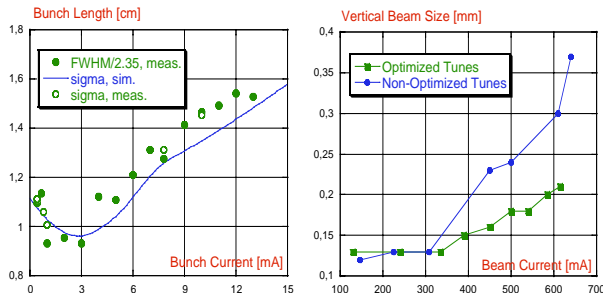


Figure 3: a) Bunch length as a function of bunch current (solid line: simulations; dots: measurements); b) Vertical beam size as a function of beam current (90 bunches) without (blue) and after tune optimization.

Such a correlation is not typical only for operation with  $\alpha_c < 0$ , but it has been also detected and studied for the DAΦNE routine lattice with  $\alpha_c > 0$  [15]. However, since the microwave threshold is lower for negative alfa, the effect is much more pronounced. It is particularly strong for the electron ring which has a higher impedance.

The only way to overcome this limitation is to move the microwave threshold beyond the nominal bunch current.

Two ways are being followed to increase the threshold. First, during the current DAΦNE shutdown 2 m long ion clearing electrodes in the wiggler sections, which account

for almost half of the electron ring impedance budget, will be removed. Second, according to the Boussard criterion [16], the threshold increases rapidly with the absolute value of the momentum compaction ( $I_{th}$  scales as  $\alpha_c^{3/2}$ ). Exploiting this property, one day before the shutdown a lattice with  $\alpha_c = -0.036$  has been implemented (instead of  $-0.021$ ) with encouraging results [17]: the threshold has been shifted from 3 up to 7-8 mA/bunch while the bunch length at the nominal bunch current remained by 50% shorter than in the operational lattice with  $\alpha_c > 0$ . We plan to resume studies of the negative momentum compaction beam dynamics after the shut down.

### SUMMARY

- The DAΦNE optics model has proved to be reliable in providing collider operation with the momentum compaction factors in the range from +0.034 [10] to -0.036.
- With negative alfa bunches in both rings shorten as predicted by numerical simulations. It has been possible to store high bunch currents with large negative chromaticities.
- No hard limit has been seen in multibunch operation. About 1 A stable currents have been stored in both rings.
- At beam currents up to 300 mA/beam a good specific luminosity has been obtained in beam-beam collisions.
- Higher current collisions have been prevented by fast growth of the electron beam vertical size with current (single beam effect). We hope to overcome this limitation by reducing the coupling impedance in the electron ring and/or applying an optics with higher  $|\alpha_c|$ .

### REFERENCES

- [1] G. Vignola, PAC93, p. 1993.
- [2] A. Gallo et al., this conference, MOPLS028.
- [3] M. Zobov et al., PAC05, p. 112.
- [4] V. V. Danilov et al., HEACC'92, p. 1109.
- [5] V. V. Danilov et al., PAC91, p. 526.
- [6] S. X. Fang et al., PAC95, p. 3064.
- [7] A. Nadji et al., EPAC96, p.676.
- [8] M. Hosaka et al., Nucl.Instr.Meth. A407, 234(1998).
- [9] H. Ikeda et al., e-print Archive:physics/0401155.
- [10] [www.lnf.infn.it/acceleratori/dafne/report/KLOE\\_acn\\_Feb\\_05.pdf](http://www.lnf.infn.it/acceleratori/dafne/report/KLOE_acn_Feb_05.pdf)
- [11] M. Zobov, e-print Archive:physics/0312072.
- [12] B. Spataro and M. Zobov, DAΦNE Note G-64, 2005.
- [13] [www.lnf.infn.it/conference/d2/TALKS/zobov1.pdf](http://www.lnf.infn.it/conference/d2/TALKS/zobov1.pdf)
- [14] A. Ghigo et al., EPAC2002, p. 1494.
- [15] [www.lnf.infn.it/acceleratori/dafne/report/High\\_momentumCompaction.pdf](http://www.lnf.infn.it/acceleratori/dafne/report/High_momentumCompaction.pdf)
- [16] D. Boussard, CERN LABII/RF/INT/75-2, 1975.
- [17] [www.lnf.infn.it/acceleratori/dafne/report/Zobov\\_Neg\\_Alfa\\_036\\_Mar06.pdf](http://www.lnf.infn.it/acceleratori/dafne/report/Zobov_Neg_Alfa_036_Mar06.pdf)

# BEAM DYNAMICS SIMULATION IN $e^-$ RINGS IN SRFF REGIME

L. Falbo INFN, Pisa, Italy

D. Alesini, INFN-LNF, Frascati, Italy; M. Migliorati, Univ. La Sapienza, Roma, Italy

## Abstract

Obtaining very short bunches is an issue for colliders and Coherent Synchrotron Radiation (CSR) sources. In strong RF focusing regime (SRFF) bunch length is not constant along the ring, but a bunch length modulation (BLM) occurs; thus allowing to obtain short bunches at a given position in the ring. Until now the bunch length modulation has been studied only in the limit of zero current; in this paper we present a simulation code suitable to study the effects of CSR and of the vacuum chamber wakefields on the single bunch longitudinal dynamics in a regime of strong RF focusing. The code has been applied to lattices that can be realized in DAΦNE for a possible experiment on bunch length modulation.

## INTRODUCTION

Short bunches are important for both  $e^+/e^-$  colliders and synchrotron light sources, the first to reach high luminosities, the second to produce CSR in a controlled way. SRFF allows to obtain short bunches thanks to the property that in this regime the bunch length changes along the ring. Length modulation in lattices with high and low momentum compaction have been widely studied at zero current without considering the microwave and microbunching instability that could strongly limit to the maximum stored current [3]. A simulation code has been written to study the effect of the CSR and vacuum chamber wakefields.

## STRONG RF FOCUSING AND APPLICATIONS IN DAΦNE

In a ring with one RF cavity placed at  $s_{RF}$  the voltage gradient can be defined as:

$$U = \frac{2\pi V_{RF}}{E_0 \lambda_{RF}} \quad (1)$$

and the longitudinal drift function is:

$$R_1(s) = \int_s^{s_{RF}} ds' \frac{\eta(s')}{\rho(s')} \quad (2)$$

where  $V_{RF}$  is the peak voltage,  $\lambda_{RF}$  the RF wavelength,  $E_0$  the nominal energy,  $\eta(s)$  the dispersion and  $\rho(s)$  the bending radius. When the voltage gradient is high and the drift function is large, the analysis of the longitudinal one turn matrix [1] shows that the natural energy spread is constant along the ring but the natural bunch length changes. There are two different ways to obtain a regime of bunch length modulation depending on the monotonicity of the

drift function. If the drift function is monotonic the momentum compaction  $\alpha_c$  and synchrotron tune  $Q_s$  are high and the minimum bunch length occurs in the zone of the ring opposite to the cavity [1]. On the contrary, when  $R_1(s)$  is non-monotonic, with large derivatives with opposite signs in two different zones of the ring, the lattice has low  $\alpha_c$  and  $Q_s$  and the minimum bunch length position occurs nearer to the cavity the lower is the momentum compaction [2].

In DAΦNE [4] there is the possibility to tune the dispersion on a wide range to reach the necessary  $R_1(s)$  variation; the  $U$  parameter can become large enough by installing, for example, a Tesla type RF cavity at 1.3 GHz with a maximum voltage of 10 MV [5] in one of the two interaction regions. Three different structures are considered: structure A in which  $R_1(s)$  is monotonic and  $\alpha_c = 0.073$ ; structure B corresponding to a non-monotonic regime with  $\alpha_c = 0.02$ ; structure C also non-monotonic but with a much lower value of  $\alpha_c$  (0.004).

## SIMULATION CODE

The C simulation code SPIDER (Simulation Program for Impedances Distributed in Electron Rings) has been written in order to study the effects of the CSR and of the vacuum chamber wakefields on the longitudinal single bunch dynamics in bunch lengthening modulation regime. In this program a bunch, described by  $N$  macroparticles, runs in the machine that is divided into an arbitrary number of longitudinal drift spaces and RF cavities. The code calculates the longitudinal phase space coordinates of each macroparticle at the end of each section (drift space or cavity) turn by turn. The used coordinates are the energy deviation  $\epsilon \equiv E - E_0$  and the displacement from the synchronous particle  $z$ .

If the section represents one RF cavity the single bunch dynamics equations are

$$\begin{cases} z(s_2) = z(s_1) \\ \epsilon(s_2) = \epsilon(s_1) + V_{cav}(z(s_2)) + V_{RF} \cos(\Phi - 2\pi c \frac{z(s_1)}{\lambda_{RF}}) \end{cases}$$

where  $s_1$  and  $s_2$  are the beginning and the end of the section, respectively,  $\Phi$  is the synchronous phase and  $V_{cav}(z(s_2))$  is the energy loss due to the cavity wakefields calculated with the distribution at the end of the section. If the section is a longitudinal drift space the equations are:

$$\begin{cases} z(s_2) = z(s_1) - \int_{s_1}^{s_2} ds' \frac{\eta(s')}{\rho(s')} \epsilon(s_1) / E_0 \\ \epsilon(s_2) = \epsilon(s_1) + V_{pipe}(z(s_2)) + V_{CSR}(z(s_2)) + V_{ISR} \end{cases}$$

where  $V_{CSR}$  and  $V_{pipe}$  are the energy losses due to the CSR

and vacuum chamber wakefields and  $V_{ISR}$  is the contribution of the incoherent synchrotron radiation given by

$$-U_0 - D\epsilon(s_1) + G\sigma_E\sqrt{2D} \quad (3)$$

where  $U_0 = 1.4 \cdot 10^{-32} E_0^4 I_2(s_2; s_1)$  is the energy radiated by the synchronous particle in the section,  $D = 1.4 \cdot 10^{-32} E_0^3 [2I_2(s_2; s_1) + I_4(s_2; s_1)]$  is the damping factor of the section,  $G$  is a gaussian random number with zero mean and unitary rms,  $\sigma_E = 1.2 \cdot 10^{-12} E_0^2 \sqrt{\frac{I_3(s_2; s_1)}{2I_2(s_2; s_1) + I_4(s_2; s_1)}}$  is the energy spread of the section without BLM, and  $I_2(s_2; s_1)$ ,  $I_3(s_2; s_1)$  and  $I_4(s_2; s_1)$  are the usual synchrotron radiation integrals calculated in the section.

## WAKEFIELDS CONTRIBUTION

CSR and vacuum chamber wakefield contributions are calculated by the convolution of the bunch longitudinal distribution and the wake functions of the considered sections.

### *Vacuum chamber wake*

The DAΦNE wake function has been calculated from the wake potential of a 2.5 mm gaussian bunch obtained by numerical codes [6]; since in the case of SRFF the bunch length is comparable with 2.5 mm, the wake function of each section has been approximated by an RLC equivalent model whose parameters have been found by fitting the wake potential. For the Tesla SC cavity, the analytic approximation of the wake function per unit length given in [7] has been used

$$w(z) = 38.1(1.165 \cdot e^{-\sqrt{z/3.65}} - 0.165) \left[ \frac{\text{V}}{\text{pC m}} \right] \quad (4)$$

where  $z$  is expressed in mm.

### *CSR wakefields*

Since the bunch length is of the order of few mm, CSR effects could be relevant. In the code different models of CSR wake function are implemented, that can be chosen depending on the considered magnet. For the dipole contribution the code includes:

- a steady state CSR wakefield model [8];
- a model considering entrance and exit transients [9];
- a model considering the pipe shielding modeled by the contribution of two parallel plates [10].

For wigglers the code includes the steady state wakefield given in [11]. All these models need the bunch distribution derivative that is obtained by a Savitzky-Golay filter [12].

## SIMULATIONS FOR THE DAΦNE EXPERIMENT ON BLM

The code has been applied to study wakefields effect in the SRFF regime of the lattices A, B and C that can be

realized in DAΦNE and with a voltage in the SC cavity equal to 3 and 9 MV. The ring has been divided in five sections: one SC cavity and four drift spaces 25 meters long. In these cases the longitudinal distributions of the bunch have been studied at the end of each section. The number of macroparticles used has been  $1.5 \cdot 10^5$ . At zero current the code reproduces the theoretical length modulation. For different bunch currents it has been studied the effect of

- beam pipe wakefield only;
- CSR wakefield only;
- beam pipe and CSR wakefields;
- beam pipe, CSR and SC cavity wakefields.

## RESULTS OF THE SIMULATIONS

For each case the instability threshold, defined by the current at which the energy spread begins to increase, has been obtained. Above the threshold the strength of the instability, up to a current of 25 mA, has been studied. The instability threshold is higher in monotonic regime (structure A) but the instability grows faster than in the non-monotonic regimes (structures B, C) and by comparing the structures B and C we may conclude that this consideration is the more relevant the lower the momentum compaction. These properties are due to the fact that, in the non-monotonic regime at a given RF voltage, the modulation factor  $F_m \equiv \sigma_{LMAX}/\sigma_{LMIN}$  is higher than in the monotonic structure. Therefore, at a given minimum bunch length, the average length along the ring is higher. Furthermore it has been verified that in the monotonic regime the modulation factor is independent on the current, while in the structure B and, above all, in the structure C,  $F_m$  increases immediately after the threshold: thanks to this, bunch lengthening and instability increase more slowly for the minimum bunch length. CSR effects are not dominant but, especially in the non-monotonic regimes, their contribution is important for the actual lengthening and the shape of the longitudinal distributions. The effect of the SC cavity wake is negligible even in cases in which the minimum bunch length is in the cavity itself. Furthermore, in order to evidence the effect of the bunch lengthening modulation, results have been compared with the ones obtained with a lattice with a very low momentum compaction (0.004) but without bunch length modulation: in the following figures this case is labelled as NO SRFF. In Figs. 1, 2 and 3 we show respectively the minimum bunch length, the length modulation factor and the energy spread as a function of current in the different cases. In Fig. 4 we report the ratio  $N^2/\sigma_{LMIN}$  where  $N$  represents the number of particles in the bunch and  $\sigma_{LMIN}$  is the minimum bunch length. This quantity gives informations about luminosity in the case of short bunch at interaction point, in the hypothesis of a vertical betatron function (in the interaction point) equal to the bunch length. In this figure the full lines represent

the trend of the function  $N^2/\sigma_{LMIN}$  if we neglect wakefields effects. As a comparison a point showing the peak luminosity of DAΦNE (in the same units) is shown [13]. In each figure error bars correspond to the strength of the instability.

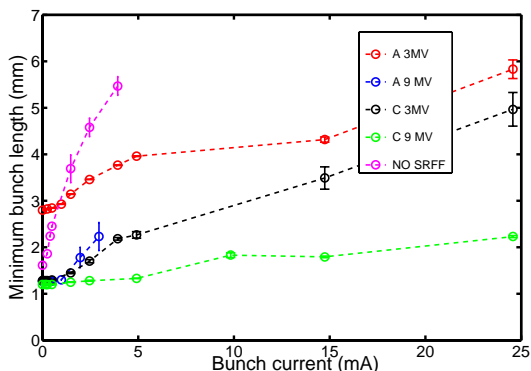


Figure 1: Minimum bunch length as a function of current

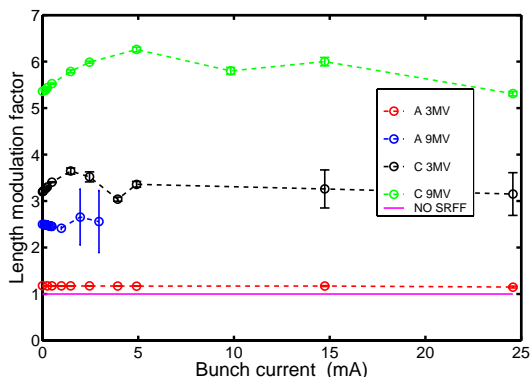


Figure 2: Modulation factor as a function of current

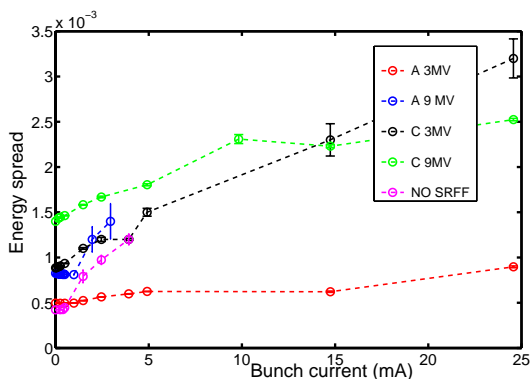


Figure 3: Energy spread as a function of current

## CONCLUSIONS

The principle of bunch length modulation along a storage ring was studied under the effect of wakefields due to

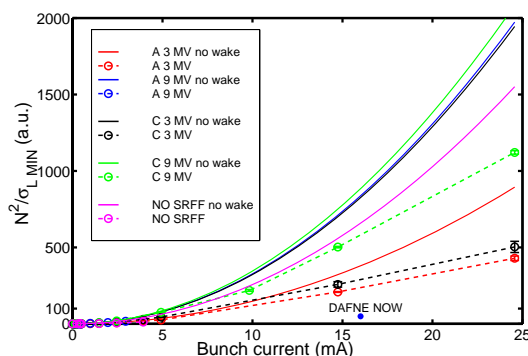


Figure 4: Ratio of the second power of the stored current over the minimum bunch length

the CSR and the interaction of the beam with the vacuum chamber by the dedicated program SPIDER. Simulations have been performed for different kinds of SRFF lattices realizable in DAΦNE to study the bunch lengthening and the instability threshold as a function of the number of particles stored in the bunch. This study showed that also in presence of wakefields the bunch length modulation given by the SRFF is maintained. In the present DAΦNE rings, bunches with lengths in the range of few mm could be obtained with bunch currents above 10 mA, while in a quasi isochronous regime and no SRFF only currents below the mA can be steadily stored.

## ACKNOWLEDGEMENTS

We would like to acknowledge C. Biscari, M. Serio and M. Zobov for helpful discussions and suggestions.

## REFERENCES

- [1] A. Gallo et al, e-Print Archive: physics/0404020
- [2] C. Biscari, PSRT-AB 8,091001 ,2005.
- [3] A. Chao, SLAC-PUB 2946, 1982
- [4] G. Vignola, DAΦNE, the Frascati Φ factory, PAC 1991-0068
- [5] D. Alesini et al, “Design of a Multi-Cell, HOM Damped Superconducting Cavity for the SRFF Experiment at DAΦNE”, PAC’05, Knoxville, Tennessee.
- [6] M. Zobov et al, LNF-95/041, 1995.
- [7] D. Edwards(ed.), TESLA 95-01,1995.
- [8] E.L. Saldin et al, Nucl.Instr. and Meth. in Phys. Res. A, 398, 1997, pp. 373-394
- [9] G. Stupakov, P. Emma, “CSR wake for a short magnet in ultra-relativistic limit”, EPAC 2002, Paris, France.
- [10] J.B. Murphy et al, Particle Accelerators Vol.57,1997, pp.9-64.
- [11] E.L. Saldin et al, Nucl.Instr.and Meth. in Phys. Res. A 417,1998
- [12] Savitzky A., and Golay, M.J.E. 1964, Analytical Chemistry, vol. 36, pp. 1627-1639
- [13] A. Gallo, DAΦNE status report, these proceedings.

## FUTURE SEEDING EXPERIMENTS AT SPARC

L. Poletto, G. Tondello, Università di Padova, Padova, Italy  
 S. De Silvestri, M. Nisoli, G. Sansone, S. Stagira, Politecnico di Milano, Milano, Italy  
 P. Musumeci, M. Petrarca, M. Mattioli, Università di Roma “La Sapienza”, Rome, Italy  
 M. Labat, O. Tcherbakoff, M. Bougeard, B. Carré, D. Garzella, G. Lambert, H. Merdji, P. Salières,  
 Service des Photons Atomes et Molécules, CEA Saclay, DSM/DRECAM, France  
 M. E. Couprie, SOLEIL, Sant-Aubin, Gif-sur-Yvette CEDEX, France  
 D. Alesini, M. Biagini, R. Boni, M. Castellano, A. Clozza, A. Drago, M. Ferrario, A. Gallo,  
 A. Ghigo, M. Migliorati, L. Palumbo, C. Sanelli, F. Sgamma, B. Spataro, S. Tommasini,  
 C. Vaccarezza, C. Vicario, V. Fusco, INFN-LNF, Frascati, Italy  
 L. Serafini, INFN, Milano, Italy  
 S. Ambrogio, F. Ciocci, G. Dattoli, A. Doria, G. P. Gallerano, L. Giannessi, E. Giovenale,  
 I. Spassovsky, M. Quattromini, A. Renieri, C. Ronsivalle, ENEA C. R. Frascati, Rome, Italy  
 A. Dipace, E. Sabia, ENEA C. R. Portici, Napoli, Italy

### Abstract

This communication describes the research work plan that is under implementation at the SPARC FEL facility in the framework of the DS4 EUROFEL programme. The main goal of the collaboration is to study and test the amplification and the FEL harmonic generation process of an input seed signal obtained as higher order harmonics generated both in crystals (400 nm and 266 nm) and in gases (266 nm, 160 nm, 114 nm). The SPARC FEL can be configured to test several cascaded FEL layouts that will be briefly analysed.

### INTRODUCTION

The SPARC FEL experiment is based on two main components, a high brightness photoinjector that is expected to provide a high quality beam at energies between 150 and 200 MeV (see Tab.I and ref.[1]) and a single pass FEL, whose undulator beam-line is composed by six undulator sections of 77 periods each, with a period length of 2.8 cm and a gap ranging from 6 to 25 mm[2].

The FEL will operate in self amplified spontaneous emission (SASE) mode at a wavelength of about 500 nm with an expected saturation length is about 10-12 m, according to the beam parameters listed in table 1. The flexibility offered by the variable gap configuration of the SPARC undulator and the natural synchronization of the electron beam with the laser driving the photoinjector, makes the SPARC layout particularly suited for a number of experiments where the FEL amplifier is seeded by an external laser source. The seed laser is driven by the same oscillator initiating the laser cascade which is used to run the photocathode and consists in a regenerative amplifier (Coherent/Legend F-HE) delivering 2.5mJ at 800 nm with a pulse duration shorter than 120 fs.

Table 1: List of the main SPARC beam parameters

Beam energy	155-200 MeV
Bunch Charge	1.1 nC
Rep. Rate	1 – 10 Hz
Peak current (>50% bunch)	100 A
Norm. emittances (integrated)	2 mm-mrad
Norm. emitt. (slice len. 300 $\mu$ m)	< 1 mm-mrad
Total correlated energy spread	0.2 %
Total uncorrelated energy spread	0.06 %
e-bunch duration (rms)	~ 4 ps

Different schemes of non-linear harmonic generation are then implemented to generate the shorter wavelength radiation for seeding the FEL. Second and third harmonic generation in LBO crystals will provide the powerful pulses required to reach saturation and study the non-linear pulse propagation in FELs and FEL cascades in superradiant regime, at 400nm and 266nm [3], [4]. The other method considered for the frequency up-conversion of the Ti:Sa fundamental wavelength, is based on the non-linear higher order harmonics generation of the Ti:Sa laser in a gas-jet or in a gas-cell [5]. While at SPARC we plan to seed the FEL with the harmonics up to the 9<sup>th</sup> of the Ti:Sa [6], the harmonic generation in gas allows to extend the seed source spectral range down to the EUV region of the spectrum and represents a promising technique to seed FEL amplifiers at shorter wavelengths.

In the following we will review some of the planned experiments with the two different seed sources.

## SEEDING WITH HIGH HARMONICS GENERATED IN GAS

The experiment of seeding high harmonics generated in gas at SPARC is based on the installation of a gas jet interaction chamber and an in vacuum optical system which matches the transverse optical mode of the harmonic to that of the e-beam in the first undulator section [6]. The UV pulse is injected into the SPARC undulator by means of a periscope and a magnetic chicane deflecting the e-beam from the straight path. High-order odd harmonics of the Ti:Sa laser may be generated at the wavelengths 266nm, 160nm, and 114nm. The undulator resonance condition is tuned at these wavelengths by varying the beam energy and undulator strength K according to the plot shown in Fig. 1.

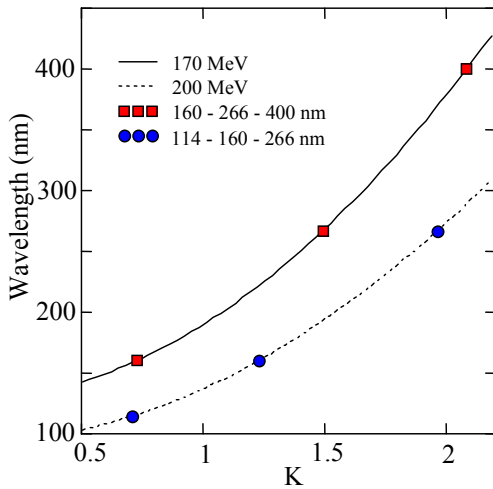


Figure 1: Seeded SPARC FEL operation wavelengths.

The high order harmonics result from the strong non-linear polarisation induced on the rare gases atoms, such as *Ar*, *Xe*, *Ne* and *He*, by the focused intense electromagnetic field of the "pump" laser. The emitted pulse is composed by a sequence of short bursts separated by one half of the fundamental laser period (400nm) and the spectrum contains the odd harmonics of the original laser. A simulation of the amplification of a pulse at 160nm with the typical time structure of harmonics generated in gas has been done with *Perseo*[7]. The laser pulse shape vs. the longitudinal coordinate is shown in Fig. 2 at different positions along the undulator. The radiation spectrum is also shown in Fig.2 and the effect of the spectral "cleaning" associated with the limited FEL bandwidth (FEL parameter  $\rho \approx 4 \cdot 10^{-3}$ ) is evident. An analogous behaviour is observed at the third harmonic generated by the non-linear FEL dynamics. More detailed simulations based on an accurate model of the seed fields distribution and including transverse effects are under study.

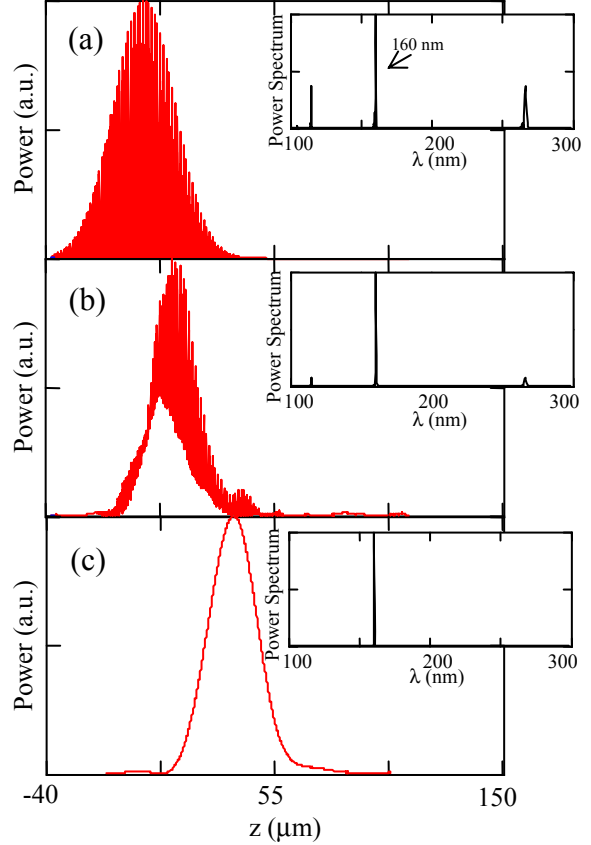


Figure 2: Power and spectrum of the radiation at different positions in the undulator for the SPARC FEL seeded at 160nm. Seed signal (a), after the first UM section (b), at the end of the undulator (c). Beam energy 200 MeV,  $K=1.226$ , the other beam parameters as in Table 1.

## SEEDING WITH 2<sup>ND</sup> AND 3<sup>RD</sup> HARMONICS OF TI:SA GENERATED IN CRYSTAL

The six SPARC undulators may be configured in order to set up a single stage cascaded FEL based on a modulator – radiator configuration, similar to the one tested at BNL [8]. The layout of this configuration is shown in Fig.3.

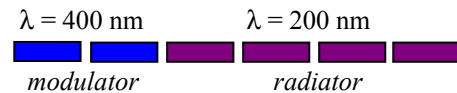


Figure 3: Single stage cascaded FEL layout.

The number of sections of the modulator and of the radiator may be tuned depending on the intensity of the laser seed. The availability of intense short pulses from the seed laser allows to test the superradiant cascade concept [4]. The seed laser power is indeed sufficient to bring at saturation a modulator made by a single undulator segment tuned at 400 nm. The pulse generated in these conditions propagates with the typical signature of superradiance in the following radiator composed by the re-

maining five sections. The feasibility of this experiment was studied in[9].

A second interesting configuration consists in the experimental test of the fresh-bunch injection technique [10]. The layout is shown in Fig.4. In this case the first two undulators (A and B) represent the modulator and radiator sections of single stage cascade, the following two undulators (C and D) are tuned off resonance with the seed wavelength and its higher order harmonics. These undulators play the role of the dispersive section where the radiation exiting the first radiator at 200 nm (B) is longitudinally separated from the electron beam part where the high quality beam has been heated in the previous sections, by the FEL interaction with the seed.

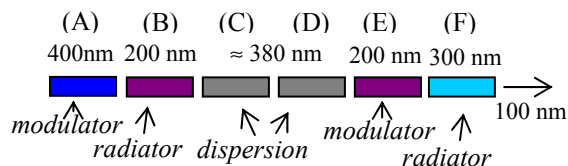


Figure 4: Fresh bunch injection technique layout.

Section (E) is the modulator of the second stage cascade and section (F) is the radiator that is tuned in order to match the resonance of its third harmonic with the second harmonic of the radiator (E). This is necessary since the K parameter excursion of the undulator is not sufficient to span the 1<sup>st</sup> to 3<sup>rd</sup> harmonic range and coupling on the higher order odd harmonics in a linear undulator based FEL has been considered [11].

The last configuration considered in this overview consists in the harmonic FEL cascade [12]. As in the last stage of the previous configuration, the two undulators are tuned at different, not-harmonic fundamental frequencies, but have instead one of their higher order harmonics in common. In the example considered in Fig. 5, we show the case corresponding to the first undulator with the fundamental resonance at 266nm and the second one tuned at 222nm. The two undulator have a common resonance at 44nm, corresponding to the 6<sup>th</sup> harmonic of the first section and the 5<sup>th</sup> of the second.



Figure 5: FEL Harmonic cascade FEL configuration.

The cascade is driven by a seed of 2~10MW of peak power at a wavelength corresponding to the third harmonic of the Ti:Sa drive laser and  $\approx 1\mu\text{J}$  of energy at the output wavelength of 44 nm is expected from simulations. The pulse shape as provided by *Perseo* is shown in Fig. 6.

## CONCLUSIONS

We have given a brief overview of some of the experiments that will be implemented at SPARC thanks to the flexibility of the SPARC configuration and of the variable gap undulator. The opportunities provided by the SPARC experiment of a deeper understanding of the amplification

process and of the FEL dynamics through a whole cascade, may affect in the future the design of the foreseen FEL facilities aiming at the generation of radiation in the VUV-EUV region of the spectrum.

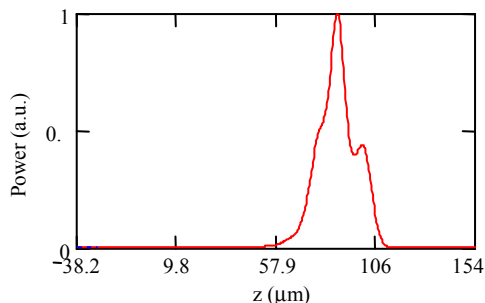


Figure 6: Longitudinal profile of the radiation power at the end of the second undulator.

## ACKNOWLEDGMENTS

Work partially supported by the EU Commission in the sixth framework programme, contract no. 011935 – EU-ROFEL.

## REFERENCES

- [1] SPARC Collaboration, Nucl. Instr. & Meth. A507 (2003) 345-349, see also <http://www.sparc.it> and these proceedings.
- [2] A. Renieri et al. Status report on SPARC project, in Proc. of the 26th FEL conference, Trieste 2004 JACoW (Joint Accelerator Conference Website) at <http://www.JACoW.org>, p. 163 (2004).
- [3] R. Bonifacio, L.De Salvo Souza, P.Pierini, and N. Piovella, Nucl.Instrum. & Meth. A 296, 358 (1990)
- [4] L. Giannessi, P. Musumeci, S. Spampinati, J. Appl. Phys. 98, 043110 (2005).
- [5] T. Brabec, F. Krausz, Rev. Mod. Phys. 72, 545 (2000).
- [6] M. Labat et al., Seeding SPARC Facility with Harmonic Generation in Gases, MOPCH003 these proceedings.
- [7] L. Giannessi, *Perseo* see <http://www.perseo.enea.it>
- [8] L. H. Yu et al. Phys. Rev. Lett. 91, 074801 (2003).
- [9] L. Giannessi, P. Musumeci, in Proc. of the 27th FEL conference, JACoW (Joint Accelerator Conference Website) at <http://www.JACoW.org>, p. 210 (2005).
- [10] I. Ben-Zvi, K.M. Yang, L. H. Yu, Nucl. Instrum. & Meth. A 318, 726 (1992).
- [11] W. B.Colson, G. Dattoli and F. Ciocci, Phys. Rev. A 31, 828 (1985).
- [12] L. Giannessi and P. Musumeci, in proc. of 46th workshop on the Physics and applications of high brightness electron beams, Erice (Tr), May 2005.

# LASER COMB: SIMULATIONS OF PRE-MODULATED $e^-$ BEAMS AT THE PHOTOCATHODE OF A HIGH BRIGHTNESS RF PHOTOINJECTOR

M. Boscolo, M.Ferrario, C. Vaccarezza, LNF-INFN, Frascati, Italy

I. Boscolo, F. Castelli, S.Cialdi, Mi-INFN, Milano, Italy

## Abstract

A density modulated electron beam generated at the photocathode of a radio-frequency electron gun evolves within an accelerator towards a homogenous beam but with an energy modulation. The density modulation is changed into energy modulation. This energy distribution can be exploited to restore the initial density profile, called *comb beam*, with a proper rf phase of the accelerating cavities and by adding a proper compressor. The comb beam at the cathode is generated driving the photocathode by the relative laser pulse train. This laser pulse is obtained with a shaping device inserted into the laser system. The dynamics is studied within the SPARC system with the PARMELA code.

## INTRODUCTION

Short electron bunches with high charge, low-emittance, and low-energy spread are generated by radio-frequency (rf)  $e^-$  gun driven by laser pulses. Applications of this kind of electron source cover free-electron lasers [1], plasma acceleration experiments and Compton scattering [2] and high brilliance linear collider [3]. The wide spectrum of applications is due to the capability of these electron sources of producing target electron beams. This feature is mostly due to the possibility of a proper modulation of the driving laser beam [4].

In this paper we study the generation of a multipulse  $e^-$  beam in the SPARC accelerator [5], aiming to produce high peak current (higher than nominal working point) and train of pulses. We investigate the dynamics of the  $e^-$  beam with PARMELA [6] simulations.

SPARC parameters of interest to our study are (see also Table 1): 10 ps pulse length, 1.1 nC bunch charge, projected emittance less than  $2 \mu\text{m}$  and electrons energy of 5.6 MeV at the exit of the rf gun. The important geometrical parameters (see Fig. 1) are: 1.6 cell rf gun operated at S-band with a peak field on the cathode of 120 MV/m followed by an emittance compensating solenoid and three accelerating cavities 3 m long of the SLAC type (2856 MHz traveling wave), the first one is embedded in a solenoid. The first traveling wave (TW) structure is set at the relative maximum of the normalized emittance oscillation and to the relative minimum of the beam envelope, according to the Ferrario’s working point [7]. This position is at 1.5 m from cathode for the nominal SPARC parameters.

The photocathode of the rf electron gun is illuminated by a Ti:Sa laser providing, in the standard operation,

10 ps long rectangular (1 ps rise time) light pulses at 266 nm (third harmonic) delivering about 500  $\mu\text{J}$  energy per pulse. Electrons emitted by cathode are accelerated in the gun. Then, they drift within a focusing magnetic field for about 1.5 m and afterwards, they enter the three accelerating sections.

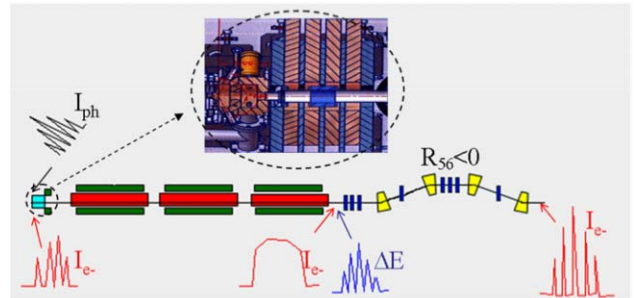


Figure 1: Experimental scheme. In the dotted circle the exploded view of the rf gun and compensating solenoid.

In this paper we study the effect of a train modulation of the 10 ps laser pulse. A train of sinusoidal oscillations modulated by a Gaussian can be created splitting the laser pulse at the exit of the third-harmonic crystal, introducing a proper time delay between the two splitted beams and then recombining them. Afterwards, the two beams have to be extended by a stretcher that brings the spectrum in time again. The two beams interfere generating a train.

The generation of a train with pulses of non-sinusoidal shape, for instance much thinner peaks (as discussed below), requires a shaping system inserted just after the amplifier system or inside the amplifier system after the multipass amplifier and before the compressor. The shaping system is a 4-f system, whose core is the liquid-crystal-spatial-light-modulator (LC-SLM) [4].

We will term the train of pulses as *comb beam*.

Table 1: SPARC beam and gun nominal parameters.

L(ps)	10
Q(nC)	1.1
Energy(MeV)	5.6
Projected Emittance( $\mu\text{m}$ )	<2
$B_{\text{gun}}$ (T)	0.273
$E_{\text{peak}}$ (MV/m)	120
$\varphi_{\text{inj}}$ (deg)	32

## COMB $e^-$ BEAM PHYSICS IN AN ACCELERATOR SECTION

The beam and machine parameters used for PARMELA beam dynamics studies are those presented in the

\*Work partly supported by Ministero Istruzione Università Ricerca, *Progetti Strategici*, DD 1834, Dec.4, 2002 and European Contract RII3-CT-PHI506395CARE.

introduction. An example of the results of these studies is shown in Fig. 3. We can remark the following:

- the initial electron bunches of equal charge wash out in such a way that the initial 100% intensity modulation is reduced to ~85% at the exit of the rf gun (Fig. 3(b) upper) and to ~25% at the exit of the drift section (Fig. 3(c) upper). The density modulation almost disappears already at the end of the first accelerating structure (Fig. 3(d) upper) and the profile starts to assume a slight pancake shape;
- an energy modulation with the periodicity of the intensity grows until the end of the drift space. Notably, the energy modulation has a saw-tooth fashion;
- the amplitude of the energy modulation  $\Delta E$  depends both on the number of the  $e^-$  beam pulses and on the initial width, as shown in left and right plots of Fig. 2, respectively;
- the beam energy structure does not change so much up to about 40 MeV, but since then it starts to evolve and it results strongly distorted after the whole accelerating section. The density beam profile at the end of the beamline shows the well-known pancake shape.

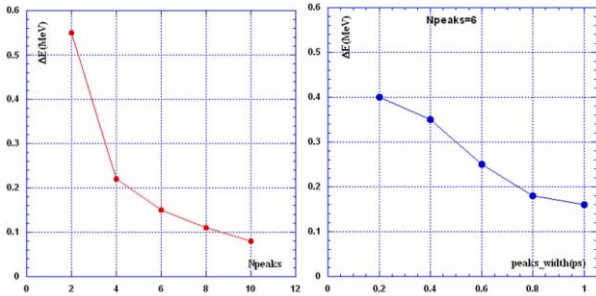


Figure 2: Energy modulation  $\Delta E$ (MeV) at 1.5 m for a 10 ps comb beam: as a function of the number of sinusoidal peaks (left); and as a function of the FWHM for  $N_{\text{peaks}}=6$  (right).

Density modulation is transformed into energy modulation. The periodic beam profile evolves towards a homogeneous one with small undulations and finally the peaks and valleys are interchanged.

The beam dynamics shown by simulations is explained by the action of the longitudinal space charge force. The internal electric field generated at the surfaces of the charge thin disks induces a either positive or negative velocity variation of the electrons, depending on the disk sides. The accelerated particles move through the inter-disk space washing out the longitudinal spatial modulation and, in the meanwhile, changing their energy. The longitudinal space charge force vanishes when particles become ultra-relativistic. In fact, from the simulations it is clear that the intensity and the energy profiles evolve within the gun and within the drift space because the beam energy is relatively low. Once electrons enter the cavities they become very soon ultra relativistic and both the energy and intensity profiles are determined by the rf field only in conjunction with the rf phase.

The very short spikes shown in the intensity profile and in the  $x$ - $\phi$  beam section (column (d) Fig. 3, 4 and 5) are low density regions.

This ‘multibunch’ beam ends up having a worse projected emittance (up to a factor 3) compared to the well known homogeneous cylindrical  $e^-$  beam.

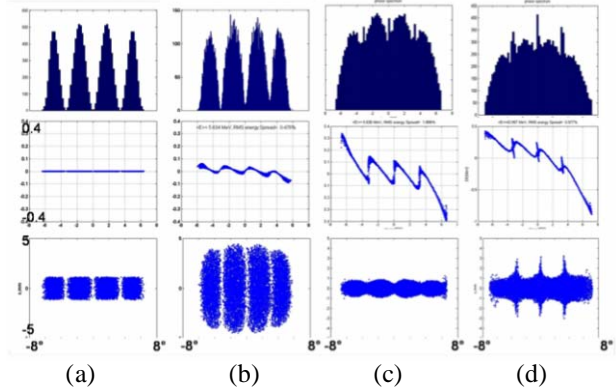


Figure 3: Evolution of a 10 ps comb beam with 4 bunches at cathode (a); at exit of gun (b); at 1.5 m (c); at  $z=4.57$  m with  $E=43$  MeV(d). Upper: longitudinal profile, middle:  $\Delta E$ (MeV)- $\phi$ ( $^\circ$ ), lower:  $x$ (mm)- $\phi$ ( $^\circ$ ).

### Energy modulation as a function of frequency sinusoidal modulation

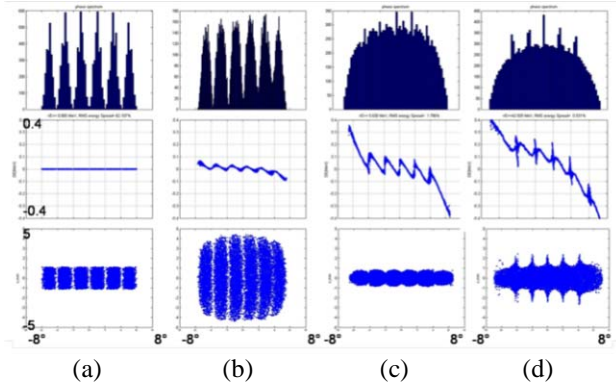


Figure 4: Evolution of a 10 ps comb beam with 6 bunches at cathode (a); at exit of gun (b); at 1.5 m (c); at  $z=4.57$  m with  $E=43$  MeV(d). Upper: longitudinal profile, middle:  $\Delta E$ (MeV)- $\phi$ ( $^\circ$ ), lower:  $x$ (mm)- $\phi$ ( $^\circ$ ).

The amplitude of the energy modulation for a sinusoidal beam decreases with the number of the peaks. As shown in left of Fig. 2 at  $z=1.5$  m  $\Delta E$  goes from ~0.22 MeV for a comb beam of 4 sinusoidal peaks to ~0.11 MeV for the 6 case and to ~0.08 MeV for the 10 peaks one. This behaviour complies with the reduction of the charge per disk, in fact:  $Q_{\text{disk}}=Q_{\text{beam}}/N_{\text{peaks}}$ .

### Energy modulation as function of the bunch widths

From Figs. 4 and 5 we may see that the thinner the disks the wider the energy modulation. In Fig. 5 is plotted a comb beam of 6 Gaussians with a FWHM of 0.2 ps, to be compared to the case of Fig. 4 where the 6 sinusoidal peaks have FWHM of 1 ps.

The behaviour complies with the fact that the thinner the charge density the higher is the charge density and, in turn, the surface electric field. In addition, the inter-disk distance increases.

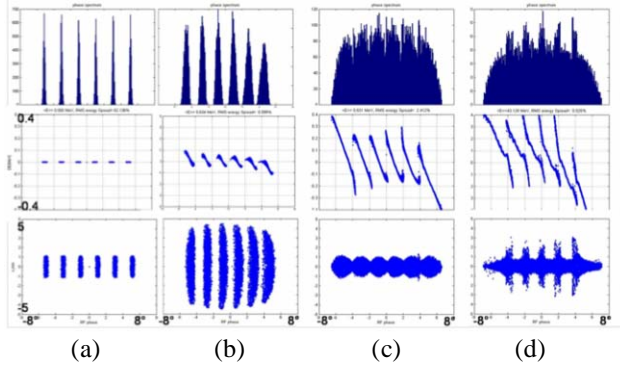


Figure 5: Evolution of a 10 ps comb beam with  $N_{\text{peaks}}=6$  and  $\text{FWHM}=0.2$  ps at cathode (a); at exit of gun (b); at 1.5 m (c); at  $z=4.57$  m with  $E=43$  MeV(d). Upper: longitudinal profile, middle:  $\Delta E(\text{MeV})-\phi(^{\circ})$ , lower:  $x(\text{mm})-\phi(^{\circ})$ .

### Comb beam compression

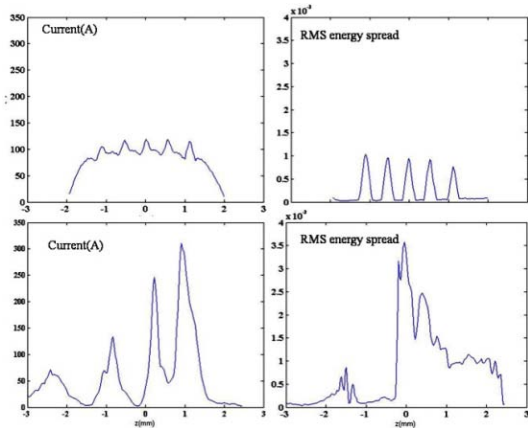


Figure 6: Comb beam before magnetic compression (upper) and after magnetic compression (lower).

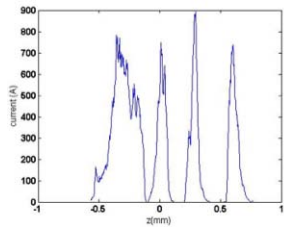


Figure 7: Beam current at the end of three TW structures in the rf compression case. The comb beam at cathode has 6 bunches and  $\text{FWHM}=0.2$  ps in 10 ps.

The comb beam with 6 bunches and  $\text{FWHM}=0.2$  ps has been compressed in order to convert the energy modulation into density modulation. Both techniques of magnetic and rf compression have been analyzed.

A magnetic compressor with  $R_{56} = -0.1$  m after the three TW sections at 155 MeV has been studied. The result of the PARMELA simulation is reported in

Fig. 6: at the entrance of the magnetic compressor the density distribution (upper left) has lost almost completely the initial comb shape, which has been converted into energy distribution (upper right); at the compressor exit high peaks current of the order of  $\sim 300$  A (lower left) are produced.

Rf compression [8] has been achieved with PARMELA simulations accelerating the beam in the first TW section  $-96^{\circ}$  off crest. The beam density at the end of the three accelerating structures is reported in Fig. 7: there are four peaks of current of about 750 A. Moreover, further optimizations of both compression techniques are underway.

## DISCUSSION

The space charge force, which is considered a destructive force, in this case is turned into a constructive force.

The intensity and energy evolution of a pulse train created at the photocathode of the SPARC injector is well explained by the action of the longitudinal space charge force connected to the charge of the disks. The density modulation is changed by the space charge force into energy modulation. The higher the charge density the higher is the energy amplitude. The profile evolution stops once the beam becomes almost homogeneous.

The profile of the energy modulation constructed before the rf cavities is completely distorted by the acceleration process. The energy modulation can be usefully exploited to generate a high energy comb beam with very high peak current, re-designing the accelerating sections in such a way that the energy profile is maintained, and then inserting a proper beam compressor. Within the technology of this machine the velocity bunching mechanism seems essential for obtaining good electron bunches in terms of phase space quality.

A comb beam accelerator relies on the capability of the laser which drives the rf gun to provide target light profiles by means of a versatile shaping system inserted in the laser system. We would like to stress that the realization of a laser pulse train in the UV band is a real challenge.

## REFERENCES

- [1] C. Vaccarezza et al., “Status of the SPARX FEL Project”, this Conf.
- [2] L. Serafini et al, “The PLASMONX Project for advanced beam physics experiments @ LNF”, this Conf.
- [3] <http://www.linearcollider.org>
- [4] I. Boscolo, S. Cialdi, F. Castelli, D. Cipriani, Report I-PHIN-CARE-JRA2-WP3, Second Task Pulse Shaping [http://www.infn.it/phin/docs\\_files/19\\_Deliverable\\_INFN\\_Mi.pdf](http://www.infn.it/phin/docs_files/19_Deliverable_INFN_Mi.pdf) and references therein.
- [5] L. Serafini et al, ‘Status of the SPARC Project’, this Conf.
- [6] J.Billen, “PARMELA”, LA-UR-96-1835, 1996.
- [7] M. Ferrario et al., “Homodyn study for the LCLS Photoinjector”, SLAC-PUB-8400, Mar 2000.
- [8] M. Ferrario et al. “Beam dynamics study of an RF bunch compressor for High Brightness beam injectors”, Proc. of EPAC02, p. 1762, June 2002 Paris.

## A BIPERIODIC X-BAND RF CAVITY FOR SPARC

L. Ficcadenti, M. Esposito, A. Mostacci, L. Palumbo, Università La Sapienza, Roma, Italy  
D. Alesini, B. Spataro, LNF-INFN, Frascati, Italy; A. Bacci, Milano-INFN, Milano, Italy.

### Abstract

The Frascati photo-injector SPARC (Pulsed Self Amplified Coherent Radiation Source) will be equipped with a X-band RF cavity for linearizing emittance to enhance bunch compression and for reducing bunch longitudinal energy spread. A biperiodic cavity working on the  $\pi/2$ -mode offers some advantages in comparison to a conventional (periodic) cavity despite the need of accurate machining. A copper prototype made of seventeen separated cells has been built following numerical simulation. In this paper we report on preliminary measurements of its RF properties. The main characteristics of the cooling system for the final device are also addressed.

### INTRODUCTION

The proposed  $\pi/2$  accelerating section represents an alternative design to the standard  $\pi$ -mode cavity [1] for longitudinal phase space compensation at SPARC [2], as the lower sensitivity (of the cavity field distribution and resonant frequency) to the machining error, cell-to-cell temperature variations and assembly errors. The price to be paid is a lower shunt impedance per unit length and major fabricating costs because of the presence of the coupling cells, with respect to the  $\pi$ -mode structure. Bead-pull measurements on a copper prototype have been done and the results are illustrated and compared with the numerical ones. The sketch of the cavity profile with dimensions is reported in Fig. 1. The X-Band structure is designed to obtain  $5MV$

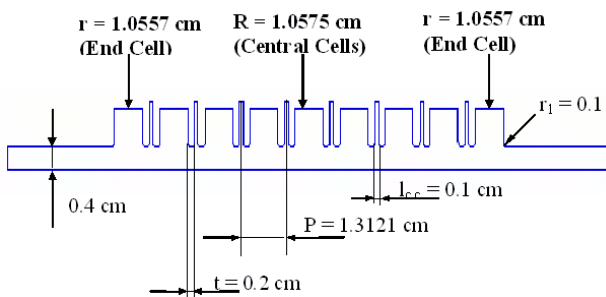


Figure 1: Longitudinal section of the cavity.

accelerating voltage with an input power of  $3MW$ . It is a 17 cells structure fed by a central coupler.

### SIMULATION RESULTS

The detailed analysis of the structure design without coupler is reported in [1]. The 2D design have been performed

using SUPERFISH code. The double periodicity of the structure operating on  $\pi/2$ -mode introduces a *stop-band* in the dispersion curve with two  $\pi/2$ -mode configurations (Fig. 2). There are two modes with  $\pi/2$  cell-to-cell phase shift: one excites the long accelerating cavities, the other one excites the short coupling cavities. In order to close

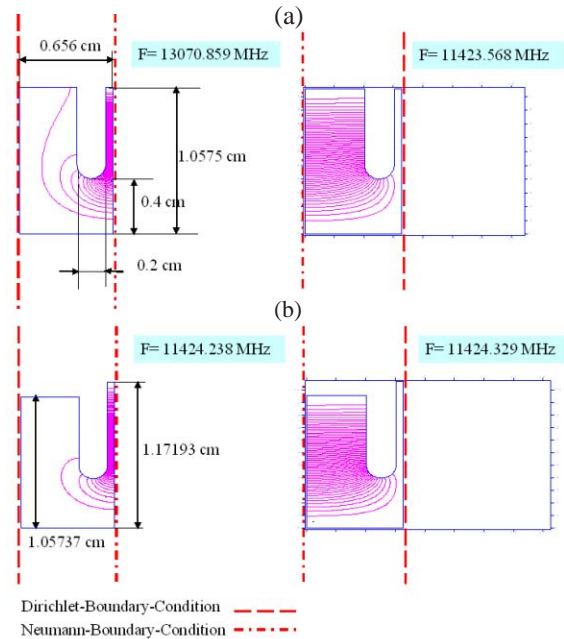


Figure 2: Half-cell simulated structure with the different configuration of the accelerating and no-accelerating electric field lines when the stop-band is open(a) or close(b).

the stop-band, the short cavity radius has been increased up to make the resonant frequencies of the two modes equal. Prototype radius of the coupling cell with open and close stop-band vary of  $0.6mm$ . The corresponding field distributions of the accelerating and coupling cells are reported in Fig. 2. The dispersion curves obtained from HFSS and GDFIDL code, compared with the one obtained from SUPERFISH, are superimposed over same Fig. 3 for the case of stop-band open and stop-band close. 3D simulation codes (HFSS and GDFIDL) have been used to design a proper feeding system for the cavity in the central cell in order not to excite the adjacent modes that have the nearest frequency to the  $\pi/2$  mode and zero field in the central cell. Therefore with central coupler we have a much greater modes separation and the working mode is less perturbed by the closest ones. The coupling cell, coupler and window dimensions are sketched in Fig. 4. The dimension

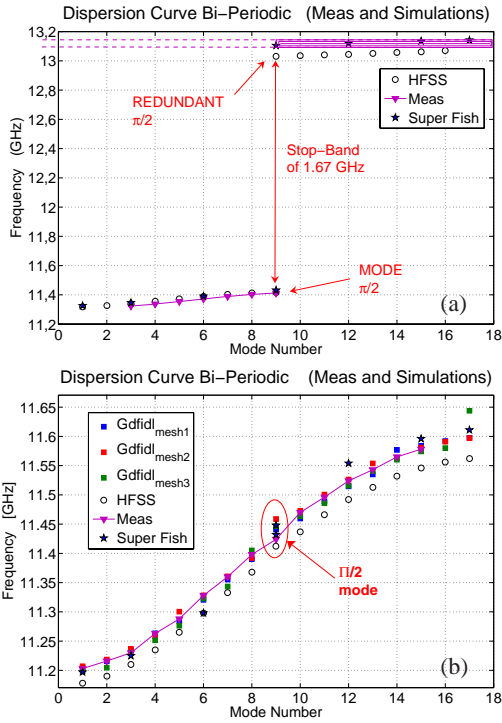


Figure 3: Measured dispersion curve in the case of: a) *stop-band open* and b) *stop-band close*, compared to simulation code results.

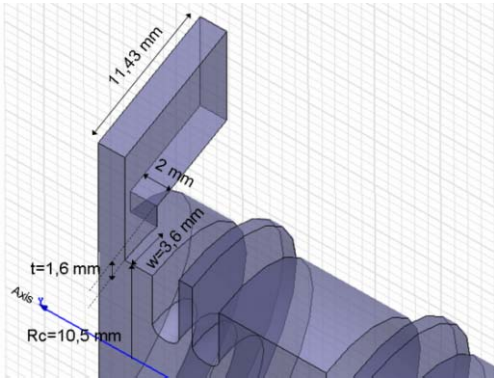


Figure 4: Sketch of the coupling cell.

of the coupler window ( $w$ ) and of the central cell radius ( $R_c$ ) have been tuned in order to obtain simultaneously a coupling coefficient  $\beta = 1$ , a resonant frequency of the whole system equal to  $11.424 GHz$  and to preserve a good field flatness. We have obtained the coupling coefficient  $\beta = 0.97$  with a good field flatness, within few percent.

## THE PROTOTYPE

### Mechanical Characteristics

Two full scale copper prototype has been constructed and it is shown in Fig. 5. The 17 cells structure has been de-

signed for brazing, but the RF tests refer to a mechanically joined structure. The material used to build this prototype is oxygen free copper. The structure has been realised by mechanical machining with a numerically controlled lathe and the obtained precision is below  $0.01 mm$ , while the surface roughness is not worst than  $0.4 \mu R_a$ . The assembling procedure foresees the joining of the seventeen cells using two stainless disks used to press the structures by means of three  $8 mm$  diameter copper rods. A torque of  $11 N/m$  was applied to every rod, corresponding to a pressure of roughly  $80 N/mm^2$ . Each accelerating cell has a tuning

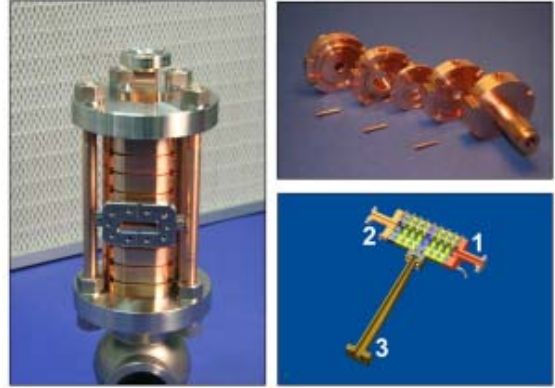


Figure 5: Copper prototype of the structure.

screw (with radius of  $3 mm$  and length of  $5 mm$ , Fig. 5) to vary the cell volume and thus the resonant frequency and field distribution. The average frequency variation due to maximum elongation for each tuner is not greater than  $0.5 MHz$ . To feed the structure two lateral small antennas are also inserted (position 1, 2 of Fig. 5). Two type of different measurements have been carried out: transmission (or reflection) scattering coefficient measurements between the two antennas or between the antennas and the central coupler (port 3 in Fig. 5) and bead pull measurements.

### Electromagnetic Characterisation

The transmission coefficient between the two small lateral antennas and between the antennas and the central coupler have been measured both in the stop-band open and stop-band close structures. As previously observed, we can excite only nine over seventeen possible modes by central coupler because we impose a non-zero field in the central cell. On the contrary with the two antennas we can excite all the possible modes. The quality factor of the resonance has been measured and compared with the numerical ones. The  $Q$  factor of the  $\pi/2$  mode in the case of stop-band close is reported in Tab. 1; the measured  $Q$  is lower than the calculated ones since the cavities are not brazed yet. The measured dispersion curve, compared with the one obtained from HFSS, GDFIDL and SUPERFISH, is reported in Fig. 3. Showing a good agreement with the simulation

Table 1: **Quality and form factors measured on the stop-band close prototype compared with the numerical results.**

	HFSS	Superfish	Meas
$Q_0$	7412	7101	5815
$R/Q(\Omega/m)$	9452	9693	$9150 \pm 200$

results.

With the bead pull technique we measured the electric field on axis [4]. To calculate the  $R/Q$  we have calibrated the bead form-factor comparing the perturbation induced by the perturbing object in a pill-box cavity working at  $1.91GHz$  on the  $TM_{010}$  mode with analytical results. Using different resonant modes of the pillbox cavity we have also checked that the form-factor does not depend on the frequency, within our measurement uncertainty. The measured longitudinal electric field on axis, for the stop-band close structure, is plotted in Fig. 6. The tuning procedure allow a field-flatness of the order of 3% at the nominal resonant frequency of  $11.424GHz$ . The mea-

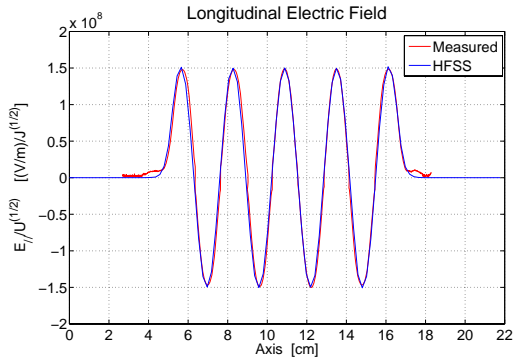


Figure 6: Measured and simulated electric field on axis at the  $\pi/2$ -mode resonant frequency.

sured  $R/Q$  per unit length is reported in Tab. 1 and it is in very good agreement with the simulation results.

### PRELIMINARY THERMAL ANALYSIS

To maintain the structure dimensions unchanged during operation, a close temperature control during the operation is needed. The main factors that affect the section temperature are the RF power losses, the heat transfer mechanism from the structure to the cooling tubes and the cooling water temperature variation.

The frequency shift behaviour versus the heating of the structure has been studied by the integration between ANSYS [3] and SUPERFISH. A temperature variation  $\Delta T = 1^\circ C$  causes a  $191kHz$  frequency shift by assuming an isotropic expansion and a  $80kHz$  frequency shift if one considers the real power distribution shown in Fig. 7. The maximum dissipated power on the surface is  $3.5W/cm^2$ .

These results show that temperature stabilisation within

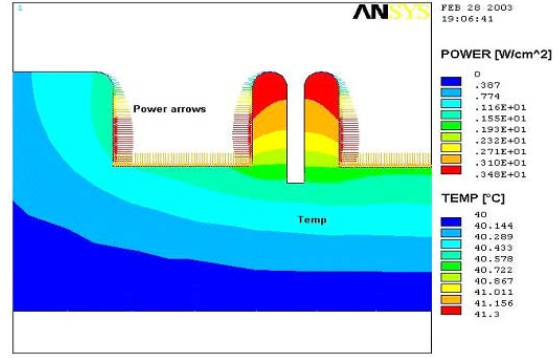


Figure 7: Thermal flux and distribution in temperature using copper, simulated by ANSYS code.

$0.1^\circ C$  has to be applied at the maximum duty cycle to keep the structure frequency within 1/100 of the frequency bandwidth.

### CONCLUSIONS

A Bi-Periodic X-Band accelerating section for linearizing the longitudinal phase space in SPARC project has been proposed and the copper prototype has been realised. Resonant frequency, quality factors and electric field have been measured on the copper prototype in the open and close stop-band cases. Even if the prototype is not brazed the measurement results are very close to the expectation. Thermal analysis has been carried out using ANSYS code. Brazing tests are now in progress in the LNF for the construction of the final device.

### ACKNOWLEDGEMENTS

The authors are grateful to Alessandro Venzaghi and Daniele Giacobello for their help in the RF measurement. V. Lollo deserves special thanks for the mechanical design and realisation of the cavity prototypes.

### REFERENCES

- [1] B. Spataro *et al.*, *Studies on a Bi-Periodic X-Band Structure for SPARC*, LNF-03/013(R), LNF-INFN, August 2003.
- [2] P. Emma, *X-Band RF Harmonic Compensation for Linear Bunch Compression in the LCLS*, LCLS-TN-01-1, SLAC, November 2001.
- [3] <http://www.ansys.com>.
- [4] J. C. Slater, L. C. Maier, *J. Appl. Physics*, 23 No.1, 1952.

# METAL FILM PHOTOCATHODES FOR HIGH BRIGHTNESS ELECTRON INJECTORS

G. Gatti\*, L. Cultrera, F. Tazzioli, C. Vicario, INFN-LNF, Frascati (Roma) Italy.  
A. Perrone, Lecce University, Physics Dept. and INFN, Lecce, Italy.

C. Ristoscu, Laser Dept., National Institute for Laser, Plasma and Radiation Physics, Bucharest-Magurele, Romania.

J. Langner, M. Sadowski, P. Strzyzewski, IPJ-Swierk, Warsaw, Poland.  
S. Orlanducci, A. Fiori, Dip. Scienze Chimiche and INFN, Rome University Tor Vergata, Roma, Italy.

## *Abstract*

Advanced high brightness injectors require photocathodes with fast response, high quantum efficiency and good surface uniformity. Both Mg films deposited by laser ablation and Pb films deposited by vacuum arc could satisfy these requirements. Their emission and morphology are compared.

## INTRODUCTION

The main requirements on photo-cathodes for the advanced electron sources of ultra-bright electron beams are prompt response, high QE, defined as the number of emitted electrons per incident photon, at wavelengths affordable by existing lasers, low thermal emittance and reasonable lifetime [1][2]. Metallic cathodes are fast (tens of femtoseconds range) but their QE is rather low as compared with alkali semiconductors. These however have a slower response and their lifetime is short. In addition they are delicate to handle, requiring UHV both during transport and in operation. Metals are sturdier and a few of them, such as Mg, Pb, Y have reasonable QEs at near UV wavelength. Bulk Mg cathodes are already in use in some injectors. Mg disks inserted by press fitting in the end Cu plate of a RF gun cavity have shown problems of RF breakdown at the junction [3]. Moreover, QE uniformity over the irradiated area can be remarkably not uniform [4]. High quality metal films deposited directly on the gun plate could circumvent such problems. Sputtered Mg films have already been tested. They are rugged and exposition to air forms a protective oxide layer that can be easily removed by laser ablation (laser cleaning) [5]. However, when tested in the very high electric fields of a RF gun, the sputtered Mg films have been damaged by discharges during RF conditioning process [6]. This is attributed to poor quality of the film, especially regarding uniformity and adhesion. A key parameter determining the quality of a deposited film is the kinetic energy of the particles impinging on the substrate. Therefore it is worthwhile to study alternative deposition processes with inherent higher particle energies, as pulsed laser deposition (PLD) [7] and vacuum arc discharge [8].

## FILM DEPOSITION TECHNIQUES

The PLD deposition apparatus is made up of an UHV chamber containing the Mg target to be ablated and the substrate to be coated. A powerful pulsed laser beam from a XeCl excimer laser (wavelength = 308 nm, pulse duration = 30 ns), injected through a quartz window, impinges on the target and forms a plume of Mg vapour. The substrate is placed in the plume cone at a suitable distance from the target. More details are reported in [9].

An advantage of the PLD method with respect to magnetron sputtering is the high kinetic energy of the evaporated material particles reaching the substrate surface. The kinetic energy distribution depends on various parameters, mainly the laser fluence. With our experimental conditions, one may estimate an average of 50 eV against 10 eV in magnetron sputtering. The high kinetic energy enhances adhesion of the coating material to the substrate. Drawbacks are the presence of droplets on the surface and limited film thickness. I.e. PLD films are limited to a few microns, while other techniques can easily grow films to a larger thickness (20 microns). Anyway different improvements have been achieved and are in course to overcome these issues.

The Vacuum Arc deposition technique is an interesting alternative because the kinetic energy of the particles is high, certainly more than in sputtering technique PLD [10]. Moreover, being the projectiles charged, it consents efficient filtering of neutral droplets. Both techniques afford the advantage of clean vacuum environment. A complete stand for the deposition of Pb films is already operative at IPJ-Swierk Laboratories. Recently it has been demonstrated that the cathodic arc can be operated under UHV conditions thus strongly reducing contaminations by residual gas impurities.

## EXPERIMENTAL APPARATUS

The QE measurement and laser cleaning apparatus consists of a test HV chamber, at  $10^{-6}$  Pa background pressure, containing a vacuum diode of which the film to be tested constitutes the cathode. An UV 266 nm laser pulse, 30 ps duration, from a mode-locked frequency quadrupled Nd:Yag laser, is injected through a quartz window and excites the cathode. Accelerating electric fields up to 2 MV/m can be applied to the diode. The laser

\* Giancarlo.Gatti@lnf.infn.it

beam crosses the anode through a fine copper wire mesh and illuminates the cathode at normal incidence. The emitted charge is sent via a coaxial cable to the input of a high speed oscilloscope or to a high sensitivity charge amplifier.

The measuring apparatus has been recently improved by building a new chamber with multiple ports that allows online mass spectrum analysis and illumination of the sample either at 0 or 70 degrees incidence. The larger angle avoids the usual anode mesh and allows studying the effect of laser beam polarization on emission.

## SAMPLE PREPARATION

### PLD Films

The PLD technique makes multilayer deposition of different materials viable within the same session, by using composite targets. That allows covering of the film with a thin layer, for protection tasks, or, alternatively, to enhance emission yield. A graphite protective layer has been tested. In that case, the target is Mg-C, with a Mg belt surrounding a Graphite core. The laser beam was shifted in succession from one zone to the other. The deposition parameters of two of these samples are shown in Table 1.

We have produced films with thickness from 0.2 to 2 microns covered with a 20 nm protective layer either of magnesium oxide or graphite. The Mg protective layer was grown by ablating the Mg target at 20 Pa oxygen atmosphere. The deposition parameters of a Mg-C sample are listed in Table 1.

Table 1. Deposition parameters of the PLD deposited sample labeled Mg LE003.

SAMPLE	LE003
TARGET	Mg-C
SUBSTRATE	Cu
T-S DISTANCE	4.5 cm
LASER SPOT SIZE	1.1 mm <sup>2</sup>
LASER FLUENCE	10 J/cm <sup>2</sup>
DEPOSITION PRESSURE	3.3x10 <sup>-6</sup> Pa
LASER PULSES	30000 on Mg & 9000 on C

### Vacuum Arc Films

The Vacuum Arc Pb films have been deposited at IPJ Swierk Laboratories with the same apparatus used for the tests of the cathode for the SC RF gun project [8]. A collaboration between LNF and IPJ is in course to set up a similar apparatus for the deposition of Mg films. (parametri del film)

## MEASUREMENTS

A computer controlled laser cleaning procedure has been implemented in order to clean the surface gradually and uniformly, thus avoiding film deterioration.

### PLD Mg

The laser beam was focused on the cathode surface, the laser spot having a diameter of about 300 μm. Once fixed the mean energy of the laser pulses to have an energy density of about 300 μJ/ mm<sup>2</sup>, each cleaning step was carried out performing a double scanning raster on the irradiated area having size approximately 2x2 mm<sup>2</sup>.

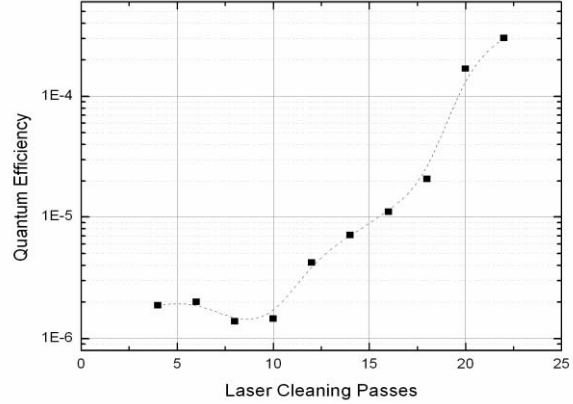


Figure 1: QE versus number of cleaning scans.

After activation process, the laser beam diameter is enlarged to cover the emitting spot and its energy is strongly decreased to perform QE measurements far from space charge saturation limit. Improvements in measured QE on number of cleaning steps is reported in Fig.1.

Finally, QE values of few 10<sup>-4</sup> have been obtained with repeatable procedure. Unless unspecified all emission measurement were performed with an electric field equal to 1 MVolt/m.

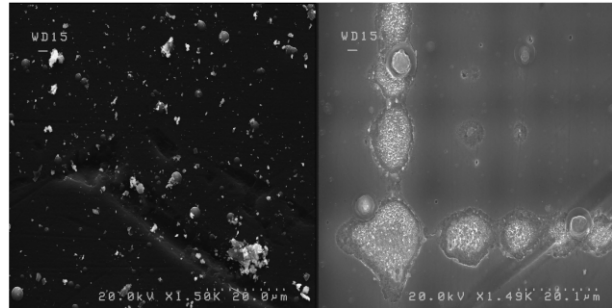


Figure 2: Left picture: As deposited sample surface; Right picture: after laser cleaning.

SEM analysis has been performed on sample surface before and after laser cleaning. The laser beam diffracted by the anode mesh creates a shadow network of high and low energy density lines that perturbs uniformity of cleaning process (calculations show 30% standard deviation in energy density through the surface). Moreover, the laser beam can act morphological and even structural changes over the surface of the film. In Fig. 2 we show the SEM pictures before and after cleaning.

It is to be noticed that the cleaning action has removed the major part of droplets, and that in this case surface looks very smooth: darker and brighter lines are due to

the diffraction pattern described above, and are not due to uniformity of the film itself.

### *Vacuum Arc Pb*

The performance of Pb as to emission efficiency is similar to the one of Mg, as expected from the close value of the two workfunctions, but the different sample synthesis technique leads to different surface morphology. A 2  $\mu\text{m}$  thick film was measured.

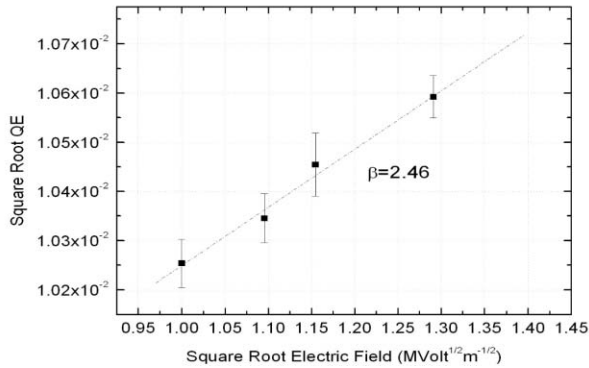


Figure 3: Pb QE vs. extraction field.

Both the environment and the cleaning procedure were the same as for the Mg case. Moreover, after laser cleaning, some QE versus field measurements were conducted, in order to calculate the  $\beta$  factor of field enhancement, in tight relation with roughness of the surface [12]. Maximum QE reached by Pb was slightly above  $10^{-4}$ , as foreseen. These results are shown in Fig.3, with a final computed  $\beta$  of 2.46.

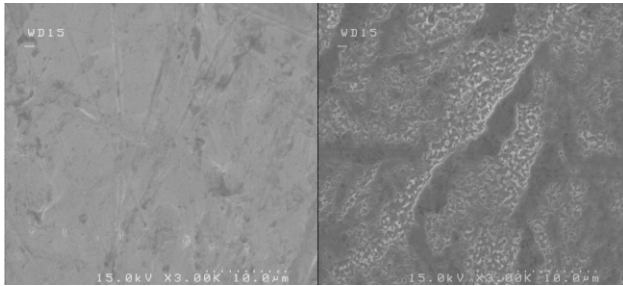


Figure 4 : Left picture: As deposited Pb sample; Right: after laser cleaning.

Post measurements analysis was performed once again by SEM. Microscopic analysis put in evidence a very good surface quality, on the untouched part of the surface. in Fig. 4 on a space scale of some micron. In the comparison between virgin surface, and after laser cleaning we can observe a changing in the surface structure, more evident in the areas of diffraction fringes maxima.

### *Final RF Gun Cathode*

One of the goals of our research is the construction of a cathode suitable for operation in an RF gun. The cathode for the UCLA-BNL type 1.6 cells RF gun is obtained by deposition of a disk of emissive material on the central

zone of the 10 cm diameter Cu end flange. Deposition tests of Mg films on dummy flanges by PLD have been successfully performed after different improvements on deposition of thick films. The final cathode is in course of construction and power tests in an RF gun are foreseen.

## CONCLUSIONS AND OUTLOOK

Metallic Films produced by Vacuum Arc or PLD are promising candidates for the photocathodes required by high brightness electron sources.

Deposition parameters to obtain uniform and high QE films have been determined. A protective thin layer of graphite or MgO allows easy handling and conservation of the cathodes before installation in the RF gun.

The construction of a cathode to be tested at full power in an RF gun is in course.

## ACKNOWLEDGEMENTS

This work is partly supported by

a) MIUR, Progetti Strategici, DD1834;

b) European Contract RII3-CT-PHI506395 CARE and contract no. 011935 -EUROFEL

## REFERENCES

- [1] Technical Design Report for the SPARC Advanced Photoinjector. <http://www.lnf.infn.it/acceleratori/sparc>
- [2] W. Graves et al., Proc. of PAC conference, Chicago 2001
- [3] X. J. Wang, M. Babzien, R. Malone, Z. Wu, LINAC Conference (2002) .
- [4] D. T. Palmer, Ph.D. thesis, Stanford University, Dpt of Applied Physics, 1998.
- [5] T. Srinivasan-Rao, J. Schill, I. Ben Zvi, M. Woodle, Rev. Sci. Instrum., Vol 69, No 6, June 1998, 2292-96.
- [6] X.J. Wang et al, Linac 2002 Conference, 142.
- [7] Pulsed laser deposition of thin films, Ed. D.B. Chrisey, Wiley, New York, 1994.
- [8] R. Russo et al, Supercond. Sci. Technol. 18 (2005) L41-44.
- [9] L.Cultrera et al., Applied Surface Science 248 (2005) 397-401.
- [10] A. Cianchi et al. Proc of EPAC 2004, 1021-1023, Lucerne, Switzerland
- [11] J.Smedley et al., PAC 2005 Conference
- [12] W. Graves et al., Proc. of PAC conference, Chicago, USA 2001, 2227-2229

## STATUS OF THE SPARX FEL PROJECT\*

C.Vaccarezza, D.Alesini, M.Bellaveglia, S.Bertolucci, M.E Biagini, R.Boni, M.Boscolo, M.Castellano, A.Clozza, L.Cultrera, G.Di Pirro, A.Drago, A.Esposito, M.Ferrario, D.Filippetto, V.Fusco, A.Gallo, A.Ghigo, S.Guiducci, M.Migliorati, L.Palumbo, L.Pellegrino, M.Preger, C.Sanelli, M.Serio, F.Sgamma, B.Spataro, A.Stella, F.Tazzioli, M.Vescovi, C.Vicario, INFN Frascati, Italy

F. Ciocci, G.Dattoli, A.Doria, F.Flora, G.Gallerano, L.Giannessi, E.Giovenale, G.Messina, P.L. Ottaviani, G.Parisi, L.Picardi, M.Quattromini, A.Renieri, C. Ronsivalle, ENEA C.R. Frascati, Italy  
S.Cialdi, C.Maroli, V.Petrillo, M. Rome, L.Serafini, INFN-Milano, Italy  
L.Catani, E.Chiadroni, A. Cianchi, C.Schaerf, INFN-Roma II, Roma, Italy  
P.Musumeci, INFN Roma, Italy

F.Alessandria, A.Bacci, F.Broggi, C.De Martinis, D.Giove, M.Mauri, INFN/LASA, Segrate, Italy  
L.Ficcadenti, M.Mattioli, A.Mostacci, University La Sapienza, Roma, Italy  
P.Emma, SLAC, Menlo Park, CA, U.S.A.  
S.Reiche, J. Rosenzweig, UCLA, Los Angeles, CA, U.S.A

### Abstract

The SPARX project consists in an X-ray-FEL facility jointly supported by MIUR (Research Department of Italian Government), Regione Lazio, CNR, ENEA, INFN and Rome University Tor Vergata. It is the natural extension of the ongoing activities of the SPARC collaboration. The aim is the generation of electron beams characterized by ultra-high peak brightness at the energy of 1 and 2 GeV, for the first and the second phase respectively. The beam is expected to drive a single pass FEL experiment in the range of 13.5÷6 nm and 6÷1.5 nm, at 1 GeV and 2 GeV respectively, both in SASE and SEED FEL configurations. A hybrid scheme of RF and magnetic compression will be adopted, based on the expertise achieved at the SPARC high brightness photoinjector presently under commissioning at Frascati INFN-LNF Laboratories [1,2]. The use of superconducting and exotic undulator sections will be also exploited. In this paper we report the progress of the collaboration together with start to end simulation results based on a combined scheme of RF compression techniques.

### THE SPARX LAYOUT

A spectral range from 13 nm to 1 nm has been considered for the radiation. SASE-FEL's in this wavelength range require high brightness beam at the undulator entrance. In Table 1 the electron beam parameter list is reported for such a source, while in Fig. 1

Table 1: Electron beam parameters.

Beam Energy	1÷2	GeV
Peak current	1-2.5	kA
Emittance (average)	2	mm-mrad
Emittance (slice)	1	mm-mrad
Energy spread (correlated)	0.1	%
Repetition Rate	50	Hz

the schematic layout of the accelerator is shown. A 150 MeV SPARC-like photoinjector [1] is meant to provide a 300÷500 A beam, adopting the velocity bunching compression scheme. A first linac section L1 rises the beam energy up to 350 MeV, where a first magnetic chicane is foreseen mainly for comparing the overall efficiency between the two compression methods at low energy. After a second linac section L2, i.e. at the energy around 0.5 GeV the main magnetic compressor is located that rises the beam peak current up to  $I_{pk} \sim 1$  kA, according to a ‘hybrid’ compression scheme consisting in one RF compression stage at low energy, plus one magnetic chicane at 0.5 GeV. A third accelerating section L3 brings the beam energy up to E~1GeV and a first extraction dogleg DL1 drives the beam through a diagnostic section and to the first undulator for SASE experiments in the radiation wavelength range of  $\lambda_r \sim 13.5 \div 6$  nm. This is

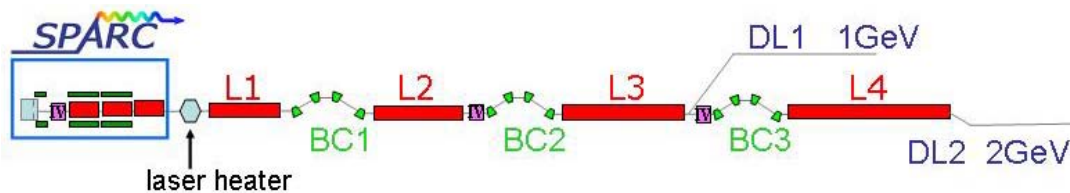


Figure 1: SPARX Linac schematic layout

\*Work partially supported by MIUR for the realization of “Grande Infrastruttura Laser ultrabrillante per raggi X multiscopo”

what is meant for the first phase of the SPARX project. For the Phase II a third magnetic chicane is foreseen downstream to compress the beam at  $E=1\text{GeV}$  and reach peak currents of the order of  $I_{pk}\sim 2\div 2.5\text{ kA}$ , and a final energy of  $E=2\text{GeV}$ , by means of a fourth linac section L4. A second extraction dogleg DL2 provides the beam diagnostics and delivery to the second undulator for the wavelength range  $\lambda_r\sim 5\div 1.5\text{ nm}$

### The RF Photoinjector

The injector design is based on the SPARC high brightness photoinjector presently under commissioning at Frascati Laboratories [1,2]. It considers a 1.1 nC bunch 10 ps long (flat top) with 1.1 mm radius, generated inside a 1.6-cell S-band RF gun of the same type of the BNL-SLAC-UCLA one [3] operating at 120 MV/m peak field equipped with an emittance compensating solenoid. Three standard SLAC type 3-m TW structures each one embedded in a solenoid boost the beam up to 150 MeV. According to the simulation results the beam compression at low energy ( $<150\text{ MeV}$ ), still in the space charge dominated regime, turns out to be feasible provided that a proper emittance compensation technique is adopted [4]. Moreover the propagation of a short bunch in the following accelerating sections reduces the potential emittance degradation caused by transverse wake fields, while a proper phasing of the linac can control the longitudinal wake fields. A systematic study based on PARMELA code simulations has been done in order to optimize the parameters that influence the compression [5], the results of computations show that peak currents up to kA level are achievable at the injector exit with a good control of the transverse and longitudinal emittance by means of a short SW section operating at 11424 MHz [6] placed before the first accelerating section. On the other side the results obtained without the IV harmonic correction prior the RF compressor, show that is anyway possible to reach good compression factors but paying for a heavy deformation of the longitudinal bunch distribution, a strong sensitivity to RF compressor phase, and a highly non linear longitudinal phase space. In Table 2 a summary is reported of the RF compression studies results. A medium RF compression factor has been chosen and presented here as the first referring case for the SPARX beam dynamics studies, it gives an average peak current  $I_{pk}\sim 400\text{ A}$  at the exit of the photoinjector, as highlighted in Table 2 and shown in Fig. 2.

### The Linac

In the present configuration the SPARX accelerator (PHASE I and II) is composed of four separate S-band linac sections L1, L2, L3, L4, with  $E=25\text{ MV/m}$  accelerating field, located downstream a SPARC-like photoinjector (see Fig. 1). At the entrance of each of the three magnetic chicanes an X-band section is provided to linearize the beam longitudinal phase space prior the magnetic compression. For the 1 GeV channel of Phase I, both L1 and L2 sections are meant to work off crest, to provide the required energy chirp to compress the beam in

Table 2: RF compressor parameter

RF phase range	B1,B2,B3 (gauss)	Current (A)	Emittance ( $\mu\text{m}$ )
$-60^\circ/-75^\circ$	1200,0,0	117-151	0.7
$-75^\circ/-83^\circ$	1200,1400,0	151-249	0.8
<b><math>-83^\circ/-87^\circ</math></b>	<b>1200,1400,0</b>	<b>249-458</b>	<b>1.3</b>
$-87^\circ/-91^\circ$	1200 $\div$ 1800	458-1180	2.8

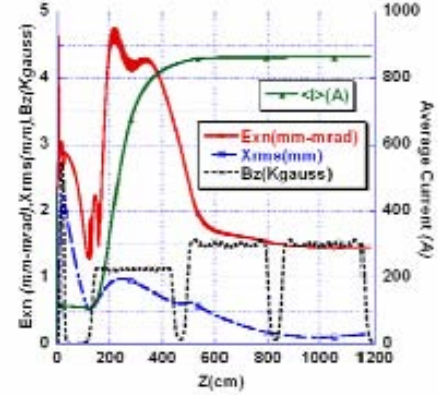


Figure 2: Average current, transverse emittance and envelope, axial magnetic field vs.  $z$  for a final 450 A electron beam., tracked with PARMELA [7].

BC2, while the on crest L3 section rises the beam energy up to  $E=1\text{ GeV}$  and contributes to the energy spread reduction. For the magnetic compression in BC3, the proper off-crest acceleration is applied also to the L3 section, while L4 contributes to the energy spread cancellation and brings the beam energy up to  $E=2\text{GeV}$ . The invariant envelope matching condition will be applied to the lattice as proposed by Ferrario *et al* [8].

### The Bunch Compression

To increase the beam current up to the kA order magnitude a magnetic compression stage is foreseen in the BC2 chicane for the beam with final energy  $E=1\text{GeV}$ ,  $I_{pk}\sim 1\text{ kA}$  (Phase I), and in the BC3 chicane for the beam with final energy  $E=2\text{ GeV}$ ,  $I_{pk}\sim 2.5\text{ kA}$  (Phase II). With the previously described setting for the RF photoinjector, a further compression factor of 2 in the BC2 chicane produces an average peak current  $I_{pk}\sim 1\text{ kA}$ , able to reach SASE saturation in the wavelength range of  $\lambda_r\sim 10\div 6\text{ nm}$  at the energy of 1GeV. The parameters of the BC2 compressor for this case are shortly listed in Table 3. The photoinjector incoming beam has been generated with PARMELA, considering a thermal emittance value of  $\epsilon_x\sim 0.6\text{ }\mu\text{m}$ , the downstream tracking in the chicane has been performed with ELEGANT [9]. The tracking in the BC2 chicane has also been checked with PARMELA and CSRtrack [10] codes in order to clarify the role played by the space charge effect in the transverse emittance dilution. In Fig. 3 the obtained results for the horizontal

Table 3: BC2 compressor parameters.

Beam Energy	$E$	GeV	0.5
Initial rms bunch length	$\sigma_{zi}$	mm	210
Final rms bunch length	$\sigma_{zf}$	mm	90
Incoming energy spread	$\sigma_{\delta i}$	%	.45
Momentum compaction	$R_{56}$	mm	-27
2 <sup>nd</sup> order mom. compaction	$T_{566}$	mm	+42

and vertical slice emittance are reported, together with the slice energy spread and current distribution along the bunch. The three codes outputs show that for a peak current around  $I_{pk} \sim 1$  kA the space charge effect doesn't heavily contribute to dilution of the transverse emittance. A detailed study is undergoing for the cases with higher compression factors both in BC2 and BC3 chicanes. The results of the beam tracking up to the undulator entrance in the 1 GeV channel are shown in Fig. 4.

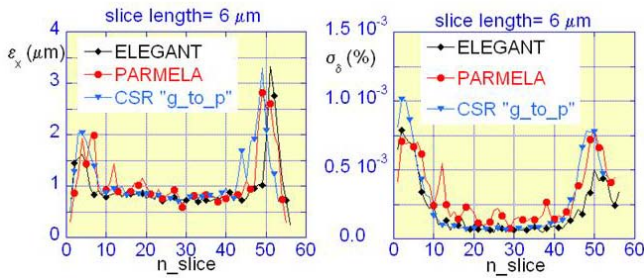


Figure 3: Slice analysis of simulation results through the BC2 compressor for the horizontal emittance and energy spread. The 50k particles have been tracked with ELEGANT, PARMELA and CSRtrack with “g\_to\_p” type forces.

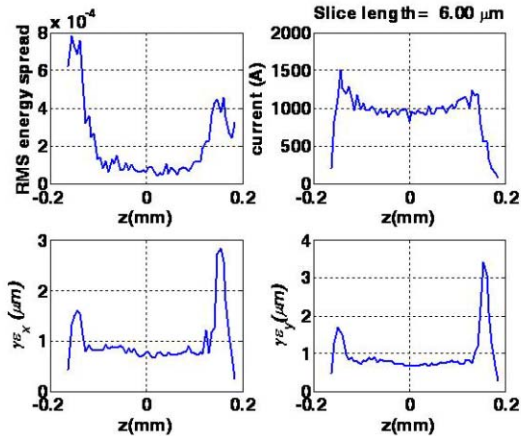


Figure 4: Energy spread, current distribution and transverse emittance along the bunch at the end of the SPARX 1GeV DL1 dogleg, tracked with ELEGANT.

### The SASE-FEL Source

Time dependent FEL simulations, performed with the code GENESIS [11] using the particle distributions produced by the Linac simulations, presented in the previous section, are in progress showing saturation for 90% of bunch slices after 25 m of active undulator length. We assume to use the same undulator of the SPARX project [1] with six additional 2.13 m long modules

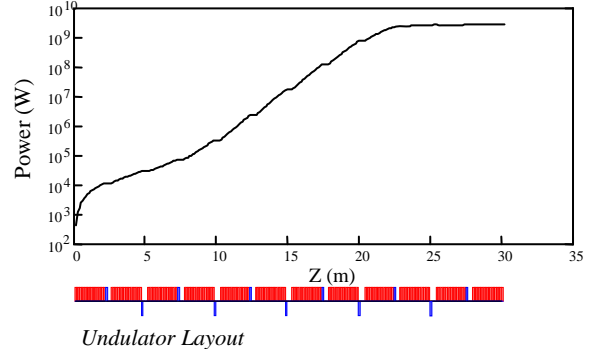


Figure 5: Genesis code simulation for the fundamental harmonic wavelength  $\lambda_r = 12$  nm.

required to saturate at 12 nm, see Fig. 5. These first preliminary results will be the starting point for further optimizations.

## CONCLUSIONS

The SPARX project aim is the generation of electron beams characterized by ultra-high peak brightness at the energy of 1 and 2 GeV, (Phase I and II), for SASE and SEEDD FEL experiments in the range of  $\lambda_r \sim 13.5 \pm 1.5$  nm. It is jointly supported by the Italian Government and Regione Lazio with a five years schedule for the first phase. The critical components such as the RF-compression scheme, magnetic chicane, etc. will be tested during the phase II of the SPARC project. A first general layout for SPARX has been proposed and first start to end simulations for the 1 GeV channel of Phase I, have been presented using a “hybrid” scheme of bunch compression with RF and magnetic compression techniques involved together.

## REFERENCES

- [1] L. Serafini, *et al*, “Status of the SPARC project”, these proceedings.
- [2] A. Cianchi, *et al*, “Characterization of the SPARC Photo-injector”, these proceedings.
- [3] D.T. Palmer, “The next generation photoinjector”, PhD. Thesis, Stanford University.
- [4] L. Serafini and M. Ferrario, “Velocity Bunching in PhotoInjectors”, AIP CP 581, 2001, pag. 87.
- [5] C.Ronsivalle, *et al*, “Optimization of RF compressor in the SPARX photoinjector”, PAC05, Knoxville(TN).
- [6] B. Spataro, *et al*, “Design and RF measurements of an X-band acc. structure”, NIM A554:1-12, 2005.
- [7] Billen, “PARMELA”, LA-UR-96-1835, 1996.
- [8] M. Ferrario, *et al*, “Beam Dynamics around transition”, ICFA panel on “The Physics and Applications of High Brightness electron Beams”, Erice, Sicily, October 14-19 2005.
- [9] M. Borland, “ELEGANT” LS-287, ANL, Argonne, IL 60439, USA.
- [10] M.D. Dohlus, T. Limberg, “CSRtrack: Faster Calculation of 3-D CSR Effects, FEL04, Trieste.
- [11] S. Reiche, Nucl. Instrum. & Meth. A429,243 (1999).

## STATUS OF THE SPARC PROJECT

D. Alesini, M. Bellaveglia, S. Bertolucci, R. Boni, M. Boscolo, M. Castellano, A. Clozza, L. Cultrera, G. Di Pirro, A. Drago, A. Esposito, M. Ferrario, L. Ficcadenti, D. Filippetto, V. Fusco, G. Gatti, A. Gallo, A. Ghigo, M. Incurvati, C. Ligi, F. Marcellini, M. Migliorati, A. Mostacci, L. Palumbo, L. Pellegrino, M. Preger, R. Ricci, C. Sanelli, M. Serio, F. Sgamma, B. Spataro, A. Stecchi, A. Stella, F. Tazzioli, C. Vaccarezza, M. Vescovi, C. Vicario (*INFN/LNF*);

F. Alessandria, A. Bacci, I. Boscolo, F. Broggi, S. Cialdi, C. DeMartinis, D. Giove, C. Maroli, M. Mauri, V. Petrillo, M. Romè, A. R. Rossi, L. Serafini (*INFN/Milano*);

D. Levi, M. Mattioli, P. Musumeci, G. Medici, D. Pelliccia, M. Petrarca (*INFN/Roma1*);

L. Catani, E. Chiadroni, A. Cianchi, E. Gabrielli, S. Tazzari (*INFN/Roma2*);

A. Perrone (*INFN/Lecce*);

F. Ciocci, G. Dattoli, A. Dipace, A. Doria, G.P. Gallerano, L. Giannessi, E. Giovenale, G. Messina, P.L. Ottaviani, S. Pagnutti, L. Picardi, M. Quattromini, A. Renieri, G. Ronci, C. Ronsivalle, M. Rosetti, E. Sabia, M. Sassi, A. Torre, A. Zucchini (*ENEA/FIS*);

J. Rosenzweig, G. Travish, S. Reiche (*UCLA*)

### Abstract

The SPARC Project has started commissioning its photo-injector. RF gun, RF sources, RF network and control, power supplies, emittance meter, beam diagnostics and control to measure the RF gun beam are installed and working inside the SPARC bunker. The photocathode drive laser has been characterized in terms of pulse shape and quality. We conducted initial beam measurements at RF gun exit using the emittance meter and a spectrometer. Preliminary indications of emittance oscillations driven by space charge in the drift downstream the RF gun are observed, in agreement to what expected from our theoretical model and numerical simulations. The design of the 12 m undulator for the FEL experiment has been completed and the first undulator section out of 6 is under test: we expect to fully characterize it at Frascati ENEA laboratory within the next months. Recent results of R&D activities on new photocathode materials are also reported.

### BEAM MEASUREMENTS WITH EMITTANCE METER

The first phase of the SPARC project[1] consists in characterizing the electron beam out of the photoinjector at low energy before the installation of the three accelerating sections. The experimental layout for this phase of the project is shown in Fig. 1. In order to study the first few meters of beam propagation, where space charge effects and plasma oscillations dominate the electron dynamics, a new sophisticated diagnostic tool was installed and commissioned, the movable emittance-meter [2]. The SLAC/BNL/UCLA 1.6 cell S-band RF gun was

conditioned up to  $> 10$  MW, corresponding to a field of 120 MV/m. The particular design of the emittance-compensating solenoid, with 4 different coils inside the magnetic yoke, allows a unique study of how different magnetic field configurations affect the electron beam dynamics, in particular varying (in sign and absolute values) the current setting independently for each coil power supply. The results of these findings are reported elsewhere in these proceedings[3].

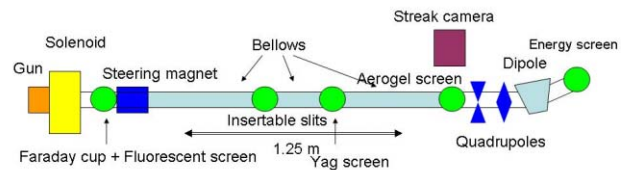


Figure 1. Block diagram for first phase of SPARC photoinjector commissioning.

The electron beam is created illuminating the cathode using a state-of-the-art laser system capable of producing flat-top laser pulses via an acousto-optics crystal for pulse-shaping[4]. The optical system that delivers the UV pulse onto the cathode i) creates the uniform transverse profile by truncating the tails of the beam distribution with an iris and ii) compensates for the 72 degrees incidence undesirable effects of beam ellipticity and amplitude front-tilt by imaging the plane of a 3560 lines/mm grating onto the cathode[5].

With a laser-based cleaning process we were able to improve the quantum efficiency both in absolute value and uniformity and reach a level of  $10^{-4}$  over a region of 2.5 mm around the cathode center (see Fig. 2).

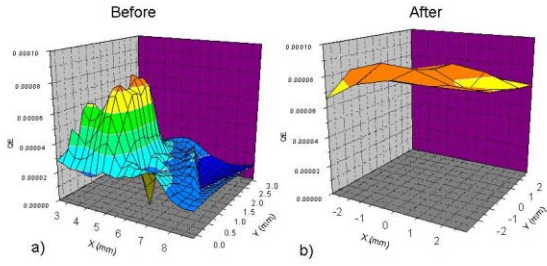


Figure 2. Quantum efficiency map before (a) and after (b) the laser cleaning procedure.

In Fig. 3 we show the beam energy and energy spread measured varying the launch phase of the laser pulse. The differences between the low and high charge case are due to longitudinal space charge effects (including the image charge at the cathode) and to the wakefield effects in the long bellows. The maximum beam energy of 5.65 MeV corresponds to a peak field in the gun of 120 MV/m, in complete agreement with RF power measurements.

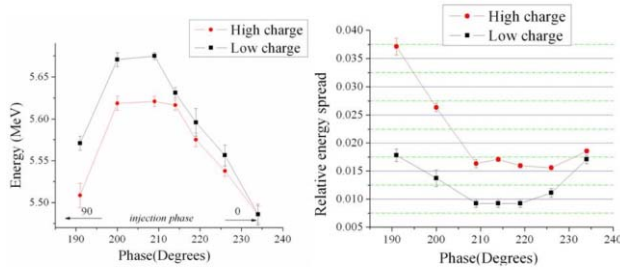


Figure 3. Beam energy and energy spread as functions of the launching phase.

A longitudinal diagnostic, based on Cherenkov radiation produced by the beam passing through a 5 mm thick aerogel slab with index of refraction  $n = 1.017$ , was installed with the main purpose of studying the photoinjector response to hundreds femtosecond long laser pulses created by the Ti:Sa laser system (blow-out regime). A field-lens narrow band filtering optical system delivers the Cherenkov light to the entrance slit of a 2ps resolution Hamamatsu streak camera enabling pulse length measurements. [6]. In Table 1 we report the beam parameters measured so far at low and high charge.

Table 1: SPARC photoinjector experimental parameters

Charge	200 pC	900 pC
Emittance	0.8 mm-mrad	2.2 mm-mrad
Energy	5.65 MeV	5.55 MeV
Energy spread	1 %	2.6 %
Pulse length	8 ps	12 ps

Using the emittance-meter we were able to observe clear indications of emittance oscillations driven by space

charge forces in the drift downstream of the RF gun, in agreement to what expected from our theoretical model and numerical simulations (see Fig.4)

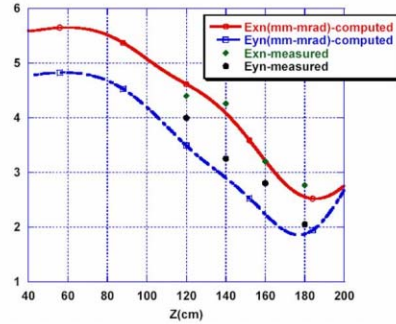


Figure 4. Measured emittance along z compared with Parmela simulations

## UNDULATOR AND FEL

The undulator system is made by six sections designed by ACCEL GmbH, under our specifications. In Figure 5 the drawing of the first undulator section is shown. The first prototype section is currently under magnetic test at ACCEL. The delivery to Frascati is expected at the end of July 2006. Field characterization is planned before the final installation in the SPARC-Hall.

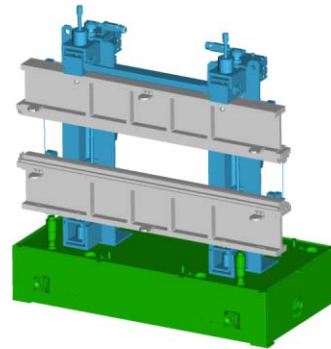


Figure 5: Technical drawing of the first undulator section

In SASE mode at 500 nm, the expected saturation length is about 10-12 m. A plot of FEL power behaviour vs. the e-beam parameters, as estimated by GENESIS 1.3, is shown in Fig. 6. Several experiments exploiting schemes of non-linear harmonic generation and seeding from external sources are also foreseen [7].

The vacuum chamber for the electron beam transport has been realised in AISI 316L stainless steel with a thickness of 0.5 mm and external dimensions of 13x8 mm. The vacuum has been both simulated and after that, experimentally tested. Results report a pressure of  $2 \cdot 10^{-7}$  mbar close to the pumping system and  $10^{-5}$  mbar at the central point of the vacuum chamber section, corresponding to the centre of the undulator. The technical design of the diagnostic chambers has been completed: a drawing is shown in Figure 7.

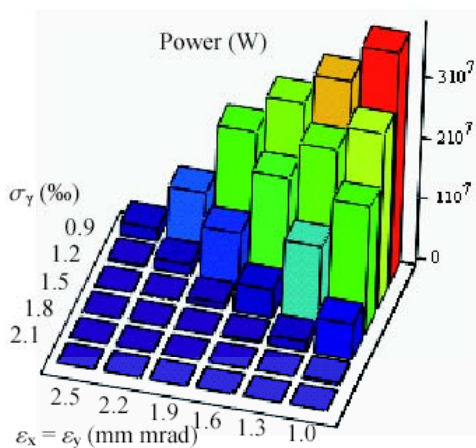


Figure 6: FEL power vs. beam energy spread and emittances from GENESIS 1.3 simulations.

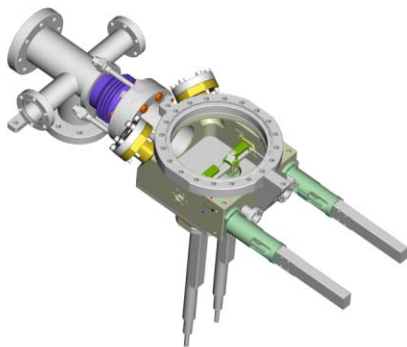


Figure 7: Diagnostic chamber drawing.

Two different, three steps, vertical actuators are hosted inside the chamber, capable of hosting different optical systems. The vertical movement is performed by precise motorised linear stages, with linear encoders in closed-loop control. The aim is to minimize detrimental effects of electron beam misalignments on the FEL amplification process. In order to minimize the impedance mismatch experienced by the electrons and to suppress the wake-field effects, we introduced a screening pipe.

### R&D ON PHOTOCATHODES

We investigated the deposition of high quality metal films directly on the RF gun cavity end plate, to be used as photocathodes. Main aim of this study is to circumvent problems of RF breakdown shown at the metal junction by Mg disks inserted by press fitting in the end Cu plate of the gun. A key parameter determining the adherence of a deposited film is the kinetic energy of the particles impinging on the substrate. Therefore it is worthwhile to study alternative deposition processes with inherent higher particle energies, as pulsed laser deposition (PLD) and vacuum arc discharge.

The PLD deposition apparatus used in this study is made up of an UHV chamber containing the Mg target to be ablated and the substrate to be coated. A powerful laser

beam from a XeCl excimer laser (pulse duration 30 ns), impinges on the target and forms a plume of Mg vapor. The substrate is placed in the plume cone at a suitable distance from the target.

Films with thickness from 0.2 to 2.5 microns, covered or not with thin protective layer either of graphite, palladium or silicon have been synthesized. A computer controlled laser cleaning procedure has been implemented in order to clean the surface gradually and uniformly, thus allowing a controlled removal of the contaminated surface layers and avoiding pure film deterioration. Mg films grown by PLD either with or without protective layers gave remarkable results in terms of QE, ranging from  $1.4 \times 10^{-4}$  up to  $7.9 \times 10^{-4}$  at low dc electric field (1 MV/m).

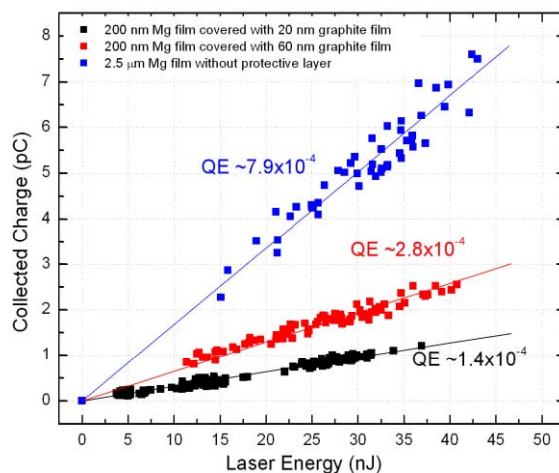


Figure 8: Emission curves of different Mg samples deposited by PLD on Cu substrates, after the laser cleaning of the protective or contaminated layers.

### REFERENCES

- [1] D.Alesini et al., *IEEE Cat. N. 05CH37623C*, (2005) 1327
- [2] A. Cianchi et al., *Characterization of the SPARC photo-injector with the Movable Emittance Meter*, these proceedings
- [3] C. Ronsivalle et al., *Study of the Effect of Multipolar Components in the SPARC Emittance Compensation Gun Solenoid*, these proceedings
- [4] M. Petrarca et al., *Production of Temporally Flat Top UV laser pulses for SPARC*, these proceedings
- [5] C. Vicario et al., *Commissioning of the Laser System for SPARC Photoinjector*, these proceedings
- [6] Dunning et al., *Optimum Beam Creation in Photoinj. Using Space-charge Expansion*, these proceedings
- [7] L. Giannessi et al., *Future Seeding Experiments at SPARC*, these proceedings

### ACKNOWLEDGEMENTS

We acknowledge many fruitful exchanges with several SLAC-LCLS members, and the loan of two SLAC 3 m S-band sections for the SPARC photoinjector.

# PRODUCTION OF COHERENT X-RAYS WITH A FREE ELECTRON LASER BASED ON AN OPTICAL WIGGLER

V. Petrillo, A. Colzato, Physics Department, University of Milan, Via Celoria,16 20133 Milano (Italy)

A. Bacci, C. Maroli, L.Serafini, Sezione di Milano INFN, Via Celoria,16 20133 Milano (Italy)  
M. Ferrario, LNF, INFN Via E. Fermi, 40 00044 Frascati (Italy)

## Abstract

The interaction between high-brilliance electron beams and counter-propagating laser pulses produces X-rays via Thomson back-scattering. If the laser source is long and intense enough, the beam electrons can bunch on the scale of the emitted X-ray wavelength and collective effects can occur. In this case, the FEL instability can develop and the system behaves like a free-electron laser based on an optical undulator. Coherent X-rays can be irradiated, with a bandwidth very much thinner than that of the corresponding incoherent emission. We analyse with a 3-D code the transverse effects in the emission. A generalized form of the Pellegrini criterion is validated on the basis of the numerical evidence.

## INTRODUCTION

A Thomson back-scattering set-up can be considered in principle as a source of intense X-ray pulses which is at the same time easily tunable and highly monochromatic. Due to recent technological developments in the production of high brilliance electron beams and high power CPA laser pulses, it is now even conceivable to make steps toward their practical realisation [1-2].

The radiation generated in the Thomson back-scattering is usually considered incoherent and calculated by summing at the collector the intensities of the fields produced in single processes by each electron [3]. If the laser pulse is long enough, however, collective effects can establish and become dominant. The system in this range of parameters behaves therefore like a free-electron laser, where the static wiggler is substituted by the optical laser pulse [4].

From the point of view of the theoretical description of the process, the possibility of generate coherent X radiation can be demonstrated with the same set of one-dimensional equations that are used in the theory of high-gain free-electron laser amplifier. However, many aspects of the process are connected with the finite transverse geometry of the electron beam and of the laser and, in order to give a quantitative evaluation of the radiation pulses it is obviously necessary to consider 3D equations [5].

In this paper, we present some particularly interesting data relevant to the solution of the 3-D equations with a discussion of their importance and some conditions for operating in a FEL mode.

## MODEL EQUATIONS AND RESULTS

We can write our model equations as:

$$\frac{d}{dt} \bar{\mathbf{r}}_j(\bar{t}) = \rho \frac{\mathbf{P}_j(\bar{t})}{\bar{\gamma}_j(\bar{t})} \quad (1)$$

$$\frac{d}{dt} P_{jz}(\bar{t}) = -\frac{\bar{a}_{L0}^2}{2\rho\gamma_0^2} \frac{1}{\bar{\gamma}_j} \left[ \frac{\partial}{\partial \bar{z}} |g|^2 \right]_{\bar{\mathbf{x}}=\bar{\mathbf{r}}_j} - \frac{2}{\bar{\gamma}_j} \text{Re al} \left[ (g^* \bar{A})_{\bar{\mathbf{x}}=\bar{\mathbf{r}}_j} e^{i\theta_j(\bar{t})} \right] + \dots \quad (2)$$

$$\begin{aligned} \frac{d}{dt} P_{j\perp}(\bar{t}) = & -\frac{\bar{a}_{L0}^2}{2\rho\gamma_0^2} \frac{1}{\bar{\gamma}_j} \left[ \bar{\nabla}_{\perp} |g|^2 \right]_{\bar{\mathbf{k}}=\bar{\mathbf{r}}_j} - \\ & \frac{4\eta}{1 + \frac{k_{\perp}}{k}} \frac{1}{\bar{\gamma}_j} \text{Im} \left[ (\nabla_{\perp} (g^* \bar{A}))_{\bar{\mathbf{x}}=\bar{\mathbf{r}}_j} e^{i\theta_j(\bar{t})} \right] + \dots \end{aligned} \quad (3)$$

$$\left( \frac{\partial}{\partial \bar{t}} + \frac{\partial}{\partial \bar{z}} \right) \bar{A}(\bar{\mathbf{x}}, \bar{t}) - i\eta \bar{\nabla}_{\perp}^2 \bar{A} = b = \frac{1}{N_s} \frac{V_b}{V_b(\bar{t})} \sum_s \frac{g(\bar{\mathbf{r}}_s(\bar{t}), \bar{t})}{\bar{\gamma}_s(\bar{t})} e^{-i\theta_s(\bar{t})} + \dots \quad (4)$$

where:

$$\theta_j(\bar{t}) = \frac{k}{2\rho k_L} \left( \left(1 + \frac{k_L}{k}\right) \bar{z}_j(\bar{t}) + \left(\frac{k_L}{k} - 1\right) \bar{t} \right) \quad (5)$$

and

$$\gamma_j^2 = 1 + \gamma_0^2 \rho^2 P_{jz}^2 + \bar{a}_{L0}^2 (|g|^2)_{\bar{\mathbf{x}}=\bar{\mathbf{r}}_j(\bar{t})} + \dots \quad (6)$$

In the preceding equations the laser of parameter  $\bar{a}_{L0} = \frac{e}{mc^2} a_{L0}$  has wavelength  $\lambda_L = 2\pi/k_L$ ,  $\sigma_L$  is the r.m.s. spot radius averaged on the laser intensity,  $g(x,y,z,t)$  is the envelope,  $\omega_L = ck_L$  the angular frequency.  $\gamma_0$  is the average value of  $\gamma$  over all electrons of the beam at  $t=0$ ,  $\bar{\gamma}_j = \gamma_j / \gamma_0$ ,  $\mathbf{P}_j = \mathbf{p}_j / \gamma_0 \rho$ ,  $\eta = \frac{k_L}{k} \rho$ .

For the radiation a single mode expression is assumed, with frequency  $\omega$ , wavelength  $\lambda$ , amplitude

$$A = -i \left( \frac{\omega_0^2 a_{L0}}{4\sqrt{2}\omega\omega_L\gamma_0\rho} \right) \frac{e\bar{A}}{mc^2}.$$

The FEL parameter is:

$$\rho = \frac{1}{\gamma_0} \left( \frac{\omega_b^2 a_{L0}^2}{16\omega_L^2} \left( 1 + \frac{\omega_L}{\omega} \right) \right)^{\frac{1}{3}} \quad (7)$$

Furthermore  $\bar{t} = 2\rho\omega_L t$  and  $\bar{x} = 2\rho k_L x$ .

We have developed a three-dimensional code that solves the set of equations (1)-(4), based on a fourth-order Runge-Kutta for the particles and on a finite-difference scheme for the radiation field. An example of solution is provided by a beam with an energy of about 15 MeV (a factor 2 lower than the typical Sparc-PlasmonX case), corresponding to  $\langle\gamma\rangle=30$ , with a mean radius  $\sigma_0=10$  micron, a total charge of 1 nC, a length  $L_b=200$   $\mu\text{m}$ , corresponding to a beam current of  $I=1.5$  KA. The laser pulse considered in this case has wavelength  $\lambda_L=0,8$   $\mu\text{m}$ . Furthermore, the focal spot has radius  $w_0$  of about 50  $\mu\text{m}$  with  $a_{L0}=0.8$  so that the radiation has  $\lambda=3,64$  Angstrom and the  $\rho = 4.38 \cdot 10^{-4}$ . The gain length is about 145  $\mu\text{m}$ , the appearance and the saturation of the collective effects (taking place in 7-12 gain lengths) being contained in 5 psec, a time of the same order of the duration of the laser pulse. The quantum parameter  $q$  is 0.5. The energy spread  $\Delta\gamma/\gamma$  is  $1 \cdot 10^{-4}$  and the initial normalized transverse emittance has been varied from 0 up to 2.

In Fig. 1 the growth of the averaged collective potential amplitude is shown in time ((b), curve (1)), as well as the bunching factor ((a)). The parameters of this calculation are: a flat laser profile inside a region with  $w_0=50$  micron, the laser parameter  $a_{L0}=0.8$ , a value of the initial emittance of  $\epsilon_n=0,88$   $\mu\text{m}$ , a detuning of  $\Delta\omega/\omega= -210^{-4}$ . The saturation level of the radiation is reached at  $t=4$  psec at  $\langle|A|^2\rangle_{\text{peak}}=0,275$ , with a total number of photons of  $1,86 \cdot 10^{10}$ , against the  $2 \cdot 10^8$  provided by the incoherent process. The peak brilliance, for this example, is  $3,7 \cdot 10^{25}$  photons/(sec  $\text{mm}^2 \text{mr}^2 \cdot 0.1\%$ ), while the coherent power is 15.5 MW.

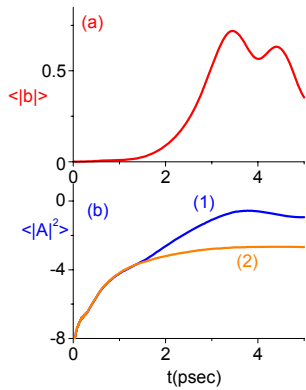


Figure 1: Averaged bunching (a) and logarithm of the radiation intensity (b) versus  $t$  in coherent (1) and incoherent (2) case for:  $\lambda_L=0.8$   $\mu\text{m}$ ,  $a_{L0}=0.8$ ,  $\Delta\gamma/\gamma=10^{-4}$ ,  $\Delta\omega/\omega=-210^{-4}$ ,  $\epsilon_n=0.88$ .

In Fig. 2 the spectrum of the radiation is reported versus  $\Delta\omega/(\rho\omega)$  for (a)  $\epsilon_n=0,44$  micron and (b)  $\epsilon_n=0,88$  micron.

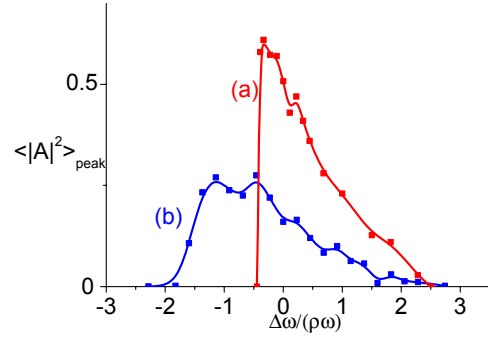


Figure 2:  $\langle|A|^2\rangle_{\text{peak}}$  versus  $\Delta\omega/(\rho\omega)$  for the case of Fig. 5 and (a)  $\epsilon_n=0,44$   $\mu\text{m}$  and (b)  $\epsilon_n=0,88$   $\mu\text{m}$ .

We can note an enlargement of a factor two of the bandwidth with increasing emittance.

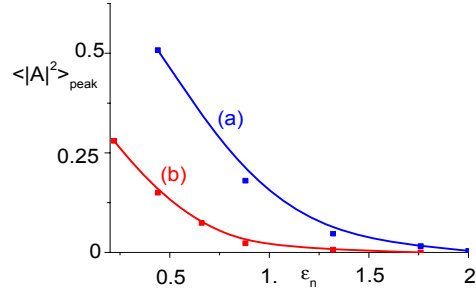


Figure 3:  $\langle|A|^2\rangle_{\text{peak}}$  versus  $\epsilon_n$  for the case of fig 5, with  $\Delta\omega/\omega=0$ , and for: (a) flat laser profile with  $w_0=50$   $\mu\text{m}$  and  $a_{L0}=0.8$  and (b) Gaussian laser profile with  $a_{L0}=0.8$  and  $\sigma_L=106$   $\mu\text{m}$ .

In Fig. 3 the dependence of the saturation radiation on the emittance is presented. Curve (a) is relevant to the situation of flat laser pulse with  $w_0=50$   $\mu\text{m}$ , while curve (b) shows the more critical situation of Gaussian profile. In this case the quantity  $\sigma_L$  is 106  $\mu\text{m}$  with  $a_{L0}=0.8$ , increasing consequently the laser power.

We note considerable emission in violation of the Pellegrini criterion [29] for a static wiggler. In fact, in case (a) of Fig 3, for instance, the emittance largely exceed the value  $\gamma\lambda/4\pi$ , that in this case is about  $9 \cdot 10^{-4}$   $\mu\text{m}$ . We can justify this result by considering that the line width in a situation dominated by emittance effects can be written as [30]

$$\frac{\Delta\lambda}{\lambda} \approx \frac{\gamma^2\theta^2}{1+a_{L0}^2} \approx \frac{\epsilon_n^2}{\sigma_0^2} \quad (8)$$

In order to have considerable emission, we must assume that the linewidth  $\Delta\lambda/\lambda < \alpha\rho$ , with  $\alpha$  a numerical factor not very much larger than 1. Hence, we can write for the emittance

$$\varepsilon_n \leq \sqrt{\alpha\rho} \sigma_0 \quad (9)$$

Considering the definitions of the gain length  $L_g = \lambda_L/(4\pi\rho)$  and that of the radiation Rayleigh length  $Z_R = 2\pi\sigma_R^2/\lambda$ , we can express the factor  $\rho$  in terms of the ratio  $Z_R/L_g$ , obtaining  $\rho = \frac{Z_R}{L_g} \frac{\lambda\lambda_L}{8\pi^2\sigma_R^2}$ . Supposing furthermore that the electron beam and the radiation overlap, so that  $\sigma_0 = \sigma_R$ , and remembering the resonance relation in its simpler expression  $\lambda_L = 4\gamma^2\lambda$ , we obtain for an optical undulator

$$\varepsilon_n \leq \sqrt{\alpha} \sqrt{\frac{Z_R}{L_g}} \frac{\lambda \gamma}{\sqrt{2\pi}} \quad (10)$$

where  $\alpha = \frac{\delta\omega}{\omega\rho}$ .

The usual Pellegrini criterion can be obtained for a static wiggler assuming  $Z_R = L_g$  and considering the resonance condition for the static undulator.

Taking into account the fact that in our situation  $Z_R/L_g = 1.18 \cdot 10^4$ , and estimating  $\alpha = 2$ , we can predict considerable emission up to an emittance value of  $\varepsilon_n = 0.3 \mu\text{m}$  (corresponding to a value of  $\varepsilon_{nx} = 0.15 \text{ mm}$ ), not far from the results of Fig. 8.

The last Fig. 8 shows the most critical effect, i. e. the dependence of the growth of the signal on the transverse energy distribution of the laser in the case of a Gaussian pulse for  $\varepsilon_n = 0.44 \mu\text{m}$ ,  $\Delta\omega/\omega = -1.10^{-4}$ ,  $a_{L0} = 0.8$ . In fact, in this case, a spot size with a radius smaller than 75 micron does not permit the instauration of the instability. The collective signal in this condition, therefore, does not grow.

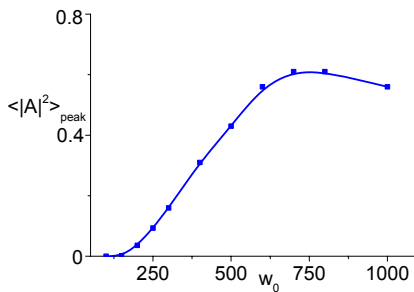


Figure 4:  $\langle |A|^2 \rangle_{\text{peak}}$  versus  $w_0$  for the case for the Gaussian laser profile for  $\varepsilon_n = 0.44 \mu\text{m}$ ,  $\Delta\omega/\omega = -1.10^{-4}$ ,  $a_{L0} = 0.8$ .

A possible remedy could be the development and use of a flat energy distribution of the laser beam obtained with a guided propagation.

This example is characterized by a choice of the electron beam with larger emittance than in the first case, not far from the best actual experimental values, but with

a larger current. However, the requirements on the total energy of the laser and on the stability of the energy transverse profile are in this case particularly demanding.

Another critical issue is the variation in the laser intensity  $\Delta = \Delta a_{L0}/a_{L0}$ , that leads to a broadening in the spectrum of

$\Delta\lambda/\lambda = 2a_{L0}^2\Delta/(1+a_{L0}^2)$ . For a FEL operation of the Thomson source, the condition  $\Delta \leq \rho \frac{(1+a_{L0}^2)}{a_{L0}^2}$  must

therefore be added. Assuming a laser pulse duration of  $c\tau = 10 L_g$ , we can derive a further threshold condition on the laser pulse energy  $U$  of the form  $U > 18.6 \lambda_L/\Delta^2$ , that in our case means  $U > 0.15/\Delta^2 \text{ J}$ .

## CONCLUSIONS

Considerable coherent X-rays radiation is possible as a result of the collective interaction between an electron beam and a counter-propagating laser pulse. If the laser pulse is long enough the FEL instability can develop and a regime of collective effects can establish. The result is an emission at least two order of magnitudes larger than the incoherent one and with a thinner and more peaked spectrum. However, the brilliance and the power delivered are a few orders of magnitude smaller than these same quantities for a static wiggler FEL in the X-ray range.

Other critical issues for the appearance of collective effects are connected with: (i) the current density carried by the electron beam which has to be large enough, (ii) the emittance of the packet which has to be not too much larger than that provided by the generalized Pellegrini criterion, (iii) the transverse distribution of the laser pulse which cannot have a sensible variation on the region occupied by the electrons, (iv) the fluctuations of the laser intensity and (v) the large laser energy needed.

## REFERENCES

- [1] I. V. Pogorelsky, I. Ben-Zvi, T. Hirose, S. Kashiwagi, V. Yakimenko, K. Kusche, P. Siddons, J. Skaritka, T. Kumita, A. Tsunemi, T. Omori, J. Urakawa, M. Washio, K. Yokoya, T. Okugi, Y. Liu, P. He and D. Cline, *Phys. Rev. S. T. Accel. Beam* **3** (2000) 090702
- [2] W. J. Brown, S. G. Anderson, C. P. J. Barty, S. M. Betts, R. Booth, J. K. Crane, R. R. Cross, D.N. Fittinghoff, D. J. Gibson, F. V. Hartemann, E. P. Hartouni, J. Kuba, G. P. Le Sage, D. R. Slaughter, A. M. Tremaine, A. J. Wootton, and P. T. Springer, *Phys. Rev. S. T. Accel. Beam* **7** (2004) 060702
- [3] P. Tomassini, A. Giulietti, D. Giulietti, L.A. Gizzi, *Appl. Phys. B* **80** (2005) 419
- [4] A. Bacci, C. Maroli, V. Petrillo, L. Serafini: *Eur. Phys. Jour. AP* (in print)
- [5] A. Bacci, M. Ferrario, C. Maroli, V. Petrillo, L. Serafini *Phys. Rev. S. T. Accel. Beam* (in print)

# PROGRESS ON THE $\pi$ -MODE X-BAND RF CAVITY FOR SPARC

L. Ficcadenti, M. Esposito, A. Mostacci, L. Palumbo, Università La Sapienza, Roma, Italy.  
 D. Alesini, B. Spataro, LNF-INFN, Frascati, Italy; A. Bacci, Milano-INFN, Milano, Italy.

## Abstract

The Frascati photo-injector SPARC (Pulsed Self Amplified Coherent Radiation Source) will be equipped with a X-band RF cavity for linearizing emittance to enhance bunch compression and for reducing bunch longitudinal energy spread. The nine cells standing wave cavity prototype made of separated cells has been already built and measured. In this paper we report on characterisation of the first brazed prototype. Heat load studies have been performed as well to design the cooling system for the final device.

## INTRODUCTION

The X-band structure operating at  $11.424\text{GHz}$ , designed to obtain  $42\text{MV/m}$  accelerating gradient, is a 9 cells  $\pi$ -mode structure fed by a central coupler. The sketch of the cavity profile with dimensions is reported in Fig. 1. The design of the structure, the cavity parameters, and the field measurements made on a non brazed copper prototype is reported in [1]. In this paper we report on the characterisation of the brazed copper prototype [2].

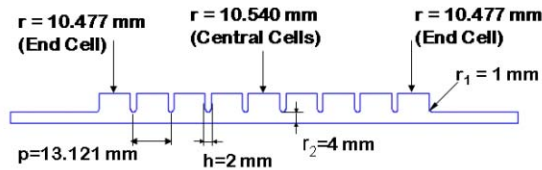


Figure 1: 2D profile of the X-band structure.

## BRAZED PROTOTYPE

The prototype geometry has been properly studied to allow a good brazing process and to avoid the diffusion of the brazing alloy inside the cavity volume. For this reason some special grooves have been machined on the contact area between contiguous cells. As Fig. 2 shows, REGION ‘A’ is the contact area, REGION ‘B’, that has a vertical dimension of a few tens of micron, will receive the liquid alloy coming from the adjacent  $0.6\text{mm}$  alloy wire that is initially located in a groove  $0.7\text{mm}$  deep and  $0.8\text{mm}$  wide (REGION ‘D’). The last area, REGION ‘C’, that is  $0.5\text{mm}$  deep, is necessary to obtain vacuum inside the cavity and to avoid that melted alloy escapes towards outside. The material used to make the RF cavity is Cu/OF, UNI 5649/71, and the brazing alloy is eutectic Ag/Cu 72/28,  $0.6\text{mm}$  wire whose melting point is  $780^\circ\text{C}$ . After cleaning procedure, the structure to be brazed is mounted inside the oven with

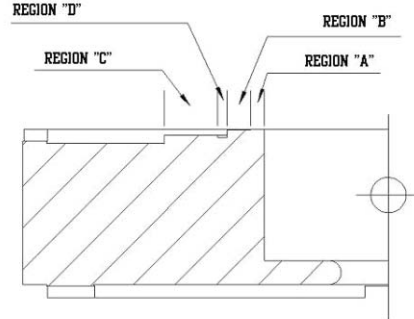


Figure 2: Brazing profile.

its axis of symmetry in vertical position. The contact pressure among the cells is obtained only with  $0.5\text{kg}$  weight, without using tie rods. Our tests have demonstrated that: the total length of the structure, as well as its coaxiality, are not modified by the brazing operation, the use of weight instead of tie rods to keep in contact the cells during the brazing is simple and effective, the working pressure during the brazing operation, roughly  $10^{-5}\text{mbar}$ , is sufficient and the results of the vacuum leak checking procedure are fully satisfactory.

## Frequency and $Q$ -factor measurements

The transmission coefficient between the small antenna, fixed on the lateral cell, and the central coupler compared with the one of the non brazed prototype is reported in Fig. 3. The brazing procedure has reduced the visibility of the unwanted modes having a zero field in the central cell, as we can see. The measured dispersion curve before

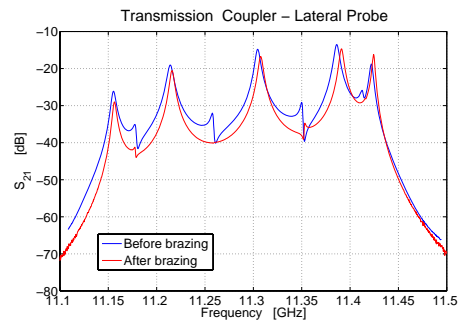


Figure 3: Transmission coefficient between the lateral antenna and the central coupler.

Table 1: Quality and form factors measured before (I) and after (II) brazing on the prototype compared with the numerical results

	HFSS	Superfish	Meas I	Meas II
$f_0(GHz)$	11.4244	11.4240	11.4239	11.4244
$Q_0$	8500	8070	7900	8066
$R/Q(\Omega/m)$	9138	9232	9440(90)	9070(20)

and after brazing, is compared with the one from HFSS in Fig. 4. The quality factor of the operating  $\pi$ -mode has been

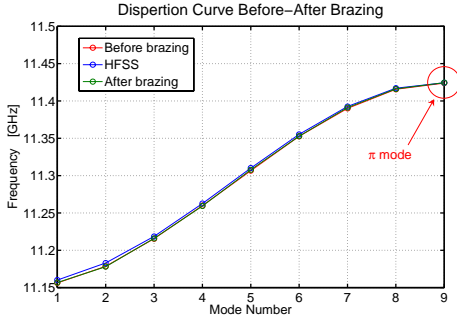


Figure 4: Dispersion curve before and after brazing.

measured on the brazed structure and compared with both the one measured on the non brazed cavity and the one calculated by HFSS and SUPERFISH code (see Tab. 1). The results point out that the brazing process brings improvements in terms of the quality factor.

### Field measurements

With the bead pull technique we measured the electric field on axis. To calculate the  $R/Q$  we have calibrated the bead form-factor comparing the perturbation induced in a pill-box cavity with analytical results. The measured longitudinal electric field on axis, for the brazed prototype, compared with the one of the non brazed cavity, is plotted in Fig. 5. Tuning the brazed structure has been

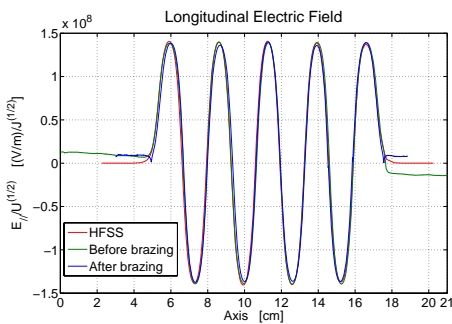


Figure 5: Measured longitudinal electric field on axis.

proved to be more difficult with respect to the structure

made by separated cells due to reduced RF losses. The field-flatness is of the order of 4% at the measured frequency of  $11.4244GHz$ . The measured  $R/Q$  per unit length is reported in Tab. 1.

## HEAT LOAD AND COOLING SYSTEM DESIGN

One of the most important requirements for an RF cavity is to have a high accelerating field. Unfortunately an upper limit for the axial electric field is given by the maximum value of surface field possible before breakdown. Experimental tests prove that a possible way to raise this breakdown limit is to use different materials for the inner surface of the structure containing the cavity. We have decided to consider, study and compare three different constructive solutions: structure totally made out of copper; structure with irises made out of Molybdenum (**Mo**) and structure with only half of the irises (the nose) made out of **Mo**, and outer half made out of **Cu**. An electromagnetic analysis of the  $\pi$ -mode operating structure has been performed for each one of the three cases above with SUPERFISH code, the obtained results have been used as input for subsequent thermal simulation performed with ANSYS [3] code. The main RF parameters are reported in [4].

### ANSYS thermal simulations

The use of **Mo** surely brings advantages in terms of the electromagnetic behaviour of the cavity since it allows to operate with higher accelerating fields, at the price of a greater power loss due to higher surface resistance, and a more difficult heat evacuation because of the lower rate of heat transfer, therefore we expect to have higher temperature gradients, greater thermal expansion and thus greater frequency variations.

In order to reduce and simplify the model to be analysed, we have considered only one full and one half cell, applying all the necessary boundary conditions (See [4]). Numerical simulations performed with ANSYS show that the maximum temperature variation within the structure, in the classical solution (all copper), is less than  $2^\circ C$ . The maximum temperature variation goes up to more than  $7^\circ C$  in the case of using **Mo** for the entire irises. The mixed **Cu-Mo** solution appears to be the best since it has both the advantages of allowing higher accelerating fields and small temperature variation (3%) as shown in Fig.6.

### The cooling system design

In order to materially obtain the temperature boundary condition on the external surface of the structure we need to supply the accelerating structure with a cooling system. This will be a closed water device with 4 tubes (of diameter  $6mm$ ), parallel to the axis of the cavity, positioned on the outer surface of the structure. The results [4] show that the temperature distributions do not differ much from the previous analysis obtained with the approximation of consid-

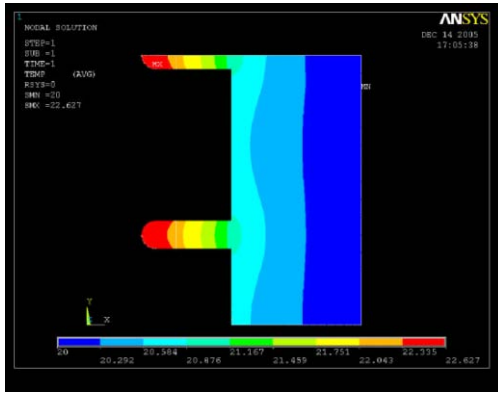


Figure 6: Thermal field in the  $\pi$ -mode cavity.

ering a constant temperature on the whole external surface. The highest temperature value obtained, even in the most critical conditions (duty cycle  $5E - 5$  with tubes at  $30^\circ$ ), is not greater than  $42^\circ C$ , and the maximum temperature variation within the structure is less than  $2^\circ C$  as we can see in Fig. 7.

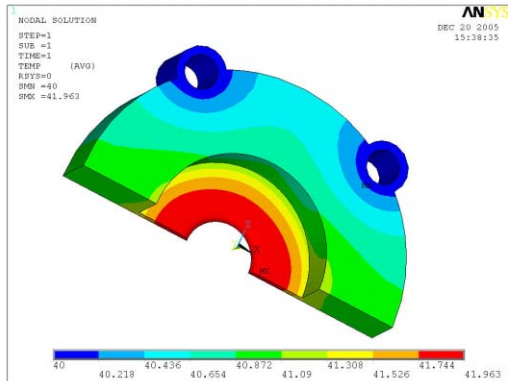


Figure 7:  $\pi$ -mode cavity with tubes at  $30^\circ$  working on duty cycle 2 ( $5E - 5$ ).

### Cooling system calculations

In the previous simulations we have considered a steady value for the wall temperature of the tubes, so we have approximated the cooling system as a perfect heat absorber. Actually it is not so, and it is necessary to calculate the needed speed and temperature for the water, in order to have a good efficiency for the cooling system. A first approximation of the water flow rate may be given by the following:

$$W = P \cdot \delta \cdot c \cdot \Delta T \quad (1)$$

in which  $W$  is the heat transferred to the water per unit time,  $P$  is the volumetric water flow rate,  $\delta$  is the water density,  $c$  is the specific heat and  $\Delta T$  is the difference of the water temperature from the beginning to the end of the

tubes. With equation (1), it is possible to establish an approximate value of the flow rate necessary. Once the speed of the water has been established we can evaluate the water temperature with the equation of convection heat transfer:

$$W = h_c \cdot S \cdot (T_w - T_b) \quad (2)$$

where  $h_c$  is the convection film coefficient,  $S$  is the total exchange surface,  $T_w$  is the wall temperature and  $T_b$  is the bulk temperature. The film coefficient has been calculated [4]. Temperature difference between inlet and outlet and between wall and bulk, corresponding to different values of water volumetric flow rate are shown in Fig. 8.

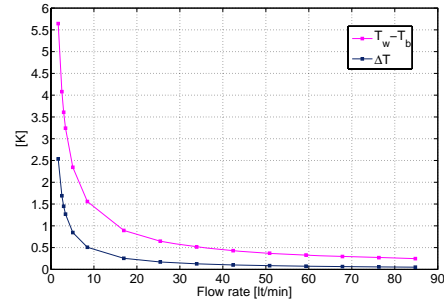


Figure 8: Thermal gradient behaviour in the cooling system.

## CONCLUSIONS

A  $\pi$ -mode cavity has been realised and brazed. Experimental tests have given satisfying results. The electromagnetic behaviour, in terms of  $E$  field on axis,  $Q$  factor and  $R/Q$  form factor does not show substantial variations. The brazing procedure has been successfully studied and carried out. Alternative solutions to reduce the peak surface field and thus to allow higher accelerating gradients have been considered and analysed. A cooling system has been designed and calculated and simulations prove that it works correctly.

## ACKNOWLEDGEMENTS

The authors are grateful to Marco Zamperini and Francesco Coppola for their help with ANSYS simulation and RF measurements.

## REFERENCES

- [1] D. Alesini *et al.*, Nucl. Instr. and Meth. A 554 (2005) 1.
- [2] P. Chimenti *et al.*, LNF-05/22(IR), LNF-INFN, November 2005.
- [3] <http://www.ansys.com>.
- [4] P. Chimenti *et al.*, SPARC-RF-06/001, LNF-INFN, February 2006.

# LHC IR UPGRADE: A DIPOLE FIRST OPTION WITH LOCAL CHROMATICITY CORRECTION\*

Riccardo de Maria, Oliver Sim Brüning, CERN, Geneva, Switzerland  
 Pantaleo Raimondi, INFN-LNF, Frascati, Italy

## Abstract

In the framework of the LHC Luminosity Upgrade, we develop a new layout of the interaction region (IR) with  $\beta^*$  equal to 25cm in which the combination-separation dipoles come first with respect to the triplet assembly (dipole first) in opposition of the nominal layout (quadrupole first). The new layout presents several advantages (separate channel for multipole error correction, straightforward crossing angle scheme with no crossing in the triplet, early separation of the beam). The payoff is a large  $\beta$  function in the triplet, which enhances the chromaticity, non-linear effects and eats up aperture. We investigate options for local chromaticity correction and their effects on long-term stability.

## INTRODUCTION

The aim of the LHC luminosity upgrade is to increase the luminosity from  $10^{34}\text{cm}^{-2}\text{s}^{-1}$  to  $10^{35}\text{cm}^{-2}\text{s}^{-1}$  by increasing the number of protons per bunch, increasing the number of bunches, reducing the longitudinal beam size and reducing  $\beta^*$  by upgrading the insertion region [1].

The upgrade of the interaction regions (IR) of the main experiments ATLAS and CMS (IR1 and IR5 respectively) is expected to provide a  $\beta^*$  of 25cm increasing the luminosity by a factor 2.

The present layout, designed for  $\beta^*$  of 55cm, is not able to provide a  $\beta^*$  of 25cm because the triplet quadrupoles cannot fulfill the required specifications on mechanical aperture. In addition the lifetime of the triplets is estimated to be limited to 7 years at the nominal luminosity due the radiation [1] coming from the IP. If no relevant changes in the design with respect to the radiation protection is performed, this time is reduced by an order of magnitude at the upgraded luminosity implying a triplet replacement on a year basis.

As an alternative to the present quadrupole first layout, we propose a new one, called dipole first layout [2], which should be able to incorporate an efficient absorber in the separation/recombination dipole assembly and to obtain a  $\beta^*$  of 25cm by taking advantage of new magnet technology. A dipole first layout is expected to ease the radiation protection issues as the first dipole can act as a open mid-plane spectrometer and absorbs the charged debris.

## LAYOUT AND OPTICS

The new layout has been designed to maintain all the LHC parameters, all the elements but the triplets and the

separation-recombination dipoles in order to keep the cost of the upgrade as low as possible.

The new magnets require a new technology, such as magnets based on Nb3Sn superconductor material, because the necessary peak field at the coil is about 15T.

The radiation heat load and radioactivity issues can be reduced by the use of an open midplane type dipole [3] which acts as a spectrometer deflecting the debris in its own absorber before they reach the triplet quadrupoles.

A detailed computation of the heat load, though quite important for a realist design, have not been taken into account and will be addressed in further studies.

Figure 1 and 2 show the beam envelope and the collision optics of the new layout.

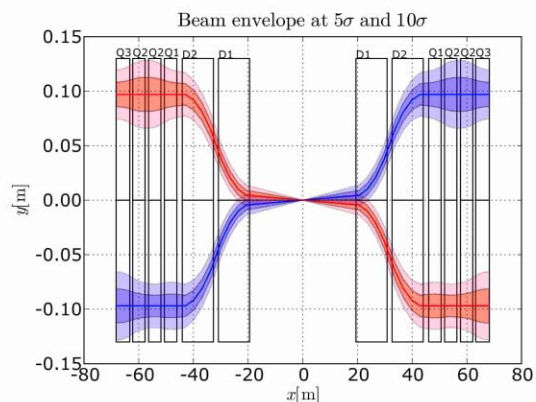


Figure 1: Beam envelope at  $5\sigma$  and  $10\sigma$ .

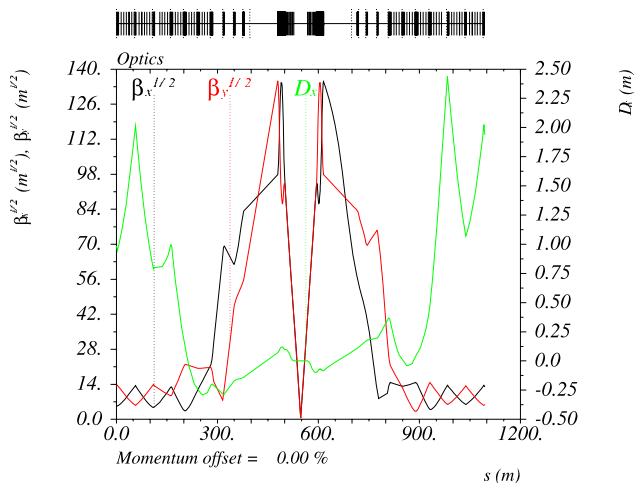


Figure 2: Collision optics for Beam 1.

Table 1 summarizes the main quantities of the layout.

\* Work supported by CERN and EPFL

Table 1: Specifications of the dipole first layout.

Mag.	Pos.	Length	Field	Inner D.
D1	19.45m	11.4m	15.0T	0.130m
D2	32.653m	11.4m	15.0T	0.080m
Q1	46.05m	4.5m	231.0T/m	0.080m
Q2A	51.87m	4.5m	-256.6T/m	0.080m
Q2B	57.69m	4.5m	-256.6T/m	0.080m
Q3	63.25m	5.0m	280.0T/m	0.080m

A previous study [4] shows that the present layout fulfills the requirements imposed by the optics squeeze (Q5 excluded due aperture limitation), presents a good tunability and allows a smooth transition to the injection optics.

## CHROMATICITY

For the LHC the energy acceptance of ( $\delta p/p = 0.8 \cdot 10^{-3}$ ) has to be preserved.

The chromaticity, tune dependence with energy  $Q(\delta)$ , is enhanced by high  $\beta$  values and, if not properly corrected, can lead to a limitation of the energy acceptance. In addition a positive slope of  $Q(\delta)$  is required in order to avoid the head-tail instability.

In the LHC there are two interleaved sextupoles families per arcs (MS) and a family of spool pieces sextupole correctors (MCS). They can be used to correct globally the first and the second order chromaticity and the off momentum  $\beta$ -beat [5].

For the correction of the linear part, all the sextupoles in the two families focusing and defocusing are equally powered. Also the spool pieces are used at the 70% of their nominal strength in order to reduce the strength of the main defocusing family.

For the correction of the second order chromaticity each family is powered individually, the first and the second order chromaticity are then calculated and minimized. Table 2 and 3 show the required sextupole strengths.

The margin in the sextupoles strengths can be still used for a compensation of the off-momentum  $\beta$ -beat.

Table 2: Required strengths of the arc sextupoles for the correction of the linear part of the chromaticity. All focusing and defocusing families respectively equally powered.

Family	$k_2$ max	Strength
MS Defoc.	$0.380\text{m}^{-2}$	68%
MS Foc.	$0.380\text{m}^{-2}$	75%
MCS	$0.130\text{m}^{-2}$	70%

Table 3: Required strengths of the arc sextupoles for the correction of the linear and second order part of the chromaticity. The MS families are individually powered.

Family	Average Str.	Max Str.
MS Defoc.	68%	74%
MS Foc.	75%	79%
MCS	70%	70%

An attempt for a local chromaticity correction has been done. A set of sextupoles correctors is installed in front of each quadrupole magnet where a small dispersion (about 10cm) is present due the dipole first layout.

The local  $\beta$ -beating proportional to the chromatic function  $W$  [6] is then minimized (Figure 4). The procedure minimizes the  $\beta$ -beating in all the machine and the chromaticity (Figure 3) is corrected with the help of the sextupoles families in the arcs.

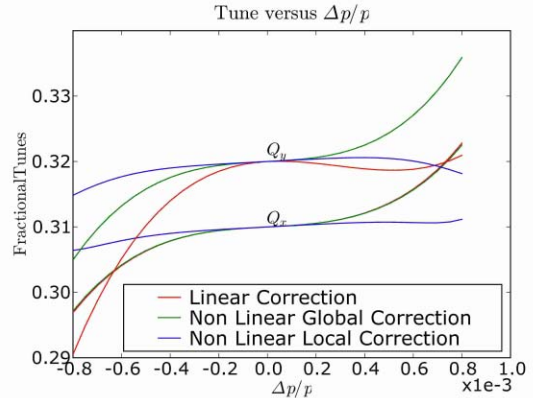


Figure 3: Horizontal and vertical chromaticity for Beam 1 after several correction options.

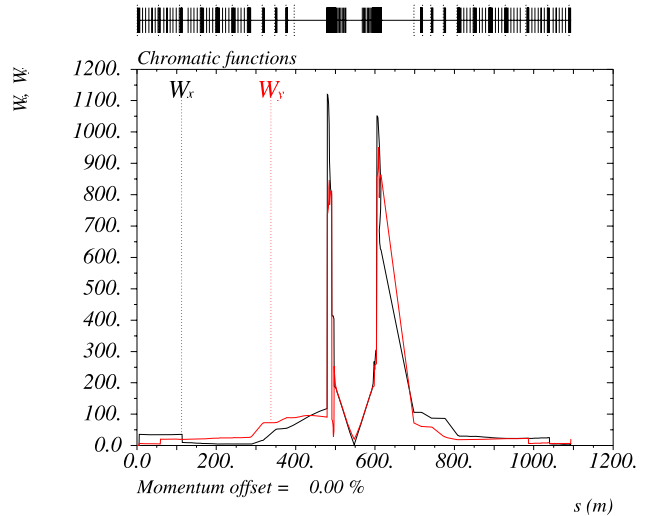


Figure 4: W function of IR5 after correction for Beam 1.

Table 4 shows the required strengths for the sextupole families in the arc. The local sextupoles require at maximum a sextupole integrated strength of about 6 times the integrated strength of one of the MS sextupoles. This field in the high  $\beta$  region is sufficient to make the dynamic aperture almost vanish.

The dispersion at the triplet can be increased without wasting too much mechanical aperture and luminosity allowing the derivative of the dispersion to be different from zero. At the first order the required sextupole strength should scale with the dispersion, but this is not the case

Table 4: Required strengths of the arc sextupoles for the correction of the linear and second order part of the chromaticity with local chromaticity correction. The MS families are individually powered.

Family	Average Str.	Max Str.
MS Defoc.	27%	31%
MS Foc.	26%	23%
MCS	0%	0%

because the non linear terms, which are probably created by a second order dispersion, are dominant.

The exercise demonstrates that the local chromaticity correction requires a careful calculation of the non linear terms up the third order and that a naive layout is not sufficient for such a task. In the particular case in which the correction is effective, the dynamic aperture is spoiled.

A true Pantaleo-Raimondi scheme would be required but the available space of the insertion is not sufficient for creating the necessary phase advance for a complete cancellation of chromatic and geometric aberrations and therefore implies modifications that go beyond the IR region.

## DYNAMIC APERTURE

The dynamic aperture (DA) of the LHC at collision is dominated by the field quality in the high  $\beta$  region, that is triplet and separation recombination magnets.

The tracking studies are performed with SIXTRACK using 60 seeds and  $10^5$  turns [2].

In the LHC the triplet is equipped with a corrector package used to minimize the Hamiltonian driving terms which are close to the working point.

Tracking studies for the nominal configuration shows that the minimum DA of LHC without triplet correction is about  $13\sigma$ .

The new layout, because of the high  $\beta$  values, requires a careful definition of the field quality allowed in the triplet and the implementation of a correction scheme.

Tracking studies are on going in order to explore the parameter space (multipole errors) for the definition of the required field quality needed for such design.

A preliminary study using an ideal machine and the field quality of the present LHC triplet magnets (Figure 5) for the new ones shows that the minimum DA over 60 seeds is about  $2.7\sigma$  without correction. Scaling by a factor of 10 the triplet errors shows an increase of the minimum dynamic aperture to  $8.3\sigma$ .

An efficient correction scheme or a better field quality is required to meet the specification of  $10\sigma$ . Tracking studies are on going for the dipole first layout with triplet correction.

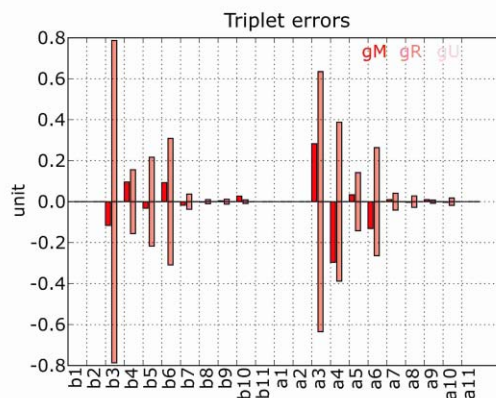


Figure 5: Triplet error used for DA studies. "gM gR gU" stays respectively for mean, random, uncertainty of the geometric component of the multipole errors.

## CONCLUSION

The present layout, challenging in terms of magnet technology and beam stability, shows that its requirements in terms of field quality and chromatic aberration can be taken under control.

The arcs sextupole correctors have the required strength for compensating the first and the second order chromaticity with some additional margin for a beta-beating correction.

The low value for the dynamic aperture may probably be restored to the LHC requirements by a corrector package or a further improvement of the field quality. A tracking campaign for their definitions is on going.

Studies for the protection of the magnets, still missing, should investigate the options for the neutron flux protection and give a complete picture of the feasibility of this upgrade path.

## REFERENCES

- [1] Francesco Ruggiero. LHC Accelerator R&D and Upgrade Scenarios. Technical Report LHC-Project-Report-666, CERN, August 2003.
- [2] O. Bruening, et al. LHC Luminosity and energy upgrade : A Feasibility Study. Technical Report LHC-Project-Report-626, CERN, dec 2002.
- [3] R. C. Gupta, et al. Optimization of open midplane dipole design for LHC IR upgrade. *Particle Accelerator Conference (PAC 05)*, may 2005.
- [4] R. de Maria. LHC IR Upgrade: a Dipole First Option. To appear in HHH-Lumi05 proceedings, sep 2005.
- [5] O. Bruening, et al. LHC Design Report. Technical Report CERN-2004-003, CERN, 2004.
- [6] F. Christoph Iselin. The MAD Program Version 8.13 Physical Methods Manual, sep 1994.

# BEAM-BEAM SIMULATIONS FOR A SINGLE PASS SUPERB-FACTORY

M.E.Biagini, Laboratori Nazionali di Frascati INFN, Frascati, Italy  
 E. Paoloni, Pisa University and INFN, Pisa, Italy  
 P. Raimondi, Stanford Linear Accelerator Center, Menlo Park, CA, USA  
 D. Schulte, CERN, Geneva, Switzerland  
 J. Seeman, Stanford Linear Accelerator Center, Menlo Park, CA, USA

## Abstract

A study of beam-beam collisions for an asymmetric single pass SuperB-Factory is presented [1]. In this scheme an  $e^-$  and an  $e^+$  beam are first stored and damped in two Damping Rings (DR), then extracted, compressed and focused to the IP. After collision the two beams are re-injected in the DR to be damped and extracted for collision again. The explored beam parameters are similar to those used in the design of the International Linear Collider, except for the beam energies. Flat beams and round beams were compared in the simulations in order to optimize both luminosity performances and beam blow-up after collision. With such approach a luminosity of the order of  $10^{36} \text{ cm}^{-2} \text{ s}^{-1}$  can be achieved.

## SINGLE-PASS SUPERB-FACTORY

The concept of combining linear and circular collider ideas to make a linear-circular B-Factory was discussed in the late 1980's, although only circular B-Factories were built in the 1990's. Recent advances in B-Factory performance and solid linear collider design progress has reopened this design avenue.

The design presented here is based on the work done at the First SuperB Workshop held in November 2005 in Frascati [2]. Schematic drawings of a first Linear Super-B Factory design are shown in Fig. 1. An  $e^+$  bunch from a 2 GeV damping ring is extracted and accelerated to 7 GeV in a SC linac. Simultaneously, an  $e^-$  bunch is accelerated in a separate SC linac to 4 GeV. The two bunches are transported to the IP through bunch compressors, then focused to a small spot and made to collide. The spent beams are returned to their respective linac with transport lines where they return their energies to the SC accelerator. The 2 GeV  $e^+$  are returned to the damping ring to restore the low emittances. The spent  $e^-$  beam is discarded. Each bunch collides at 120Hz, there will be about 10000 bunches. Thus, the collision rate is about 1.2 MHz. A small electron linac and positron source is used to replenish lost positrons in the colliding process and natural beam lifetime. This scheme would reduce the demands on the electron gun but increase the site AC power.

These schemes present several complexities and challenging requirements for several subsystems. Moreover several technical solutions proposed have never been tested and proven before, a lot of R&D and extremely detailed studies, in order to ensure the success of the machine, is henceforth required.

## BEAM-BEAM SIMULATIONS

The beam parameters are listed in Table 1.

Table 1: Preliminary Super-B Factory collision parameters.

Parameter	LEB	HEB
Beam Energy (GeV)	4	7
Number of bunches	10000	10000
Collision freq/bunch (Hz)	120	120
IP energy spread (MeV)	5	7
$N_{\text{part}}/\text{bunch} \times 10^{10}$	10	10
$\beta_x^*/\beta_y^*$ (mm)	22/0.5	22/0.5
Emittance (x/y) (nm)	0.7/0.0016	0.7/0.0016
$\sigma_z$ (mm)	0.35	0.35
Lumi enhancement $H_d$	1.07	1.07
IPx/y size ( $\mu\text{m}$ )	4/0.028	4/0.028
x/y Disruption	1.7/244	0.9/127
Luminosity ( $\times 10^{34}/\text{cm}^2/\text{s}$ )	100	100

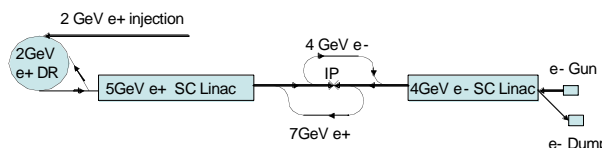


Figure 1: Linearly colliding Super-B Factory layouts.

The beam-beam interaction in a linear collider is basically the same Coulomb interaction as in a storage ring, with extremely high charge densities at IP, leading to very intense fields; since in this case quantum behaviour becomes important it is necessary to use a beam-beam code to predict luminosities and related backgrounds. The “classical” effects of the beam-beam interaction are characterized by a parameter called “disruption”, which can be seen as the equivalent to what the linear beam-beam tune shift is in storage rings. Typical values for D in the vertical plane are less than 30 in ILC, and more than 50 in a “linearly colliding” SuperB-Factory. The horizontal D is kept near or below 1 to reduce energy spread in the beam. The beam-beam interaction in such a regime can be highly non linear and unstable, leading to loss of luminosity, rather than gain, and to emittance blow-up. Since the beams must be recovered in this scheme, emittance blow-up should be kept at minimum in order to decrease the number of damping time necessary before the beams can collide again. Let’s now recall some of the scaling laws that have to be considered in the choice of the collision parameters.

The beam-beam disruption is defined as:

$$D_{x,y}^{\pm} = \frac{N^{\mp} \sigma_z^{\mp}}{\gamma^{\pm} \sigma_{x,y}^{\mp} (\sigma_x^{\mp} + \sigma_y^{\mp})} \quad (1)$$

where  $N$  is the number of particles in one bunch,  $\sigma_z$  is the bunch length,  $\gamma$  is the beam energy in terms of electron mass,  $\sigma_x$  and  $\sigma_y$  are the beam spot sizes at collision. All the quantities refer to the opposite beam, except for the beam energy factor. On the other hand the luminosity is proportional to:

$$L_B \propto \frac{N^+ N^-}{\sigma_x \sigma_y} \quad (2)$$

and the center of mass (cm) energy spread during collision can be defined as:

$$\sigma_E^{cm} \propto \frac{N^2}{(\sigma_x^2 \sigma_z)} \propto \frac{D_x N}{\sigma_z^2} \propto \frac{L \sigma_y}{(\sigma_x \sigma_z)} \quad (3)$$

For “linearly colliding” beams a large contribution to the energy spread comes from the beam-beam interaction via the “beamstrahlung”, synchrotron radiation produced during collision. Due to the high fields at the interaction the beams lose more energy and the cm energy spread increases. This is an unwanted effect, since the Y(4S) is relatively narrow (10 MeV), so the cm energy spread should be as small as possible. As it can be seen from the previous formulas there are conflicting requirements for the collision parameters; for example increasing the number of particles gives higher luminosity but also higher energy spread. Also, a short bunch gives less disruption and more luminosity, since  $\beta_y^*$  can be decreased, but this produces larger cm energy spread.

The strong-strong collision regime requires a simulation, since analytical treatment is limited. Preliminary beam-beam studies have been performed with the “GuineaPig” code by D. Schulte (CERN) [3], which includes backgrounds calculations, pinch effect, kink instability, quantum effects, energy loss, and luminosity spectrum. This code has been used for ILC studies of beam-beam performances and backgrounds. An intensive study of the luminosity as a function of  $N$ ,  $\sigma_z$ ,  $\sigma_{x,y}$ ,  $\epsilon_{x,y}$  and energy asymmetry has been performed, while trying to keep small the cm  $\sigma_E$  and the outgoing beam emittances. Some preliminary conclusions can be drawn from the large number of runs performed with different collision parameters:

- $\sigma_z$  should be as short as possible, this allows to decrease  $\beta_y^*$  and disruption;
- given the maximum storable beam current in the DR the number of bunches should be as big as possible, i.e. the number of particles/bunch should be as low as possible (see for example Fig. 2), compatibly with the increase of the cm  $\sigma_E$ ;
- increasing the beam aspect ratio, i.e. having flat beams, helps to overcome the kink instability. As a result the spent beam emittances are less disrupted,

$D_y$  is smaller and the cm  $\sigma_E$  is weakly affected by the interaction.

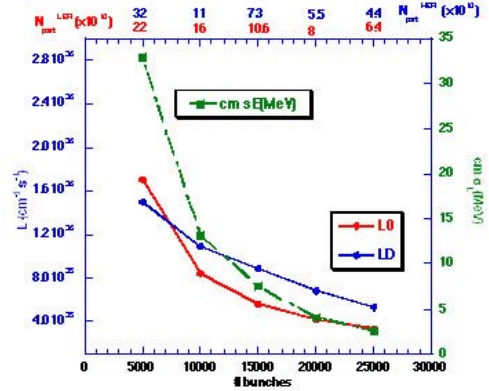


Figure 2: L and cm  $\sigma_E$  vs  $N_{\text{bunches}}$  for a fixed current in the DR. Red: geometric L, Blue: disrupted L, Green: cm  $\sigma_E$ .

As an example of spent beams emittances, in Fig. 3 the  $(x,x')$  and  $(y,y')$  space phase plots after collision for the Low Energy Beam are shown. The different colours refer to different longitudinal bunch slices, from the bunch head to the bunch tail, the vertical emittance growth in a single collision being about 300.

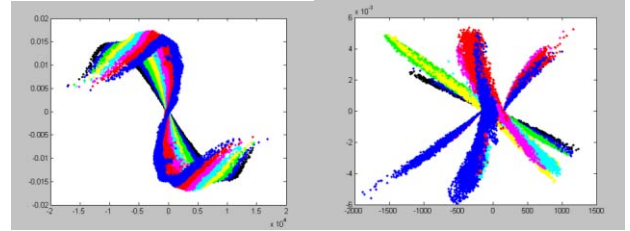


Figure 3: LEB  $(x,x')$  (left) and  $(y,y')$  (right) phase spaces.

## INTERFACE WITH MATHEMATICA

The study of beam-beam parameters requires a huge number of simulations. In particular both round and flat beams and collision with 2 and 4 beams were studied. To speed up this process an interface among Mathematica [4] and GuineaPig has been developed. It is then possible to make subsequent runs by varying the parameters in a multi-dimensional space and find the optimum set for the Luminosity.

The best parameters set is obtained by maximizing the figure of merit  $Q$  defined as  $Q=L/T$ , being  $L$  the luminosity and  $T = \text{Log}(\epsilon_i^{\text{out}}/\epsilon_i^{\text{in}})$ .  $T$  is directly proportional to the time spent by the beams in the rings to recover their emittances after the collision (subscript  $i$  ranges over  $x,y,z$  for each beam). Both  $L$  and  $T$  are predicted by GuineaPig.

This procedure was effective in finding the optimal parameter set for a round case scenario. The beam parameters are listed in Table 2. As an example of this optimization procedure Fig. 4 shows Luminosity scan in the  $(\sigma_x, \sigma_y)$  plane and the figure of merit  $Q$  in the  $(\beta_x, \sigma_x)$  plane, with the blue region corresponding to the maximum.

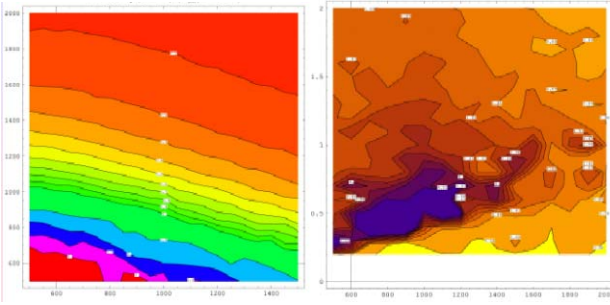


Figure 4: (a) Scan of L in the the  $(\sigma_x, \sigma_y)$  plane, (b) Scan of L in the the  $(\beta_x, \sigma_x)$  plane

In order to understand the behaviour of intense and low-size beams in collisions the previous studies were performed with symmetric energies (5 GeV). However the final SuperB asymmetric energies are required to allow tracking particle vertices in the collisions. A study of the flat beams case blow-up, with the parameters listed in Table 1 has been performed with a 4 GeV beam colliding with a 7 GeV beam. The vertical emittance blow-up is the same for the 2 beams if we use the “transparency condition” of having current inversely proportional to the beam energies. Another option to have the same blow-up in the 2 beams is to keep same currents but have different bunch lengths: 3 mm LEB colliding with a 5.3 mm HEB.

Table 2 Round beams collision parameters

Parameter	LEB	HEB
Beam Energy (GeV)	4	7
Number of bunches	10000	10000
Collision freq/bunch (Hz)	120	120
$N_{\text{part}}/\text{bunch} \times 10^{10}$	7	7
$\beta_x^*/\beta_y^*$ (mm)	0.55/0.55	0.55/0.55
Emittance (x/y) (nm)	1.54/1.54	1.54/1.54
$\sigma_z$ (mm)	0.8	0.8
IPx/y size ( $\mu\text{m}$ )	0.92/0.92	0.92/0.92
x/y Disruption	24/24	14/14
Luminosity ( $\times 10^{34}/\text{cm}^2/\text{s}$ )	120	120

## FOUR BEAMS SIMULATIONS

The four-beam DCI-like [6] beam charge compensation scheme (allowing the beams to collide again before being sent back into the Linac), was also studied. In principle this scheme could reduce the disruption, allowing much smaller IP sizes, together with very little emittance growth, relaxing the requirements on beam current and damping time. However the 4 beams scheme turned out to be more unstable than the 2 beams, being highly disrupted, with larger emittance blow-ups and with a resulting lower luminosity. This is mainly due to the kink-instability that is now much larger due to the defocusing

forces of the same-charges colliding beams. The analysis performed was not exhaustive and a better working parameter set could be found in the future. From the present results it seems that in this scheme shorter beams, with larger horizontal beam size, could work better. Fig.5 shows a comparison of the  $(x, x')$ ,  $(y, y')$ ,  $(z, \Delta E/E)$  phase spaces after collision for 4 (upper) and 2 (lower) beam case.

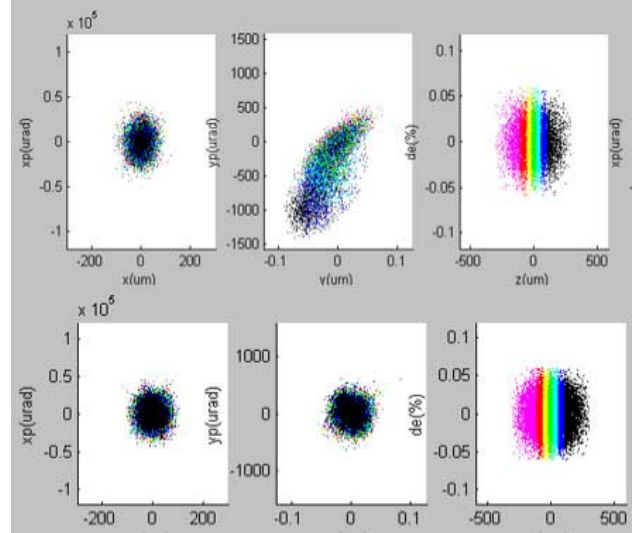


Figure 5:  $(x, x')$ ,  $(y, y')$ ,  $(z, \Delta E/E)$  phase spaces after collision for the 4 beams (upper) and the 2 beams (lower).

## CONCLUSIONS

Beam-beam studies have been performed for the design of a linearly colliding, single pass SuperB-factory. Both round and flat beams have been considered. The required luminosity of  $10^{36} \text{ cm}^{-2}\text{s}^{-1}$  can be achieved, but the required parameters for the damping rings are very challenging.

A solution with a novel collision regime, called “crabbed waist”, that will allow to collide in two conventional rings with the ILCDR characteristics was proposed at the Second SuperB Workshop in Frascati [5,6] and is being intensively studied [7] and beam-beam simulations with weak-strong and strong-strong codes are being performed.

## REFERENCES

- [1] <http://arxiv.org/abs/physics/0512235>
- [2] First LNF Workshop on SuperB, Frascati, Nov. 2005, <http://www.lnf.infn.it/conference/superbf05/>.
- [3] D. Schulte, PhD Thesis, Hamburg, 1996.
- [4] Mathematica: A System for Doing Mathematic by Computer. Wolfram Research Inc.
- [5] Second LNF Workshop on SuperB, Frascati, Nov. 2005, <http://www.lnf.infn.it/conference/superbf06/>
- [6] P. Raimondi’s talk in [5], to be published.
- [7] J. Seeman et al., “Design of an Asymmetric Single-pass Super-B Factory”, this Conference.

## DAΦNE STATUS REPORT

A. Gallo, D. Alesini, M.E. Biagini, C. Biscari, R. Boni, M. Boscolo, B. Buonomo, A. Clozza, G. Delle Monache, E. Di Pasquale, G. Di Pirro, A. Drago, A. Ghigo, S. Guiducci, M. Incurvati, P. Iorio, C. Ligi, F. Marcellini, C. Marchetti, G. Mazzitelli, C. Milardi, L. Pellegrino, M. Preger, L. Quintieri, R. Ricci, U. Rotundo, C. Sanelli, M. Serio, F. Sgamma, B. Spataro, A. Stecchi, A. Stella, S. Tomassini, C. Vaccarezza, M. Vescovi, M. Zobov INFN/LNF, Frascati (Roma); E. Levichev, S. Nikitin, P. Piminov, D. Shatilov BINP SB RAS, Novosibirsk; G. Benedetti CELLS, Bellaterra (Cerdanyola del Vallès); L. Falbo INFN-Pisa, Pisa; J. Fox, P. Raimondi, D. Teytelman SLAC, Menlo Park, California

### Abstract

The operation of DAΦNE, the 1.02 GeV c.m.  $e^+e^-$  collider of the Frascati National Laboratory with the KLOE experimental detector was successfully concluded in March 2006. Since April 2004 it delivered a luminosity  $> 2 \text{ fb}^{-1}$  on the peak of the  $\Phi$  resonance,  $> 0.25 \text{ fb}^{-1}$  off peak and a high statistics scan of the resonance. The best peak luminosity obtained during this run was  $1.5 \cdot 10^{32} \text{ cm}^{-2}\text{s}^{-1}$ , while the maximum daily integrated luminosity was  $\approx 10 \text{ pb}^{-1}$ . The KLOE detector has been removed from one of the two interaction regions and its low beta section substituted with a standard magnetic structure allowing for an easy vertical separation of the beams, while the FINUDA detector has been moved onto the second interaction point. Several improvements on the rings have also been implemented and are described together with the results of machine studies aimed at improving the collider efficiency and testing new operating conditions.

### INTRODUCTION

The DAΦNE [1] lepton collider complex consists of two independent rings sharing two common interaction regions (IR), and of a full energy injector composed by an S-band linac followed by a damping/accumulator ring and beam transfer lines to the main rings. The main parameters of the collider are listed in Table 1.

Table 1: DAΦNE Parameter list

Energy	0.51 GeV
Trajectory length	97.69 m
RF frequency	368.26 MHz
Harmonic number	120
Damping time, $\tau_E/\tau_x$	17.8/36.0 ms
Bunch length at full current $e^-/e^+$	2.8/2.2 cm
Beam currents $e^-/e^+$	2/1.4 Amps
Number of colliding bunches	111
Beta functions $\beta_x/\beta_y$	1.7/0.017 m
Emittance, $\epsilon_x$ (KLOE)	0.34 mm·mrad
Coupling at 0 current	0.3 %
Tunes $\nu_x/\nu_y$	0.091/0.166 $e^-$ 0.109/0.191 $e^+$

Since year 2000 DAΦNE has been delivering luminosity to three experiments: KLOE, FINUDA and DEAR. The first interaction region (IR1) has been so far dedi-

cated to the KLOE experiment, while FINUDA and DEAR detectors have shared, one at a time, the second interaction region (IR2).

An intense physics activity is also ongoing at the DAΦNE beam test facility (BTF), a dedicated transfer line delivering electron or positron beams from the DAΦNE Linac in the energy range 25-725 MeV with intensities varying from  $10^{10}$  particle/pulse to a single-electron. Moreover, two separate beam lines from one wiggler and one bending magnet of the  $e^-$  ring deliver synchrotron radiation (SR) to a dedicated LNF facility.

In the last two years (from April 2004 to March 2006) the DAΦNE activity has been mainly devoted to the KLOE data taking. The details of the last KLOE run are shown in Figure 1.

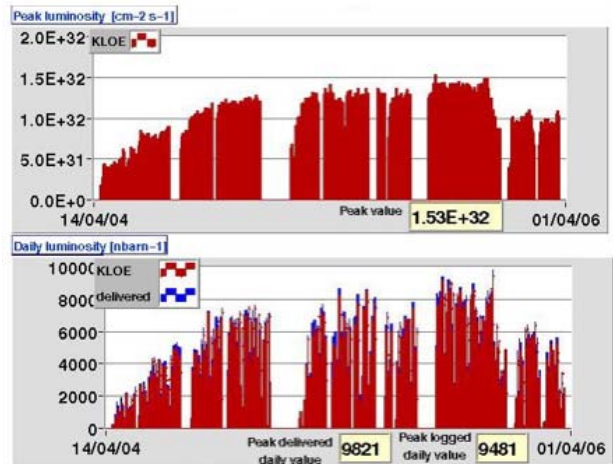


Figure 1: Last KLOE run peak and integrated luminosity.

### LAST KLOE RUN

In the 2004-2006 KLOE run DAΦNE has delivered an integrated luminosity in excess of  $2 \text{ fb}^{-1}$  on energy (1019.4 MeV) and, in the last part of the run,  $> 0.25 \text{ fb}^{-1}$  off-peak (1000 MeV). A high statistic scan of the  $\Phi$  resonance has been also performed collecting more than  $10 \text{ pb}^{-1}$  per point at 4 different energies (1010, 1018, 1023 and 1030 MeV).

As shown in Fig. 1, the machine performances have been continuously improving during the on-energy run.

With respect to the past physics runs, the final obtained improvement in both peak and integrated luminosity is a factor  $\approx 2$ .

The highest peak and daily integrated luminosities measured by KLOE have been  $L_{\text{peak}} = 1.53 \cdot 10^{32} \text{cm}^{-2} \text{s}^{-1}$  and  $L_{\text{day}} \approx 10 \text{pb}^{-1}$ , respectively. The luminosity has been optimized through many machine improvements, such as:

- Colliding current increase, due to the vacuum conditioning and the continuous improvements of the feedback systems, especially those fighting the electron cloud horizontal instability limiting the  $e^+$  current;
- Coupling correction;
- Optimization of the  $\beta$  functions at the IP and of the tune working point;
- Improvements of the non-linear dynamics with octupoles and sextupoles optimization, monitored through the measurement of the de-coherence time;
- Closed orbit correction and control (very important also for background reduction);
- Adiabatic day-by-day tune-up of the machine

The machine performances have also benefited from some hardware upgrades implemented during the long shutdown of year 2003 [2] such as the new interaction regions, the modifications of the wiggler magnet poles, the reduction of the injection kicker pulse duration and the installation of additional feedback amplifiers.

The ultimate limits to a further luminosity increase in the run were:

- Positron beam instability limiting the maximum total current to 1.4 A;
- The increase of bunch length and transverse sizes with current in the  $\mu$ -wave regime. This effect has been especially harmful in the  $e^-$  ring where the presence of Ion Clearing Electrodes (ICEs) in the wiggler chambers almost doubles the beam coupling impedance with respect to the  $e^+$  ring.
- Vertical beam-beam blow-up of the beams;
- Lifetime degradation due to parasitic crossings.

As reported in the following, we are planning measures to alleviate all the above mentioned problems.

## MACHINE PHYSICS ACTIVITIES

Several machine study shifts have been performed during the KLOE run, and especially in the last two weeks of operation (March 2006). They have been devoted to:

- Bunch length measurements with a large negative momentum compaction ( $\alpha_c < 0$ ) optics;
- Test on the wires for Beam Beam Long Range interaction (BBLR) compensation;
- Test of the new transverse feedback in the  $e^+$  vertical plane;
- Study of background to KLOE during injection and as a function of the scrapers position;
- Test on the new acquisition system for the single turn orbit measurements;
- Injection from the Linac switching off the chicane downstream the  $e^+$  converter (towards a continuous injection scheme foreseen for the collider upgrade);

Negative  $\alpha_c$  is a promising way to limit the bunch lengthening and weaken the effects of the  $\mu$ -wave

regime [3]. The short range wakefields are mainly focussing in this case, and the bunch starts lengthening only above the  $\mu$ -wave threshold as a consequence of the energy spread increase.

In the DAΦNE IRs the beams experience 24 parasitic crossings (Beam-Beam Long Range Interactions) acting as a non-linear lens on both beams reducing their lifetimes, the maximum storable current and the integrated luminosity. Numerical simulations have shown that BBLR interaction can be compensated to a certain extent by current-carrying windings [4]. We have tested this principle in DAΦNE obtaining a significant lifetime improvement.

## MACHINE SHUTDOWN FOR EXPERIMENT CHANGEOVER

Beginning from April 3<sup>rd</sup> 2006, machine operation has been stopped to allow the KLOE detector roll out from IR1 and the FINUDA detector roll in IR2. Meanwhile, maintenance of the various machine sub-systems and some hardware upgrades have been done.

The KLOE detector has been displaced from the beam line for the first time since spring 1999 when it was rolled in IR1 to begin its physics enterprise. The detector is now parked in a dedicated hall separated from the DAΦNE one by a dismountable concrete-block wall. It will undergo some maintenance, while future data taking runs are not planned yet. A new vacuum chamber has been installed in IR1 to replace the KLOE one, equipped with 4 electromagnetic quadrupoles allowing a flexible optics and an easy separation of the beams in IR1. Pictures of IR1 before and after KLOE roll out are shown in Fig. 2.



Figure 2: DAΦNE IR1 before and after KLOE roll-out.

The FINUDA detector is going to be rolled back in IR2 for a data taking run of approximately 9 months up to the delivery of  $1 \text{fb}^{-1}$ . The collider operation restart is scheduled for July 17<sup>th</sup>, while the DAΦNE BTF operation has been already resumed on June 26<sup>th</sup>.

Among the various maintenance activities it is worth mentioning the substitution of all the cooling pipe spigots ( $\approx 150$  per piece) in the 8 wiggler magnets, whose water leakages were responsible for a significant fraction of machine downtime in the past.

Hardware upgrades carried out during this shutdown are also relevant.

We decided to remove all ICEs from the wiggler vacuum chamber of the  $e^-$  ring, since they strongly contributed to the broadband impedance [5] making the

$e^-$  bunches significantly longer than the  $e^+$  ones and limiting the possibility of reducing the vertical  $\beta^*$  to increase the luminosity. Moreover, we have experimental observations of the vertical size increase of the  $e^-$  bunches above the  $\mu$ -wave threshold, which also affected the luminosity and limited our possibilities to take full advantage from different collider regimes such as negative  $\alpha_c$ . We estimate a luminosity gain of  $\approx 20\div 30\%$  from ICEs removal. To extract the ICEs from the chambers and to cut the metallic fingers keeping them in place, a special dedicated device remotely controlled through an endoscope has been designed and built. Two out of four electrodes have been already removed, together with some other shorter ICEs located elsewhere in the vacuum chamber that have proved to be broken or ineffective.

Other relevant hardware upgrades consisted in:

- Installation of wires for BBLR compensation in the IR2;
- Feedback upgrade (III generation digital bunch-by-bunch feedback designed for Super B-factory in the SLAC-KEK-LNF collaboration framework);
- New Beam Position Monitors (BPMs) for measurements of linear and non-linear optics parameters ( $v_{x,y}$ ,  $\beta_{x,y}$ ,  $\kappa$ ,  $c_{11}$ , ...) based on turn-by-turn position tracking;
- TiN coating on a short straight section to allow the first direct e-cloud test measurement on the  $e^+$  ring;
- Control System upgrades;
- Installation of a photon tagged source and of a pulsed magnet to improve the duty cycle from 40% to 80% in the Beam Test Facility

## DAΦNE FUTURE PLANS AND UPGRADES

After the end of the FINUDA run, expected by mid 2007, a run of the SIDDHARTA experiment is already scheduled. Official programs beyond the SIDDHARTA run are not yet defined.

DAΦNE hardware improvements are planned in the near future. We intend to install in the machine new fast injection kickers designed at LNF to cope with the requirements of the ILC damping rings [6] which could be very fruitfully used in DAΦNE to leave all the stored bunches unperturbed during injection (with the only exception of the bunch selected for the injection plus the 2 adjacent ones). We have experimental evidence that the transient excitation of the bunches at injection is one of the mechanisms that drive the fast horizontal instability in the  $e^+$  ring. Then we expect to increase the stored  $e^+$  current by using the new kickers, which also provide better deflecting field uniformity and smaller beam coupling impedance with respect to the devices presently used at DAΦNE. The installation of a first set of new injection kickers is planned for the end of this year.

On a longer time scale there are proposals for more ambitious upgrades. The installation of new independent transfer lines to inject the two beams simultaneously

(trickle injection) can keep the collider luminosity constantly at its maximum value, allowing also a better optimization of the collider parameters at the maximum currents. We have also a proposal to test the Strong RF Focusing (SRFF) principle at DAΦNE [7]. In this case the installation of a 1.3 GHz SC, TESLA-like cavity providing voltage in the 10 MV range, together with the implementation of a suitable lattice structure providing large or oscillating  $R_{56}$  functions allows the machine to explore the bunch length modulation regime. Short intense bunches ( $\approx 2$  mm @ 10 mA) are obtainable, according to our simulations based on SPIDER [8], a tracking code purposely developed to study the bunch  $\mu$ -wave behaviour in the SRFF regime.

The study of a crab crossing system to collide the beams head-on in spite of the finite crossing angle by properly tilting the bunch equilibrium distribution at the IP is in progress [9]. A basic design of the crab cavities has been defined, and the expected luminosity gain is of the order of  $\approx 2$ .

Recently, the crabbed waist collision scheme [10] has been proposed to overcome the hourglass effect by increasing the crossing angle and decreasing the horizontal size of the bunch at the IP. A proposal to test in the near future this promising luminosity-boosting idea at DAΦNE by implementing a new dedicated IR is in preparation.

## CONCLUSIONS

The Frascati  $\Phi$ -factory DAΦNE has successfully completed the run of the KLOE experiment delivering  $> 2 \text{ fb}^{-1}$  at the  $\Phi$  resonance peak energy and  $\approx 0.3 \text{ fb}^{-1}$  off-peak in the period from April 2004 to March 2006, with a luminosity increased by  $\approx 2$  with respect to the previous runs. Meanwhile, the machine continued to operate regularly also for the Beam Test Facility and for the Synchrotron Radiation Facility. After a 3 months shutdown for experiment changeover, machine maintenance and hardware upgrades, DAΦNE is ready for the 2<sup>nd</sup> run of the FINUDA experiment.

There are many proposals to upgrade the machine and test new ideas to improve its performances: new fast injection kickers, new transfer lines, strong RF focusing, crab crossing, crabbed waist. Many of this items are of primary interest for the whole lepton collider community.

## REFERENCES

- [1] G. Vignola et al. , PAC93, p. 1993.
- [2] C. Milardi et al. , EPAC 2004, p. 233.
- [3] M. Zobov et al. , TUODFI02, this conference.
- [4] C. Milardi, THPCH011, this conference.
- [5] B. Spataro, M. Zobov, DAΦNE Technical Note G-64, 2005.
- [6] D. Alesini et al. , TUPLS009, this conference.
- [7] C. Biscari et al. , PAC 2005, p. 336.
- [8] L. Falbo et al. , WEOFIO3, this conference.
- [9] A. Gallo, MOPLS029, this conference.
- [10] P. Raimondi, 3<sup>rd</sup> SuperB Workshop, SLAC, 2006 [www-conf.slac.stanford.edu/superb/](http://www-conf.slac.stanford.edu/superb/)

# PRELIMINARY STUDY OF A CRAB CROSSING SYSTEM FOR DAΦNE

Alessandro Gallo, David Alesini, Fabio Marcellini, Pantaleo Raimondi, Mikhail Zobov ,  
INFN/LNF, Frascati (Roma), Italy

## Abstract

The implementation of a crab crossing scheme at the Frascati  $\Phi$ -factory DAΦNE is under consideration, together with several other ideas and upgrades to increase the collider luminosity. The crab crossing is beneficial to the luminosity because it is expected to optimize the geometrical superposition of the colliding bunches and to weaken the synchro-betatron beam-beam resonances. The basic specifications of such a system, the expected luminosity increase, a preliminary design of the crab cavities and the architecture of the dedicated RF system are presented.

## INTRODUCTION

The double-ring Frascati  $\Phi$ -factory DAΦNE is in operation since spring 1999 and will continue delivering luminosity to the experiments until year 2009. The time remaining before the end of the machine operation will be used also to improve the machine performances and to test different ideas to increase the luminosity, as described in [1]. This accelerator physics experimental activity is considered of primary importance by the DAΦNE team since the results may contribute to confirm or re-address the design criteria of the next generation lepton factories.

The DAΦNE layout includes two Interaction Regions (IRs) where the two rings merge to accommodate the experiments, and in both of them the beam trajectories cross with an horizontal angle  $\vartheta_{cross}$  ranging from  $\pm 11$  to  $\pm 17$  mrad. One of the most promising ways to increase the luminosity is to implement the “crab-crossing” system [2,3] to compensate the horizontal crossing angle and colliding the bunches in a head-on like configuration. The luminosity is expected to increase because of a better superposition of the two beams at the Interaction Point (IP). The geometrical reduction of the luminosity caused by a  $\pm 16.5$  mrad horizontal crossing angle has been analytically calculated for DAΦNE with the collider parameter set of the KLOE run [4]. For an average bunch length of  $\approx 2.5$  cm, the estimated geometrical reduction of the luminosity has been  $\approx 8\%$  in the KLOE run.

However, the major mechanism of luminosity reduction caused by the crossing angle is the excitation of beam-beam synchro-betatron resonances that produce beam blow-up. Crab crossing weakens the resonances, leading to smaller bunch sizes of the colliding beams. Estimates of the luminosity increase expected from crossing angle compensation can be drawn from beam-beam simulation codes. The case of DAΦNE at the KLOE run working point has been studied with the LIFETRAC code and simulation results are summarized in Table 1. The perfect compensation of the crossing angle can provide up to %70 of luminosity increase for bunch currents of 10 mA.

Table 1: DAΦNE luminosity vs. crossing angle

	I [mA]	L/L <sub>0</sub>
$\vartheta_{cross} = 0$ mrad	6	0.88
$\vartheta_{cross} = 15$ mrad	6	0.69
$\vartheta_{cross} = 0$ mrad	10	0.75
$\vartheta_{cross} = 15$ mrad	10	0.43

## CRAB CROSSING SYSTEM DESIGN

There are different ways to implement a crab crossing system in a circular collider. The most straightforward one consists in placing 2 crab cavities per ring in symmetrical positions around the IP at a betatron phase advance of  $\pi/2$  with respect to the IP. In this case the first cavity provides a horizontal tilt in order to eliminate the crossing angle at IP, while the second one removes completely the tilt. Thus the bunch equilibrium envelope is horizontally tilted only in the region between the cavities around the IP.

If only one crab cavity per ring is used, the equilibrium envelope is tilted all around the ring. The crabbing voltage produces a single particle closed orbit distortion dependent on the longitudinal position of the particle itself. For usually small values of the synchrotron tune the bunch envelope is horizontally tilted at the IP by an angle  $\theta_{crab}$  given by [5]:

$$\theta_{crab} = \frac{\pi \sqrt{\beta_{IP} \beta_{cav}}}{\lambda_{RF} \sin(\pi Q_x)} \frac{e V_{\perp}}{E} \cos(|\phi_{IP} - \phi_{cav}| - \pi Q_x) \quad (1)$$

where  $V_{\perp} = p_{\perp} c / e$  is the peak horizontal kick voltage,  $Q_x$  is the horizontal tune,  $\beta$  and  $\phi$  are local values of the horizontal betatron function and phase advance, and  $\lambda_{RF}$  is the RF wavelength of the crab cavity deflecting mode.

We propose to implement the single cavity crabbing scheme in DAΦNE since there is very limited space available on the machine. Moreover, this scheme is very efficient at low horizontal tunes, and it requires half of the hardware (cavities and RF power sources) with respect to the two-cavities, insertion-like scheme.

The crab crossing compensation is optimal when the crabbing angle  $\theta_{crab}$  at the IP is equal to the crossing angle. The required transverse voltage to fulfil this condition is given by eq. (1). The optimal betatron phase advance between crab cavity and IP is given by:

$$|\phi_{IP} - \phi_{cav}| = (n + Q_x) \pi \quad (2)$$

Large values of the horizontal  $\beta$  function and small values of  $\lambda_{RF}$  are preferable to increase the system efficiency. However, the transverse kick is reasonably linear only over a portion of the wavelength ( $\pm\lambda_{RF}/6$ ) and this put a limit on the choice of  $\lambda_{RF}$  to tilt the beam envelope without distortion over the full bunch length ( $\pm 3\sigma_z$ ). The trade-off between linearity on one side and efficiency and compactness on the other side leads to the choice of designing the crab crossing system for DAΦNE at 736 MHz, i.e. the 2<sup>nd</sup> harmonic of the main RF systems. The design parameters of the DAΦNE crab crossing system are summarized in Table 2.

Table 2: Parameters of the DAΦNE crab crossing system

Crossing Angle	$\vartheta_{cross}$	17 mrad
RF freq. /wavelength	$f_{RF}/\lambda_{RF}$	736.5 MHz / 0.41 m
$\beta_x$ -function @ IP / Cav	$\beta_{IP}/\beta_{Cav}$	1.5 / 9 m
Horizontal betatron tune	$Q_x$	< 0.15
Peak transverse voltage	$V_{\perp}$	< 120 kV
Crab cavity shunt imp.	$R_{\perp}$	1 MΩ
RF power	$P_{RF}$	< 10 kW

In analogy with the accelerating modes, the transverse mode shunt impedance is defined as  $R_{\perp} = V_{\perp}^2/2P$ .

### CRAB CAVITY DESIGN

The crab cavity design for DAΦNE is based on a single-cell bell-shaped resonator working on the TM110-like horizontal mode at room temperature. Since a peak transverse voltage of 120 kV is a relatively modest value, the cavity design is mainly addressed to optimize the cavity compactness, the efficiency and simplicity of the HOM damping, and to reduce the costs.

The basic 2D profile of the cavity is shown in Fig. 1. The cell diameter essentially defines the resonant frequency of the operation mode, while the cavity efficiency (i.e. the transverse impedance) has been optimized by tuning the length of the cell.

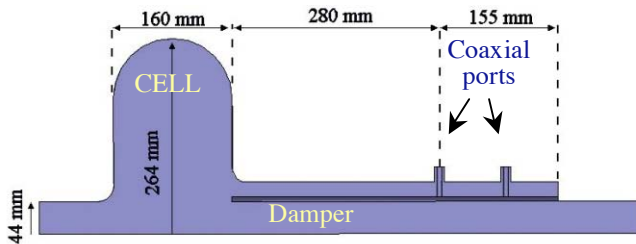


Figure 1: Basic profile of the DAΦNE crab cavity.

The HOM damping is obtained by an integrated coaxial coupler whose inner conductor is the prolongation of the beam tube. The whole coaxial coupler acts like a huge antenna loading the cavity HOM, and the HOM power travelling in the damper is extracted through 8 smaller

coaxial transducers connected to matched loads through vacuum feedthroughs. The transverse shape of the outer conductor and the penetration of the inner conductor into the cell are both crucial to obtain a satisfactory HOM damping without affecting the operation mode.

The transverse cut-view of the coaxial damper is shown in Fig. 2. The coaxial TEM mode, which couples with the cell longitudinal (monopole) modes has no cut-off. This allows coupling the cavity lowest mode (TM010-like, 470 MHz) provided the damper inner conductor protrudes sufficiently into the cell.

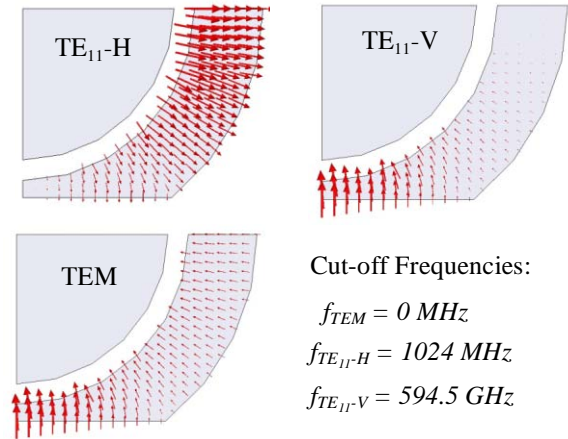


Figure 2: Damper propagation modes - Field distribution.

The transverse (dipole) modes of the cell couple to the coaxial damper TE11 modes. The shape of the outer conductor, as shown in Fig. 2, has two flat cuts parallel to the horizontal plane to decrease the vertical separation of the 2 conductors. With this shape the cut-off frequencies of the TE11 polarities are widely split so that the vertical polarity of the cell TM110 dipole mode can propagate in the damper, while the horizontal polarity (i.e. the operation mode) is under cut-off and remains undamped.

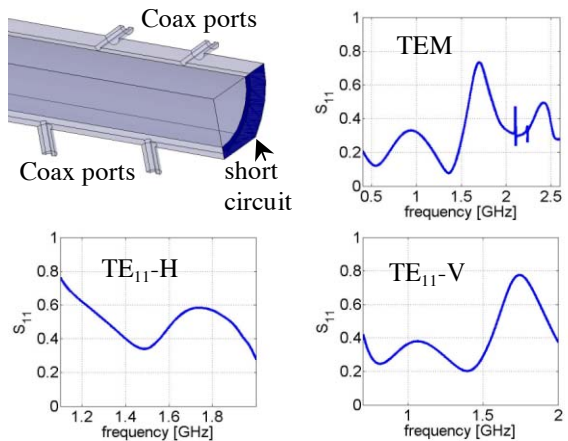


Figure 3: Matching of the damper with coax transducers.

The coaxial damper is terminated through 8 RF ports connected with match loads. The geometry of the transducers is optimized to reduce as much as possible the reflection of the various propagating modes in the

damper. A view of the vertical and horizontal transducer together with their frequency response over the bandwidth required to damp the cell HOMs as computed by the 3D code HFSS are shown in Fig. 3.

### CRAB CAVITY 3D SIMULATIONS

The cell equipped with the coaxial damper and the 8 small coaxial transducers has been modelled in the 3D electromagnetic code HFSS, as shown in Fig. 4. The complete scattering matrix referred to the various ports of the whole structure has been computed, and the parameters of the loaded modes has been worked out from the transmission frequency responses. The list of the modes together with their resonant frequencies, R/Q factors and external (damper loading) Q-factors are reported in Table 3.

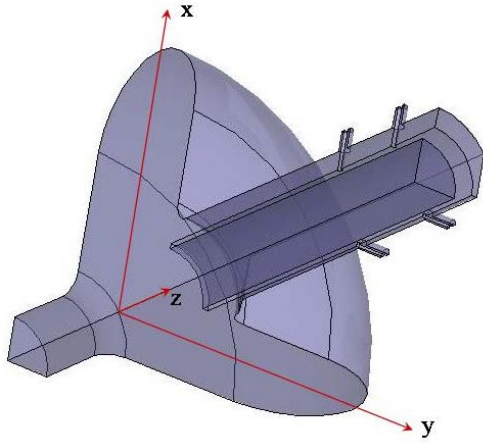


Figure 4: 3D HFSS model of cell and damper assembly.

It may be seen in Tab. 3 that the operation mode is very weakly loaded by the damper ( $Q_{\text{ext}} > 3 \cdot 10^5$ ) while all the other modes couple to the damper, with  $Q_{\text{ext}}$  values ranging from few tens to few thousands. The least damped HOMs are transverse, with impedances up to  $R_{\perp} \approx 20 \text{ k}\Omega$ . Even in the pessimistic case of full coupling with beam betatron sidebands, the coupled bunch instability growth rate would be  $\alpha \approx 10 \text{ ms}^{-1}$  for a stored current of  $I_b = 2 \text{ A}$ . The DAΦNE transverse feedback system provides damping rates  $\alpha_f > 100 \text{ ms}^{-1}$  [6] and it is expected to strongly damp residual instabilities coming from the cavity HOMs. It may be noticed that the list in Table 3 includes a dipole mode whose field distribution can not be described in terms of pill-box modes. For this mode the fields are localized in the region where the damper is connected to the cell, and the residual transverse impedance is a modest value ( $R_{\perp} \approx 3.5 \text{ k}\Omega$ ).

### THE CRAB CAVITY RF SYSTEM

The DAΦNE crab cavities will be powered through a coupling port consisting in a loop magnetically coupled to the cell in the equator region, very similar to the DAΦNE main cavity one. A tuning plunger will be located opposite to the coupling port, to compensate temperature variations and to follow beam loading second order effects. In fact,

bunches travelling along the symmetry axis in a pure dipole field do not interact with the mode, while a modest coupling is expected for off-axis trajectories, proportional to the orbit error.

Table 3: Parameters of the DAΦNE crab cavity modes.

	MODE	f [MHz]	R/Q [Ω]	$Q_{\text{ext}}$
Horizontal	<b>TM<sub>110</sub>-like (H)</b>	<b>736</b>	<b>31.8</b>	<b>338000</b>
	Cell-damper trans.	924	2.05	1700
	TE <sub>111</sub> -like (H)	1042	4.12	300
	TM <sub>111</sub> -like (H)	1261	11.2	100
	TM <sub>120</sub> -like (H)	1315	3.24	7300
	TE <sub>121</sub> -like (H)	1365	0.51	400
	TE <sub>112</sub> -like (H)	1702	5.93	480
Vertical	TM <sub>121</sub> -like (H)	1749	3.72	2500
	TM <sub>110</sub> -like (V)	736	31.8	90
	TE <sub>111</sub> -like (V)	980	4.12	80
	TM <sub>111</sub> -like (V)	1251	11.2	186
	TM <sub>120</sub> -like (V)	1314	3.24	5306
	TE <sub>121</sub> -like (V)	1360	0.51	198
Mon.	TE <sub>112</sub> -like (V)	1705	5.93	707
	TM <sub>121</sub> -like (V)	1749	3.72	3055
	TM <sub>010</sub> -like	473	85	234
	TM <sub>020</sub> -like	1073	---	<50
	TM <sub>011</sub> -like	1118	---	<50

There is a wide variety of RF commercial sources covering the crab cavity frequency band, mainly for the broadcasting market. A commercial 10 kW solid state source seems a very suitable choice because of its simplicity and reliability.

### CONCLUSIONS

The study of a crab crossing system to be installed in DAΦNE is well in progress. The proposed system is based on a single crab cavity per ring, with bunch equilibrium distribution tilted in the x-z plane all along the ring. According to beam-beam simulations, a collider luminosity increase up to a factor  $\approx 2$  is expected in case of perfect compensation of the crossing angle. The electromagnetic design of the cavity is almost complete. The proposed crab cavity is tuned on the 2<sup>nd</sup> harmonic of the main DAΦNE RF cavities, and is based on a single-cell working on the horizontal polarity of the TM<sub>110</sub>-like mode loaded by a special coaxial damper integrated on one of the cavity beam tubes. Modes different from the operation one are well damped. The cavity is also sufficiently compact and efficient, and can provide the required peak voltage being powered with a commercial, 10 kW RF power source.

### REFERENCES

- [1] A. Gallo et al., MOPLS028, this conference.
- [2] K. Oide, K. Yokoya, Phys. Rev. A40, p. 315,1989.
- [3] K. Ohmi et al., PRST Vol. 7, 104401 (2004).
- [4] D. Alesini et al., DAΦNE Tech. Note G-62, 2004.
- [5] A. Gallo, DAΦNE Tech. Note, to be published.
- [6] A. Drago et al., proc. of 2005 PAC, p. 1841.

# MAD-X/PTC LATTICE DESIGN FOR DAPHNE AT FRASCATI

Etienne Forest, KEK, Ibaraki, Japan, Catia Milardi, INFN/LNF, Frascati, Italy  
Frank Schmidt, CERN, Geneva, Switzerland

## Abstract

In absence of a program that takes as an input the desired or known location of the magnets in the tunnel, accelerator designers have been using MAD that looks at a ring as a sequence of magnets without a connection to the tunnel. In many simple examples that is just fine, but once more complicated structures are treated one is bound to play tricks with MAD. Here PTC comes to the rescue. It is shown how pieces of this machine that exist in MAD-X format are used in PTC to create this double ring, as found on the accelerator floor, with a proper survey in the forward and backward direction. Special elements have been implemented in MAD-X to allow the full PTC description of the machine.

## INTRODUCTION

The Frascati  $\Phi$ -factory DAΦNE is an  $e^+e^-$  collider operating at the energy of the  $\Phi$ -resonance (1.02 GeV c.m.) [1].

DAΦNE is an accelerator complex consisting of a double-ring collider, an S-band linear accelerator, an intermediate damping ring to make injection easier and faster and 180 m long transfer lines connecting the different parts.

In the past five years DAΦNE has delivered luminosity to three different experiments: KLOE [2], FINUDA [3] and DEAR [4] running one at a time, and installed the first one on IR1 and the other two, alternatively, on IR2. The best peak luminosity reached is  $1.5 \times 10^{32} \text{ cm}^{-2} \text{ s}^{-1}$  with a maximum daily integrated luminosity of  $\sim 10 \text{ pb}^{-1}$  [5].

High current bunched beams are stored in each ring, usually the number of adjacent filled buckets is in the range 109÷111 out of 120 available. A short gap is needed for ion clearing. It's worth mentioning that in DAΦNE the bunch separation is the shortest among all existing colliders and particle factories (2.7 ns). In order to minimize the effect of parasitic crossings [6] of the closely spaced bunches, the beams collide under a crossing angle in the range of 10 to 20 mrad.

The DAΦNE model has been implemented using the MAD8 [7] design code which imposes some severe limitations. In fact MAD cannot handle two rings at the same time, cannot describe correctly the beam trajectory off-axis in the IRs, does not evaluate correctly the beam emittance and damping times, computed by using the synchrotron integrals, and cannot predict correctly the beam lifetime.

It therefore came handy when CERN introduce the new MAD-X [8] code that combines most of the valuable ingredients of MAD with the object oriented PTC [9] code, called MAD-XP in the following, which provides

all the more advanced features that should be expected from a modern accelerator design code.

In particular, PTC offers a proper description of all accelerator elements available in MAD-X. With PTC the notorious MAD problem of incorrect delta-p/p dependence of various accelerator parameters is a thing of the past. A proper treatment of SBEND and RBEND magnets has been provided with PTC early on. Recently, it became apparent to some of our users that the CAVITY is treated in PTC with the proper transit time factor while in MAD this has always been ignored. The code offers the exact or expanded Hamiltonian of each element. Accelerator elements can be placed at their proper three-dimensional position according to the accelerator floor in the real world. Besides particle tracking, PTC does perform also MAP tracking with all the subsequent and well tested Normal Form techniques and it allows to track the beam envelop tracking that can be used to get correct values for the beam emittance and for the beam dynamic aperture. This has been achieved by keeping both MAD-X and PTC as independent codes but linking them via a converter that transforms the MAD-X accelerator data base into the PTC world. Since PTC has in principle more options for the proper treatment of accelerator elements we are using the very flexible input structure of MAD-X to add more and more features that are controlled by MAD-X but only available in PTC.

With MAD-XP one can therefore avoid all the typical MAD limitations. In fact, it can deal with the real three dimensional disposition of the ring elements in space and can handle two rings at the same time.

The DAΦNE model has been first converted to MAD-X format and then the MAD-X input file has been used to generate the double ring model by means of PTC.

A reliable design code is expected to be even more important for the future DAΦNE upgrade options [10] looking for an increase at least of a factor 3 in the peak luminosity by means of higher currents, smaller emittances and a sophisticated crabbed waist collision scheme [11], much more demanding in terms of dynamic aperture and beam lifetime estimate.

## DAΦNE MODEL

DAΦNE is a very compact machine (97.98 m long), with no periodicity at all. The KLOE and FINUDA detectors are surrounded by large superconducting solenoid magnets with a 2.4 Tm field integral, that is not negligible if compared to the ring magnetic rigidity ( $B\rho = 1.7 \text{ Tm}$ ), and must be taken into account in the machine model.

Each ring in DAΦNE consists of a long external arc and a short internal one based on a quasi-achromatic cell

built using a bending-wiggler-bending sequence. The cells are based on four different kinds of dipoles: two sector magnets and two rectangular ones deflecting the beam respectively by  $49.5^\circ$  and  $40.5^\circ$ .

The MAD limitation in evaluating the beam emittance comes from the estimate of the I4 synchrotron integral for the rectangular magnets which does not include the contributions coming from the magnet wedges. Such terms are negligible for large accelerator with long dipoles with small deflection angles but become very relevant for short magnets as in the case of DAΦNE.

The presence of the wiggler in the region of maximum dispersion doubles the radiation emitted in the dipoles, reduces the damping times and, as a consequence, increases instability thresholds. Moreover the optimal optics flexibility (all quadrupole magnets are powered independently), makes it possible to tune the beam emittance by changing the dispersion in the wigglers at constant field.

In a low energy lepton collider the beam lifetime is mainly limited by the Touschek effect which in MAD is computed assuming the RF energy acceptance as a limit for the stable particle. As a matter of fact in DAΦNE the energy acceptance due to the dynamic aperture is smaller than the RF energy acceptance and this leads to overestimate the beam lifetime by a factor 2.

### PTC MODEL OF DAΦNE

The code PTC contains Fortran90 structures which allow two novel things: the placements of magnets in arbitrary locations and the sharing of beam lines. Beam lines can be shared between different lattices as in a collider or shared within a single lattice as in a recirculator or a combination of both.

The present example consists of a collider made out of two rings. The first ring is depicted below in ure 1. This ring is made of 4 parts which are quite standard. In fact in MAD-X, they are created as 4 standard beam lines.

They are then passed to the code PTC as 4 simple “layouts” of PTC. While a beam line in MAD-X is a simple link list of magnets, in PTC, the layout is a slightly more complex object: a link list of containers (Fibres) with pointer to a magnet.

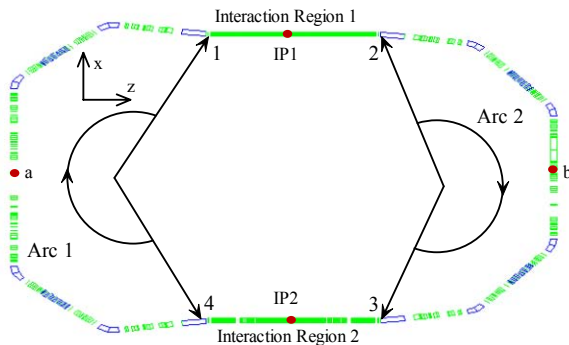


Figure 1: First Ring of DAΦNE.

The fibre also contains a pointer to a 3 dimensional chart locating the magnet precisely in space and a pointer to patches. The patches permit the dynamical connection between different magnet maps. They are translations and rotations. The two rotations which involve the direction of propagation become drifts in polar coordinates while the translation along the direction of propagation is a regular Cartesian drift.

### SURVEY COMMAND OF PTC

When fibres are created “à la MAD”, the magnets are all located at the origin. The survey command places them in the usual MAD survey position. The PTC survey command propagates the initial frame of reference through the lattice using the local coordinate frames attached to the magnets and the patches. Since the patches are all set to identity, we get the regular MAD survey by construction. This is an arbitrary choice in PTC. PTC could have any survey convention. Ideally, PTC should be connected to a CAD program and the magnet placed where ever we want.

### POSITIONING THE 4 LAYOUTS

Thus initially, the 4 layouts are created and surveyed. Since all the magnets within each of them are at a standard position, the beam lines are properly constructed. However they all start at the global origin. Looking at the engineering floor plans, we can move and rotate the four beam lines into their real positions. In practice, the position of red dots (a, b, IP1, IP2) was read and the beam lines were placed.

At the four intersections (1, 2, 3, 4), the beam lines were not matched properly. Thus 4 patches were computed between PTC’s fibres at locations 1, 2, 3, and 4. The PTC survey command serves as a self-consistency check. We survey the ring. If it moves, the patches are incorrect or forgotten. If the ring stays in place, then the ring is ready for tracking.

### SECOND RING

DAΦNE is a collider. The two interaction regions are common to two rings. PTC has reversed propagators and thus the exact same magnets can be traversed in opposite directions. These magnets are exact in the computer sense as well: though a common magnet belongs to a different layout and a different fibre, it occupies the same place in memory. Anything that happens to this magnet in one ring (misalignments, mispowering, etc.) automatically happens in the other ring.

In Figure 2 both rings are shown with an indication of direction of particle motion. Note that the lines going through the centre of the elements are actually obtained by tracking a trajectory through each separate ring.

To our knowledge this is the first time ever that an accelerator modelling code has been successfully applied to track trajectories backwards and forwards in a model of

an existing accelerator which consists of a double ring structure with long common beam-line sections.

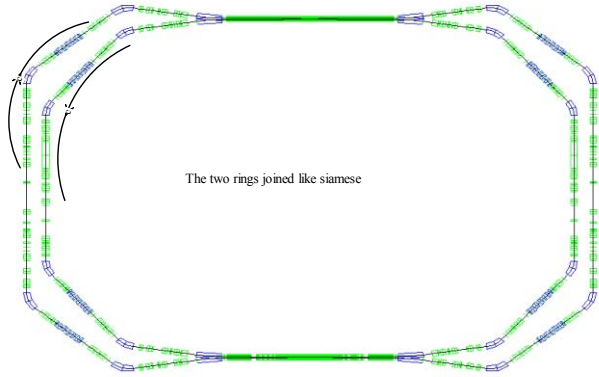


Figure 2: Both Rings of DAΦNE.

### CONCLUSIONS

It has been shown that the combined code MAD-XP can be used to study complex double ring structures with common beam lines. MAD-X plays the part of the front-end to read-in the various beam lines with the standard and flexible MAD-X input language. The accelerator data base is then transferred to the PTC code which is used to

actually build up the complex double ring structure DAΦNE using forward and backward propagators. Closing trajectories have been tracked through both rings.

We are at the starting point of applying MAD-XP to complex structures like DAΦNE for which the full capabilities of PTC are required. Considerable progress has been made but further effort will be needed to handle properly various subtle issues.

In particular the reader should not yet expect a turn key ready code for any kind of complex structures which is the goal to be reached in the near future. Presently, some expert intervention is still mandatory.

### REFERENCES

- [1] G. Vignola, PAC93, p.1993.
- [2] The KLOE Collaboration, LNF-92/019 (IR), 1992.
- [3] The FINUDA Collaboration, LNF-93/021 (IR), 1993.
- [4] The DEAR Collaboration, LNF-95/055 (IR), 1995.
- [5] A. Gallo et al., this conference, MOPLS028.
- [6] C. Milardi et al., this conference, THPCH011.
- [7] MAD8, <http://mad.home.cern.ch/mad/mad8web/mad8.html>.
- [8] MAD-X, <http://mad.web.cern.ch/mad/>.
- [9] Forest *et al.*, "Introduction to the PTC Code", KEK Report 2002-3.
- [10] [http://www.lnf.infn.it/Infadmin/direzione/DANAE\\_LOI.pdf](http://www.lnf.infn.it/Infadmin/direzione/DANAE_LOI.pdf).
- [11] P. Raimondi, <http://www-conf.slac.stanford.edu/superb/>.

## A LUMINOSITY OF $10^{34}$ $\text{CM}^{-2}$ $\text{S}^{-1}$ IN THE PEP-II B-FACTORY\*

J. Seeman<sup>†</sup>, M. Browne, Y. Cai, W. Colocho, F.-J. Decker, M. Donald, S. Ecklund, R. Erickson, A. S. Fisher, J. Fox, S. Heifets, R. Iverson, A. Kulikov, A. Novokhatski, V. Pacak, M. Pivi, C. Rivetta, M. Ross, P. Schuh, K. Sonnad, M. Stanek, M. Sullivan, P. Tenenbaum, D. Teytelman, J. Turner, M. Weaver, D. Van Winkle, U. Wienands, W. Wittmer, M. Woodley, Y. Yan, G. Yocky, SLAC, Menlo Park, CA 94025, W. Kozanecki, CEA/Saclay, France; M. Biagini, INFN, Frascati, Italy.

### Abstract

PEP-II is an  $e^+e^-$  asymmetric B-Factory Collider located at SLAC operating at the Upsilon 4S resonance (3.1 GeV x 9 GeV). It has reached a luminosity of  $1.09 \times 10^{34}/\text{cm}^2/\text{s}$  and has delivered an integrated luminosity of  $884 \text{ pb}^{-1}$  in one day. PEP-II has delivered, over the past seven years, an integrated luminosity to the BaBar detector of over  $375 \text{ fb}^{-1}$ . PEP-II operates in continuous injection mode for both beams boosting the integrated luminosity. The peak positron current has reached 2.995 A in 1722 bunches. The electron current has reached 1.78 A. The goal over the next several years is to reach a luminosity of  $2.1 \times 10^{34}/\text{cm}^2/\text{s}$ . The accelerator physics issues being addressed in PEP-II to reach this goal include the electron cloud instability, beam-beam effects, parasitic beam-beam effects, high RF beam loading, shorter bunches, lower  $\beta_y^*$  interaction region operation, and coupling control. Figure 1 shows the PEP-II tunnel.

### PARAMETERS

The present parameters of PEP-II are shown in Table 1 compared to the design. The present peak luminosity is over 3.6 times the design and the best integrated luminosity per day is  $0.884 \text{ fb}^{-1}$ , over 6.8 times the design. The highest luminosity in each month is shown in Figure 2, the integrated luminosity for each month since the startup of PEP-II is shown in Figure 3 and the integrated luminosity for Run 5 in Figure 4.



Figure 1: View of the PEP-II tunnel. The LER beam line is above the HER beam line.

\*Supported by US DOE contract DE-AC02-76SF00515.

<sup>†</sup>

Table 1: PEP-II June 2006 Parameters

Parameter	PEP-II Design	PEP-II Present
HER Vertical tune	23.64	23.61
u114		
HER Horizontal tune	24.62	24.503
LER Vertical tune	36.64	36.59
LER Horizontal tune	38.57	38.505
HER current (mA)	750	1776
LER current (mA)	2140	2950
Number of bunches	1658	1722
Ion gap (%)	5	1.6
HER RF klystron/cav	5/20	10/26
HER RF volts (MV)	14.0	15.6
LER RF klystron/cav.	2/4	4/8
LER RF volts (MV)	3.4	4.35
$\beta_y^*$ (mm)	15-25	9-10
$\beta_x^*$ (cm)	50	40-105
Emittance (x/y) (nm)	49/2	30-50/0.8
$\sigma_z$ (mm)	11	11-12
Lum hourglass factor	0.9	0.82
Crossing angle(mrad)	0	<0.05
IP Horiz. size $\Sigma$ ( $\mu\text{m}$ )	222	160
IP Vert. Size $\Sigma$ ( $\mu\text{m}$ )	6.7	6.9
HER Horizontal $\xi_x$	0.03	0.113
HER Vertical $\xi_y$	0.03	0.062
LER Horizontal $\xi_x$	0.03	0.027
LER Vertical $\xi_y$	0.03	0.047
Lumin. ( $\times 10^{33}/\text{cm}^2/\text{s}$ )	3.00	10.88
Int. Lum/month ( $\text{fb}^{-1}$ )	3.3	17.04

Total Int. Lum. ( $\text{fb}^{-1}$ )    30/year    > 375 total

The progress in integrated luminosity has come from correcting the orbits, lowering  $\beta_y^*$ , moving the fractional horizontal tunes in both rings to just above the half integer ( $\sim 0.505$ ), and trickle injection of both beams.

### RUN 5B STATUS

PEP-II [1-6] has been providing colliding beams for the BaBar detector since May 1999. The present Run 5 started in April 2005 and will end in August 2006. There will be a four month down starting August 2006 for safety checks and installation. During the recent run, colliding beams occupied 68% of the time, 25% for repairs, and 7% for machine development and accelerator physics studies. About 87% of the data logged by BaBar was on the Upsilon 4S resonance and 13% off-resonance about 40 MeV lower. The highest luminosity in PEP-II is  $10.88 \times 10^{33} / \text{cm}^2 / \text{s}$  with the corresponding parameters listed in Table 1. The horizontal beam size of the LER is enlarged at this peak luminosity by about 20%. Also, the vertical beam size of the HER is enlarged by about 15% at the peak luminosity. Both increases are due to the beam-beam effect.  $844 \text{ pb}^{-1}$  has been delivered in 24 hours. The present delivered luminosity to BaBar is over  $375 \text{ fb}^{-1}$ .

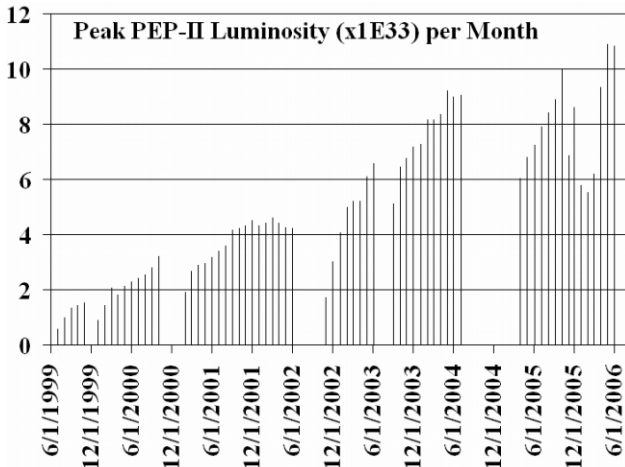


Figure 2: Peak luminosity each month since May 1999. The highest luminosity is  $1.088 \times 10^{34} / \text{cm}^2 / \text{s}$ .

### BEAM-BEAM INTERACTION

At low currents, the luminosity increases as the product of the electron and positron bunch charges. At higher currents the LER-x and HER-y beam sizes enlarge due to beam-beam and somewhat by interaction region parasitic collisions. The HER and LER bunch charges are appropriately balanced to produce near equal beam-beam effects. If there is a miss-balance, flip-flop effects can occur. The horizontal tunes of both rings were recently moved closer to the half integer ( $\sim 0.505$ ) and an increase of about 15% in luminosity occurred. In order to move the HER to the half integer, the horizontal beta beats in the HER had to be fixed. Moving close to the half integer tune makes any beta beats larger. Computer codes (MIA,

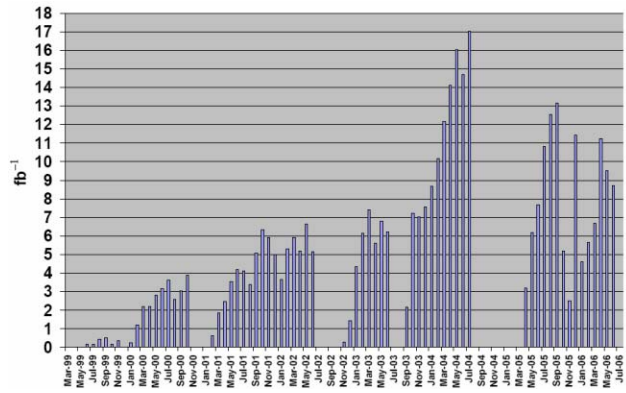


Figure 3: Integrated luminosity per month. PEP-II delivered over  $17 \text{ fb}^{-1}$  in the month of July 2004.

ORM, Phase-Advance) have been used to improve the coupling and betas in the rings. Further horizontal beta beats in both rings are under investigation.

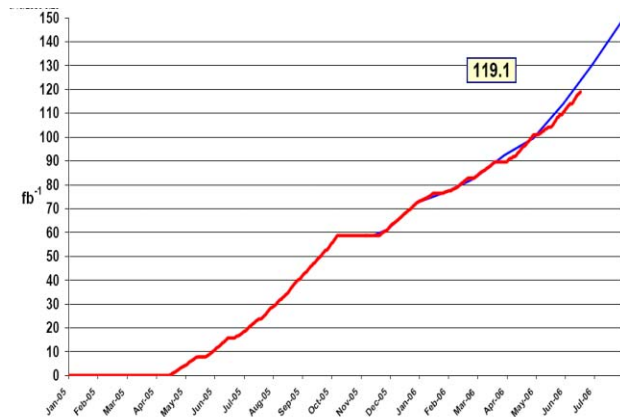


Figure 4: Delivered integrated luminosity to BaBar by PEP-II for Run 5. A total of over  $119 \text{ fb}^{-1}$  has been delivered from April 2005 to May 2006. The blue curve is the projected luminosity for this run. This projection was made in March 2006.

Since October 2003, PEP-II has operated with bunches in every two RF buckets but with mini-gaps of a few RF buckets after about 66 bunches. A plot of the bunch luminosity over the whole train is shown in Figure 6. Over the train, there are no signs of Electron Cloud Instability ECI in the positron beam. The parasitic crossing beam-beam effects are largest in the vertical plane where the vertical betas are much larger than the horizontal betas at the parasitic collisions displaced 63 cm from the IP on both sides ( $\Delta x = 3.2 \text{ mm}$ ). As the  $\beta_y^*$  is lowered the parasitic effects will become stronger but so far at most a few percent ( $< 5\%$ ) luminosity loss. In September 2004 we filled in all of the mini-gaps to get the maximum number of bunches into the rings.

Beam-beam parameters in the vertical from 0.047 to 0.062 are now routinely achieved in PEP-II that far exceed the design of 0.03.

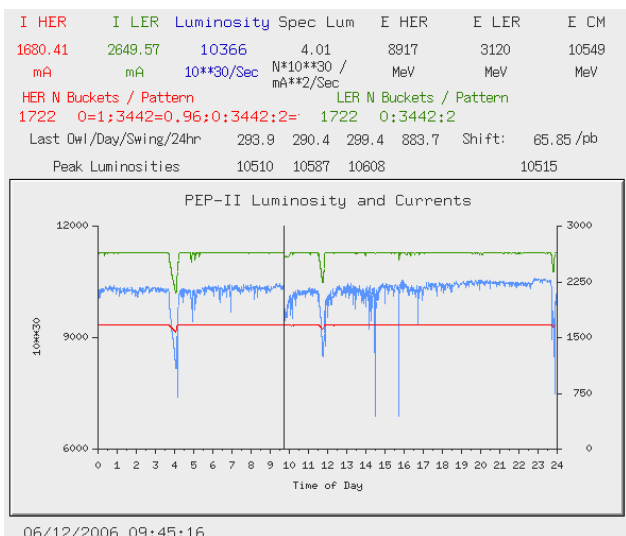


Figure 5: PEP-II’s best day showing trickle injection and 844 pb<sup>-1</sup> of integrated luminosity.

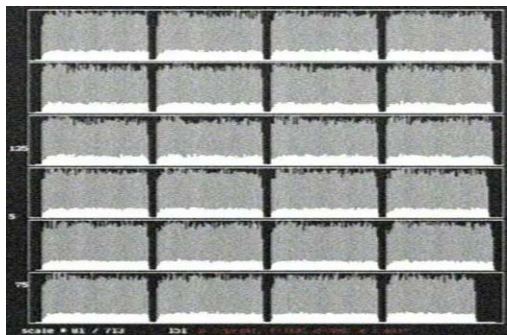


Figure 6: Bunch luminosity along the train with every 2<sup>nd</sup> RF bucket filled and a 1.8% ion gap at the end of the train. There are mini-gaps of about 12 RF buckets.

### CONTINUOUS (TRICKLE) INJECTION

Continuous injection was made to work in November 2003 when the PEP-II and BaBar teams reduced the backgrounds to an acceptable level to allow BaBar to take data continuously. The improved efficiency for data delivery was about 30% within a few days. Trickle injection for positrons uses about five injection pulses per second from the SLAC linac, resulting in the positron current being stable to about 0.1% with BaBar recording better than 98% of the data. The electron ring at PEP-II proved more difficult and studies continued until March 2004 before trickle injection was successful. About three linac pulses per second is needed to keep the electron current stable to 0.1%. Since March 2004, both PEP-II rings are trickle injected simultaneously with BaBar taking data. So PEP-II has true trickle injection with either beam injected pulse-by-pulse with very steady currents and steady luminosity, see Figure 5. The overall integrated luminosity efficiency jumped 10% with the HER ring and to just over 40% with both rings together.

### FUTURE PLANS

PEP-II has an upgrade plan that is leading towards a luminosity of greater than  $2.0 \times 10^{34}$  in FY2008.

$$L = 2.17 \times 10^{34} (1+r) \xi_y \left( \frac{EI}{\beta_y^*} \right) \text{ cm}^{-2} \text{ sec}^{-1} \quad (1)$$

with  $r$  the  $y$  to  $x$  aspect ratio ( $\sim 0.03$ ),  $E$  the beam energy,  $I$  the beam current, and  $\beta_y^*$  the vertical beta at the collision point. In order to get a factor of 2.0 above the present luminosity (to  $2.0 \times 10^{34}$ ), the currents will be raised about a factor of 1.4, the tune shifts increased about 15% and  $\beta_y^*$  reduced from 10 mm to about 8.5 mm. The number of RF stations in the HER will be increased from ten to twelve in order to achieve about 2.2 A. The LER has sufficient RF stations to store 4 A. To shorten the bunch length to reduce the hourglass effects, a lower alpha lattice will be used in HER and a higher RF voltage.

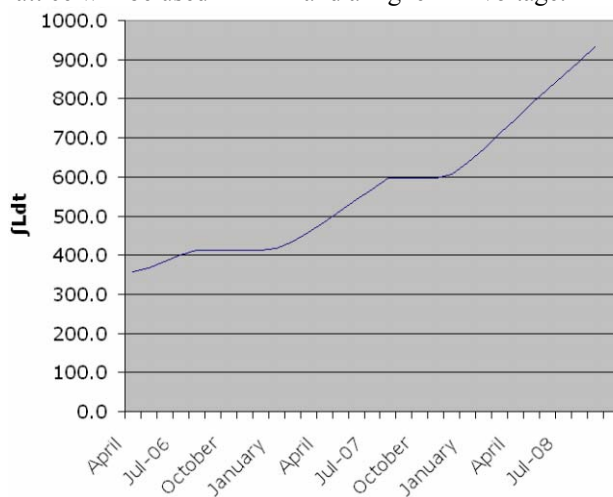


Figure 7: Projected integrated luminosity (fb<sup>-1</sup>) for PEP-II through September FY2008.

### REFERENCES

- [1] M. Sullivan *et al.*, “Anomalous High Radiation Beam Aborts in the PEP-II B-Factory,” EPAC 2006 proceedings, June 2006.
- [2] A. Bevan *et al.*, “Monitoring of Interaction-Point Parameters using 3-D Luminosity Measurements,” EPAC 2006 proceedings, June 2006.
- [3] U. Wienands *et al.*, “Tracking Down a Fast Instability in the PEP-II LER” EPAC 2006 proceedings, June 2006.
- [4] S. Weathersby *et al.*, “New HOM Water Cooled Absorber for the PEP-II B-Factory Low-Energy Ring,” EPAC 2006 proceedings, June 2006.
- [5] Y. Cai *et al.*, “Luminosity Improvement at PEP-II Based on Optics Model and Beam-Beam Simulation,” EPAC 2006 proceedings, June 2006.
- [6] Y. Cai *et al.*, “Doubling the PEP-II Luminosity in Simulations,” EPAC 2006 proceedings, June 2006.

## DESIGN OF AN ASYMMETRIC SUPER-B FACTORY\*

Y. Cai, S. Ecklund, A. Novokhatski, J. Seeman<sup>†</sup>, A. Seryi, M. Sullivan, U. Wienands,  
 SLAC, 2575 Sand Hill Road, Menlo Park, CA 94025, USA  
 M. Biagini, P. Raimondi, INFN, Frascati, Italy

### Abstract

A Super Flavor Factory, an asymmetric energy  $e^+e^-$  collider with a luminosity of order  $10^{36} \text{ cm}^{-2}\text{s}^{-1}$ , can provide a sensitive probe of new physics in the flavor sector of the Standard Model. The success of the PEP-II and KEKB asymmetric colliders [1,2] in producing unprecedented luminosity above  $10^{34} \text{ cm}^{-2}\text{s}^{-1}$  has taught us about the accelerator physics of asymmetric  $e^+e^-$  colliders in a new parameter regime. Furthermore, the success of the SLAC Linear Collider [3] and the subsequent work on the International Linear Collider [4] allow a new Super-Flavor collider to also incorporate linear collider techniques. This note describes the parameters of an asymmetric Flavor-Factory collider at a luminosity of order  $10^{36} \text{ cm}^{-2}\text{s}^{-1}$  at the  $\Upsilon(4S)$  resonance and perhaps about  $10^{35} \text{ cm}^{-2}\text{s}^{-1}$  at the  $\tau$  production threshold. Such a collider would produce an integrated luminosity of about  $10,000 \text{ fb}^{-1}$  ( $10 \text{ ab}^{-1}$ ) in a running year ( $10^7 \text{ sec}$ ) at the  $\Upsilon(4S)$  resonance.

### DESIGN FROM PAST SUCCESSES

The construction and operation of modern multi-bunch  $e^+e^-$  colliders have brought about many advances in accelerator physics in the area of high currents, complex interaction regions, high beam-beam tune shifts, high power RF systems, controlled beam instabilities, rapid injection rates, and reliable uptimes (~95%):

- 1) Colliders with asymmetric energies can work.
- 2) Beam-beam energy transparency conditions are weak.
- 3) Interaction regions with two energies can work.
- 4) IR backgrounds can be handled successfully.
- 5) High current RF systems can be operated (3 A x 1.8 A).
- 6) Beam-beam parameters can reach 0.06 to 0.09.
- 7) Injection rates are good and continuous injection is done in production.
- 8) The electron cloud effect (ECI) can be managed.
- 9) Bunch-by-bunch feedbacks at 4 nsec spacing work.

Lessons learned from SLC and subsequent linear collider studies (for ILC) and experiments (FFTB, ATF, ATF2) have also shown new successful concepts:

- A) Small horizontal and vertical emittances can be produced in a damping ring with a short damping time.
- B) Very small beam spot sizes and beta functions can be achieved at the interaction region.
- C) Bunch length compression can be performed.

### LUMINOSITY

The design of a  $10^{36} \text{ cm}^{-2}\text{s}^{-1} e^+e^-$  collider combines extensions of the design of the present  $B$  Factories and linear collider concepts to allow improved beam parameters to be achieved. The luminosity  $\mathcal{L}$  in an  $e^+e^-$  collider is given by the expression

$$L = \frac{N^+ N^- n_b f_c H_d}{4\pi \sigma_x \sigma_y} \quad (1)$$

$$\sigma = \sqrt{\beta \epsilon}$$

where  $n_b$  is the number of bunches,  $f_c$  is the frequency of collision of each bunch,  $N$  is the number of particles in the positron (+) and electron (-) bunches,  $H_d$  is the disruption enhancement factor from the collisions,  $\sigma$  is the beam size in the horizontal (x) and vertical (y) directions,  $\epsilon$  is the beam emittance and  $\beta$  is the beta function (cm) at the collision point for each plane.

### COLLIDER CONCEPTS STUDIED AT THE FIRST SUPER-B WORKSHOP

Schematic drawings of the Super-Flavor Factory as initially considered at the First Super-B workshop [5] is shown in Figure 1. A positron bunch from a 2 GeV damping ring is extracted and accelerated to 7 GeV in a superconducting (SC) linac. Simultaneously, an electron bunch is generated in a gun and accelerated in a separate SC linac to 4 GeV. The two bunches are prepared to collide in a transport line where the bunch lengths are shortened. These bunches are focused to a small spot at the collisions point and made to collide. The spent beams are returned to their respective linacs with transport lines where they return their energies to the SC accelerator. The 2 GeV positrons are returned to the damping ring to restore the low emittances. The spent electron beam is discarded. The process is repeated with the next bunch. It is expected that each bunch will collide about 120 times each second and that there will be about 10000 bunches. Thus, the collision rate is about 1.2 MHz. A small electron linac and a positron source are used to replenish lost positrons in the colliding process and natural beam lifetime. See Figure 1.

\*Supported by US DOE contract DE-AC02-76SF00515.

<sup>†</sup>seeman@slac.stanford.edu

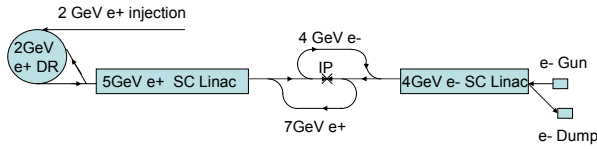


Figure 1: Former Linearly Colliding Super-F Factory

This scheme was necessary in order to save power for cooling the beams that are heavily disrupted after the collision. As shown in Fig.2, the vertical emittance growth in a single collision is about 300. Running the rings at a low energy is the only mean to bring the power requirements for the facility to the 100MW levels.

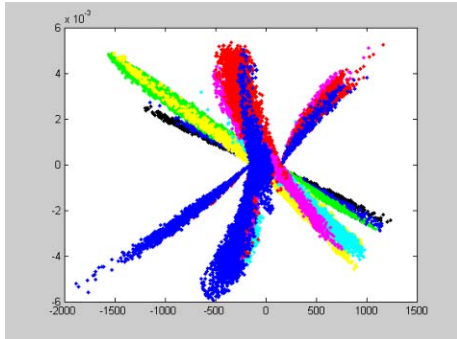


Figure 2: Plot of the  $(y, y')$  phase space after collision in the earlier design. Each color refers to one longitudinal bunch slice.

The scheme studied in [5] presents several complexities and challenging requirements for several subsystems. In particular the low energy required for the rings, in combination with the high current, low emittance, small energy spread and short bunch length, is more challenging than the already challenging solution studied for ILC.

## DESIGN PROGRESS PRESENTED AT THE SECOND SUPER-B WORKSHOP

The IP parameters have been re-optimized in order to minimize the disruption due to the beam-beam forces. The proposed values, shown in Table 1, do produce a much smaller luminosity for a single pass, but the emittance blowup for a single crossing is of the order of a few parts in  $10^3$  and, thus, only modest damping is needed between collisions. The new scheme is shown in Table 1 and Figure 3. It is possible to increase the collision frequency, and collide continuously in the ring with near ILC requirements with very small blowup. The proposed parameters in the second column for the DR are nearly the ones proposed for ILC except the number of bunches is about 4 times larger. The required Final Focus is also exactly the one designed for ILC with the energy rescaled.

## COLLISION PARAMETERS OPTIMIZATION

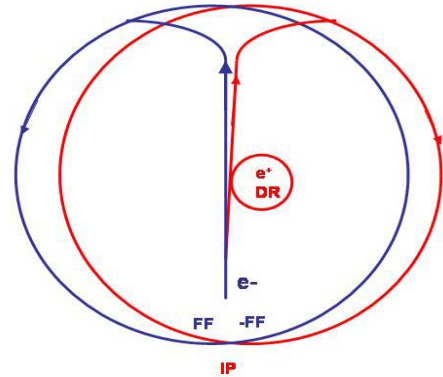


Figure 3: Super-Flavor Factory layout.

Table 1: Preliminary Super-F Factory collision parameters

	1 <sup>st</sup> LNF Workshop Best Working Point	2 <sup>nd</sup> LNF Workshop Best Working Point
$\sigma_x^*$ ( $\mu\text{m}$ )	30 (1.0 $\sigma_x$ betatron)	2.67
$\eta_x$ (mm)	1.5 LER/-1.5 HER	0.0
$\sigma_y^*$ (nm)	12.6	12.6
$\beta_x^*$ (mm)	1.25	8.9
$\beta_y^*$ (mm)	<b>0.080</b>	0.080
$\sigma_z^*$ (mm)	0.100	6.0
$\sigma_E^*$	<b><math>2 \times 10^{-2}</math></b>	$10^{-3}$
$\sigma_E$ Lum	$10^{-3}$	$0.7 \times 10^{-3}$
$\epsilon_x$ (nm)	0.8	0.8
$\epsilon_y$ (nm)	0.002	0.002
$\epsilon_z$ ( $\mu\text{m}$ )	2.0	4.0
$\theta_x$ (mrad)	Optional	$2 \times 20$
$\sigma_z$ DR (mm)	4.0	6.0
$\sigma_E$ DR	<b><math>0.5 \times 10^{-3}</math></b>	$10^{-3}$
$N_{\text{part}} (10^{10})$	<b>7.0</b>	2.0
$N_{\text{bunches}}$	12000	12000
$I$ (A)	<b>6.7</b>	1.9
$C$ DR (km)	6.0	6.0
$\tau_{x,v}$ (ms)	10	20
$N_{\text{turns bet.}}$	50	1
$f_{\text{coll}}$ (MHz)	12.0	650
$L_{\text{singleturn}} (10^{36})$	1.5	1.2
$L_{\text{multiturn}} (10^{36})$	1.1	1.0

The optimization for the “collisions in the ring” option [6] is based on the requirements to not have any need for bunch compression and acceleration. The needs to have small IP spot sizes, small beta functions and tune shifts are satisfied with the combination of small emittances and a crossing angle. The low emittances reduce the beam sizes; the second one simultaneously reduces the tune shift in both planes [7] and the longitudinal overlapping region. Since the interaction region now is short, it is

possible to decrease the vertical beta to very small values, further decreasing the vertical size and tune shift. In addition, further minimization of the beam-beam nonlinearities can be performed [8] with a crab waist, to greatly reduce the residual emittance blowup due to the crossing angle.

Beam-beam studies have been performed with the “GuineaPig” computer code by D. Schulte (CERN) [6, 9], which includes backgrounds calculations, pinch effect, kink instability, quantum effects, energy loss, and luminosity spectrum. The beams are tracked through the ring similarly to what is done in [10], and the emittances and luminosity are evaluated after equilibrium is reached. Fig.4 shows an example of such tracking.

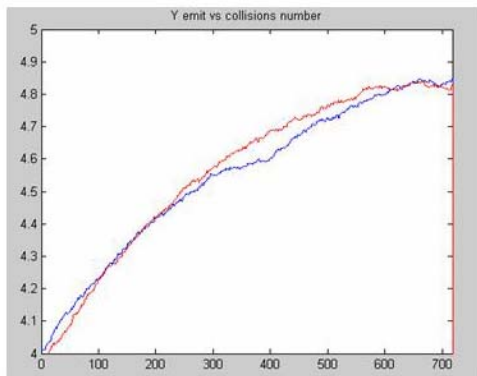


Figure 4: Vertical emittance vs turn number.

### INTERACTION REGION PARAMETERS

The interaction region is being designed to leave about the same longitudinal free space as that presently used by *BABAR* but with superconducting quadrupole doublets as close to the interaction region as possible [11].

A preliminary design of the Final Focus, similar to the NLC/ILC ones, has been performed for the IP parameters in Table 1, second column. The total FF length is about 70 m and the final doublet is at 0.5m from the IP. A plot of the optical functions in the incoming half of the FF region is presented in Fig. 5. The need for a finite crossing angle at the IP greatly simplifies the IR design (Fig. 6), since the two beams are now naturally separated at the parasitic collisions.

### POWER REQUIREMENTS

The power required by this collider is the sum of magnet and the accelerator operation. The present estimates indicate about 45 MW for the ring RF, 10 MW for the linac, and 10 MW for the ring magnets for 65 MW total.

### SYNERGY WITH ILC

There are many similarities between this linear Super-B collider and the ILC. The project described here will capitalize on R&D projects that have been concluded or are on-going within the ILC collaboration. The damping ring and interaction region designs between the two projects are very similar.

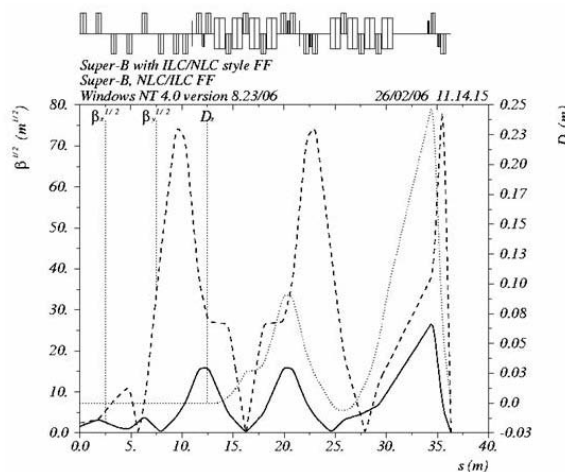


Figure 5: Optical functions in half Final Focus region.

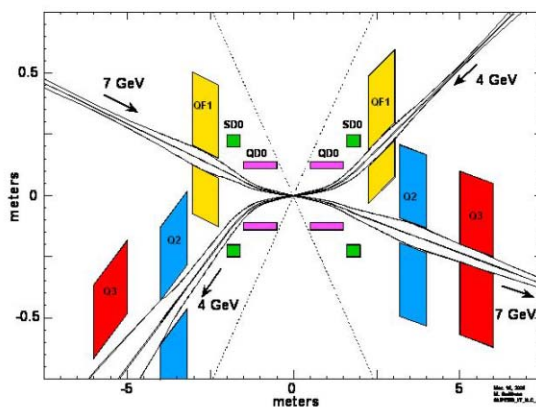


Figure 6: Plan view of a possible IR layout.

### REFERENCES

- [1] PEP-II Status report PAC 2005 Knoxville, TN.
- [2] KEKB Status report PAC 2005 Knoxville, TN.
- [3] The SLC Design Handbook, SLAC November 1984.
- [4] International Linear Collider Technical Review Committee, Second Report 2003, ICFA SLAC-R-606.
- [5] First LNF Workshop on SuperB, Frascati, Nov. 2005, <http://www.lnf.infn.it/conference/superbf05/>.
- [6] M. Biagini *et al.*, “Beam-Beam Simulations for a Single Pass Super-B Factory,” EPAC 2006 proceedings, June 2006.
- [7] D. Shatilov, M. Zobov, “Tune shift in Beam-Beam collisions with an arbitrary crossing angle”, DAΦNE Tech. Note G-59, May 1003.
- [8] P. Raimondi, 2<sup>nd</sup> LNF Workshop on Super-F, Frascati, 16-18 March 2006, <http://www.lnf.infn.it/conference/superbf06/>
- [9] D. Schulte, “Study of electromagnetic and hadronic background in the Interaction Region of the TESLA Collider”, PhD Thesis, Hamburg, 1996.
- [10] Y. Cai, A. Chao, S. Tzenov, “Simulation of the bb effects in e<sup>+</sup>e<sup>-</sup> storage ring with a method of reduced region of mesh”, PRST, AB, Vol.4, 2001.
- [11] M. Sullivan, LNF Workshop on Super-F, Frascati, 16-18 March 2006.

# DESIGN OF A STRIP-LINE EXTRACTION KICKER FOR CTF3 COMBINER RING \*

I. Rodríguez<sup>#</sup>, L. García-Tabarés, F. Toral, CIEMAT, Madrid, Spain  
A. Ghigo, F. Marcellini, INFN, Frascati, Italy.

## Abstract

The new CLIC test facility (CTF3) is the latest stage to prove the technical feasibility of the CLIC project. An extraction kicker is necessary for the combiner ring, and it will be a strip-line type device due to lower coupling impedances and straightforward fabrication. The field uniformity together with a correct beam dynamics are the most challenging issues of this design. The main parameters of the kicker are analytically calculated using standard analytic formulae. The numeric modelling and simulation of several possible straight sections are reported, and the characteristic impedance is matched with the 50 Ω load. The field homogeneity, the kick angle and the scattering parameters are calculated in a 3D finite element model. Several manufacturing issues for the first prototype are also outlined.

## KICKER DESCRIPTION

Strip-line kickers consist of two long metallic parallel plates fed at the ends by two coaxial feedthroughs and generally supported by several insulators inside a beam pipe. The structure is similar to a pair of strip-lines where each electrode forms with a half beam pipe a transmission line of characteristic impedance  $Z_c = 50 \Omega$ . The characteristic impedance of the coaxial input and output ports must be matched with the load to avoid any reflection of the input power.

Table 1: Kicker and pulsed power supply specifications

MAGNITUDE	VALUE	UNITS
Max. Beam Energy	<b>300</b>	MeV
Deflection Angle	<b>8</b>	mrاد
Transverse voltage $V_{\perp}$	<b>2.4</b>	MV
Rise/Fall-times (0-100%)	$\leq 70$	ns
Pulse length (max.)	<b>200</b>	ns
Flat-top reproducibility	$\pm 0.1$	%
Flat-top stability (incl. droop)	$\pm 0.25$	%
Repetition rate(Initial-Nominal)	<b>5-50</b>	Hz
Available length	<b>2000</b>	mm
Vertical aperture	$\geq 40$	mm
Horizontal aperture	$\geq 40$	mm
Field homogeneity area ( $< \pm 1\%$ )	<b>30</b>	mm

In order to generate a transverse kick, the kicker should be driven in differential mode, creating a TEM wave that exerts a combined Lorentz force over the charged particles.

As the particles are relativistic and in TEM propagation modes the modulus of  $E$  is related with  $B$  by the speed of light, the electric and magnetic components of the Lorentz force are identical.

Table 1 shows the latest specifications released by CTF3 team. Some of them are for the pulsed power supply, which is also strongly linked to the kicker.

## STRAIGHT SECTION DESIGN

Four possible straight sections have been considered to start with the design of the kicker. The characteristic impedance of each one has been calculated and optimized to 50 Ω with HFSS code [1] (see figs. 1 and 2). Lossless materials are used because the characteristic impedance is a geometrical parameter in vacuum working conditions.

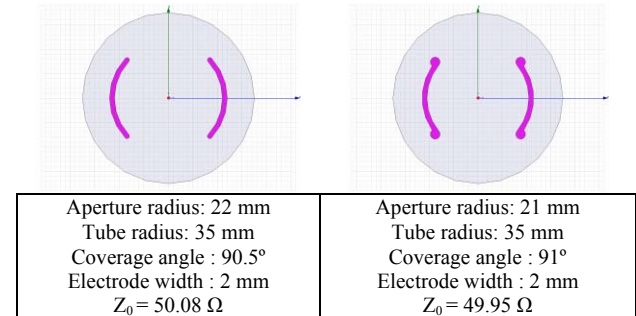


Figure 1: Circular straight sections

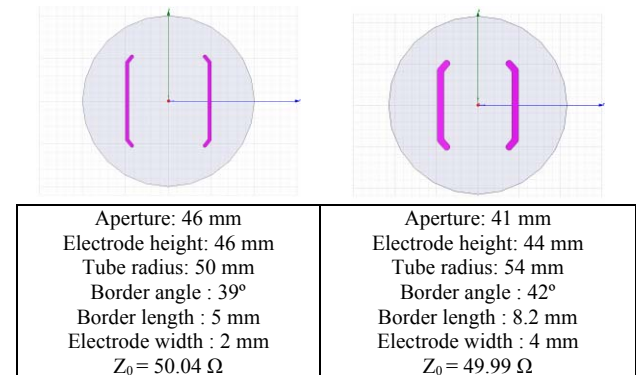


Figure 2: Planar straight sections

The fourth straight section yields the best field homogeneity due to the planar electrodes and the optimization of final edges. Also the mechanical stiffness of the electrodes is enhanced by the final edges.

\*Work supported by Spanish Ministry of Education and Science under project FPA2004-20954-E

<sup>#</sup>iker.rodriiguez@ciemat.es

## ANALYTICAL CALCULATIONS

Assuming a constant force along the kicker, the increment of speed and momentum necessary to deflect a 300 MeV particle, arriving only with longitudinal speed, is given by:

$$\Delta v_{\perp} = v \cdot \tan \alpha = 2.99792 \cdot 10^8 \cdot \tan(0.008) = 2.398 \cdot 10^6 \frac{\text{m}}{\text{s}}$$

$$\Delta p_{\perp} = m \cdot \Delta v_{\perp} = (m_c + m_0) \cdot \Delta v_{\perp} = 1.282654 \cdot 10^{-21} \frac{\text{kg} \cdot \text{m}}{\text{s}}$$

The transverse voltage  $V_{\perp}$  is a characteristic magnitude of a transverse kicker that measures the normal component of the Lorentz force over the particle.  $V_{\perp}$  is defined as the integral of that force along the beam axis  $Z$ .

$$V_{\perp} = \int_0^l (\vec{E} + \vec{v} \times \vec{B})_{\perp} dz$$

That integral can only be calculated by means of numerical simulations. But the transverse voltage can also be calculated by using the relativistic momentum increment [2]:

$$V_{\perp} = \frac{\beta \cdot c \cdot \Delta p_{\perp}}{q} = 2.400044261 \cdot 10^6 \text{ V}$$

The efficiency of the kicker can be measured by the transverse shunt impedance  $R'_s$ , which relates the transverse voltage (strength) with the input power  $P$ . The definition for sinusoidal excitation is:

$$R'_s = \frac{V_{\perp}^2}{2 \cdot P}$$

As the input power is not yet known, a definition for a strip-line transverse kicker powered in differential mode can be used [2], based on geometrical parameters:

$$R'_s = 2 \cdot Z_c \cdot \left( \frac{\tanh[\pi \cdot \omega / (2 \cdot h)]}{k \cdot h} \right)^2 \cdot \sin^2(k \cdot l) \quad (1)$$

where  $k = \omega / c$ ,  $h$  is the half aperture and  $l$  is the electrode length. For the selected straight section,  $h$  is 0.0205 m and the electrode length is 1.7 m.

The transverse shunt impedance variation with frequency is depicted in figure 3. First zeroes of  $R'_s$  appear at 88.17 MHz and at 176.35 MHz. Those points will be repeated periodically each 88.17 MHz (roughly  $c/2l$ ) and will show the possible resonant frequencies of the device.

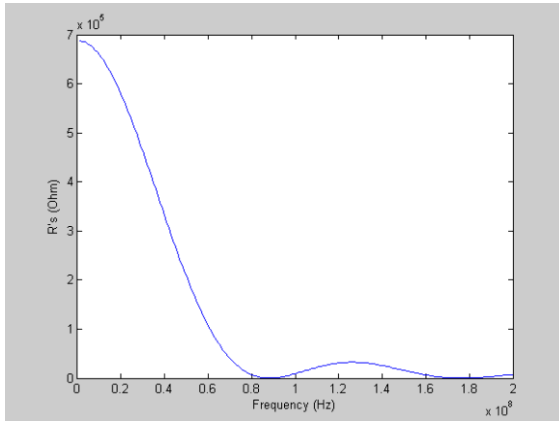


Figure 3: Transverse shunt impedance

Taking into account that the pulse flat-top length is 200 ns and the kicker electrodes are 1.7 m long, the calculations should be done as for a DC pulse. From Eq. 1:

$$R'_{sDC} = \lim_{f \rightarrow 0} (R'_s) = 2 \cdot Z_c \cdot \left( \frac{l}{h} \right)^2 = 687686 \Omega$$

Therefore, input power DC pulse excitation for 2 electrodes should be calculated as:

$$P_{DC} = \frac{V_{\perp}^2}{R'_{sDC}} = \frac{(2.400044261 \cdot 10^6)^2}{687686} = 8.37627 \text{ MW}$$

This value is, consequently, one half for one electrode:  $P_{1DC} = 4.188135 \text{ MW}$ . With this power, it is possible to calculate the pulse voltage necessary for one electrode and the peak current that appears on each strip-line:

$$V_{kDC} = \sqrt{P_{1DC} \cdot Z_c} = 14471 \text{ V} \quad I_{kDC} = \frac{V_{kDC}}{Z_c} = 289.42 \text{ A}$$

If the maximum repetition rate is 50 Hz, the averaged time power demanded from the power supply is:

$$P_{avg} = \text{Duty} \cdot P_{peak} = \frac{200}{20 \cdot 10^6} \cdot 8.376 \cdot 10^6 = 83.7 \text{ W}$$

## NUMERICAL SIMULATIONS

### Field homogeneity

For field homogeneity calculations, a fine 2D meshed sheet has been used in HFSS, although Ansys and Superfish 2D straight sections have also been modelled and simulated using an electrostatics solver for cross-checking. The homogeneity does not depend on the input power, as the problem is linear. For the circular straight section, the calculated homogeneity is  $\pm 15\%$  within a 15mm radius, far away from the specifications. The planar electrodes straight section (with square aperture) calculated homogeneity is  $\pm 3\%$ . Finally, rectangular aperture has fulfilled the specifications with homogeneity of  $\pm 0.74\%$ .

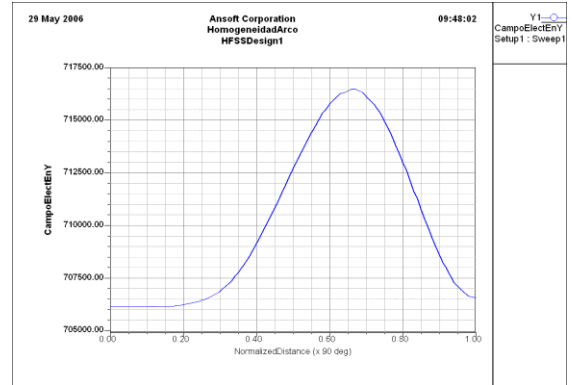


Figure 4: Transverse E field in a 15 mm arc quadrant

### Full field solution

For the analysis of high order modes and the longitudinal impedance, a full 3D kicker model has been developed in HFSS (see fig. 5). This model has been simulated at 2.5 MHz, which is the main harmonic of a typical 200 ns flat pulse with 70 ns rise/fall time, so a full field solution is available.

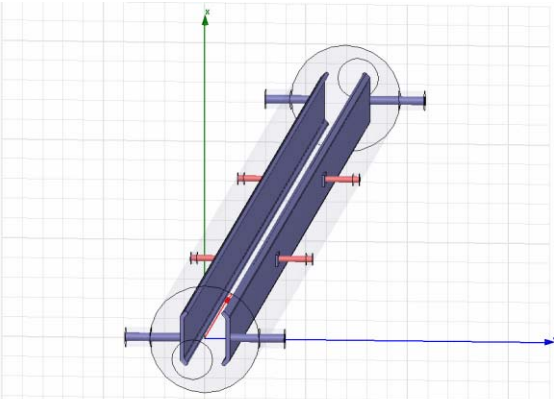


Figure 5: HFSS 3D kicker model (rectangular aperture)

Calculation of the 3D homogeneity is done for the integrated electric field  $E_y$  along the kicker. The obtained value is  $\pm 0.69\%$  for the rectangular aperture straight section. The electric field map in the middle plane of the kicker is shown in figure 6.

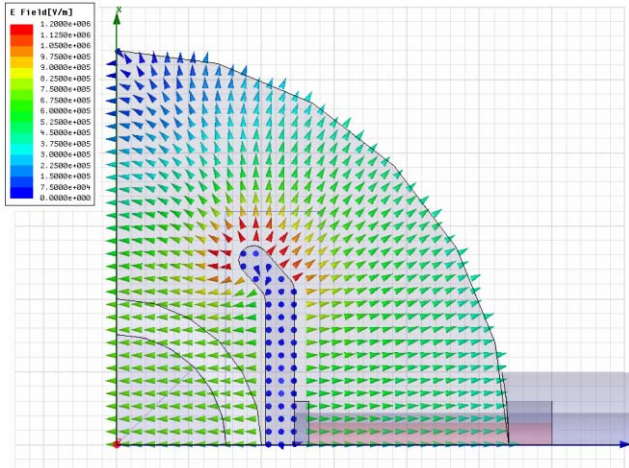


Figure 6: Electric field in rectangular aperture kicker

Electrodes voltage and current, besides the transverse voltage, have been numerically calculated [1] and they perfectly agree with the analytical results:

$$V = \int_0^l \vec{E} \cdot d\vec{l} = 14513 \text{ V} \quad I = \oint_c \vec{H} \cdot d\vec{l} = 290.4 \text{ A}$$

$$V_{\perp} = \int_0^l (\vec{E} + \vec{v} \times \vec{B})_{\perp} dz = 2418789 \text{ V}$$

Figure 7 shows the electric field  $E_y$  distribution shifting X and Z coordinates (plane  $Y=0$ ). The top is very flat.

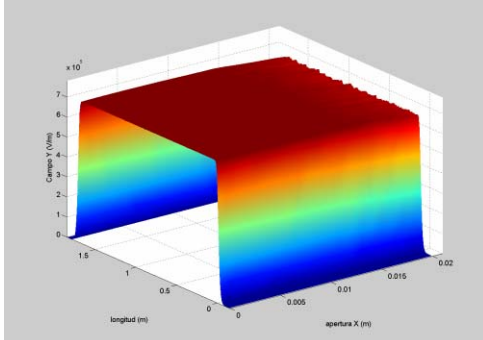


Figure 7: Electric field distribution in plane  $Y=0$

### Scattering parameters

Figure 8 shows a frequency sweep of  $S_{11}$  parameter [3]. Its value is 0.00174 at 2.5 MHz, what means that only  $|S_{11}|^2 = 3.036 \times 10^{-4} \%$  of the input power reflects to the input port at that frequency [4]. It is worth to notice that reflection is negligible in the operating bandwidth (0 to 50 MHz), with a reflected power less than 0.03 %.

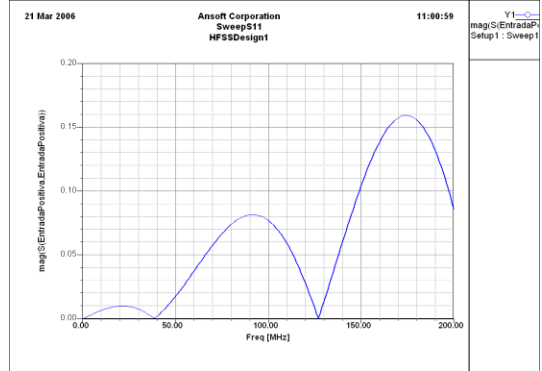


Figure 8: Reflection frequency response at inputs ( $S_{11}$ )

## FABRICATION

A first prototype of the kicker will be constructed based on this design. Concerning fabrication, several considerations have to be taken into account:

- The electrodes and the kicker tube will be made of stainless steel because of the high length of the device, so fewer stand-offs are necessary. The increment of the broadband impedance compared to aluminium is not critical. Stand-offs will be ceramic.
- The power feedthroughs and the mechanical stand-offs will slide over the electrodes to avoid thermal stress caused by differential thermal contractions. There will be only one fixed point on each electrode.
- The tapered ends will be fabricated with the higher possible length to decrease the wakefields effects.

## CONCLUSION

The technical design and analysis of the CTF3 strip-line kicker is presented. Analytical results match perfectly with numerical simulations and all the specifications are fulfilled. Longitudinal impedances, damping and HOMs in the kicker are to be presented in the near future.

## REFERENCES

- [1] ANSOFT Corporation “ANSOFT HFSS Fields Calculator Cookbook”, (2000), www.ansoft.com
- [2] D.A. Goldberg and G.R. Lambertson, “Dynamic Devices, a Primer on Pickups and Kickers”, Lawrence Berkeley Laboratory California, American Institute of Physics (1992).
- [3] A. Gallo, A. Ghigo, F. Marcellini, M. Serio, B. Spataro, M. Zobov, “The Transverse Feedback Kicker”, DAFNE Technical Note, INFN-LNF Accelerator Division (1995).
- [4] JUAS RF Course 2006 notes. F. Caspers, T. Kroyer, February 2006.

## COMMISSIONING STATUS OF THE CTF3 DELAY LOOP

R. Corsini, S. Döbert, F. Tecker, P. Urschütz, CERN, Geneva, Switzerland  
 D. Alesini, C. Biscari, B. Buonomo, A. Ghigo, F. Marcellini, B. Preger, M. Serio, A. Stella,  
 INFN/LNF, Frascati, Italy

### Abstract

The CLIC Test Facility CTF3, built at CERN by an international collaboration, aims at demonstrating the feasibility of the CLIC scheme of multi-TeV electron-positron linear collider by 2010. In particular, one of the main goals is to study the generation of high-current electron pulses by interleaving bunch trains in delay lines and rings using transverse RF deflectors. This will be done in the 42 m long delay loop, built under the responsibility of INFN/LNF, and the 84 m long combiner ring that will follow it. The delay loop installation was completed and its commissioning started at the end of 2005. In this paper the commissioning results are presented, including the first tests of beam recombination.

### INTRODUCTION

The aim of the CLIC (Compact Linear Collider) Study is to investigate the feasibility of a high luminosity, multi-TeV linear  $e^+ e^-$  collider [1]. In order to limit the total length, CLIC employs normal-conducting accelerating structures operating at a very high gradient (150 MV/m), and powered by 30 GHz RF pulses with a peak power of 150 MW. Since conventional RF sources cannot provide such pulses, CLIC is based upon a two-beam-acceleration concept [2], in which a high current electron beam (drive beam) runs parallel to the main beam and is decelerated to produce the RF power. The generation of the high-intensity drive beam pulses with the right time structure is one of the main challenges in CLIC. Initially, a long pulse is accelerated using a low frequency normal-conducting linac. Funnelling techniques in delay lines and rings are then used to give the beam the desired structure while increasing its intensity. In this process the electron bunches are interleaved by the use of transverse RF deflectors. The bunch spacing is thus reduced and the beam current is increased.

It is generally accepted that CLIC technology is the only path to multi-TeV colliders. However, several critical issues still need to be addressed. The experimental program of the new CLIC Test Facility (CTF3) tackles the main issues, i.e., the generation and use of the drive beam and the testing of 30 GHz structures and components, with the goal of demonstrating the CLIC feasibility before 2010, when the first LHC results should be available.

CTF3 [3] is presently being built and commissioned at CERN by an international collaboration, including Ankara and Gazi Universities (Turkey), BINP (Novosibirsk), Helsinki Institute of Physics, IAP (Nizhny Novgorod), CIEMAT (Spain), DAPNIA (Saclay), Finnish industry, INFN-LNF (Frascati), JINR (Dubna), LAL (Orsay), North-Western University of Illinois, RAL (Oxford), SLAC (Stanford) and Uppsala University (Sweden).

The facility is located in the buildings of the former LEP pre-injector complex, whose hardware is partly re-used, and is designed to work at a lower beam current and a lower energy than the CLIC drive beam (3.5 A instead of 5.7 A and 150 MeV instead of 2.4 GeV). In its final configuration it will include a 70 m long drive-beam linac followed by two rings, where the beam manipulations will be carried out: a 42 m delay loop and an 84 m combiner ring. After such manipulations the drive beam will have a current of 35 A and will be transported to an experimental area to produce 30 GHz RF power for structure tests. In the same area, another linac will provide a main beam for a CLIC two-beam module [4] and a test decelerator will be used for drive beam stability studies [5]. CTF3 also has a second 30 GHz RF power station (halfway along the linac) working at a lower drive beam current.

In 2003-2004 the injector, linac, the mid-linac power station and an end-of-linac magnetic chicane with variable momentum compaction were installed and commissioned. The installation of the delay loop, under full responsibility of INFN-LNF, was completed during 2005 (see Fig. 1). The loop has a two-fold symmetry, with double injection/extraction septa, 10 bending magnets and 10 independent quadrupole families. It includes an RF deflector used for injection (as described later) and a wiggler employed to tune its path length. INFN provided sextupoles, correctors, the wiggler, the vacuum system, the 1.5 GHz RF deflector, waveguides and some beam diagnostics. CERN provided the dipoles, quadrupoles, power converters, the septa, controls, the 1.5 GHz RF system, vacuum pumps and infrastructure (cabling, alignment, water, installation support).

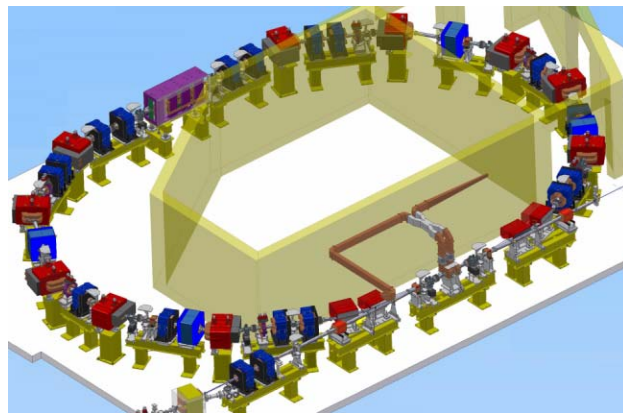


Figure 1: Delay loop layout. The beam comes from the bottom left corner. Septa and dipoles are red, quadrupoles appear in blue. Also visible are the waveguide network feeding the deflector (bottom right) and, on the opposite side, the wiggler (violet).

## THE RECOMBINATION PROCESS

The role of the delay loop in CTF3 is to sub-divide the 3.5 A, 1.4  $\mu$ s long beam-pulse accelerated in the drive-beam linac into five 140 ns long pulses, separated by 140 ns “holes”, increasing at the same time both the initial current and the bunch repetition frequency by a factor 2.

The procedure is schematized in Fig. 2 and described in the following. The incoming pulse is composed by ten 140 ns long sub-pulses, in which bunches occupy either even or odd 3 GHz RF buckets. Such time structure is obtained in the injector, where three sub-harmonic buncher (SHB) cavities at 1.5 GHz are followed by a 3 GHz bunching system composed of a single-cell standing-wave pre-buncher and a graded- $\beta$  travelling-wave buncher. The sub-harmonic cavities and their sources are wide-band systems and allow a fast switching of the RF by 180° [4]. When they are powered, only one every second 3 GHz buckets is populated (apart from a small fraction of the charge, captured in parasitic “satellite” bunches). The sub-pulses can then be easily “phase coded”, putting the main bunches in odd or even buckets. The phase switch can be repeated several times as needed and is very fast, of the order of 5-6 ns [4]. A transverse RF deflector working at 1.5 GHz sends the first sub-pulse (labelled as even RF buckets in the figure) into the delay loop. The loop length of 42 m corresponds to the sub-pulse length of 140 ns, thus the “even” bunches are coming back at the deflector at the same time as the “odd” bunches of the next sub-pulse from the linac. The delay loop length is precisely tuned to be an integer number of the RF wavelength, therefore odd and even bunches arrive with opposite phases and receive opposite kicks.

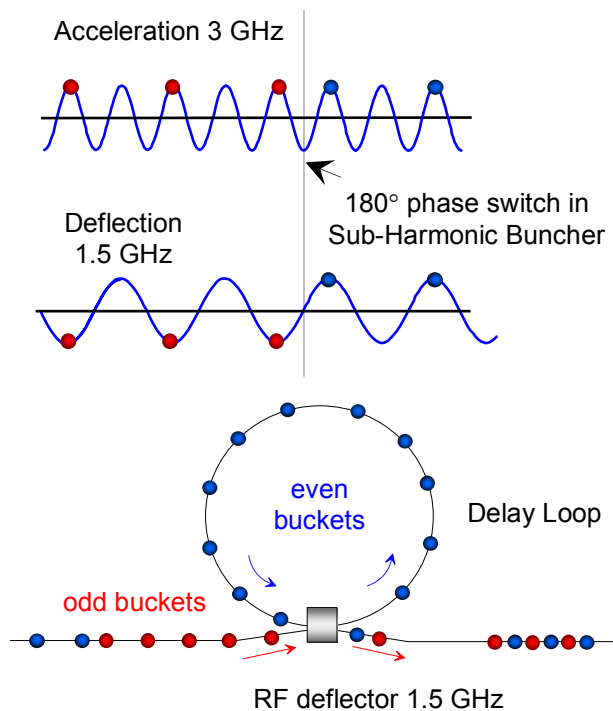


Figure 2: Schematic of the delay loop recombination.

However, since their incoming angles are also opposite, they are interleaved and combined into the same orbit. The process also naturally produces a gap of 140 ns, which is essential for clean extraction by a kicker in the next combiner ring stage. The bunch spacing is now 10 cm and the current of the train is doubled.

It should be noted that, in alternative of the RF deflector, two small horizontal dipoles located close to it can be used to kick the beam in and out of the delay loop. Of course in such a magnetic injection configuration (essentially used for setting-up during commissioning), the whole beam is sent either around the loop or straight past it and no re-combination is possible.

## DELAY LOOP COMMISSIONING

### *The 2005 run*

Beam commissioning of the delay loop started in November 2005. The beam-time available was only about 3 weeks and operation was hampered by the fact that, due to delays in the delivery of components, only one SHB cavity out of three and 6 beam position monitors (BPM) out of 17 were available. In spite of that, a circulating beam was obtained in a very short time, first using magnetic injection, as described above, and then RF injection. The delay loop optics used was relaxed with respect to the nominal isochronous one, which implies relative strong focusing. Initially the SHB system was turned off, and the beam was bunched at 3 GHz, but in the last few days of the run the one available SHB cavity was put in operation, together with the fast phase switch control, and a first re-combination test could be performed. Beam current and pulse length in the linac were limited in this period to less than 1 A and 300 ns for radiation safety, in order to allow access during operation to the klystron gallery located on top of the building, even in case of large losses in the delay loop. Therefore the re-combination yielded a single 140 ns pulse, with slightly more than 1 A beam current. During these tests, a detailed setting-up procedure was developed and validated, starting with magnetic injection and following several steps to determine experimentally the optimum power and phase in the RF deflector. A bunch length measurement test using the same deflector was also performed. In such a test, the beam was sent straight past the delay loop using the small dipoles, and the RF deflector was powered and phased such that the beam arrived at the RF zero crossing. The head and the tail of each bunch were then kicked in opposite directions, and the subsequent increase of the beam size, observed in a downstream optical transition screen, was used to determine the bunch length, showing a resolution of the order of a picosecond.

### *The 2006 run*

Commissioning continued from March to May 2006, for a total of about 8 weeks. In the meanwhile, two additional BPMs were installed. Current and pulse length were not limited any more, since access to the klystron gallery was controlled, and the nominal values (3.5 A,

1.5  $\mu$ s) were used in the linac, for a final momentum of 100 MeV/c. The nominal isochronous optics was implemented in the delay loop, and the available beam-time was sufficient to perform systematic optics measurements. Transverse beam properties (emittance and Twiss parameters) at the entrance of the delay loop were determined through quadrupole scans [5], and the dispersion function at the position of the delay loop BPMs was measured as well. This was done by scaling up and down the current of all delay loop magnets and recording the corresponding beam position. The orbit difference, normalized to the relative magnet scaling, is then equal to the dispersion function. Such a measurement was indeed very useful, since a comparison with the model of the first data allowed to identify a calibration error of about 20 % in three quadrupole families. Once the calibration was corrected, a reasonable agreement was found (see Fig. 3). The slight asymmetry in the model prediction reflects a small energy mismatch, identified after the measurement.

As mentioned before, the beam time-of-flight in the delay loop must be precisely equal to an integer number of RF deflector periods. The delay loop wiggler is indeed used to tune the path length accordingly. This is done experimentally as follows: the beam is sent straight past the loop and its phase measured using an RF pick-up, in which the beam induced signal at 3 GHz is mixed with a reference. The beam is then sent around the loop, with the wiggler off. The phase difference is measured, the wiggler is turned on and its current adjusted. A phase difference of 10° (5° at 1.5 GHz) was measured with the wiggler off and compensated with a wiggler current of about 50 A.

Synchrotron light ports built in the vacuum chambers of two dipoles were used, together with a streak camera, to check the beam time structure. The bunch length was also measured for two different settings of the upstream chicane. The measured values ( $\sigma_z = 4.5$  and 9 ps for momentum compaction  $R_{56} = 0.22$  and 0.45, respectively),

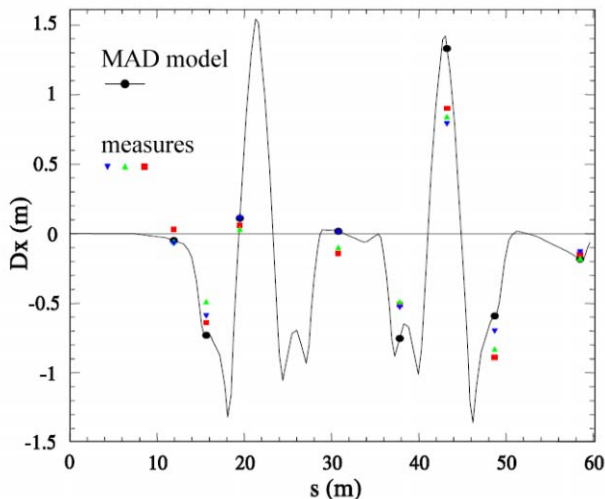


Figure 3: Values of the horizontal dispersion function at 8 BPMs inside and around the delay loop, obtained from three measurements (coloured symbols) and compared with the MAD model prediction (line with black dots).

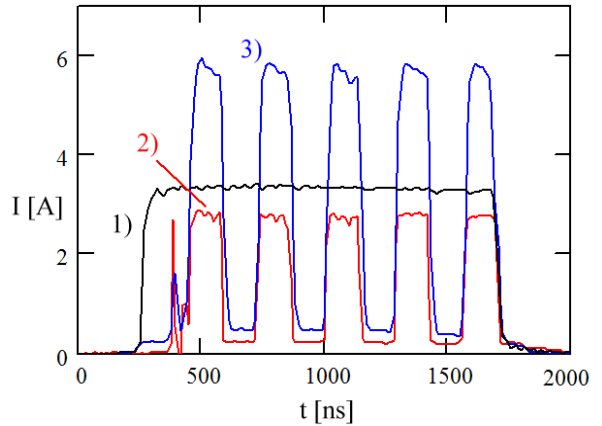


Figure 4: Beam current as a function of time, measured: 1) before the delay loop 2) in the loop 3) after the loop, showing the final recombination in five 140 ns pulses.

were consistent with expectations.

The final beam re-combination is shown in Fig. 4. The 1.5  $\mu$ s, 3.3 A incoming pulse is converted in a series of five 140 ns pulses with a current of 5.8 A. About 8.5 % of the initial current is contained in “satellite” bunches, as expected from simulations [4]. This fraction of the beam is not combined in the main pulses, as shown in Fig. 4, where it can be seen in the space between them.

## CONCLUSIONS

The CTF3 delay loop commissioning started in November 2005 and has been essentially completed in May 2006, when a recombination of five 140 ns long pulses with a current close to the nominal value was successfully obtained. Several beam dynamics and optics measurements were performed, in good agreement with simulations. Further studies will take place in the next running period, to confirm and extend the first data.

## REFERENCES

- [1] G. Guignard (Ed.), “A 3 TeV e+e- linear collider based on CLIC technology”, CERN 2000-008, 2000.
- [2] R. Corsini (Ed.), “The CLIC RF power source”, CERN 99-06, 1999.
- [3] G. Geschonke and A. Ghigo Eds, “CTF3 Design Report”, CERN/PS 2002-008 (RF).
- [4] T. Ekelöf, M. Johnson, V. Ziemann, H. Braun, S. Döbert, G. Geschonke, J. Sladen, W. Wuensch, “The Two-Beam Test-Stand in CTF3”, these Proceedings.
- [5] S. Döbert, G. Rumolo, D. Schulte, I. Syratchev, D. Carrillo, “Progress on the CTF3 Test Beam Line”, these Proceedings.
- [6] P. Urschütz, H. Braun, R. Corsini, S. Döbert, T. Lefevre, G. McMonagle, J. Mourier, J. Sladen, F. Tecker, L.Thorndahl, C. Welsch, “Beam Dynamics and First Operation of the Sub-Harmonic Bunching System in the CTF3 Injector”, these Proceedings.
- [7] P. Urschütz, H. Braun, R. Corsini, S. Döbert, F. Tecker, A. Ferrari, “Beam Dynamics Studies and Emittance optimization in the CTF3 Linac at CERN”, these Proceedings.

# THE DAΦNE BEAM TEST FACILITY: FROM 1 TO 10 MILLIARDS OF PARTICLES

G. Mazzitelli, B. Buonomo, L. Quintieri, INFN/LNF, Frascati, Italy  
P. Valente, INFN-Roma1, Roma, Italy

## Abstract

The DAΦNE Beam Test Facility is operating since 2002, providing electrons, positrons and photons from the single particle up to  $10^{10}$  particles per spill and from 25 to 750 MeV. During these years, the facility has hosted tens of high energy physics test and experiments from all over Europe, operating in very different conditions of multiplicity and energy. Operation performance and parameters, tools and diagnostics, as well as the main results obtained, are presented.

## INTRODUCTION

The Beam Test Facility (BTF) started operation at the Frascati National Laboratory (LNF) of the INFN in October 2002; it is a part of the DAΦNE accelerator complex, a double ring electron-positron collider, optimised for the production of the Phi meson, at the centre of mass energy of 1019.2 MeV. Its injector, a high current electron/positron linear accelerator, can alternatively inject beams into the accumulator ring (and from there into the DAΦNE main rings), or provide beam to the BTF area [1]. The main applications of the facility are: high energy detector calibration, low energy calorimetry, low energy electromagnetic interaction studies, detector efficiency and aging measurements, test of beam diagnostic devices, etc. The beam line has been optimised in order to provide 49 pulses/sec of 1 or 10 ns duration and with a number of particles ranging from a single electron or positron per pulse up to DAΦNE LINAC maximum current, equivalent to  $10^{10}$  particles/pulse. The energy can be adjusted between 25 MeV and 750 MeV.

Since the end of 2005 a photon tagging system has been installed and started operation with the first users.

## THE FACILITY

The DAΦNE LINAC provides a beam with energy up to 800 MeV for the electrons, with a maximum current of 500 mA, and 550 MeV for the positrons, with a maximum current of 100 mA. The pulse time width can be 10 ns or 1 ns, while the maximum repetition frequency is tunable from fractions of Hz to 50 Hz [2].

The injector system provides beam both to the DAΦNE damping ring and to the test beam area. A 3 degree pulsed magnet injects all the available LINAC bunches in the BTF transfer line, where they are manipulated in order to tune multiplicity and energy required by users.

The minimum LINAC beam current that can be conveniently detected by the DAΦNE current monitors is  $I \approx 1$  mA, and the corresponding number of electrons (positrons) is  $10^7$ /pulse.

In order to tune the beam intensity down to a single electron per bunch, it is necessary to strongly reduce the number of particles. The reduction is obtained by strongly increasing the beam energy spread by means of a removable copper target intercepting the primary LINAC beam: three different thickness values can be selected corresponding to 1.7, 2.0, 2.3 radiation lengths. The emerging particles are then selected by a couple of collimators, which reduce the beam divergence at the entrance of the energy selector system, consisting of a bending magnet and a second slit system. This allows selecting the momentum with a resolution better than 1%.

After the energy selector, the beam is driven by a 12 m transfer line into the experimental hall by means of a focusing system of four quadrupoles. The BTF transfer line includes a complete diagnostic set including: 2 beam wall current monitors, 2 fluorescent targets and 2 horizontal and vertical correctors, which can be used to optimally set the beam transport. At the end of the BTF line a second bending magnet allows to use two separate beam-lines alternatively: a straight line is used when the magnet is off, while particles exit from a 45 degrees curved line when the magnetic field is properly set.



Figure 1: The BTF experimental hall.

A 100m<sup>2</sup> area (shown in Fig. 1) is available for hosting experiment, fully equipped with diagnostic system [3,4], Data Acquisition system, High Voltage power supply, scope, network, crates, etc\*. A dedicated control room (shown in Fig. 2) with consoles for beam controls, PCs, network and cabling of different type with the experimental hall is also available, within a meeting room and office dedicated to users.



Figure 2: The BTF control room.

\* A complete and updated list of diagnostic tools, DAQ, and equipments of the DAΦNE Beam Test Facility is available at <http://www.lnf.infn.it/acceleratori/btf/techdoc/>

At the beginning of 2005, the AGILE team and the DAΦNE-BTF staff started a collaboration to design and realize a Photon Tagging Source in the BTF experimental hall. Photons in BTF are produced by Bremsstrahlung of electrons (with maximum momentum of 750 MeV/c) on an active target made by four silicon micro-strip planes (two  $x$  and two  $y$  views) placed at the inlet of the 45 degrees bending magnet downstream in the BTF transfer line (see Fig. 3).

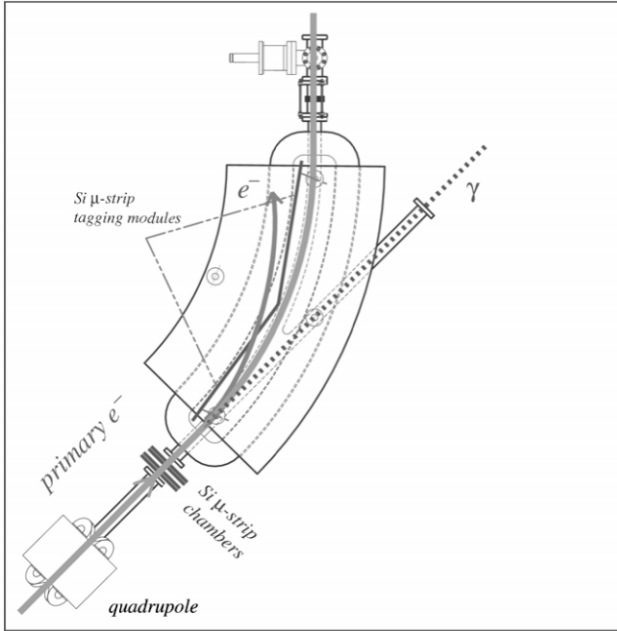


Figure 3: Schematic view of the tagged photon source showing the last part of the BTF line, the active target (silicon micro-strip chambers), and the tagging modules inside the bending magnet.

The four silicon planes,  $8.9 \times 8.9 \text{ cm}^2$  of active area, are  $380 \text{ }\mu\text{m}$  thick silicon detectors with a strip readout pitch of  $242 \text{ }\mu\text{m}$ . The energy of the radiated photon is obtained from the momentum lost by the emitting electron, measured in the magnetic field of the last bending magnet, by means of a set of tagging silicon micro-strip detectors arranged inside the magnet itself along the curved beam-pipe (on the left of the curved beam pipe in Figure 3): depending on the energy lost in the photon production, the emitting electron will hit different strips, once the dipole magnetic field is set to the nominal value of the electron beam, while non-irradiating electrons will be transported inside the curved pipe. The correlation between the direction of the electron, measured by the  $x$ - $y$  micro-strip chambers, and the position where the electron impinges on the micro-strip module inside the magnet allows tagging the produced photons, with an energy resolution of  $\sim 7\%$  (A Bremsstrahlung spectrum is shown in Fig. 4).

The tagging detectors are divided in 12 modules of  $2 \text{ cm}$  active height and 384 strips each, with a readout pitch of  $300 \text{ }\mu\text{m}$ . Together with the four chamber planes, a total of 6144 micro-strip signals are read by TAA1

ASICs (IDEAS, Norway, 128 channels/chip), the analog signals are then multiplexed with a  $5 \text{ MHz}$  clock and acquired by sampling ADCs and C-RAMs (CAEN V550). The system is presently being integrated in the BTF data acquisition system in order to record on disk the reconstructed photon energy together with the electron beam parameters.

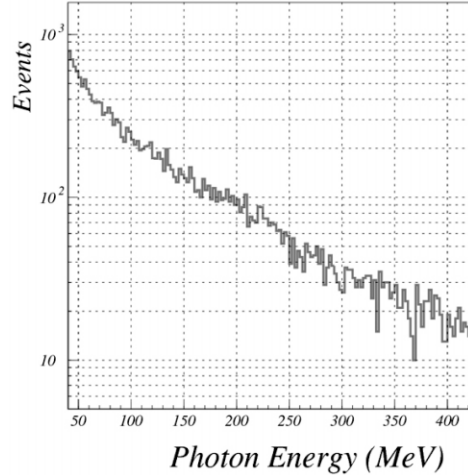


Figure 4: Photon spectrum obtained by Bremsstrahlung starting from a 450 MeV primary electron beam.

The beam spot size and divergence should be kept as small as possible in order not to spoil the photon energy resolution and in order to minimise mis-tagged events, mainly due to electrons scattered at large angles and hitting the tagging modules (see Fig. 5). These spurious events can be reduced offline by selecting single tracks in the active target silicon chambers, and by cutting on the primary electron angle, but this results in a reduction of useful tagged photon events. The contribution of the Coulomb scattering is minimised by using thin ( $0.5 \text{ mm}$ ) beryllium beam-pipe exit windows, and keeping a vacuum (at the level of  $1 \text{ mbar}$  or less) also in the last part of the beam-pipe inside the magnet.

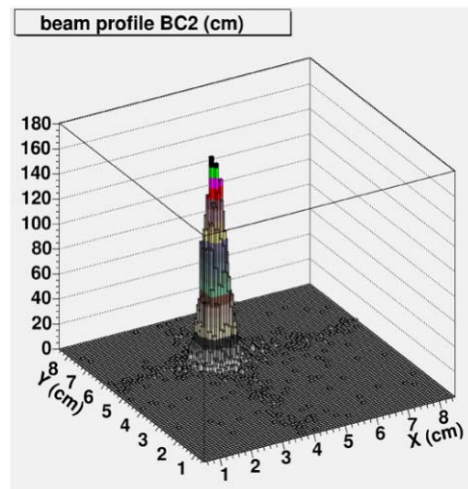


Figure 5: Beam spot size measured on the silicon micro-strip chambers at the entrance of the last dipole magnet.

A dedicated study investigating the possibility of producing low momentum neutrons with the BTF electron beam on a dedicated target has also started; simulations using hadronic interactions simulation packages like FLUKA are presently under way.

## OPERATION AND PERFORMANCE

The operation parameters for the DAΦNE Beam Test Facility are listed in Table 1. Up to now the facility essentially worked in time-sharing with injection into the rings of DAΦNE. The duty cycle was then limited to about 40% due to the continuous topping-up during the operation of DAΦNE collider experiments.

Table 1: BTF parameters for electron/positron beam; 1) left time-sharing with the DAΦNE collider operation, right continuous operation; 2) left single particle value, right high multiplicity value.

Energy range	25-500 MeV / 25 – 750 MeV <sup>(1)</sup>
Repetition rate	20-50 Hz / 50 Hz <sup>(1)</sup>
Pulse duration	10 ns / 1 or 10 ns <sup>(1)</sup>
Duty cycle	40 / 80 % <sup>(1)</sup>
Multiplicity	1 – 10 <sup>3</sup> (allowed) up to 10 <sup>10</sup> (waiting for approval)
Spot size ( $\sigma_x * \sigma_y$ )	~ 2x2 – 10 mm <sup>(2)</sup>
Divergence	~ 2 – 15 mrad <sup>(2)</sup>
Energy resolution	< 1%

During the last DAΦNE shutdown in 2006 a pulsed dipole magnet has been inserted at the end of the LINAC, allowing to continuously deliver beam in the BTF experimental area. Even when beams are injected into the DAΦNE rings, the BTF beam can still be delivered, with a lower repetition rate, since not all the LINAC bunches are needed for the filling the accumulator ring. Obviously, in this operation scheme the pulse duration and the primary beam energy must be the same of DAΦNE. This is not a strong limitation, since the facility is mainly operated in single particle mode (electrons/positrons), which is the ideal configuration for detectors calibration and testing; in this case the beam characteristics (see Table 1) are largely determined by the energy selector magnetic field and by the positioning of the slits.

The values listed in Table 1 are average values: the beam parameters can be further tuned depending on the needs of the user group, from the point of view of beam intensity, energy and beam spot size.

Concerning the beam multiplicity the limit of thousands of particles can be overcome as soon as radio-protection safety permissions will be granted by the Regional Environment Protection Agency, in order to bring all the LINAC current in the area, equivalent to 10<sup>10</sup> electrons.

## CONCLUSIONS

In almost four years of operation the DAΦNE Beam Test Facility hosted tens of international research groups testing devices and detectors in many different conditions.

The BTF demonstrated very good flexibility and optimal performances in a wide range of different applications and conditions. More technical and detailed information are available on the facility web site: <http://www.lnf.infn.it/acceleratori/btf/>

## ACKNOWLEDGMENTS

We are deeply grateful to all the DAΦNE operators who ensured a steady and effective operation of the LINAC and BTF beams from the beginning, and to all our colleagues of the Accelerator Division for their efforts in minimising the BTF dead times.

One of us (P. V.) wants to dedicate this paper to the memory of Sabrina Picucci.

## REFERENCES

- [1] G. Mazzitelli, A. Ghigo, F. Sannibale, P. Valente and G. Vignola, “Commissioning of the DAΦNE beam test facility” Nucl Instr. Meth A 515 (2003) 516.
- [2] H. Amankath, et al, "Installation and Commissioning of the e+/e- Injector for DAΦNE at Frascati", Particle Accelerator Conference, Dallas, Texas, 1-5 May 1995.
- [3] B. Buonomo, G. Mazzitelli and P. Valente, “Performance and upgrade of the DAΦNE Beam Test Facility”, IEEE Nuclear Science symposium, Rome 2004.
- [4] B. Buonomo et al, “Profile Monitors for Wide Multiplicity Range Electron Beams”, DIPAC 2005, Lyon, France, 6-8 June 2005.

# CHOOSING A BASELINE CONFIGURATION FOR THE ILC DAMPING RINGS \*

A. Wolski<sup>†</sup>, University of Liverpool and the Cockcroft Institute, UK  
 J. Gao, IHEP, Beijing, China  
 S. Guiducci, INFN-LNF, Frascati, Italy

## Abstract

The damping rings for the International Linear Collider must be capable of accepting large beams from the electron and positron sources, and producing highly damped beams meeting demanding stability specifications, at the machine repetition rate of 5 Hz. Between March and November 2005, a program of studies was undertaken by an international collaboration of 50 researchers, to compare a number of configuration options, including ring circumferences between 3 and 17 km. Here, we outline the studies and discuss the principle considerations in the choices of the baseline and alternative damping ring configurations.

## INTRODUCTION

Early in 2005, the goal was set of defining a baseline configuration for the International Linear Collider (ILC). For the damping rings, this required the selection of a number of high-level parameters, including the circumference and energy, as well as the technology choice for various technical subsystems such as the injection and extraction kickers and the damping wigglers. The baseline configuration would be developed for the Reference Design Report and cost estimate, to be produced in 2006, and making a choice taking full account of technical and cost issues was therefore important. Alternatives to the baseline configuration, allowing trade-offs between cost and technical risk, could also be specified.

Selecting the baseline configuration for the damping rings was a complicated issue because of the large number of conflicting requirements. For example, choice of the circumference depended on consideration of beam dynamics issues, cost, and availability. Some of the beam dynamics issues (e.g. fast-ion instability, electron cloud) favor a larger circumference, while others (e.g. dynamic aperture, space-charge) favor a smaller circumference. For a large circumference (approximately 17 km) ring, considerable cost savings may be achieved by selecting a “dog-bone” layout in which long straight sections share tunnel with the main linac, and the arcs are relatively short (approximately 1 km circumference). Concerns with the dog-bone layout included limitations on dynamic aperture from the poor symmetry, and the effects of stray fields from the high power RF components in the linac tunnel. A shorter

Table 1: Specifications for the ILC damping rings.

Pulse repetition rate	5 Hz
Max. injected betatron amplitude	0.09 m-rad
Max. injected energy deviation	$\pm 0.5\%$
Extracted norm. horizontal emittance	8 $\mu\text{m}$
Extracted norm. vertical emittance	0.02 $\mu\text{m}$
Extracted rms bunch length	6 mm
Extracted rms energy spread	0.13%
Total particles per pulse	$5.6 \times 10^{13}$
Number of bunches (nominal)	2800
Number of bunches (maximum)	5600

(e.g. approximately 6 km) ring may save costs from the reduced lengths of vacuum system and damping wiggler required, but will require more tunnel than a dogbone layout.

In this paper, we describe some of the outcomes of a wide range of studies that supported a systematic approach to the selection of the baseline configuration. We also briefly describe the process by which choices were made between the different configuration options. The studies supporting the configuration recommendations are documented in a report [1] completed in February 2006. A technical outline of the baseline configuration appears elsewhere in these proceedings [2].

## REFERENCE LATTICES

Any damping ring design must achieve the general specifications set by the “global” parameters of the ILC, including damping rate and beam current. These specifications are shown in Table 1. Any damping ring configuration must be capable of delivering the performance specifications given in Table 1.

Lattice designs are necessary for evaluating the impact of a variety of beam dynamics effects, for estimating costs, and for studies of reliability and availability. The number of configuration options, including ranges of circumference, beam energy and lattice styles, meant that it was not practicable to produce and study lattices representing every single combination of configuration options. However, six new damping rings lattices were produced that covered three different circumferences (roughly: 3 km, 6 km and 17 km), two different energies (3.7 GeV and 5 GeV), and three different lattice styles (FODO, TME and PI arc cells). These six lattices provided reasonable coverage of the principle configuration options, and were there-

\* This work was supported by the Director, Office of Science, High Energy Physics, US Department of Energy under contract number DE-AC02-05CH11231.

<sup>†</sup> awolski@lbl.gov

Table 2: Circumference, energy and lattice style of the seven damping ring configuration studies reference lattices.

Lattice name	Circumf. (km)	Energy (GeV)	Lattice style	Layout
PPA	2.82	5.0	PI	circular
OTW	3.22	5.0	TME	racetrack
OCS	6.11	5.0	TME	circular
BRU	6.33	5.0	FODO	dogbone
MCH	15.94	5.0	FODO	dogbone
DAS	17.01	5.0	PI	dogbone
TESLA	17.00	5.0	TME	dogbone

fore used as “reference” lattices for the damping rings configuration studies. To support objective evaluation, while allowing a convenient means of referring to each of the lattices, a naming scheme was adopted consisting of three (seemingly arbitrary) letters: the names and principle parameters of the reference lattices are shown in Table 2.

The damping ring design for the TESLA proposal has received extensive study in the past, including for the TESLA TDR [3] and for the International Linear Collider Technical Review Committee Second Report [4]. The TESLA damping ring lattice was therefore included for benchmark comparisons with the six new lattices.

Working groups were organized to evaluate specific aspects of the damping rings, including a variety of beam dynamics issues, and the performance requirements for a number of technical subsystems. The objectives were: firstly, to perform each evaluation consistently across the reference lattices, so as to produce results allowing direct comparisons; and secondly, to verify the results of the evaluations using more than one simulation code, where possible. A good example of these objectives was provided by the studies of the effect on the dynamic aperture of non-linear field components in the damping wiggler. Since the wiggler provides around 90% of the radiation loss in the damping rings, the wiggler can have a significant impact on the dynamics. Several tracking codes now include models to represent the wiggler field in a realistic way. Calculations of the dynamic aperture in each of the reference lattices were carried out using a number of different codes; good agreement was found between the codes for the impact of the damping wiggler on the dynamic aperture in each lattice.

## BEAM DYNAMICS

Critical beam dynamics issues include the acceptance, low-emittance tuning, and collective effects that potentially limit beam stability. Here, we mention briefly three of the issues particularly relevant to the circumference choice; namely, the acceptance, space-charge effects, and electron-cloud effects.

A large acceptance is needed to ensure good injection efficiency for the large beam produced by the positron source. The average injected beam power is 226 kW, so

even small losses may quickly lead to radiation damage of critical components (such as the damping wiggler). The impact that the configuration can have on the dynamic aperture is complicated, because the dynamic aperture depends on details of the lattice design, such as sextupole location and phase advance. To try to understand the impact that the configuration can have on the acceptance, a variety of analysis techniques were applied to the reference lattices, including map calculation and frequency map analysis. As a result of the studies, a picture emerged in which the achievable dynamic aperture in the dogbone lattices was limited by the low degree of symmetry. In particular, the large local chromaticity resulting from the long straights made it difficult to achieve a good acceptance for off-energy particles. Although it was felt possible in principle to achieve the necessary dynamic aperture, the smaller lattices (6 km or 3 km) in which a higher degree of symmetry could be achieved, allowed a more comfortable safety margin. Characterization of the dynamic aperture included studies of the effects of systematic and random multipole errors and realistic wiggler models; these errors may lead to significant reduction of the dynamic aperture, and make a good margin in the error-free lattice essential.

The demanding requirements for beam quality and stability in the damping rings make collective effects a particular concern, even though the beam currents are not large by comparison with some existing machines, for example the B-factories. Any effect that leads to transverse or longitudinal emittance growth or jitter in beam position or beam size has to be carefully evaluated. Such effects include classical impedance-driven instabilities (including microwave instability and resistive-wall instability), intra-beam scattering, space-charge effects, electron cloud and fast-ion instability.

Space-charge effects were identified as a potential limitation in the TESLA damping ring, because of the large circumference for the moderate beam energy [5]. Studies using a linearized model of space charge indicated significant vertical emittance growth. For the configuration studies, results from two codes (Marylie/Impact and SAD) both using a nonlinear model of space charge, were compared. The results indicated that for the 17 km lattices, the effects of space charge could be much less than predicted from the linear model; however, the effects could still be significant, depending on the lattice design. It was also found that the coupling bumps, proposed to eliminate the space-charge emittance growth in the TESLA damping ring, could drive coupling resonances, and limit the available area in tune space for operating the damping ring. In the 6 km lattices, space-charge effects were visible in one lattice design (BRU) but completely negligible in the other (OCS).

Experience with the B-factories has led to significant concerns over electron cloud effects in the ILC positron damping ring. Studies of the build-up of electron cloud and the threshold for beam instabilities were performed for all the reference lattices. The results of several different sim-

ulation codes were found to be in good agreement. Benchmarks were also performed for the B-factories, and the results found to be consistent with observations. The cloud density increases as the bunch spacing decreases, which makes smaller rings less attractive. While the build-up of the cloud could likely be suppressed sufficiently in the 17 km rings by coating the vacuum chamber with a material having low secondary electron yield (SEY), effective suppression would be much more difficult in the 6 km rings. However, halving the beam current (by using two stacked 6 km rings) could again bring the damping rings into a regime where a low-SEY coating on the chamber would be effective at suppressing the electron cloud.

## TECHNICAL SUBSYSTEMS

The technical subsystems, including the vacuum system, magnets, damping wiggler, RF system, injection/extraction kickers, instrumentation and diagnostics, will all be critical for successful commissioning and operation of the damping rings. Here, we discuss briefly the damping wigglers and the injection/extraction kickers.

The short damping time required in the damping rings leads to a need for long, high-field wigglers. The 17 km rings require around 400 m of wiggler with 1.6 T peak field. Options considered for the wiggler technology included: permanent magnet; normal-conducting electromagnet; superconducting. The issues that must be considered for the damping rings configuration include field quality, physical aperture, power consumption, and resistance to radiation damage. Various wiggler models, representing the three technology options, were used for comparison. For two of the most important issues (field quality and physical aperture), the CESR-c superferric wigglers [6] demonstrated the requirements for the damping rings. Although there were concerns with resistance to radiation damage (which applied also to the permanent magnet option), on balance it was felt that the superferric option provided the best alternative.

The injection/extraction kickers have particularly demanding requirements, having to provide 0.6 mrad deflection of 5 GeV bunches, with rise/fall times of the order of a few ns, with repetition rates of 6 MHz for 1 ms bursts, and kick amplitude stability of better than 0.1%. Two principle options were considered: “Fourier” kickers based on deflecting cavities with RF pulse compression using (for example) dispersive waveguide; and “conventional” kickers using striplines fed by fast, high-power pulsers. Significant progress has been made with theoretical studies of “Fourier” kickers [7]. However, experimental tests at the KEK-ATF have demonstrated the feasibility of relatively conventional kickers using striplines and fast pulsers, and it was considered that less R&D would be required to demonstrate kickers based on the latter technology. It was noted that RF deflecting cavities could be used to increase the bunch spacing for injection/extraction by directing successive bunches down parallel beamlines; this would ease

the requirements on the rise/fall times of the kickers, and remains an option though further studies are needed.

## DECIDING THE RECOMMENDATIONS

A meeting to review the results of the configuration studies and make recommendations was held at CERN in early November 2005. Results included the outcome of studies of beam dynamics and technical subsystems, as well as reliability and availability estimates and cost estimates. The meeting was attended by 35 of the nearly 50 people who worked on the configuration studies. To guide the process of making the configuration options, a “ranking” system was agreed, that could be applied to each of the decisions needing to be made. For each decision, the relevant issues were ranked from A (critical) to C (minor impact); each issue was then assigned a technical risk from 1 (no risk) to 4 (technical solution unlikely), or a cost from 1 (lowest cost) to 4 (more than three times lowest cost option). Discussions were structured on reaching agreement on the significance and risk rankings for each issue. The results are recorded in the Configuration Studies Report [1].

The principle configuration decisions include:

- A single 6 km damping ring for the electrons, and two stacked 6 km rings for the positrons.
- Beam energy of 5 GeV.
- Superferric damping wigglers.
- A superconducting 500 MHz RF system<sup>1</sup>.
- Electromagnet main magnets (dipoles, quadrupoles, etc.)

## REFERENCES

- [1] A. Wolski, J. Gao, S. Guiducci, “Configuration Studies and Recommendations for the ILC Damping Rings”, LBNL-59449 (February 2006).
- [2] S. Guiducci, “The ILC Damping Rings,” these proceedings (2006).
- [3] TESLA Technical Design Report, DESY 2001-011 (March 2001).
- [4] International Linear Collider Technical Review Committee 2nd Report, SLAC-R-606 (2003).
- [5] W. Decking and R. Brinkmann, “Space Charge Problems in the TESLA Damping Ring,” proceedings of EPAC 2000, Vienna, Austria (2000).
- [6] D. Rice et al, “Production and Testing Considerations for CESR-c Wiggler Magnets,” proceedings of PAC 2003, Chicago, Illinois (2003).
- [7] G. Gollin et al, “Performance Modeling of a Fourier Series Pulse Compression Kicker for the ILC Damping Rings” (2006).

<sup>1</sup>The RF frequency was later changed to 650 MHz, to allow a higher harmonic number (for the low-Q ILC parameter set), and to simplify phase-locking between the damping rings and the linac RF systems.

# TURN BY TURN MEASUREMENTS AT DAΦNE BASED ON THE LIBERA BEAM POSITION PROCESSOR

A. Stella, M. Serio, INFN-LNF, Frascati, Italy

## Abstract

The BPM detection electronics Libera, developed by Instrumentation Technologies implements digital receivers technology to measure the beam position from the amplitude of pick-up signals. Besides the average closed orbit mode, the Libera module can be operated also in the *Turn by Turn* mode. Operational experience with Libera at the  $e^+e^-$  collider DAΦNE has been initially focused on this functionality. Data obtained from DAΦNE are processed with well established extraction algorithms to accurately measure the betatron tunes from a small number of turns, providing instantaneous information on tune variations occurring even during fast damped decays after a kick. Hardware and software implementation together with experimental data are reported.

## INTRODUCTION

The  $e^+e^-$  collider DAΦNE consists of two symmetrical storage rings at 1.02 GeV centre of mass energy, sharing a common vacuum chamber in each of the two interaction regions.

The 120 RF buckets of each ring are spaced by 2.7 ns. The design single bunch current is 44 mA (achieved  $> 200$  mA) and, during operations for collisions up to 109 consecutive bunches of  $\sim 15$  mA are typically stored. The total stored current is of the order of  $\sim 1$  A. Other bunch patterns are sometimes used for machine studies.

Pickup signals from a beam position monitor (BPM) installed in the positron ring have been connected through 50 m long coaxial cables to a Libera Electron board [1]: RF signals are processed in the analog stage for filtering and gain adjustment, then sampled, down-converted using an under-sampling technique, and digitally filtered.

The beam position monitor used for this evaluation has four button electrodes placed symmetrically around a circular vacuum chamber of 44 mm radius.

Beam position is deduced onboard by comparing amplitudes between the sampled signals. The module provides several parallel data paths with different measurement bandwidths.

## TURN BY TURN MEASUREMENTS

The frequency spectrum around the RF harmonic of the revolution frequency  $f_0$ , which is the line present in DAΦNE with every possible bunch pattern, is selected for sampling by Libera in the BPM signals.

The device supports *Turn by Turn* (TBT) measurements of beam position with a bandwidth of  $f_0/2$ . Once triggered, Libera stores up to 200k samples in a memory buffer and, on demand, provides it to the user.

An embedded single board computer (SBC) is equipped with a Linux operating system. It provides the platform for the software routines used for configuration, operation and diagnostics, and can be accessed across the Ethernet network through the TCP protocol.

Dedicated software, which has been developed on a remote host running the Matlab package, accesses the SBC at the application level using the SSH protocol, to control the data acquisition, collection and processing.

To test the TBT acquisition, data have been collected in different operating conditions and post-processed with the analysis tools developed with Matlab.

The resolution of the measurements performed with the DAΦNE BPMs changes with beam stored current as shown in Fig. 1. The product resolution times beam current is  $\sim 0.8$  mm-mA, constant for total currents below  $\sim 35$ mA; beyond this threshold the onboard RF input attenuators must be used to expand the dynamic range.

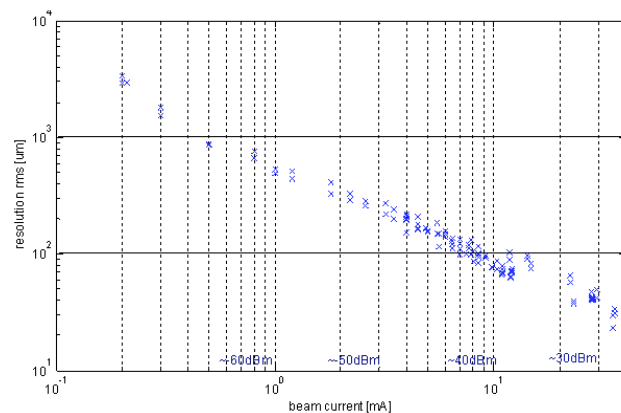


Figure 1: TBT resolution vs. beam current.

The device can operate also for a single beam passage. Figure 2 shows results obtained by injecting a single bunch of 1.5 nC into the positron ring while the RF cavity is switched off, so to simulate a condition occurring after a major shutdown or hardware modifications, when the beam is not yet stored. Measurements of the first turns of the bunch, characterized by large betatron oscillations, are recorded until the whole charge is lost.

## Tune Measurements

The betatron tune  $Q$  can be measured by sampling for  $N$  turns the transverse position of the beam coherently oscillating and performing the FFT of the stored data to detect the frequency of the oscillation.

The stored beam is shock excited with a kicker magnet. A trigger signal, generated a few  $\mu$ s before the shot, is provided by the accelerator control system to Libera to start the acquisition of beam position.

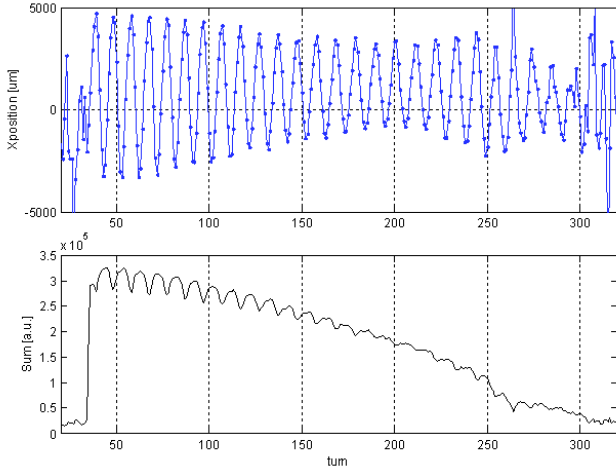


Figure 2: First turns data without RF: radial beam position (top) and sum of pickup signals (bottom) vs. turns.

Figure 3 (top) shows a typical damped betatron oscillation of the radial beam position to the pulse of the injection kicker.

The decay time is considerably shorter than the incoherent radiation damping time (110 kturns) because of the head-tail damping and of the decoherence induced by the nonlinear terms of the optics.

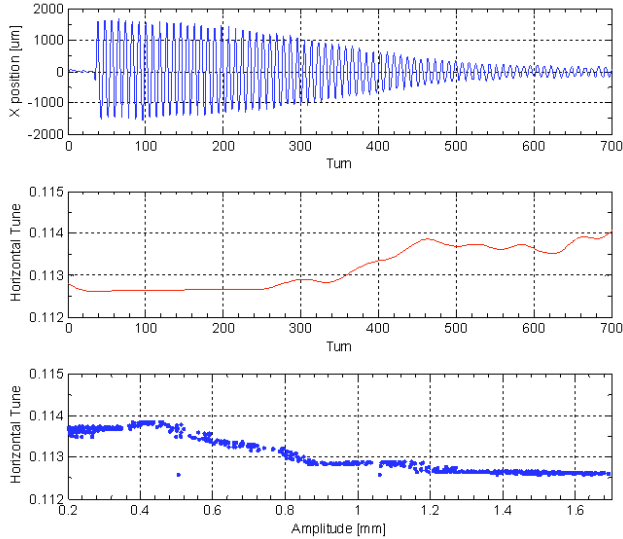


Figure 3: Radial beam position oscillation and horizontal tune measurements after a kicker pulse (beam current  $I_b \sim 10\text{mA}$ ).

This fast decay limits the number of turns  $N$  during which the beam oscillation can be measured. The resolution of tune measurement based on a simple FFT is proportional to  $1/N$  and has been enhanced:

- by improving the accuracy of the Fourier analysis using Hanning window filters,
- by interpolating the shape of the spectrum around the main peak with the continuous spectrum of a pure sinusoidal signal.

The error associated to this method is in principle proportional to  $1/N^4$  in the absence of noise.

Tunes are computed with the following interpolation formula [2]:

$$Q = \frac{k}{N} + \frac{1}{2\pi} \arcsin \left[ A \left( \phi_k, \phi_{k+1}, \cos \frac{2\pi}{N} \right) \sin \frac{2\pi}{N} \right] \quad (1)$$

where the function  $A$  is given by:

$$A(a, b, c) = \frac{-(a+bc)(a-b) + b\sqrt{\Delta}}{a^2 + b^2 + 2abc} \quad (2)$$

and

$$\Delta = c^2(a+b)^2 - 2ab(2c^2 - c - 1) \quad (3)$$

$\phi_k$  and  $\phi_{k+1}$  are the two values of the FFT amplitude spectrum with larger amplitudes.

The horizontal betatron tune values in Fig. 3 have been extracted by the above algorithm, from consecutive blocks of  $N=128$  turns and are shown vs. turn number and vs. oscillation amplitude (deduced from the magnitude of the Hilbert transform of the beam position data). Evaluation of the tunes over a sliding window of  $N$  turns, rather than on the whole set of data, allows measuring an amplitude dependent tune shift.

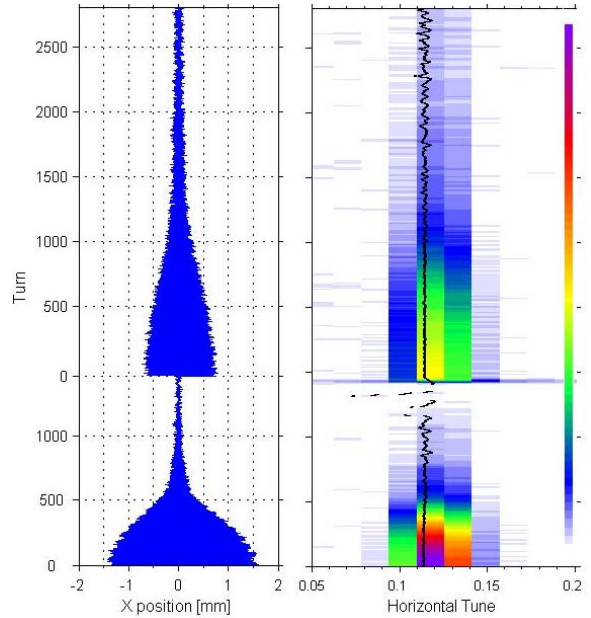


Figure 4: Horizontal beam position vs. turns and spectrogram with interpolated tune value ( $N=64$ ) for two kicks of different amplitudes.

In Fig. 4 (left), radial response of the beam to two kicker pulses, whose second amplitude is halved with respect to the first, have been collected.

In the right figure we show the spectrogram of the FFT amplitude of each block of consecutive  $N=64$  turns

together with the tunes computed using the interpolation technique on the same block of data. The tune obtained with the interpolated data is plotted (black trace) on the plain FFT spectrogram to show the finer accuracy.

The residual betatron oscillations excited by the injection kick, have been acquired to evaluate the tune values during normal collider operation.

Figure 5 (top) reports the horizontal and vertical beam position together with the plot of the magnitude of the FFT and the interpolated tune values  $Q_x$ ,  $Q_y$  over  $N=128$  turns following an injection pulse in the positron ring..

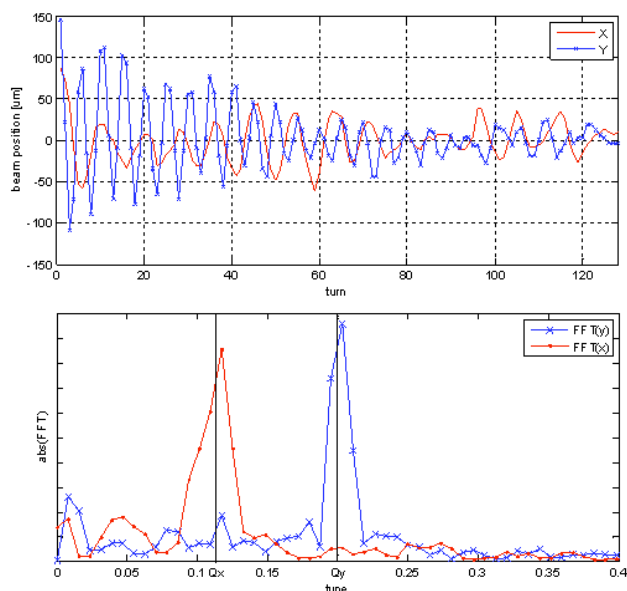


Figure 5: Tune measurements during beam injection.

An amplitude oscillation in the vertical plane has been also observed, probably due to an initial vertical angle of the injected beam and/or to an uncompensated vertical kick component.

### Effect of noise on tune evaluation

The effect of the finite resolution of the turn by turn measurements reduces the precision by which the tune is determined with the interpolating procedure.

A bench test has been performed to evaluate how the errors affect the tune reconstruction, in order to characterize the measurements obtained with the DAΦNE beam. To simulate the beam signals coming from the BPM pickups during a betatron oscillation, Libera has been connected to CW signals at  $f = 120f_0$ , generated by an oscillator. One of the four inputs has been amplitude modulated with a frequency  $\Delta f$  variable in the  $0 \div f_0/2$  range. Power levels of the carrier and of the modulation signal have been adjusted to reproduce the spectrum of the DAΦNE beam signal with current in the 0.1-1000 mA and oscillations of  $\sim 1000 \mu\text{m}$ .

Turn by turn data acquired by Libera, locked with a clock signal to the nominal frequency of  $120f_0$ , have been post processed with the described algorithm to compute

the frequency of the modulating signal, so to simulate a tune measurement.

In Fig. 6 we report results obtained for different signal to noise ratios, equivalent to different ratio between beam current and amplitude of the beam oscillation, so to estimate the resolution of the tune measurements computed over blocks of  $N$  data.

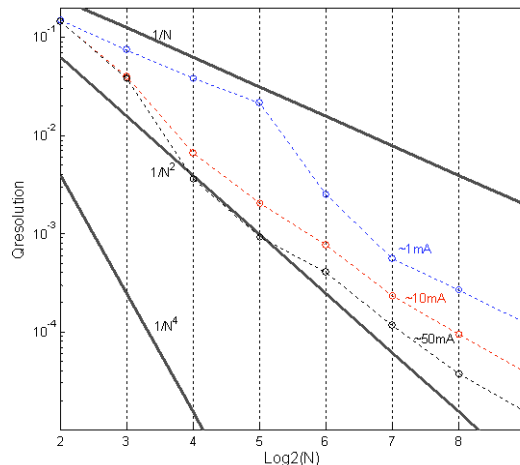


Figure 6: Expected tune measurements resolution based on  $N$  turns at beam currents corresponding to Signal/Noise ratios of  $\sim 2$ ,  $\sim 15$ ,  $\sim 100$ .

Due to the noise, the precision of the tune is reduced but scales always better than  $1/N$ , which should be associated with an extrapolation based on a plain FFT.

## SUMMARY

The Libera TBT acquisition mode has been tested in DAΦNE at different working conditions. An interpolating technique has been applied to extract betatron tunes from experimental data. Beam results have been complemented by bench tests.

The development of software dedicated to control, management and data analysis, turns Libera into a useful tool for beam diagnostics during both collider operation and machine studies.

## ACKNOWLEDGMENTS

The authors wish to thank Instrumentation Technologies for fruitful collaboration. We acknowledge the contribution of O. Coiro, D. Pellegrini, C. Mencarelli for the prompt and accurate technical support.

## REFERENCES

- [1] Instrumentation Technologies, "Libera Electron User Manual", 2006.
- [2] R. Bartolini et al., "Tune Evaluation in Simulations and Experiments", Particle Accelerators, 1996, Vol. 52, p. 147.

# DESIGN AND TESTS OF NEW FAST KICKERS FOR THE DAΦNE COLLIDER AND THE ILC DAMPING RINGS

David Alesini, Susanna Guiducci, Fabio Marcellini, Pantaleo Raimondi,  
INFN/LNF, Frascati, Roma

## Abstract

In this paper we illustrate the design of new, fast stripline kickers to inject or extract bunches in electron/positron rings. The kickers have been designed for the injection upgrade of the  $\Phi$ -factory DAΦNE and as injection/extraction devices for the International Linear Collider (ILC) damping rings. The design is based on tapering the striplines in order to simultaneously obtain low impedance and an excellent uniformity of the deflecting field. The design has been done using 2D and 3D electromagnetic codes such as Superfish and HFSS. High voltage test results on prototypes are also shown.

## INTRODUCTION

The injection system is one of the challenging issues of the International Linear Collider (ILC) project [1] and the injection and extraction kickers are one of the most critical issues for the ILC Damping Rings (DR) [2]. In fact the bunch distance in the ring and therefore the choice of the ring circumference are related to the kicker pulse duration; moreover the stability of the beam position at the IP depends also on the kicker pulse stability. R&D programs are in progress in different laboratories at a global level both on the fast pulsers and on the stripline electrodes. The injection and extraction kickers for the positron DR, which has a minimum bunch distance of 6.2 ns, should satisfy the following requirements:

- a) ultra short rise and fall time (total pulse duration <12.4 ns);
- b) high integrated strength;
- c) good uniformity of the deflecting field, within few percent over 90% of the beam stay clear;
- d) impedances of the structure as low as possible;
- e) 3 MHz repetition rate.

There is a similarity between the ILC injected beam and kicker parameters and the DAΦNE ones, as shown in Table 1. Therefore stripline kickers studied for the ILC damping ring can be used for an upgrade of the DAΦNE injection system. The installation of these new kickers at DAΦNE is an important test for the ILC project, since it should demonstrate with beam measurements the achievement of the kicker performances. These kickers could also be used, in the framework of the ILC collaboration, to test new fast pulsers produced by different laboratories or industry. Compared to the present DAΦNE injection kickers [3] the new ones have:

- a) much shorter pulse ( $\approx 12$  ns instead of  $\approx 150$  ns);
- b) better uniformity of the deflecting field;
- c) lower impedance;
- d) higher injection rate (max 50 Hz).

The much shorter pulse allows perturbing only the injected bunch and the two adjacent ones while, at present, a large fraction of the stored bunches (50/110 with 2.7 ns bunch spacing) are affected by the injection kick. This improvement can increase the current threshold of the transverse instability in the positron ring (as it has already been observed experimentally at DAΦNE).

The better uniformity of the deflecting field can increase the injection efficiency at high currents and reduce the background to experiments during injection.

The broadband impedance, according to the calculations, is reduced by a factor 3 with respect to the present kickers. Moreover, since the new kickers have been designed with the same beam pipe cross section of the dipoles, no taper transition are needed between the dipoles and the kicker and this also contributes to the reduction of the machine impedance.

Finally, the possibility of injection at 50 Hz can be useful for future upgrades of the whole injection system.

Table 1: Kicker and beam parameters for ILC DR (\*) and DAΦNE.

	ILC DR	DAΦNE
Energy [GeV]	5	0.51
Bunches time spacing [ns]	6.2	2.7
Bunch length [mm]	6	35
Deflection [mrad]	0.7	5
Total defl. voltage [MV]	3.5	2.5
Kicker length [cm]	87	73
Input pulse length [ns]	5.9	5.3
Horizontal beam stay clear @ kicker (diameter) [mm]	50	50

## KICKER DESIGN

A detailed discussion on the kicker design criteria is reported in [4]. The design of the new kickers is based on the idea to properly taper the striplines. The kicker structure is shown in Fig. 1a. Each transverse section has constant  $50\Omega$  impedance equal to the output impedance of the high voltage pulse generator. The tapered striplines allow to:

- a) reduce the broadband beam coupling impedance of the device;
- b) improve the deflecting field quality obtaining a uniform transverse deflection as a function of the transverse coordinate (horizontal in particular);

\* Referred to the positron ring with horizontal  $\beta$ -function at the kicker equal to 70 m.

- c) obtain a better matching between the generator and the kicker structure at high frequency<sup>†</sup>;
- d) reduce the beam transfer impedance;
- e) have a uniform beam pipe cross section between the dipole region (that has a rectangular cross section) and the kickers region.

Concerning the uniformity of the deflecting field as a function of the transverse coordinates, it should be pointed out that, for a given transverse section of the kicker, the behaviour of the deflecting field depends on the coverage angle. The length of the tapers with respect to the straight section and the internal dimensions of the structure have been optimized using the electromagnetic codes Superfish [5] and HFSS [6] to obtain a uniform integrated deflecting field along the horizontal coordinate. The deflecting field as a function of the horizontal and vertical coordinates is shown in Fig. 2.

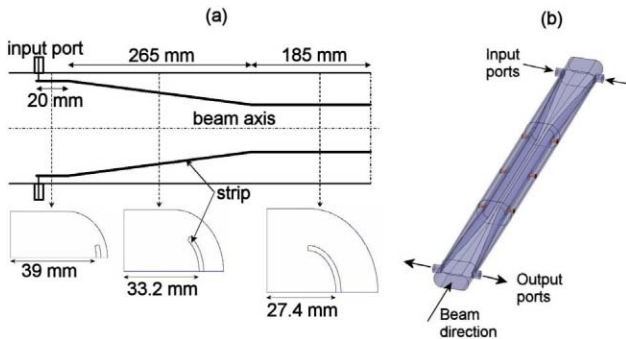


Figure 1: Sketch of the half kicker and HFSS 3D model.

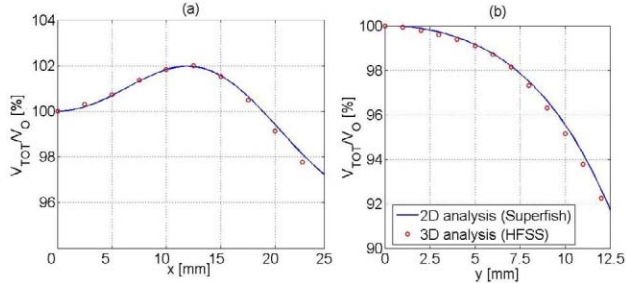


Figure 2: Deflecting field as a function of the horizontal (x) and vertical (y) coordinates.

Better matching between the pulse generator and the kicker structure is assured by reducing the stripline section and placing it very close to the kicker vacuum chamber in the coaxial-stripline transition region. This reduces the longitudinal and transfer impedance of the device also [7].

With a signal of the type sketched in Fig. 3a, which reproduces schematically the input signal from the pulser that we intend to use, the total deflecting field as a function of time is shown in Fig. 3b and the required voltage per strip to reach the desired bunch deflection is  $\sim 45$  kV. As the figure shows the two bunches that are 5.4 ns away from the injected one, receive a small kick.

<sup>†</sup> This can avoid multiple reflections of the deflecting pulse in the kicker structure that can perturb the stored bunches especially in the ILC case. Moreover it can allow extracting all the power release to the HOM of the structure by the beam.

The kicker design can be applied, with minor modifications, to the ILC positron damping ring. Assuming a 3 MHz and 5 kV input pulse per strip, the total required number of kicker is  $\sim 12$ .

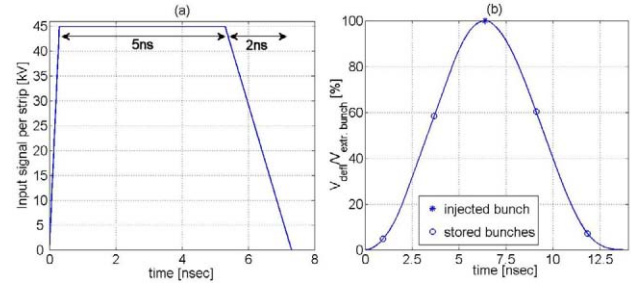


Figure 3: (a) Input pulse signal and total deflecting field (b).

With the code HFSS we have also calculated the longitudinal and transverse beam coupling impedances of the structure and the beam transfer impedance (using the wire method technique [8]). Figures 4a and 4b show, as an example, the calculated longitudinal coupling impedance and the transfer one. From the transfer impedance it is possible to evaluate the peak voltage into the ports and the average power for a given beam current. The maximum induced peak voltage on the upstream port is of the order of 100 V with a 6 nC bunch while the average power induced on the ports is of the order of few tens of Watts with a 2 A beam. No longitudinal and horizontal HOMs are trapped in the structure and the longitudinal loss factor is  $\sim 5 \cdot 10^{-3}$  V/pC for 1 cm bunch length. Concerning the vertical impedance there are four trapped HOM (TE<sub>11n</sub>-like) with vertical impedance of the order of few tens of kV per meter. These give, in the worst case, growth rates of the order of 1 ms<sup>-1</sup> at a total current of 2A that are about two orders of magnitude lower than the damping rates provided by the DAΦNE vertical feedback system.

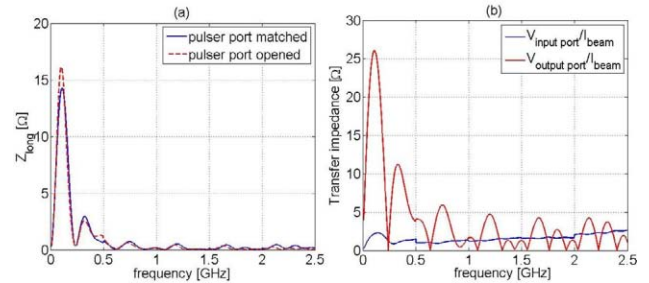


Figure 4: (a) Longitudinal beam coupling impedance and beam transfer impedance (b) calculated by HFSS.

## HIGH VOLTAGE TESTS

The mechanical drawing of the kicker is shown in Fig. 5. Since for DAΦNE 45 kV are applied to each strip of the kicker, high voltage (HV) tests on prototypes are necessary to verify if there are discharges on vacuum feedthroughs, connectors or between the strip and the vacuum chamber. To this purpose a small prototype of the kicker has been constructed and is shown in Fig. 6. The device has a uniform strip with a cross section exactly

equal to the cross section of the first part of the kicker (where the strip has the minimum distance from the outer chamber and therefore the electric field is higher). The strip is connected to the high voltage pulse generator through vacuum feedthrough of the type that we intend to use in the final structure. First high voltage tests have been performed using a 24 kV 7ns pulse generator courtesy of Fid GmbH Company [9].

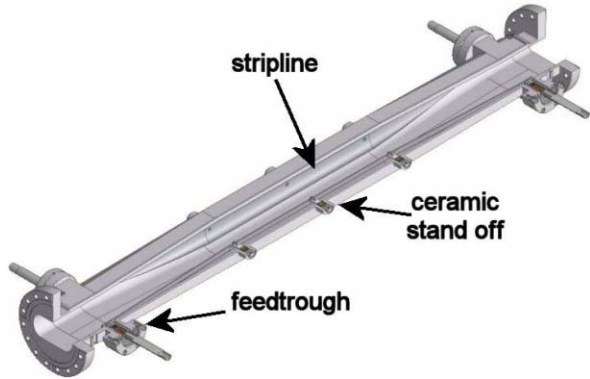


Figure 5: Mechanical drawing of the kicker.

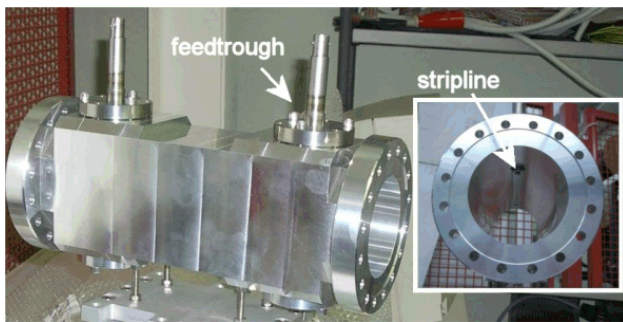


Figure 6: Prototype of the kicker for HV tests.

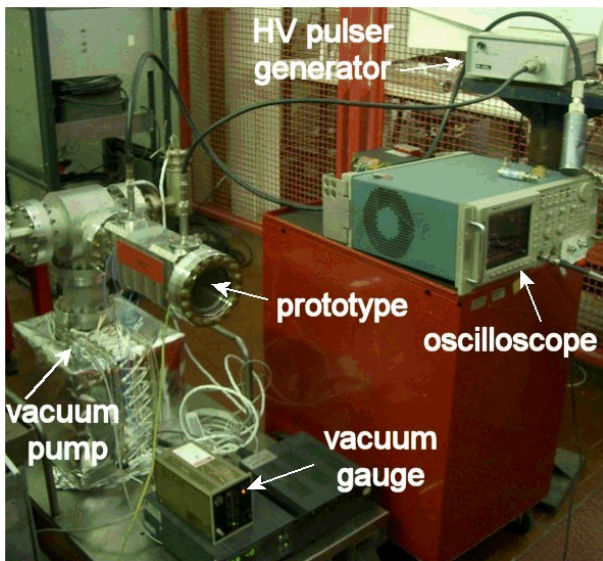


Figure 7: Setup for HV test on prototype.

The prototype test setup is shown in Fig 7. The pulses measured with an oscilloscope at the pulse generator output and at the stripline output are shown in Fig. 8. The difference between the two results is given by the

frequency response of cables that we have used. No discharges have been registered.

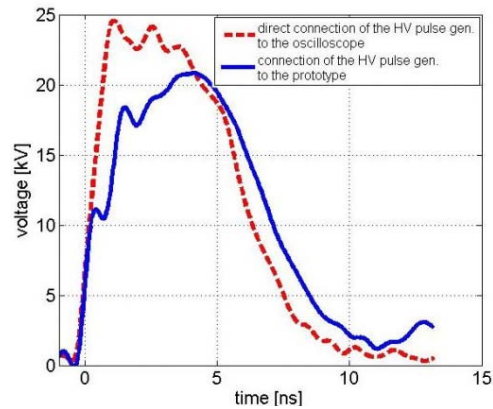


Figure 8: HV pulse measured with an oscilloscope directly connected to the pulse generator and after the prototype.

## CONCLUSIONS

We illustrated the design of new, fast stripline kickers to inject or extract bunches in electron/positron rings. The kickers have been designed for the injection upgrade of the  $\Phi$ -factory DAΦNE and as injection/extraction devices for the International Linear Collider (ILC) damping rings. The design is based on tapering the striplines in order to simultaneously obtain low impedance and an excellent uniformity of the deflecting field. The uniformity of the deflecting field as a function of the horizontal coordinate is of the order of  $\pm 2\%$  over the kicker horizontal aperture ( $\pm 2.7$  cm) while it is less than 10 % over  $\pm 1$  cm along the vertical one. The required voltage per strip in the DAΦNE case is  $\cong 45$  kV while, in the ILC case, assuming a 3 MHz and 5 kV input pulse per strip, the total required number of kickers is  $\sim 12$ . HV tests on a prototype have been successfully done with a 7 ns 24 kV pulse generator.

## ACKNOWLEDGEMENTS

We would like to thank G. Sensolini for the technical support. This work is supported by the Commission of the European Communities under the 6<sup>th</sup> Framework Programme, contract number RIDS-011899.

## REFERENCES

- [1] S. Guiducci, PAC05, Knoxville, (USA), May 2005.
- [2] A. Wolski, et al., LBNL-59449, 2006.
- [3] S. De Simone and A. Ghigo, EPAC92, Berlin, 1992.
- [4] D. Alesini, et al, DAΦNE tech. note I-17, EUROTeV-Report-2006-025, 2006.
- [5] J. H. Billen and L. M. Young, Part. Acc. 7, 1976.
- [6] www.ansoft.com.
- [7] D.A. Goldberg and G.R. Lambertson, LBL-31664 ESG-160, 1992.
- [8] F. Caspers, in Handbook of Accelerator Physics and Engineering, World Scientific, 1999.
- [9] <http://www.fidtechnology.com>

# STUDY OF THE EFFECT OF MULTIPOLAR COMPONENTS IN THE SPARC EMITTANCE COMPENSATION GUN SOLENOID\*

M. Ferrario, M. Migliorati, P. Musumeci, L. Palumbo, M. Preger, C. Sanelli,  
INFN-LNF, Frascati (Roma),Italy,

G. Dattoli, L. Picardi, M. Quattromini, C. Ronsivalle, ENEA-CR,Frascati(Roma), Italy

J. Rosenzweig,UCLA, Los Angeles(CA),USA, G. Bazzano,CNAO Foundation (Milano), Italy

## Abstract

The SPARC photoinjector rf gun requires a solenoid immediately downstream for emittance compensation. The analysis of the measured solenoid magnetic maps shows the existence of multipolar components added to the pure solenoid field.

The effect of these added fields on beam dynamics and possible correction schemes have been studied from the theoretical point of view and by numerical calculations based on PARMELA/TREDI codes. An accurate 3D numerical modelization by using CST EM Studio has been done, in order to investigate the source of these multipolar components and to suggest some design modifications aimed to reduce their magnitude. The results of this study are presented here.

## THE SPARC SOLENOID

The SPARC project, based on a collaboration among ENEA-INFN-CNR-Universita` di Roma Tor Vergata-INFM-ST, consists in a high brightness photoinjector driving FEL experiments using SASE, seeding and non-linear resonant harmonics [1].

The photocathode RF gun is followed by a solenoid immediately downstream for proper emittance compensation. The SPARC solenoid (Fig. 1) was designed to be similar to the standard BNL/LCLS type of device. Like previous versions, it employs field stiffening iron between coil sections, but uses only four coils that are independently powered, in order to shape the field profile with the aim to optimize the emittance compensation process.

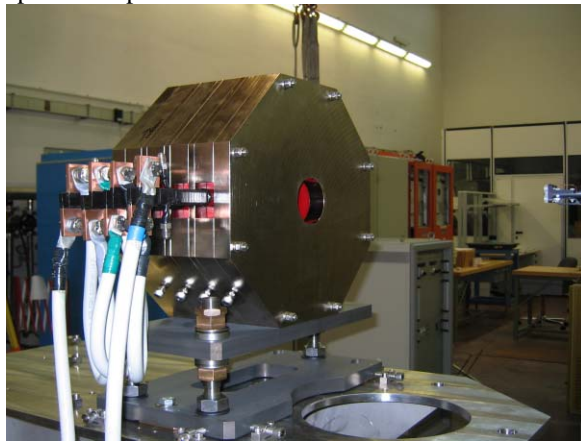


Figure 1: The SPARC emittance compensating solenoid

## Magnetic measurements analysis

The axial component of the magnetic field  $B_z(x,y,z)$  was scanned by an Hall probe. The scan was performed on a length on the z axis of 70 cm with a step size of 10 mm in a transverse grid defined by  $-10 \text{ mm} < x, y < 10 \text{ mm}$  with a step size of 5 mm.

In order to extract the  $B_x$  and  $B_y$  components accordingly with the Maxwell equations in the beam region we did a conditioned bi-dimensional least square fit of the measured values of  $B_z$  up to the second order in  $x, y$ :

$$B_z = b_0(z) + b_1(z)x + b_2(z)y + b_3(z)x^2 + b_4(z)y^2 \quad (1)$$

with

$$b_0(z) = B_z(x = y = 0)$$

$$b_3(z) = -b_0(z)'' / 4 + \delta(z)$$

$$b_4(z) = -b_0(z)'' / 4 - \delta(z)$$

The conditions imposed on the coefficients  $b_0, b_3, b_4$  allow to satisfy  $\text{div} \vec{B} = 0$  near the axis [2].

For a pure solenoid  $b_1 = b_2 = 0$  (no dipolar terms),  $\delta = 0$  (no skew quadrupolar terms).

Finally the transverse components  $B_x$  and  $B_y$  were retrieved from  $B_z$  accordingly with  $\text{curl} \vec{B} = 0$ .

From this analysis carried on the measured map at the operating current of 140 A  $b_1, b_2$  and  $\delta$  result different from zero:  $b_1$  and  $b_2$  correspond to dipolar fields of the order of 10 gauss, while the longitudinal integral of  $\delta$  gives a skew quadrupole with a focal length at 5.6 MeV of about 10 m. These spurious fields retrieved in such way are shown in figure 2.

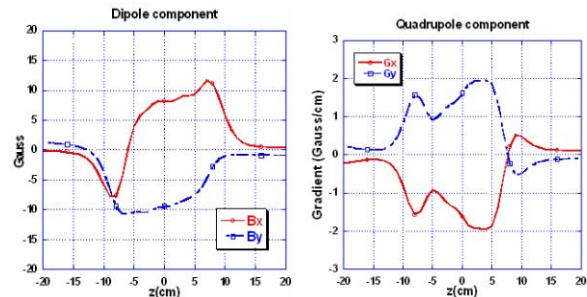


Figure 2 Added fields to the SPARC solenoid retrieved by the analysis of the longitudinal field measured map

\*Work supported by EUROFEL

### 3D model

One of the possible sources of the quadrupolar component has been found by performing very accurate 3D computations (with 5 million of meshcells) based on CST EM Studio code.

The multipolar content has been computed by a Fourier analysis of the field on a  $r_{ref}=1$  cm radius at different  $z$  positions accordingly with

$$B_{\theta}(r = r_{ref}) = \sum_{n=1}^8 [a_n \cdot \cos(n\theta) + b_n \cdot \sin(n\theta)] \quad (2)$$

with  $a_n$ =amplitudes of normal multipoles,  $b_n$ =amplitude of skew multipoles.

The comparison between the iron geometries shown in figure 3 put in evidence the presence of a skew quadrupolar component of the same order of magnitude of the measured one located in the fringing fields region of the SPARC magnet due to the lack of holes in the top and bottom of the iron shield.

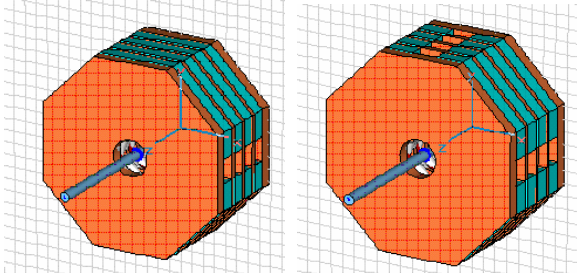


Figure 3: (Left) SPARC magnet geometry: not quadrupole compensated iron geometry, (Right) quadrupole compensated iron geometry

This is shown in figure 4, where the computed normal and skew components up to the octupole are plotted for the two compared geometries. One can see that in a symmetrized geometry a weak skew octupole appears. Other effects given by misalignments or real coils geometry have not been taken into account.

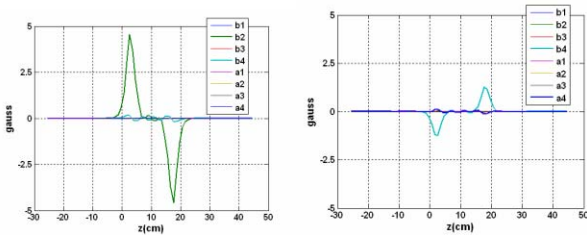


Figure 4: (Left) Multipole content in the SPARC geometry (Right) Multipole content in a quadrupole compensated iron geometry

## EFFECT ON BEAM DYNAMICS

The effect of the multipolar components on the beam evolution in the post-gun drift region has been evaluated by numerical computations and a semi-analytical model. In the beam dynamics calculations we used a 3D magnetic field map built starting from the measurement of the only longitudinal component of the field accordingly with the method described above. In this way

it was possible to separate the effect of the dipolar and quadrupolar components by putting  $\delta=0$  (only dipolar components) or  $b_1=b_2=0$  (only quadrupolar component) in the magnetic field expansion of equation (1).

The results are shown in figures 5,6; the dipolar component essentially is a steerer, acting in different ways in the two transverse planes accordingly with the different shapes of  $B_x$  and  $B_y$  on the axis (see fig.2). As to the skew quadrupolar component, it transforms the initial round beam into an elliptical beam and gives a projected emittance growth of a factor 1.7 respect to the ideal case.

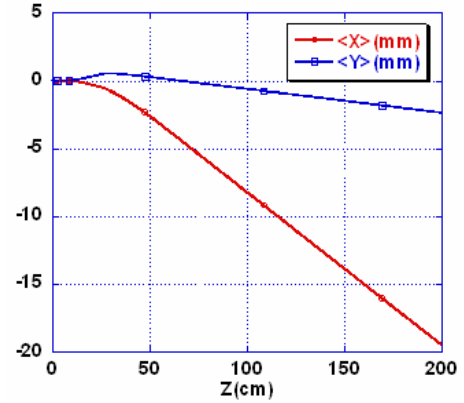


Figure 5: PARMELA computed X-Y centroids motion due to the dipolar components superimposed to the solenoid field

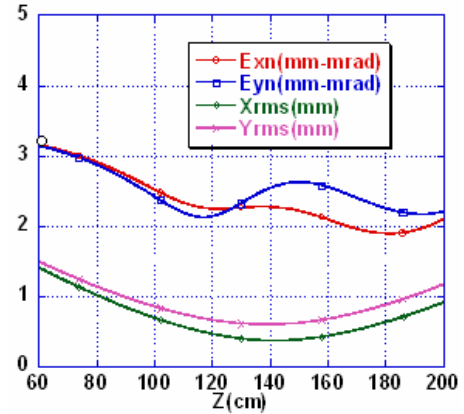


Figure 6: PARMELA computed rms X-Y envelopes and transverse normalized emittance vs  $z$  with only quadrupolar components superimposed to the solenoid field

This last effect is mainly due to the quadrupole-induced coupling of  $x$ - $y$  planes.

In fact when a bunch passes through a skew quadrupole, even if the 4D emittance remains invariant, there is a change in the projected  $x$ - $y$  emittances due to the coupling of the two planes induced by the quadrupole itself. The same effect occurs if the quadrupole (skew or not) is superimposed to a solenoidal magnetic field that rotates the bunch. As a consequence, even in the ideal case of a bunch passing through a hard edge solenoid with inside a quadrupole thin lens, the projected emittances vary. We can call this a ‘geometrical’ effect: the 4D

emittance remains invariant and the effect is reversible. For example, by using the matrix formalism, we evaluate analytically the bunch transverse dimensions after passing through a hard edge solenoid of length  $L_1+L_2$  with a thin lens skew quadrupole at a position  $L_1$ . If the bunch enters the system with zero emittances and  $\sigma_x$  and  $\sigma_y$  transverse dimensions, at the exit the transverse emittances are

$$\varepsilon_x^2 = \varepsilon_y^2 = \frac{\sigma_x^2 \sigma_y^2}{f^2} \cos^4(kL_1) \cos^2(kL_2) \quad (3)$$

with  $f$  the quadrupole focal length and  $k$  the Larmor wave number of the solenoid. If we substitute in the equation the typical values obtained for SPARC ( $f=10\text{m}$ ,  $\sigma_x=\sigma_y=1.5\text{mm}$ ,  $\gamma=10$ ), the maximum value of the emittance is  $\varepsilon_{nx}=\varepsilon_{ny}=2.25\text{mm mrad}$  that is very close to that obtained with PARMELA code.

A more detailed analysis based on the formalism of the classical evolution operators is reported in [3]. This analysis shows that it is the described geometrical effect the most important contribution to the quadrupole induced emittance growth, while the space charge acts almost independently. This result is confirmed in figure 7 where we plotted the 4D transverse matrix determinant obtained with PARMELA code (that includes the space charge), with and without a skew thin lens quadrupole superimposed to the solenoidal magnetic field. As can be seen, the two curves almost coincide well beyond the exit of the solenoidal field (at about 40 cm). As a consequence the observed emittance growth is actually due to geometrical projection of the 4D invariant along the  $x$ - $y$  planes.

One important conclusion is that the emittance growth can be almost totally compensated by using one or more rotated quadrupoles since it is mainly due to geometrical projection of the 4D determinant. These quadrupoles can be placed immediately out of the solenoid before that the space charge introduces other correlations during the beam evolution in the post-gun drift region.

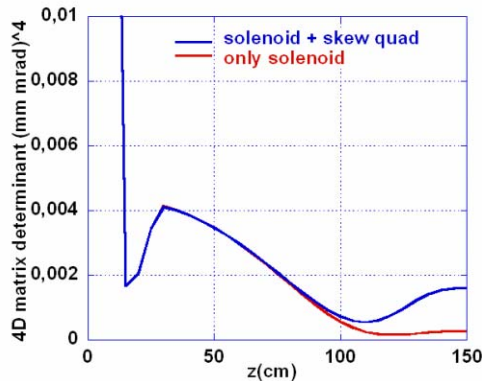


Figure 7: 4D transverse matrix determinant as a function of the longitudinal coordinate, obtained with PARMELA code with and without a skew thin lens quadrupole superimposed to the solenoid.

## EXPERIMENTAL TESTS

The SPARC solenoid uses four different coils that can be powered by different power supply. Taking advantage

of this particular capability, three different options were tested, whose main characteristics in terms of excitation current, rotation angle and steering current are reported in Table 1.

Table 1. Different solenoid configurations.

	Current signs	Current Value	Larmor angle*	Horizontal steering	Vertical Steering
A	++++	125 A	58.8°	3 A	-11 A
B	----	125 A	-58.8°	-2 A	15 A
C	--++	200 A	0°	4 A	1 A

\* $\pm 1.5^\circ$

The value of the current is chosen in order to keep constant the solenoid focusing power and is different between the configurations A,B and the configuration C due to the fact that the magnetic field cancels out (going to zero in the middle of the solenoid) when the coils are not powered with the same sign of current.

The angle of Larmor rotation was measured moving the laser beam on the cathode along horizontal and vertical directions and recording the directions of movement respectively of the electron beam on a target screen located 1.2 m downstream of the cathode.

The last two columns show for the three configurations the different setting of the current on the steering magnet located downstream of the solenoid: the configuration A requires the maximum correction due to the foreseen strong dipolar component superimposed to the solenoid field. A drastic reduction in the steering strength is achieved in the configuration C, where the dipole kicks are applied with different signs and cancel out. Another advantage of configuration C (which on the other hand requires a higher current in the coils) is that the Larmor angle is zero and the horizontal and vertical axes are preserved throughout the system. This simplifies the alignment procedure between the axis of the gun and of the solenoid and allows to study the effects of the ellipticity and/or uniformity of the laser beam on the cathode without recurring to image rotation filters.

As to the effect of the foreseen quadrupolar component: the experimental measurements are not yet conclusive to separate its effect from other sources of beam spot shape deformation and quality degradation (multipoles in the RF gun, misalignments in the compensation system of the laser oblique incidence, beam non uniformities...).

We plan to use more extensively the ability to change the larmor rotation angle independently from the focusing power of the solenoid in order to investigate the different effects.

## REFERENCES

- [1] L. Serafini, “Status of the SPARC Project”, this conference.
- [2] Y. Papaphilippou et al. “Deflection in magnet fringe fields”
- [3] F. Ciocci, et at., “Generalized Twiss Coefficients Including Transverse Coupling and E-beam Growth”, this conference.

# ANALYSIS OF RADIATIVE EFFECTS IN THE ELECTRON EMISSION FROM THE PHOTOCATHODE AND IN THE ACCELERATION INSIDE THE RF CAVITY OF A PHOTOINJECTOR USING THE 3D NUMERICAL CODE RETAR

Vittoria Petrillo, Cesare Maroli, Giorgia Alberti - University of Milan (Italy)  
 Alberto Bacci, Andrea R. Rossi, Luca Serafini - INFN-Milan (Italy)  
 Massimo Ferrario - INFN-LNF, Frascati (Italy)

## Abstract

The three-dimensional fully relativistic and self-consistent code RETAR has been developed to model the dynamics of high-brightness electron beams and, in particular, to assess the importance of the retarded radiative part of the emitted electromagnetic fields in all conditions where the electrons experience strong accelerations. In this analysis we evaluate the radiative energy losses in the electron emission process from the photocathode of an injector, during the successive acceleration of the electron beam in the RF cavity and the focalization due to the magnetic field of the solenoid, taking also into account the e.m. field of the laser illuminating the cathode. The analysis is specifically carried out with parameters of importance in the framework of the SPARC and PLASMONX projects.

$$Q_B = -\frac{n \times (\dot{\beta}(1-n \cdot \beta) + \beta(n \cdot \dot{\beta}))}{c|x-x'| \sqrt{(1-n \cdot \beta)^2}} - \frac{(n \times \beta)(1-n \cdot \beta)^{-2}}{\gamma^2|x-x'|^2}$$

In addition,  $n = (x-x')/|x-x'|$ ,  $\beta = v(t)/c$ , and all time dependent quantities in (3) and (4) are calculated at the retarded time  $\tau$ .

In this paper we will analyse the radiation emitted by a high charge (1 nC) bunch of electrons moving in assigned electric and magnetic fields and under the effect of the self consistent field. We performed the analysis of the electron beam during the extracting from the photocathode and the tracking into a RF Gun. A solenoid field is present to perform the emittance compensation scheme [2-3]. We are interested in the particular aspects of the effects of the retarded radiation on beam dynamic and its exploiting for a non destructive diagnostic.

## INTRODUCTION

RETAR is a hybrid point to point 3D tracking code for the beam dynamic of charged particles, in particular we are focusing on high brightness electron beams. The code is fully relativistic and calculates the self-fields directly from convenient integral forms that can be obtained from the usual retarded expressions [1].

The electric and magnetic field used into the motion equations take into account both external and self-fields. The self-fields are calculated directly in terms of charge density  $\rho(\vec{x}, t)$  at time  $t$  and at all preceding times through the following equations:

$$E(x, t) = \int dx' \rho(x', t) Q_E(x-x', t)$$

$$B(x, t) = \int dx' \rho(x', t) Q_B(x-x', t)$$

where  $\tau = t - \frac{1}{c}|x-x'|$  and

$$Q_E = \frac{n \times ((n-\beta) \times \dot{\beta})}{c|x-x'| \sqrt{(1-n \cdot \beta)^2}} + \frac{(n-\beta)(1-n \cdot \beta)^{-2}}{\gamma^2|x-x'|^2}$$

## CHARGE EXTRACTION

In a point to point tracking code, to simulate the electrons extraction from the photocathode surface in a refined way, it is necessary a huge number of macro-particles (mp) that involves very high time-machine. If the simulations are performed with a low number of mp, numerical noises appear in the phase-spaces, like stratifications and unphysical correlations. To avoid these problems, by using a reasonable numbers of mp, it has been developed an algorithm able to manage the mp like 3D distributions that grow up from the cathode in a gradual way, with an adaptable charge scaled by the outer portion and with an adaptable position fixed in the distribution barycentre. In Fig. 1 (top) there are shown transversal and longitudinal phase-spaces, at 1ps and 2ps, for a flat-top 10ps bunch length and 1 nC bunch charge and the respective transversal views accompanying with their self-fields.

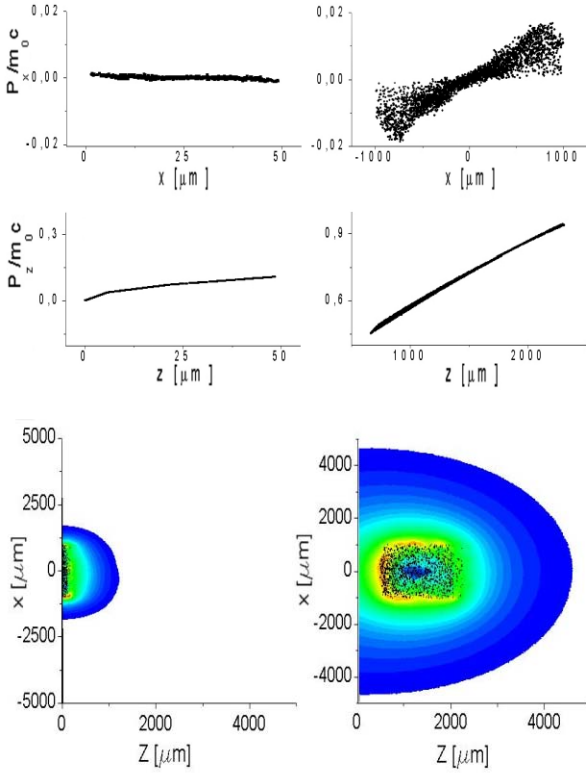


Figure 1: Longitudinal and transverse phase-spaces and electric field density plot for a 1 nC bunch at times  $t=1$  ps (left) and  $t=12$  ps (right)

## ACCELERATION AND RADIATION LOSSES

The amount of emitted radiation is negligible during the extraction process, due to the low accelerations experienced by the electrons. Here the dynamic is dominated by space charge effects: the electric field, starting from a minimum in the centre of the bunch, increases linearly and approaches its maximum on the bunch's edge, as is expected from a uniform cylindrical charge distribution. In particular, from Fig 1 (bottom), we see the strong electric fields generated by the image charges and affecting mostly the trailing area of the bunch. The situation radically changes as the beam begins to gain energy due to the external RF field. In Fig. 2, we see that two wings of emitted radiation build up around the bunch. They manifest a cylindrical symmetry around the  $z$  axis, as expected from the symmetry properties of the source. Such wings are only the most intense portion of a spherical-like wave, with the bunch on the right edge. We note also that the granularity present in the exit phase due to the macroparticle scheme is completely smeared out.

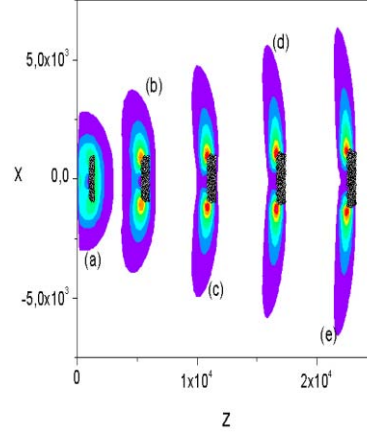


Figure 2: A density plot of the electric vector field for a 1 nC at different times: (a)  $t=17$ psec, (b) 34psec, (c) 51psec, (d) 67psec (e) 84psec

An evaluation of the radiative losses can be given by computing the flux of the Poynting vector through a surface (for instance a cylinder  $S$ ) surrounding the electron beam.

The power irradiated is in fact

$$P_R = \int E \times B \cdot n \, da \quad (1)$$

and the total energy irradiated is given by

$$W_R = \int dt \int E \times B \cdot n \, da \quad (2)$$

The power  $P_R$  on a cylinder surrounding the beam and with a radius  $r=5$ mm as function of time is represented in Fig 3.

The power is initially zero until a time  $t \sim r/c$ , due to the delay in arriving on the surface of the cylinder, is elapsed, followed then by a sequence of maxima and minima.

From the comparison between the shape in time of the power emitted and the shape of the external electric and magnetic fields as seen by the electrons of the bunch, we can say that the first peak of radiation is due to the first maximum of the accelerating electric field, reshaped by the retard effects, while the second peak corresponds to the second peak of acceleration, superimposed with the entrance into the magnetic field. Afterwards there is a less accentuated peak of radiation, corresponding to the exit from the solenoid, that for the case of the larger charge is not visible on the scale of the graph.

The evaluation of the power emitted by the beam on the basis of the Larmor formula (3), applied as if the beam were a single charge of 1 nC, gives a peak of radiation of  $P=8.3 \cdot 10^4$  Watt. Accounting for the internal structure of the beam diminishes this value of a factor 10-20%, and this difference increases with increasing charges.

The integration in time of the power gives the total energy. For the values  $Q=1$  nC and  $5$  nC the total energy is respectively  $E=2,25 \cdot 10^{-5}$  J and  $E= 1,9 \cdot 10^{-4}$  J. Values of this order should not be difficult to measure experimentally.

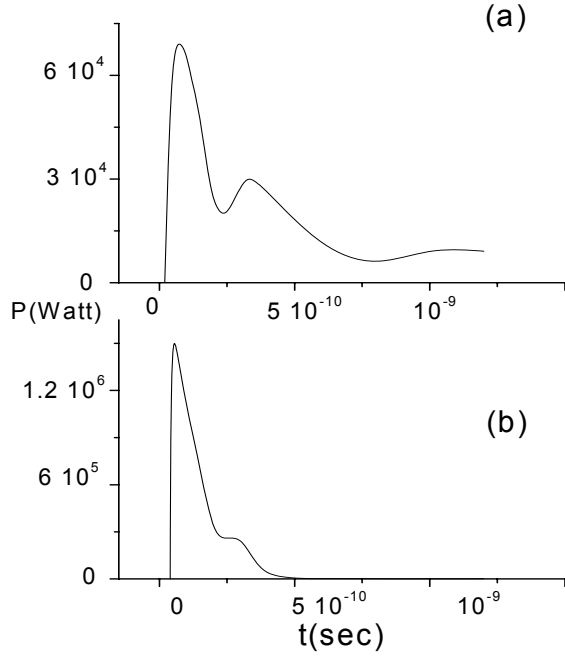


Figure 3: Total emitted power for (a)  $Q=1$ nC and (b)  $Q=5$  nC

### Using of the Radiated Energy/Power as a Diagnostic Tool

The monitoring of the emitted retarded radiation can be used to gain information about the bunch. As an example, from the Liénard result that generalizes the Larmor formula for point-like charge far from the source

$$P = \frac{2}{3} \frac{q^2}{c} \gamma^6 [(\dot{\beta})^2 - (\beta \times \dot{\beta})^2] \quad (3)$$

we see that the total emitted energy scales with the square of the bunch charge. Deviations from this dependence can appear for large values of beam charge due to space charge effects and for measurements taken near to the beam. For a  $1$  nC bunch, the total radiated energy (over  $2\pi$  angle) is about  $22.5 \mu\text{J}$ ; the power pulse can be thought of as an emission peak with a rise time of about  $100$  ps and a  $70$  kW peak value, followed by a  $400$  ps tail.

For sake of simplicity we model it as a  $75$  kW square pulse of  $300$  ps duration, yielding the same pulse energy, and expect an associated bandwidth of about  $3$  GHz. Assuming a  $1\%$  coupling to a  $1$  GHz device, we have a coupled peak power of  $750$  W. For a  $1$  Hz bunch

repetition rate the average power is  $0.225 \mu\text{W}$ . These results agree with the data shown in Fig. 4, where the electric field calculated in a point far from the beam is shown as a function of time (top), together with its FFT (bottom).

Typical diode detector sensitivities are about  $0.5 - 1$  mV/ $\mu\text{m}$  so an output voltage of about  $0.1 - 0.2$  mV should be expected, for a CW or long pulse. Because of its short duration, the single pulse measurement is not feasible, but an integrated and averaged measure over many pulses can be achieved. In this way indication of the bunch charge can be obtained.

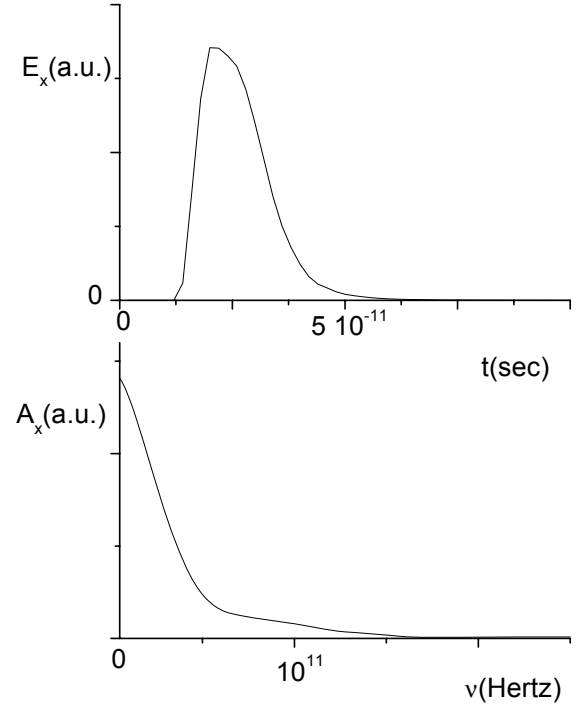


Figure 4: The electric field as a function of time(top) and the signal FFT (bottom).

### REFERENCES

- [1] A. Bacci, C. Maroli, V. Petrillo, L. Serafini, “Self-Consistent 3D PIC code of high-brightness beams”, proceeding of the 2003 Particle Accelerator Conference.
- [2] L. Serafini and J. B. Rosenzweig, “Envelope analysis of intense relativistic quasilaminar beams in rf photoinjectors: A theory of emittance compensation” Phys. Rev. E **55**, 7565-7590 (1997).
- [3] M. Ferrario et al., “Recent Advances and Novel Ideas for High Brightness Electron Beam Production based on Photo-Injectors”, INFN Rep. LNF-03/06 (P), May 2003; published in The Physics & Applications of High Brightness Electron Beams, J.Rosenzweig and L. Serafini ed., World SCI.

# THE RF DEFLECTOR FOR THE CTF3 DELAY LOOP

Fabio Marcellini, David Alesini, INFN-LNF, Frascati (Rome) - Italy

## Abstract

In the CLIC Test Facility 3 (CTF3), a 42 m long ring, called Delay Loop (DL), is used to halve the distance between bunches in the drive beam. The compression is obtained by merging two adjacent bunch trains from the linac deflected in opposite directions by an RF device, in such a way that the first train is forced to perform a full revolution in the DL, while the second one passes through. The length of the ring is an odd multiple of half the distance between bunches in the beam from the linac. The RF deflector (RFD) consists of two identical cavities connected to the RF power source through a hybrid junction that equally splits the power and isolates the klystron from reflections. Its innovative design, the results of electromagnetic simulations and expected performances are described, together with low level RF measurements for test and characterization of the device before installation. Preliminary recombination results with the CTF3 beam are also shown. The RFD has also been used to measure the length of the accelerated bunches.

the beam takes the same deflection in the two gaps. The cavity deflecting mode is the  $TM_{110}$ . The Q is determined by proper dimensioning of the input coupler and the chosen value results from a compromise between the needs to have enough shunt impedance and sufficiently fast rise time as response to the RF pulse. The cavities reflect back the incident power both during the transients (the resonance has finite bandwidth) and the flat-top of the pulse (the input coupling coefficient is  $\beta \neq 1$ ). However the HJ isolates the klystron from this reflected power, while it is dissipated in the load.

## DEFLECTOR DESIGN

All the waveguide components of the system have been manufactured by Mega Industries [3] and are WR650 standard products. They are reinforced to stand the 3 bar SF6 over-pressure. Only the HJ has been externally dimensioned to fit the separation between the two cavities. Four directional couplers have been inserted close to the cavities, the load and the klystron to have a monitor of the forward and reflected power.

## DEFLECTOR SYSTEM DESCRIPTION

The RFD is essential in the bunch frequency doubling process that takes place in the DL [1].

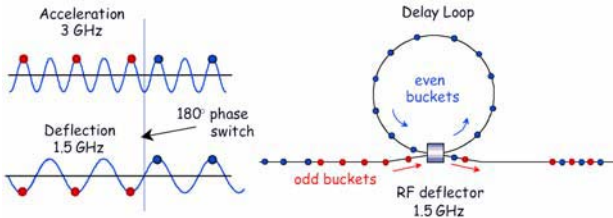


Figure 1: Sketch of the bunch frequency multiplication in the CTF3 Delay Loop.

Referring to the scheme illustrated in Fig. 1, the beam coming from linac is composed of an alternate sequence of so called even and odd trains, which differ for a  $180^\circ$  phase jump between each other. This sequence of 140ns long sub-trains is realized by a pre-bunching system. The RF deflector gives kicks of the same amplitude but opposite sign to the incoming even and odd trains. The even trains are injected into the ring and, after a turn, they are extracted and interleave with the following odd train.

The RFD system deflects of  $\pm 15$  mrad beam with energy up to 300 MeV. The total train length is  $1.4 \mu\text{s}$  and the deflection given to the bunches is uniform within 1%. Peak power and duration of the RF pulses feeding the RFD are 20 MW and  $5 \mu\text{s}$  respectively.

The RFD has been conceived [2] as two cavities fed by the same klystron through a  $90^\circ$  hybrid junction (HJ). Being the cavities  $(1+1/4)\lambda_{\text{RF}}$  apart, where  $\lambda_{\text{RF}}$  is the free space wavelength at the RF frequency (1.499275 GHz),

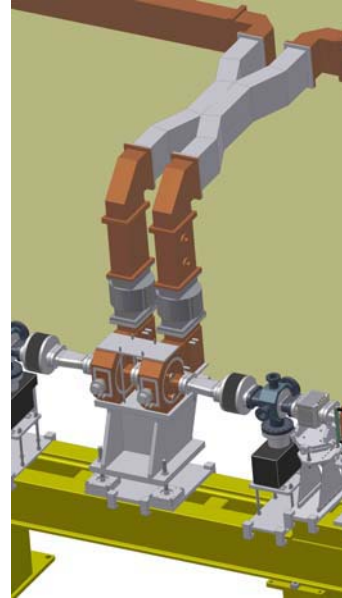


Figure 2: CAD drawing of the Delay Loop region with the RF deflector system.

In the drawing of Fig. 2 the two vacuum windows that separate the SF6 from the vacuum environments are also visible (in grey, flange coupled to the cavities). Their manufacture has been made by Thales [4] on the same design of the window on the klystron output. In the two branches between the cavity couplers and the HJ the RF wave configuration is partially standing, being the cavities over coupled. Then, for safety reasons, the window position has been chosen in correspondence of a minimum of the fields along the waveguide line.

The cavities (see Fig.3) have a pill-box shape with a rectangular beam pipe. The input coupler is realized with a section of WR650 waveguide terminated on a short circuit and it is placed to one side of the cavity.

Waveguide and cavity volumes communicate through a coupling hole. The position and the diameter of this hole determine the coupling coefficient  $\beta$ .



Figure 3: Picture of the two RF cavities of the deflector.

On the opposite side respect to the coupler, the cavities have a 15mm diameter cylindrical tuning plunger. It can be manually moved to vary its penetration into the cavity and to adjust the frequency of the deflecting mode. The frequency sensitivity to the tuner penetration is about 150 kHz/mm.

Two probes, which monitor the field inside the cavity, are placed on the external flat plate of each cavity.

The cavities have been completely designed with the HFSS code [5]

The cavities, fabricated in Poland by the A. Soltan Institute [6] according to the electromagnetic and mechanical design developed at Frascati, are made of OFHC copper and are provided with five coils where the water for temperature stabilization ( $30 \pm 0.1^\circ\text{C}$ ) flows.

## TUNING UP AND MEASUREMENTS

The frequency responses of each component of the system have been measured to verify their correspondence with the design specification and with the results obtained from HFSS simulation code.

In particular, the most critical parameters, such as the phase relation and the balancing between the HJ output ports or the load SWR, have been verified to be within the specified tolerances.

Moreover, to optimize the isolation of the klystron from the reflected power, all the components connected to the two lower branches of the HJ (cavities, windows, bends and drift waveguides), must be as identical as possible, so that the impedance seen from those ports of the HJ is the same. For this reason an accurate tuning of the resonant frequency of the cavity operating mode is necessary.

The frequency response of each of the two cavities has been measured with a network analyzer connected between the input port (the klystron side port) of the HJ and the cavity probes. After the installation, with the vacuum pumps switched on and the temperature of the cooling water stabilized, the transmission response has been centred at the working frequency for both the

cavities acting on the tuner penetration depth. In Fig. 4 the measured frequency response of one of the two cavities after its tuning is reported.

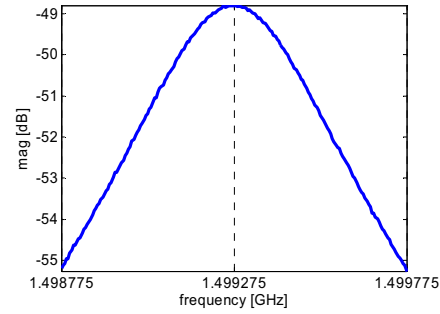


Figure 4: S21 from HJ input port to one cavity probe.

The cavity Q values are evaluated from S21 measurements as well; they differ for less than 7% but are within the range (3000-3500) fixed as requirement. The resulting cavity rise times are fast enough to limit the drop of the deflecting voltage along the 1.4  $\mu\text{s}$  train at less than 1%. Fig.5 shows the time domain signal monitored from one cavity when the 5  $\mu\text{s}$  RF pulse is applied. The voltage in the last 1.4  $\mu\text{s}$  of the pulse is flat enough.

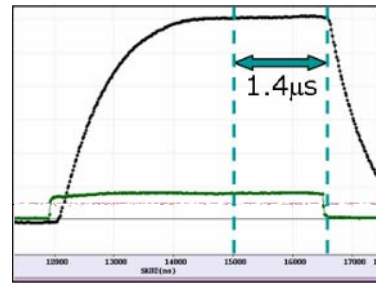


Figure 5: Cavity voltage vs. time with 5ns input pulse.

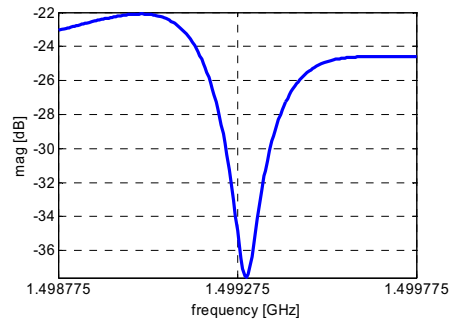


Figure 6: S11 HJ input port after fine tuning.

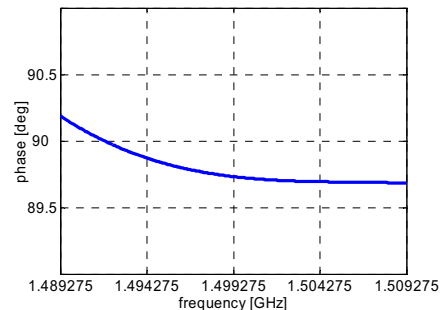


Figure 7: phase difference between the signals taken from the two cavities fed through the HJ.

In Fig.6 and Fig. 7 the reflection response at sinusoidal CW excitations measured at the HJ input port and the measured phase difference between the signals in the two cavities are shown respectively.

## OPERATION PERFORMANCES

The RFD has been successfully used during the first phases of the DL commissioning. It started to work for a few days in November '05 only for beam injection and extraction in and out the DL. In the following shift of operation, when the bunch trains from the linac had the right phase encoding and they are differentiated between even and odd trains, the recombination was soon obtained and then improved within the period of a couple of weeks.

Fig.8 illustrates the results of recombination procedure. The beam current, equally distributed along the ten incoming sub-trains, results almost doubled where the trains are recombined and near to zero elsewhere.

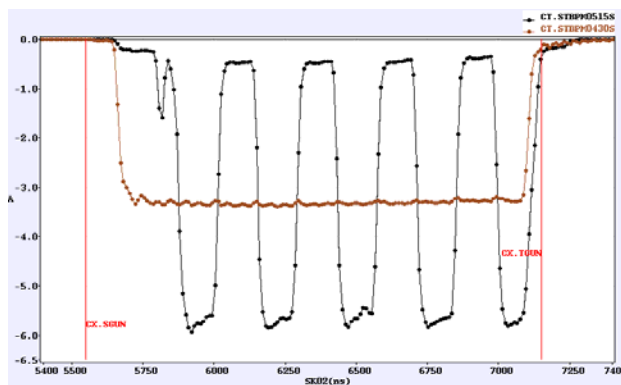


Figure 8: The beam current in the transfer line before the DL (brown) and after recombination (blue).

The RFD can be used as a diagnostic device to measure the bunch length: if the RF phase is 90 deg shifted respect to normal operation condition, the bunches cross the cavities where the field amplitude is zero and time derivative is maximum. Then the field in the RFD induces a strong correlation between particle longitudinal position in the bunch and transverse position after the kick; a measurement of the beam profile downstream of the RFD gives direct information of the bunch longitudinal length before the kick.

Fig.9 shows two beam images taken on the first OTR after the RFD when it was switched off and fed at 10 MW respectively.



Figure 9: Unprocessed bunch images. Left: RFD switched off. Right: RFD on, at zero-crossing phase.

If the phase is different from the zero-crossing condition, the even and the odd bunches receive deflections with opposite direction and the image presents two separated beam.

The images of Fig.9 and others obtained at different phases ( $\pm 5^\circ$ ,  $\pm 10^\circ$  and  $\pm 15^\circ$ ) have been processed [7] to get the measure of the bunch length that, at this stage of machine commissioning, results 5.45mm.

## CONCLUSIONS

The RF Deflector system for the CTF3 Delay Loop is a non conventional device realized with two SW TM<sub>110</sub> resonating cavities connected to the RF power source through a 90° Hybrid Junction. This device has the twofold function to feed with the right phase relation the cavities and to isolate the klystron from the power reflections. Very good results have been obtained from low power measurements, which have confirmed the predictions of simulations and the feasibility of this scheme.

The deflector has started to work successfully at about half of maximum input power since the energy of the beam has not yet reached the 300MeV upper limit. First results of the train recombination indicate that the deflector performances fulfil the expectations.

## ACKNOWLEDGMENTS

All the CTF3 team at CERN has given a fundamental contribution to the realization of the deflector: several discussions with the project leader G. Geshonke and RF group people have led to the definition of parameters; special thanks to G. Mc Monagle and G. Rossat for the technical information about plants and the logistic support and S. Mathot for the suggestions concerning the brazing procedure.

As in the case of the Combiner Ring deflector, the collaboration with Soltan Institute for the fabrication of the cavities has given very good results.

Thanks also to D. Filippetto e B. Preger for the post-processing of the raw images of the beam in the bunch length measurement.

## REFERENCES

- [1] "CTF3 Design Report", CERN PS 2002-008 (RF), Geneve, (2002).
- [2] F. Marcellini, D. Alesini "Design Options for the RF Deflector of the CTF3 Delay Loop", EPAC'04, Lucerne, July 2004, p. 689, <http://www.jacow.org>.
- [3] <http://www.megaind.com/>
- [4] <http://www.thalesgroup.com/electrondevices>
- [5] <http://www.ansoft.com/products/hf/hfss/>
- [6] <http://www.ipj.gov.pl/>
- [7] D.Filippetto and B. Preger: *private communications*.

## THE PLASMONX PROJECT FOR ADVANCED BEAM PHYSICS EXPERIMENTS

D. Alesini, M. Bellaveglia, S. Bertolucci, R. Boni, M. Boscolo, M. Castellano, A. Clozza, G. Di Pirro, A. Drago, A. Esposito, M. Ferrario, L. Ficcadenti, D. Filippetto, V. Fusco, G. Gatti, A. Gallo, A. Ghigo, M. Incurvati, C. Ligi, F. Marcellini, M. Migliorati, A. Mostacci, L. Palumbo, L. Pellegrino, M. Preger, R. Ricci, C. Sanelli, M. Serio, F. Sgamma, B. Spataro, A. Stecchi, A. Stella, F. Tazzioli, C. Vaccarezza, M. Vescovi, C. Vicario (INFN/LNF);

F. Alessandria, A. Bacci, R. Bonifacio, F. Broggi, M. Cola, C. DeMartinis, D. Giove, C. Maroli, M. Mauri, V. Petrillo, N. Piovella, R. Pozzoli, M. Romè, A. R. Rossi, L. Serafini, L. Volpe (INFN/Milano);

D. Levi, M. Mattioli, P. Musumeci, G. Medici, D. Pelliccia, M. Petrarca (INFN/Roma1);

U. Bottigli, B. Golosio, P. Oliva, A. Poggiu, S. Stumbo, INFN/Cagliari and Univ. of Sassari, Italy

A. Barbini, W. Baldeschi, C.A. Cecchetti, M. Galimberti, A. Giulietti, D. Giulietti, L.A. Gizzi, P. Koester, L. Labate, S. Laville, A. Rossi, P. Tomassini, CNR-IPCF/Pisa and Univ. of Pisa

### *Abstract*

The Project PLASMONX is well progressing into its design phase and has entered as well its second phase of procurements for main components. The project foresees the installation at LNF of a Ti:Sa laser system (peak power > 170 TW), synchronized to the high brightness electron beam produced by the SPARC photo-injector. The advancement of the procurement of such a laser system is reported, as well as the construction plans of a new building at LNF to host a dedicated laboratory for high intensity photon beam experiments (High Intensity Laser Laboratory). Several experiments are foreseen using this complex facility, mainly in the high gradient plasma acceleration field and in the field of monochromatic ultra-fast X-ray pulse generation via Thomson back-scattering. Detailed numerical simulations have been carried out to study the generation of tightly focused electron bunches to collide with laser pulses in the Thomson source: results on the emitted spectra of X-rays are presented.

### **CPA 100 TW-CLASS LASER SYSTEM**

While the SPARC Project is in its commissioning phase at LNF, where the first high brightness electron beams produced by the SPARC photo-injector are under characterization [1], its long term upgrade, based on the project PLASMONX, has entered its acquisition phase, after completion of the design of the system [2]. The first phase, after approval by INFN, is aimed at building at LNF a 100 TW-class laser system as the core system of a High Intensity Laser Laboratory (HILL), and a final goal of constituting a national facility merging advanced technologies and expertises in high brightness electron

beams and high intensity laser beams, as well as plasma wave formation, control and diagnostics. Under this respect, the collaboration between INFN and CNR-IPCF is considered to be strategic to the realization of the final phase of the facility, where synchronized electron and photon beams of ultra-high performances, in terms of brightness, intensity and brevity will be driven to interact in several fashions, in order to allow investigations of high gradient acceleration techniques and/or X-ray production via Thomson back-scattering in the spontaneous incoherent mode or, eventually, in the coherent collective mode. The proposed time schedule for this initiative is tightly correlated with the progress of the SPARC project: according to this schedule, final completion of the SPARC&PLASMONX facility is foreseen by the year 2009.

The proposed laser system [3] must have unique performances in terms of power, pulse duration, flexibility and reliability: it will be installed inside the dedicated HILL building at LNF, located just outside the underground SPARC bunker. The laser system, based upon the C.P.A. technique, will deliver < 50 fs, 800 nm, >100 TW, laser pulses at 10 Hz rep. rate. The 5 J laser pulses will be transported uncompressed from the HILL laboratory down into the SPARC bunker. The proposed system combines the reliability of established Ti:Sa technology with novel additional devices aimed at overcoming known issues typical of large Ti:Sa systems.

One of these issues concerns the power contrast ratio, namely the ratio between the main CPA pulse and the so-called “pedestal”, a spurious precursor radiation arising from amplified spontaneous emission (ASE) by amplifiers. The block diagram of Figure 1 shows the main components of the system, including the devices necessary for ensuring the high quality of the final output.

The oscillator produces a 10 fs pulse that is stretched and pre-amplified by a two stage amplifier up to the 30 mJ level per pulse. Approximately half of this energy is extracted and compressed to provide a low energy beam for probing/diagnostic purposes. The remaining part of the pulse is further amplified to the 8 J level and finally compressed under vacuum. Besides the standard vacuum spatial filter necessary for beam cleaning, we plan to insert an adaptive optics before the vacuum compressor. This device will enable us to remove aberrations on the beam which may result in a poor performance of the compressor as well as poor quality of the focal spot after focusing. Concerning the control of the pulse duration, the system includes a Dazzler device which will enable correction of the spectral features of the pulse prior to stretching. These corrections are necessary in order to keep the final pulse-length well below the 100 fs level. In fact, we aim at reaching the  $< 50$  fs pulse-length which is now regarded as the minimum pulse duration achievable in a multi-joule Ti:Sa laser system. The main beam characteristics after the vacuum compressor are foreseen to be: pulse energy 5 J, peak power  $> 100$  TW, contrast ratio  $< 10^{-5}$ .

We plan to conduct R&D on the OPCPA technique, that exploits the non-linear properties of some crystals for the amplification of optical pulses: we aim at an inherently low ASE system in which the ASE level is drastically reduced in the initial amplifier stages. In fact, it is estimated that with an OPCPA system in place, the final pulse length could be as short as 30 fs, thus leading to a peak power as high as 170 TW on target and a contrast ratio smaller than  $10^{-8}$ .

Most of the proposed programme relies on the synchronisation of the laser system with the SPARC Linac and, in particular, with the photoinjector laser system. This can be done either using an electro-optics

based approach or optically. In the first way the laser oscillator is synchronized with an external rf signal, by changing dynamically the oscillator cavity length: a jitter between the rf and the laser pulse of less than 1ps is typically achieved. The fully optical approach consists in synchronising the two laser systems. This can be done either by using the same oscillator for both lasers or by measuring the change in delay between the two laser pulses (*i.e.* using a single shot second order cross correlator) with a precision of tens of femtoseconds, and then adjust dynamically a delay line in one of the two laser system.

### X-RAY THOMSON SOURCE

We studied the head-on collisions between the SPARC electron beam and the FLAME photon beam with the aim of producing mono-chromatic Thomson X-rays with energy tunable in the range 20-900 keV. We report here the result of the optimization study performed with start-to-end simulations starting from the photocathode and producing the angular and frequency spectra of the emitted X-rays. Only the case of 20 eV photons is reported, which is of interest for a planned experiment of digital mammography using mono-chromatic X-rays.

The main challenge regarding the electron beam generation is to focus down a high charge beam (1-2 nC) to focal spot sizes below 10 microns in the collision point, which in turns implies to accurately take under control emittance and energy spread of the beam itself [4].

This is necessary in order to reach high fluxes in the X-ray beam, which scales like the inverse of the square of the spot size.  $10^{10}$  photons/sec is the goal of the mammography experiment, which means  $10^6$  photons per collision at the SPARC rep rate of 10 Hz (the FLAME laser has similar rep rate as well).

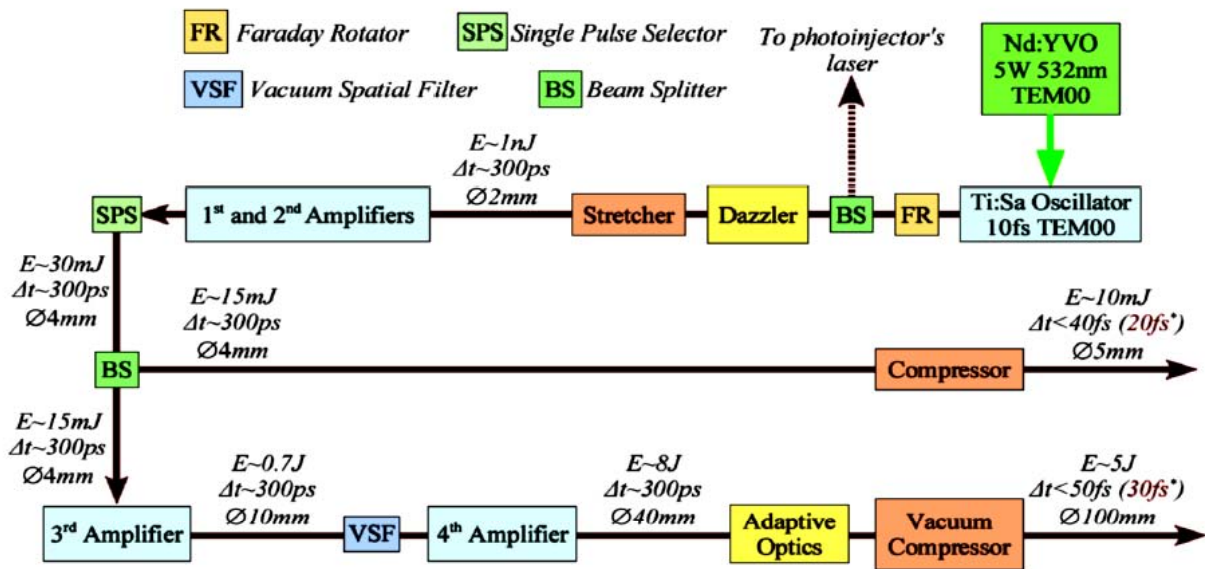


Figure 1: Lay-out of the FLAME Laser System.

ASTRA simulations of the SPARC photo-injector operated to produce a 30 MeV electron beam to the collision point show that by properly correcting the correlated energy spread with the use of a 4-th harmonic cavity we can reach a longitudinal phase space distribution as shown in Figure 2, displaying a rms energy spread smaller than  $2 \cdot 10^{-4}$ .

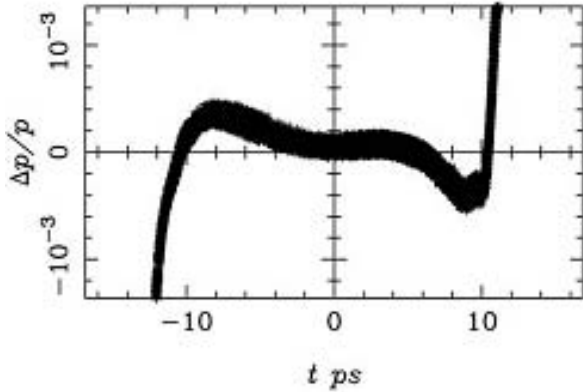


Figure 2: Longitudinal phase space distribution at Linac exit.

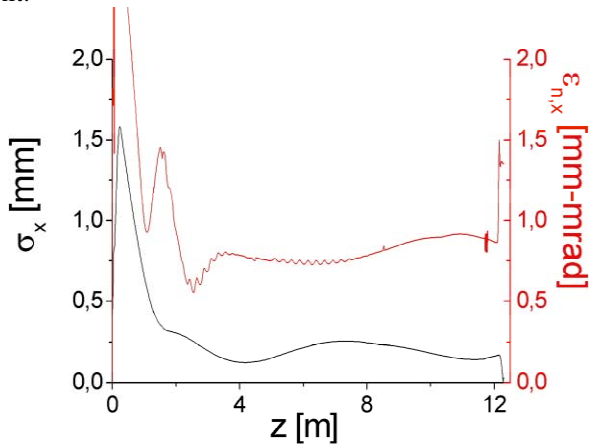


Figure 3: Beam emittance and envelope along z

A careful emittance compensation performed through the injector leads to a sub-micron rms normalized transverse emittance at the final focus, as shown in Fig.3. The resulting rms focal spot size is 9 microns. This allows

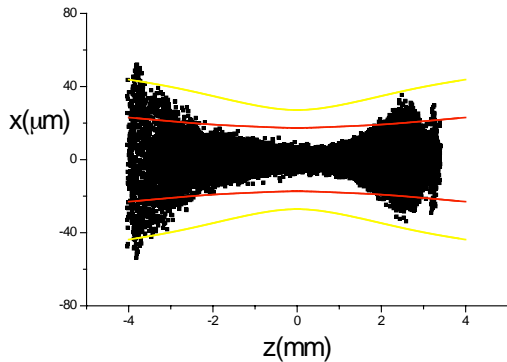


Figure 4: Electron bunch and laser pulse overlap at the final focus in the collision point

in turns to maximize the number of X-ray photons generated in the collision. The frequency spectrum is shown in Figure 5 at different angle of collimation [5].

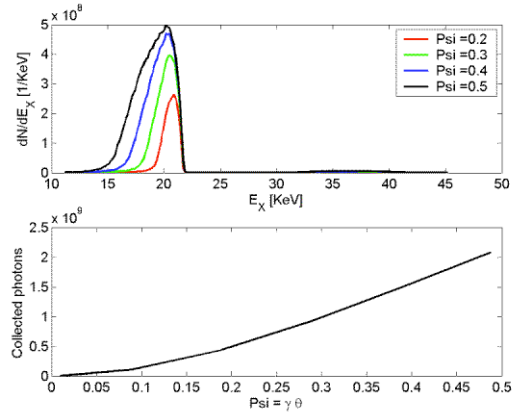


Figure 5: X-ray spectra for different solid angle collimation

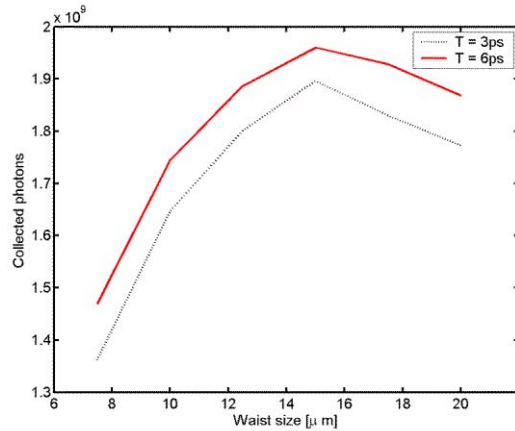


Figure 6: X-ray yield vs. laser spot size and pulse length

The total number of emitted photons within a frequency bandwidth of 5% rms is given in Fig.6 as a function of the laser spot size and for 3 and 6 ps, respectively, of laser pulse length. We can reach about  $2 \cdot 10^9$  photons per pulse, which is considered, at 10 Hz rep rate, a satisfactory flux to perform advanced radiological imaging with monochromatic X-rays [6].

## REFERENCES

- [1] D. Alesini et al., Status of the SPARC Project, these proceedings
- [2] D. Giulietti et al., PLASMONX: Conceptual Design Report on PLASma acceleration and MONochromatic X-ray production, unpublished
- [3] D.Alesini et al., IEEE Cat. N. 05CH37623C, (2005) 820
- [4] W.J. Brown et al, Phys. Rev. STAB 7 (2004) 060702
- [5] P. Tomassini, et al, Appl. Phys. B 80 (2005) 419
- [6] A. Bacci, M. Ferrario, C. Maroli, V. Petrillo, L. Serafini, Phys. Rev. STAB (in print)

# THE DESIGN OF A HYBRID PHOTOINJECTOR FOR HIGH BRIGHTNESS BEAM APPLICATIONS

David Alesini, Massimo Ferrario, Valeria Fusco, Bruno Spataro (INFN/LNF, Frascati (Roma))  
 Luca Ficcadenti, Andrea Mostacci, Luigi Palumbo (Rome University La Sapienza, Roma)  
 Brendan O'Shea, James Rosenzweig, Gil Travish (UCLA, Los Angeles, California)

## Abstract

In this paper, we illustrate the electromagnetic and beam dynamics design procedure of a new class of photoinjector, a hybrid standing/traveling wave structure. In this device a standing wave RF gun section is integrated with a downstream traveling wave structure through a coupling cell that feeds simultaneously the two sections. We discuss the advantages in RF and beam performance of the hybrid photoinjector compared to conventional systems. The electromagnetic design has been performed using the 3D electromagnetic code HFSS. Results of beam dynamics simulations in different operating conditions are also discussed.

## INTRODUCTION

The most prevalent photoinjector design in use today employs an arrangement of two accelerating structures: a standing wave (SW) gun and a post accelerating linac. The two structures are fed independently and, since the SW structure reflects nearly all of the input power at the beginning of the RF fill process, circulators and isolators need in order to protect the RF power source. A considerable interest exists for the implementation of compact photoinjectors that can produce low emittance beam with energies in the 20-30 MeV range and are scalable to high frequency. The hybrid structure (HS) that we have designed for this purpose is shown in Figure 1. It begins at the upstream end with the SW RF gun section in the initial cells, which is coupled on-axis to the RF power that is fed from the waveguide into the structure through a standard traveling wave (TW) coupling cell. This coupling cell also serves as the initial cell of a downstream TW linac section. The main advantages of this device are that:

- a) this scheme serves to nearly eliminate impedance mismatches, and therefore reflected RF power, both during and after the RF filling of the SW section; the near complete removal of the transient RF reflected power allows scaling to high frequency where circulators and isolators are more difficult to construct;
- b) the device requires a much simpler high power RF system than a split photoinjector: there is one klystron only and waveguide sections, attenuators, and phase shifters are avoided;
- c) the device is much more compact than a split system;
- d) since, for beam dynamics reasons, lower gradient can be used in the SW section, it is possible to scale the design at high frequency (without reaching intolerable field gradients);

- e) the acceleration dynamics are robust, allowing flexibility in operating energy by simply changing RF power and laser injection parameters;
- f) the HS avoids the bunch lengthening observed after the exit of the SW gun during the drift in a split photoinjector;
- g) a simpler system allows a more feasible approach to turn-key operation;
- h) the TW section will be more straightforward to fabricate than a long SW accelerator.

In the first part of the paper we illustrate the general procedure to design the HS. In particular we will discuss the results of the electromagnetic simulations obtained with HFSS [1]. In the second part of the paper we illustrate the results on beam dynamics simulations.

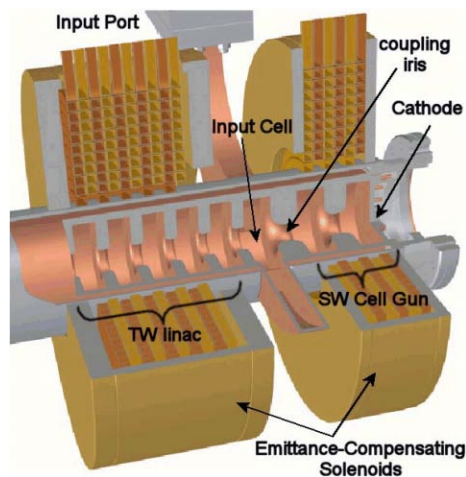


Figure 1: 3D drawing of the compact hybrid structure.

## HYBRID PHOTOINJECTOR RF DESIGN

The structure can be divided in two main parts: the SW and the TW sections. In the ideal case they are divided by a perfect magnetic plane in the center of the coupling iris (see fig. 1) corresponding to the zero crossing of the longitudinal electric field. As a consequence it is possible to design the two structures separately with a perfect magnetic plane in the center of the coupling iris in order to achieve a uniform field flatness of the longitudinal electric field ( $E_z$ ) in the SW gun and a zero reflection coefficient at the waveguide input port of the TW section, at the working frequency of the whole system. The final tuning of the HS can be done after this first step assembling the two parts and slightly adjusting the SW cell dimensions to perfectly tune the SW gun on resonance. It should be pointed out that, in principle, the coupler cell length and the coupling iris dimensions

(diameter and thickness) should be chosen in order to have, simultaneously, the desired ratio between the maximum amplitudes of  $E_z$  in the SW and TW sections ( $E_{z\_SW}/E_{z\_TW}$ ) and the correct  $E_z$  phase seen by the accelerated particles. In our design we have considered a 1.6 cell SW gun and  $2\pi/3$  mode accelerating TW structure and we have tuned the HS using HFSS whose 3D model is shown in Fig. 2.

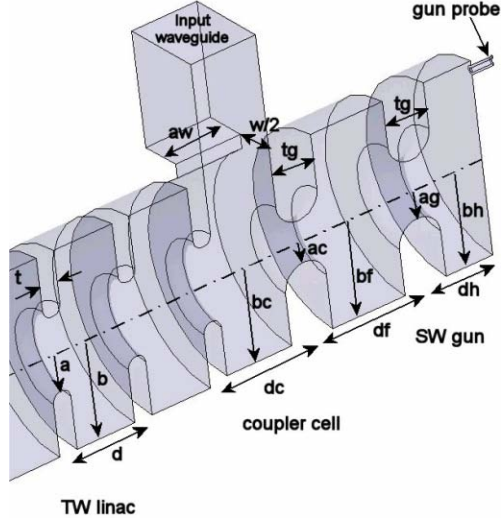


Figure 2: HFSS 3D model of the HS.

### Properties of the Electromagnetic Field in the HS

The accelerating field in the structure can be written in the general form as:

$$E_z(z, t) = E_0(z) \cos(Ph_E(z) + \omega_{RF}t)$$

where  $E_0(z)$  and  $Ph_E(z)$  are the complex amplitude and phase of the accelerating field. There are several properties of  $E_z$  that can be summarized as follows:

- the phase difference between the full cell of the SW gun and those of the input coupler cell does not depend on the geometry of the input coupler cell and iris dimensions and is about 90 deg. Typical  $E_0$  and  $Ph_E$  profiles are shown in fig. 3 as a function of the longitudinal coordinate. The result is referred to an HS operating at 2.856GHz tuned using HFSS but can be easily generalized to other working frequencies. This result could be justified with an equivalent circuit model of the structure;
- the coupling iris diameter allows adjusting the ratio  $E_{z\_SW}/E_{z\_TW}$ : in particular if we increase the diameter we increase this ratio;
- for values of the ratio  $E_{z\_SW}/E_{z\_TW}$  up to 5 the perturbation on the matching of the waveguide input port with respect to the situation without SW gun is completely negligible. This is shown in Fig. 4 where the reflection coefficient at the input port of the structure is plotted with and without the SW structure. In the same plot the transmission coefficient between the gun probe and the waveguide input port is also reported.

Since  $E_z$  phase between the SW gun and the TW section is fixed, the accelerating field and the beam can be

synchronized by properly choosing the length of the input coupler cell ( $dc$ ). In particular with  $dc = 2/3\lambda_{RF}$  the beam enter in the TW section exactly on crest while with  $dc = 5/12\lambda_{RF}$  the bunch enter in the TW section on the slope of the  $E_z$  and it can be longitudinally compressed using the velocity bunching technique [2]. We call the first option continuous acceleration (CA) and the second one velocity bunching acceleration (VB). In table 1 we report the main dimensions of the two structures referred to Fig.2.

Table 1: Main dimensions in mm of the HSs

Dim	CA	VB	Dim.	CA	VB
dc	69.98	43.74	aw	36.07	30.21
df	52.48	52.48	w	33.3	35.2
dh	31.48	31.48	a	16	16
d	34.99	34.99	b	42.89	42.89
bc	40.53	40.93	ag	12.5	12.5
bf	41.66	41.7	ac	9	9
bh	41.65	41.67	tg	19.05	19.05

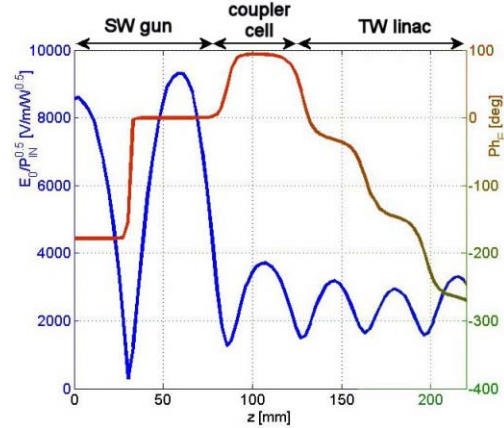


Figure 3: typical plot of  $E_z$  in the HS (HFSS simulation).

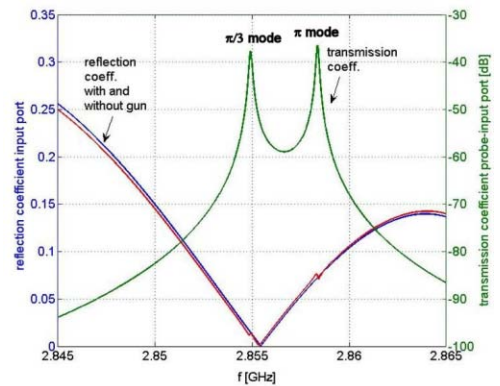


Figure 4:  $S_{11}$  at the waveguide input port and  $S_{21}$  between the gun probe and the waveguide input port.

The phase between the SW and the TW structures has a high sensitivity to the resonant frequency of the SW structure itself, as shown in Fig. 5a where  $Ph_E(z)$  has been plotted for different resonant frequencies of the SW gun. In the same figure the amplitude of the accelerating field

$E_0(z)$  is also reported. This sensitivity requires very good temperature stabilization of the SW section since  $\sim 0.5\text{deg/kHz}$  corresponds to  $\sim 22\text{ deg}^\circ\text{C}$ . On the other hand, with good temperature control, it is possible to tune the phase difference between the two structures optimizing the photoinjector performances during operation without changing the amplitudes of the accelerating field.

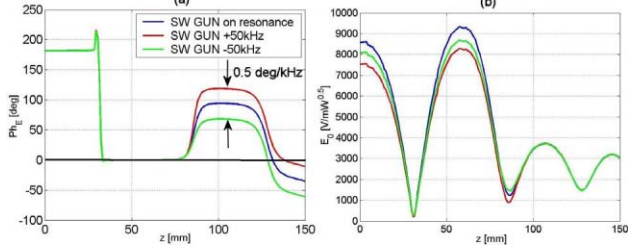


Figure 5: (a)  $E_0$  and (b)  $Ph_E$  as a function of the longitudinal position for different resonant frequencies of the SW gun.

## BEAM DYNAMICS SIMULATION

Beam dynamics simulations have been done in both cases of CA and VB using the PARMELA [3] and HOMDYN [4] codes. The amplitude of the  $E_{z,SW}$ ,  $E_{z,TW}$  accelerating fields, the solenoid field in the SW and TW structures ( $B_{z,SW}$ ,  $B_{z,TW}$ ) and the laser input phase have been optimized to maximize the brilliance of the beam at the end of the structure. The results of preliminary simulations in term of beam energy, normalized emittance, energy spread and bunch length along the structure are reported in the Figs. 6-7 for the case CA and VB respectively, using the parameters reported in table 2. The beam parameters at the end of the HSs are summarized in table 3.

Table 2: Parameters of HS beam dynamics simulations

Parameter	CA	VB
Charge [nC]	1	1
Laser pulse length [ps]	10	10
Laser spot size radius [mm]	1.6	1.6
Total length of the HS [m]	2.2	3.1
$B_{z,SW}$ [T]	0.2	0.15
$B_{z,TW}$ [T]	0	0.05
$E_{z,SW,acc}$ ( $E_{z,SW,peak}$ ) [MV/m]	35 (70)	35 (70)
$E_{z,TW,acc}$ ( $E_{z,TW,peak}$ ) [MV/m]	13.5 (18)	13.5 (18)

Table 3: Beam parameters at the end of the HS

Parameter	CA	VB
Rms norm emittance [mm mrad]	1.8	3.3
Energy [MeV]	31	19
Energy spread [%]	0.8	2.6
Rms bunch length [mm]	0.95	0.14

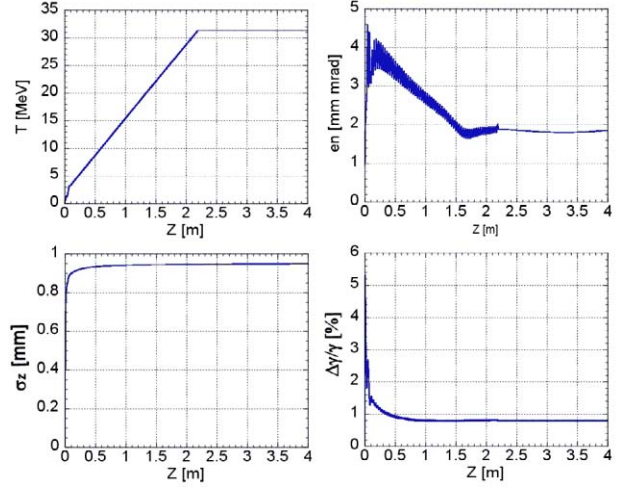


Figure 6: Beam parameters along the HS CA structure.

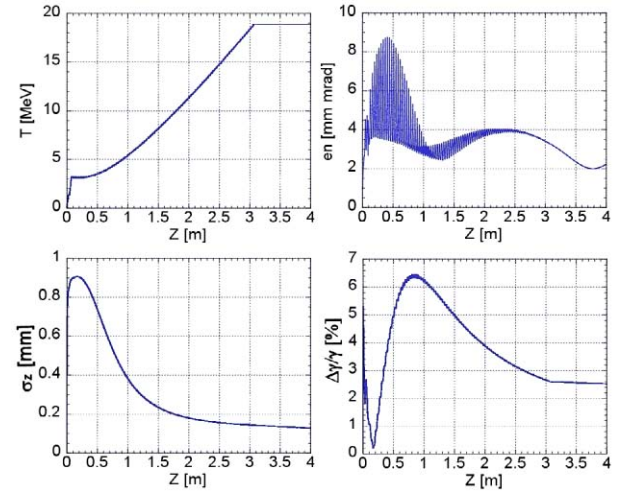


Figure 7: Beam parameters along the HS VB structure.

## CONCLUSIONS

We illustrated the electromagnetic and beam dynamics design procedure of a new class of photoinjector, a hybrid standing/traveling wave structure. There are several advantages in RF and beam performance of this system compared to conventional systems: no impedance mismatch both during and after the RF filling of the SW section, much simpler high power RF system than a split photoinjector, compactness, lower RF gradient, ecc. Two different structures have been designed for acceleration and velocity bunching. The beam energies are in the range of 20-30 MeV while the norm. emittances between 2-3 mm·mrad, according to simulations. Bunch length of 0.15 mm can be reached in the velocity bunching design while the energy spread is below 3%.

## REFERENCES

- [1] www.ansoft.com.
- [2] L.Serafini, M.Ferrario, AIP Conf. Proc. No 581, 2001.
- [3] J. Billen, “PARMELA”, LA-UR-96-1835, 1996.
- [4] M. Ferrario et al., SLAC-PUB-8400.

# CLIC POLARIZED POSITRON SOURCE BASED ON LASER COMPTON SCATTERING

F. Zimmermann, H. Braun, M. Korostelev, L. Rinolfi, D. Schulte, CERN, Geneva, Switzerland; E. Bulyak, P. Gladkikh, NSC/KIPT, Kharkov, Ukraine; S. Araki, Y. Higashi, Y. Honda, Y. Kurihara, M. Kuriki, T. Okugi, T. Omori, T. Taniguchi, N. Terunuma, J. Urakawa, KEK, Ibaraki, Japan; K. Moenig, DESY, Zeuthen, Germany; A. Variola, F. Zomer, LAL, Orsay, France; X. Artru, R. Chehab, M. Chevallier, IPN, Lyon, France; V. Strakhovenko, BINP, Novosibirsk, Russia; J. Gao, IHEP, Beijing, China; S. Guiducci, P. Raimondi, INFN/LNF, Frascati, Italy; V. Soskov, LPI, Moscow, Russia; M. Fukuda, K. Hirano, M. Takano, NIRS, Chiba, Japan; T. Hirose, K. Sakaue, M. Washio, Waseda U., Tokyo, Japan; T. Takahashi, H. Sato, Hiroshima U., H., Japan; A. Tsunemi, Sumitomo Heavy Industries Ltd., Tokyo, Japan (“POSIPOL collaboration”)

## Abstract

We describe a possible layout and parameters of a polarized positron source for CLIC, where the positrons are produced from polarized gamma rays created by Compton scattering of a 1.3-GeV electron beam off a YAG laser. This scheme is very energy effective using high finesse laser cavities in conjunction with an electron storage ring. We point out the differences with respect to a similar system proposed for the ILC.

## INTRODUCTION

At Snowmass 2005, a polarized-positron source based on laser-Compton scattering was proposed for the ILC [1]. Polarized photons generated by laser-electron scattering are here converted into polarized positrons via pair production in a target. Two novel features distinguish the “new” ILC Compton source from its single-pass predecessor developed for the JLC in the 1990’s [2], namely photon stacking using high-finesse optical cavities in a Compton storage ring and positron stacking in a damping ring, both of which relax the laser requirements. The case of a Compton source is bolstered by recent experimental results from the KEK/ATF, where the production of  $10^4$  polarized positrons per bunch with  $73\% \pm 15(\text{stat})\% \pm 19(\text{syst})\%$  polarization has been demonstrated [3], as well as by an improved understanding of compact Compton storage rings [4, 5]. In this paper we discuss how the ILC Compton scheme can be adapted, and scaled down, to CLIC.

## ILC COMPTON SCHEME

The ILC Compton source [1] comprises a Compton ring with 30 optical cavities, which are either coupled in a daisy chain or powered by separate lasers. Various types of lasers can be used. In Ref. [1], YAG or CO<sub>2</sub> lasers were considered, which require a different beam energy of 1.3 GeV or 4.1 GeV, respectively, and a different ring circumference of 277 m or 649 m. During 100 or 50 Compton-ring turns  $10 \times 2800$  “bunch-lets” of about  $2 \times 10^8$  polarized positrons are produced from polarized photons generated in 30 laser-electron collisions. Next, a 100-Hz s.c. linac accelerates these positrons to 5 GeV. On 10 successive damping-ring turns, positron bunch-lets are injected 10 times into each

of 2800 ILC damping-ring rf buckets. Then the injected positron emittance is damped by synchrotron radiation for 10 ms. The entire process is repeated 9 times, always leaving a 10-ms damping time between sets of 10 consecutive injections. After 90 ms the accumulation is completed. The ILC damping ring now stores the full-intensity positron bunches for 100 further ms before extraction to the main linac. A major challenge in the ILC Compton-ring design are the 30 laser-beam interaction points (IPs), which result in a large energy spread, reducing the photon yield, and which likely compromise the dynamic aperture. In case the 30 cavities are coupled, a novel multi-chamber feedback is needed.

Table 1: CLIC and 3-km ILC damping ring parameters.

variable	CLIC	ILC
energy	2.424 GeV	5 GeV
circumference	360 m	3230 m
bunch population	$2.56 \times 10^9$	$2 \times 10^{10}$
# bunches per train	110	280
gap (missing bunches)	$\geq 47$	80
# trains per pulse	2	10
bunch spacing	0.533 ns	2.8 ns
hor. normalized emittance	600 nm	5 $\mu\text{m}$
vert. normalized emittance	5–10 nm	20 nm
rf frequency	1.875 GHz	650 MHz
repetition rate	150 Hz	5 Hz

## ILC-CLIC DIFFERENCES

The positron sources for ILC and CLIC must provide the bunches required in the respective damping rings. From Table 1, we infer the main differences between ILC and CLIC: (1) The CLIC bunch charge is almost 10 times lower and the number of bunches per pulse about 20 times smaller than for the ILC. (2) The bunch spacing for CLIC is about 6 times shorter. (3) The CLIC repetition rate is higher by a factor 30.

As a consequence of the first point, the number of laser cavities in the CLIC Compton ring can be reduced, ideally to a single one, a case which will soon be tested experimentally in the ATF damping ring.

## CLIC SCHEME

Figure 1 displays a schematic of the polarized positron source proposed for CLIC. Its main components are a compact Compton ring with a single optical cavity, a photon target and positron collection system, a 2.4-GeV 150-Hz n.c. linac, and the 2.424-GeV pre-damping ring used for accumulation. Table 2 compares preliminary parameters of the CLIC source with those of the ILC.

For simplicity, we here consider only the case of a YAG laser. Due to its 10 times shorter wavelength  $\lambda_L$ , for the YAG laser the injection linac is 3 times shorter and the Compton-ring energy 3 times lower than for a  $\text{CO}_2$  laser.

Table 2: YAG-laser Compton-source parameters.

parameter	CLIC	ILC
Compton ring energy	1.3 GeV	1.3 GeV
C.-ring circumference	42 m	277 m
rf frequency	1.875 GHz	650 MHz
bunch spacing	0.16 m	0.923 m
number of bunches	220	280
bunch population	$6.2 \times 10^{10}$	$6.2 \times 10^{10}$
no. of optical cavities	1	30
total $\gamma$ 's/bunch/turn	$2.8 \times 10^9$	$5.8 \times 10^{10}$
selected $\gamma$ 's/bunch/turn	$6.9 \times 10^8$	$1.36 \times 10^{10}$
pol. e+/bunch/turn	$9.8 \times 10^6$	$1.9 \times 10^8$
injections/bunch	300	100
total # injections	$6.6 \times 10^4$	$2.8 \times 10^5$
# e+/pulse	$6.5 \times 10^{11}$	$5.3 \times 10^{13}$
# e+/second	$9.7 \times 10^{13}$	$2.7 \times 10^{14}$
# Compton-ring turns	300	100
Compton-pulse duration	42 $\mu\text{s}$	90 $\mu\text{s}$
pause between cycles	6.1 ms	9.9 ms

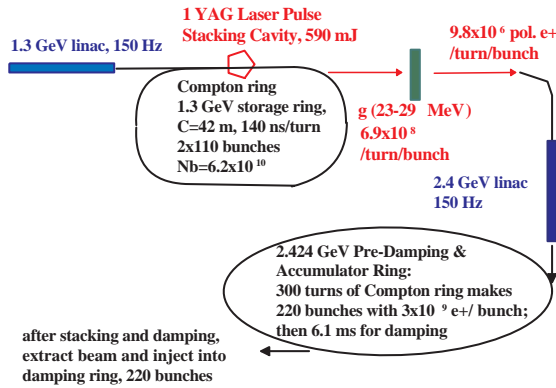


Figure 1: Schematic view of CLIC Compton source.

## COMPTON RING

The Compton ring can be designed as a racetrack with four straight sections [1, 4, 5]. Two of these accommodate wigglers, counteracting the effect of the Compton collisions by enhanced longitudinal damping, one houses an rf system which restores the energy lost in Compton collisions and in the wigglers, and the last one contains the Compton collision point with optical cavity.

Parameters for the Compton collision point are summarized in Table 3. The maximum back-scattered photon energy is 29 MeV. Photons between 23.2 and 29 MeV are selected for polarized positron generation. Laser pulse depletion from Compton scattering is negligible compared with losses on the optical mirrors. Also nonlinear Compton effects can be ignored. Transverse emittance growth due to either the ponderomotive force or quantum diffusion in the laser field is small too.

Table 3: Parameters of Compton collision.

parameter	value
e- bunch length at Compton IP	5 mm
e- rms hor./vert. beam size	25, 5 $\mu\text{m}$
e- beam energy	1.3 GeV
e- bunch charge	10 nC
laser type	YAG
laser photon energy	1.164 eV
rms laser radius	5 $\mu\text{m}$
laser pulse energy	592 mJ
# laser cavities	1
crossing angle	$\sim 10^\circ$
photons in cavity pulse	$3.2 \times 10^{18}$
polarized $\gamma$ 's/bunch/turn	$6.9 \times 10^8$
positron yield e+/ $\gamma$	0.014
effective e+ yield/ $\gamma$	$3.5 \times 10^{-3}$

A simulation of the turn-by-turn photon yield per electron which considered an optimized 1st order momentum compaction  $\alpha_{c,1} = 2 \times 10^{-6}$ , a zero second order  $\alpha_{c,2}$ , and strong wiggler damping, predicts an average total photon yield per electron of about 0.0447, which is close to the ideal value expected for a longitudinally point-like bunch [5]. The yield stays almost constant as a function of time, unlike for the ILC [1, 5]. The positron yield per collision and per Compton-ring electron is estimated by multiplying the simulated total photon yield with a factor 0.248 (about 25% of the photons are selected) [1] and with a factor 0.014 for the approximate positron yield per photon [1].

The electron-beam energy spread induced in a Compton collision is [6]  $\Delta\sigma_E \approx \sqrt{(7/10)E_\gamma(\Delta E)}$ , with  $E_\gamma$  the photon energy,  $\Delta E = (32\pi/3)r_e^2\gamma^2 E_L/(Z_R\lambda_L)$  the average energy loss,  $E_L$  the laser pulse energy,  $r_e$  the classical electron radius, and  $Z_R$  the laser Rayleigh length. The YAG laser requires a large momentum acceptance of 7–8% in the Compton-ring, which may be difficult to achieve. Possible remedies include decreasing the turn number and increasing the number of electron bunches (and ring circumference), introducing additional wigglers, or using a  $\text{CO}_2$  laser with higher  $\lambda_L$ . Many other improvements considered for the more demanding ILC conditions, such as rf phase manipulation, low & nonlinear momentum compaction factor, pulsed momentum compaction lattice, and strong rf focusing with minimum bunch length at the Compton IPs [5, 7], could also be applied at CLIC.

## LASER AND OPTICAL CAVITY

The laser system, sketched in Fig. 2, consists of three stages. The mode-locked laser oscillator produces seed pulses with about 170 nJ energy. The solid-state amplifier provides a gain by about a factor 3500 via chirped pulse amplification (CPA). For comparison, the existing amplifier of the ATF rf-gun laser achieves a factor 10000. The final enhancement by a factor 1000 to about 600 mJ pulse energy is accomplished by stacking in a high-finesse optical cavity. The optical cavities at the ATF have demonstrated enhancement factors of 300 (pulsed laser wire) and 1000 (cw laser wire).

Several alternatives exist: (1) increasing the laser pulse energy and decreasing the optical-cavity quality factor; (2) replacing the YAG laser by a 0.21 mJ/pulse CO<sub>2</sub> laser; (3) continuous mode operation (with fiber laser?) at 50 MHz and 10 μJ/pulse combined with a higher cw optical-cavity quality factor of 10<sup>4</sup> – 10<sup>5</sup> [8]; (4) feedback on the laser (LAL scheme) and/or on the optical cavity (KEK scheme).

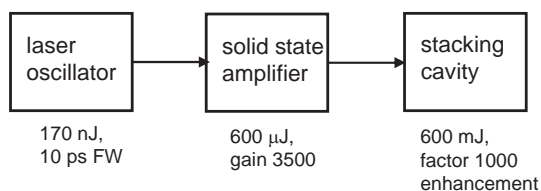


Figure 2: Schematic layout of laser system, including pulse energy and gain factors [9].

At the intersection of optical cavity and beam pipe, the latter features two elongated holes for the laser beam. The minimum cavity length is estimated as  $l \approx 2d/\phi \approx 0.28$  m, where  $d \approx 25$  mm is the size of the optical mirror, and  $\phi \approx 10^\circ$  the laser-beam collision angle. This implies that, for CLIC, at least 3 or 4 pulses are stored in the same cavity.

Instead of using a mode-locked laser at the CLIC bunch frequency, also a lower-frequency laser can be employed. The latter could feed a larger optical cavity whose length is tailored such that successively injected laser pulses are properly interleaved and the laser frequency is multiplied, as is illustrated in Fig. 3.

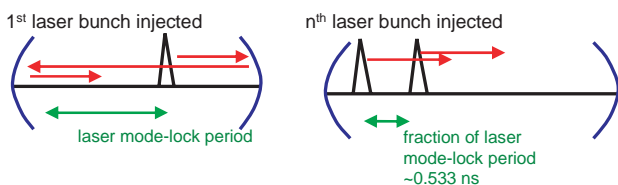


Figure 3: Schematic of laser frequency multiplication.

## POSITRON STACKING

The accumulation ring used for positron stacking must have a large longitudinal and transverse acceptance, as well as provide fast damping. The only economical solution for the ILC is to use one or several of the 3 or 6-km long main damping rings for stacking, as the ILC accumulator ring should have at least the same circumference as

the main damping ring. By contrast, at CLIC the pre-damping ring can be used for accumulation. The minimum required circumference for accommodating 220 positron bunches is only 42 m. In addition, this ring can be optimized for accumulation efficiency fully independently of any damping-ring constraints. The former 2-GeV 200-m NLC pre-damping ring optics [10] is a good candidate. It features a 10-fold symmetric double-bend achromat structure, wiggler damping equal to twice the arc damping, 0.4-m bunch spacing, 2-ms longitudinal damping time, 100–150 Hz repetition rate, and a dynamic aperture of 0.2 m-rad for  $\Delta p/p = \pm 1.5\%$ .

## OUTLOOK

The Compton ring design is challenging due to the high current. Further optimization of ring circumference, bunch spacing, and bunch charge will likely be required.

An ongoing R&D programme at the KEK/ATF addresses the design and fabrication of laser-pulse stacking cavities with high enhancement factor and small spot size, the design of an IP with minimum collision angle, and the installation of laser-pulse stacking cavities in the ATF damping ring, culminating in X-ray generation. A parallel proposal to the European Union’s 7th framework programme includes technological R&D on high-power high-repetition rate lasers and optical cavities, a design study of the Compton ring, collection system, and stacking schemes, as well as experiments at ATF and DAFNE.

Over the last decade, the output power of cw double-clad fiber lasers with diffraction limited beam quality has increased by a factor 400 [7, 11]. The demonstrated value of 2 kW is close to the power needed for the CLIC source (if a single laser is used). Extrapolating past evolution, an 8-kW cw fiber laser should become available around 2008/2009.

## ACKNOWLEDGEMENTS

We thank Z. Huang for helpful discussions. This work is supported by the Commission of the European Communities under the 6th Framework Programme “Structuring the European Research Area”, contract RII3-CT-2003-506395.

## REFERENCES

- [1] S. Araki et al, KEK-Preprint 2005-60, CLIC Note 639 (2005).
- [2] T. Omori, KEK Preprint 99-188 (1999).
- [3] T. Omori et al, Phys. Rev. Lett. 96, 114801 (2006).
- [4] E. Bulyak, P. Gladkikh, V. Skomorokhov, arXiv, p. 5 *physics/0505204v1* (2005).
- [5] E. Bulyak et al, this conference, WEPCH097 (2006).
- [6] Z. Huang, R.D. Ruth, Phys. Rev.Lett. 80, 976 (1998).
- [7] Posipol 2006 workshop <http://www.cern.ch/posipol2006>.
- [8] A. Variola and F. Zomer at [7].
- [9] J. Urakawa, POSIPOL meeting, KEK, 04.11.2005.
- [10] A. Wolski, EPAC’02, p. 521 (2002); A. Wolski, I. Reichel, EPAC’04, 827 (2004).
- [11] A. Tünnemann et al, J. Phys. B 38, S681 (2005).

# CNAO RESONANCE SEXTUPOLE MAGNET POWER CONVERTERS

Marco Farioli, Filippo Burini, Saverino Carrozza, Mario Cavazza, Simone Minisgallo,  
Miguel Pretelli, Giuseppe Taddia, O.C.E.M. S.p.A., Bologna  
Davide Bagnara, Andrea Tilli, Manuel Spera, Manuel Toniato, CASY, Bologna  
Ivan de Cesaris, CNAO Foundation, Milan  
Maurizio Incurvati, Claudio Sanelli, INFN/LNF, Frascati/Roma

## Abstract

The CNAO Resonance Sextupole Magnet Power Converter requirements for the Storage Ring of the CNAO Project are described together with performance and initial operating experience. In particular the achieved performances will be compared with the specification and the extensive modelling that was done during the design phase. Not only the tight required performances were emphasized during the design phase but also particular attention was put on reliability and minimization of the repairing time (MTTR). Some fundamental criteria, like component de-rating and standardisation, have also been taken into account during the component choice phase. All converters adopt the switching technology with full digital control and a common control interface, that, as for the other CNAO power converters, uses the same digital controller, under licence from the Diamond Light Source.

## INTRODUCTION

A synchrotron machine, capable to accelerate either light ions or protons, will be the basic instrument of the CNAO (Centro Nazionale di Adroterapia Oncologica), the medical center dedicated to the cancer therapy, that is under construction in Pavia (Italy). The machine complex consists of one proton-carbon-ion linac that will accelerate the particles till the energy of 7 MeV/u. An injection line will transport them to the synchrotron ring where the injected particles will be accelerated and extracted with an energy ranging from 60 to 250 MeV for protons and from 120 to 400 MeV/u for carbon ions.

Protons and light ions are advantageous in conformal hadrontherapy because of three physical properties. Firstly, they penetrate the patient practically without diffusion. Secondly, they abruptly deposit their maximum energy density at the end of their range, where they can produce severe damage to the target tissue while sparing both traversed and deeper located healthy tissues. Thirdly, being charged, they can easily be formed as narrow focused and scanned pencil beams of variable penetration depth, so that any part of a tumour can accurately and rapidly be irradiated. Thus, a beam of protons, or light ions, allows highly conformal treatment of deep-seated tumours with millimeter accuracy.

This paper is organized as follows. In the first part Power supply specifications are given. In the second part the system topology is faced, while in the third one control design

is described. Finally, in the last part, simulations results are reported.

## POWER SUPPLY SPECIFICATION

The sextupole is a special magnet of the CNAO synchrotron used to extract the particles from the main ring. It must stay at zero current during particles injection and acceleration, and ramp up to the specified current, different from cycle to cycle, in an overall time of about 50ms.

The corresponding current reference for the sextupole power supply is presented in figure 1.

The detailed power supply specification can be found in Table 1: it's worth to note the short rising time (25 ms) and the small tracking error (less than 50 ppm).

Table 1: Specification for power supply.

Three phase, 50 Hz input mains voltage	400 V $\pm$ 10%
Maximum Output Current	650 A
Maximum Output Voltage	$\pm$ 40 V
Maximum Output Power	> 24kVA
Load Inductance (including cables)	3.26 mH
Load Resistance (including cables)	38.65 m $\Omega$
Current Setting and Control Range	0.5 to 100% f.s.
Normal Operating Range (N.O.R.)	0.5 to 100 % f.s.
Current Setting Resolution	< $\pm 1 \times 10^{-4}$ f.s.
Current Reproducibility	< $\pm 5 \times 10^{-5}$ f.s.
Current Readout Resolution	< $\pm 1 \times 10^{-4}$ f.s.
Residual Current Ripple (peak to peak) in N.O.R	< $\pm 1 \times 10^{-4}$ f.s.
Linearity Error [(Iset - Iout)/Iset]	< $\pm 5 \times 10^{-5}$ f.s.
Ambient Temperature	0° to +40° C
Current Stability (.I/Iset over the normal operating range)	< $\pm 1 \times 10^{-4}$
Maximum ramp up/down time in the N.O.R.	25 ms
Maximum first ramp up time	150 ms

## TOPOLOGY

The first proposed solution for the sextupole power supply used a Pulsed Power Supply Topology. It was composed by a Pulse Section (essentially a capacitor with thyristor bridge, resonant with the load inductance) and a Switching Section as regulator converter. After some considerations on the specification the Pulsed solution was abandoned. In fact, the same aim is achievable using a simpler and more standard switching topology.

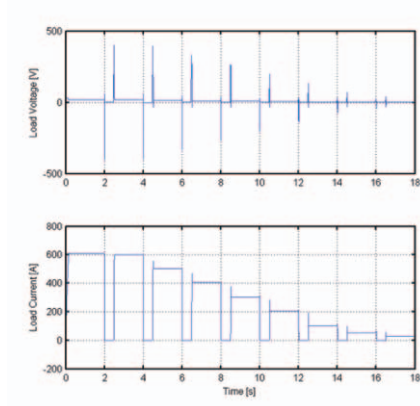


Figure 1: Load voltage and current during a treatment plan where the beam energy decrease cycle by cycle.

The adopted solution is composed by an input stage and an output stage (see figure 2). The input stage is made up of a  $\Delta - Y$  transformer, a diode bridge and an input passive filter. The output stage is made up of two parallel connected IGBT full-bridges and an output filter. The load is parallel connected to the output filter.

### Input Stage Dimensioning

The most important parameter to evaluate in the sizing of the input stage is the DC-link capacity. This value is estimated considering that the current drawn from the DC-link in the worst case is a ramp with a slope of 26000 A/s for  $T_{ramp} = 25$  ms. Hence, balancing the involved energies and considering the physical limitations of the components, a DC-link capacitance  $C_{Fi} = 165$  mF is chosen.

Then, in order to have the input filter resonance frequency at  $f_0 = 22.5$  Hz, an inductance value of 300  $\mu$ H is adopted.

### Output Stage Dimensioning

Each full-bridge module is driven by a PWM signal at a frequency of 10 kHz. Since no phase displacement techniques are used, the resulting voltage ripple has an equivalent frequency of 20 kHz. The maximum current ripple is reached when the modulation index is equal to  $\frac{1}{2}$ . In order to maintain the ripple under the specification threshold the resulting low pass filter parameters are:  $L_{Fumod1} = L_{Fumod2} = 60 \mu$ H,  $C_{Fu1} = 320 \mu$ F,  $C_{Fu2} = 80 \mu$ F,  $R_{CFu} = 0.66 \Omega$

## CONTROL DESIGN

The aim of the digital control is twofold: make the power supply satisfy the specification (mostly the small rising time) and make the two output modules work in the same way by drawing the same amount of current from both of them.

Analyzing the electrical circuit made up of output filter and load, the following equations hold:

$$\begin{cases} V_1(s) - sL_{Fumod}I_1(s) = I_s(s)Z_b(s) \\ V_2(s) - sL_{Fumod}I_2(s) = I_s(s)Z_b(s) \end{cases}$$

where:

- $V_i$  is the voltage input of the  $i$ -th module;
- $I_i$  is the current flowing in the inductance of the  $i$ -th module;
- $Z_b$  is the equivalent impedance corresponding to the parallel of output filter capacitor and load impedance;
- $I_s = I_1 + I_2$ ;
- $L_{Fumod1} = L_{Fumod2} = L_{Fumod}$ .

Performing the change of coordinates

$$\begin{bmatrix} I_s \\ I_d \end{bmatrix} = T \begin{bmatrix} I_1 \\ I_2 \end{bmatrix}, \quad \text{where } T = \begin{bmatrix} 1 & 1 \\ 1 & -1 \end{bmatrix}$$

the following equations are obtained:

$$\begin{cases} I_s(s) = \frac{V_1(s) + V_2(s)}{sL_{Fumod} + 2Z_b(s)} = \frac{V_s(s)}{sL_{Fumod} + 2Z_b(s)} \\ I_d(s) = \frac{V_1(s) - V_2(s)}{sL_{Fumod}} = \frac{V_d(s)}{sL_{Fumod}} \end{cases}$$

As the real target of the control is  $I_{load}$ , considering the current divider the plant equations are:

$$\begin{cases} I_{load}(s) = \frac{1}{sL_{load} + R_{load}} \frac{Z_b(s)}{\frac{sL_{Fumod}}{2} + Z_b(s)} \frac{V_s(s)}{2} = \\ = H_{1,2}(s) \frac{V_s(s)}{2} \\ I_d(s) = \frac{1}{sL_{Fumod}} V_d(s) = H_d(s) V_d(s) \end{cases}$$

The regulator developed for  $H_{1,2}(s)$  is a PI controller:

$$R_{1,2}(s) = k_p + \frac{k_i}{s}$$

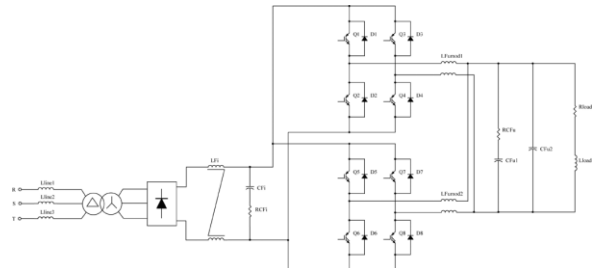


Figure 2: Topology of sextupole magnet power supply.

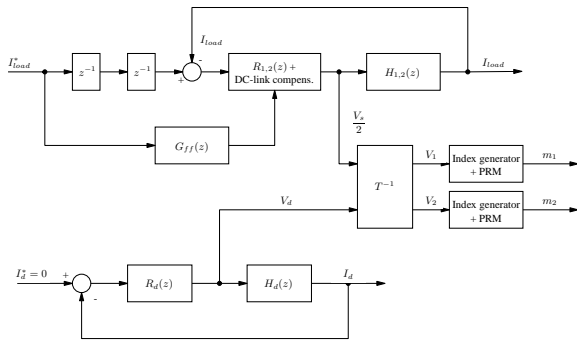


Figure 3: Structure of digital controller.

with  $k_p = 7.08$  and  $k_i = 7117$  while the regulator for  $H_d(s)$  is a simple P controller with very slow dynamics

$$R_d(s) = 0.0562$$

Then, in order to implement controllers on a DSP board, both regulators and plants have been discretized using the ZOH method with a sample time of  $100 \mu\text{s}$ , i.e. a frequency of 10 kHz. The control action is performed by generating appropriate PWM indexes that are calculated from  $V_s$  and  $V_d$  with a suitable change of base.

The overall performances can be improved by means of the following feedforward action based on the load discretized model inversion.

$$G_{ff}(z) = 32.6193 \frac{z - 0.9988}{z}$$

Since the relative degree of the controlled system is 2, the digitalized current reference is 2 samples delayed in order to synchronize it with the feedforward action.

Final improvements on the control system are the *DC-link voltage compensation*, introduced to avoid drawing more current than available on the DC-link, and a combination of PWM and PRM (Pulse Repetition Modulation) techniques to increase the accuracy of digitalization.

## SIMULATIONS RESULTS

To test the topology and the adopted control strategies, extensive simulations have been carried out using Matlab and Simulink. A Simulink model of the system has been implemented using SimPowerElectronics components initialized with parameters of table 1. All the tests have been performed both in nominal  $V_{line}$  conditions and in critical  $V_{line}$  conditions when input mains voltage can be either 110% or 90% of nominal value (see figures 4, 5 and 6 for 90% case).

Delivery of Sextupole magnet power supply is scheduled for July 2006.

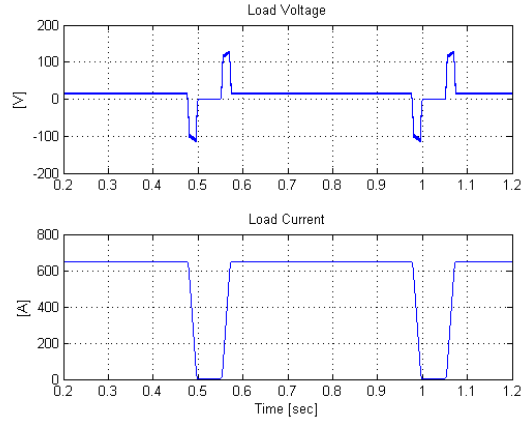


Figure 4: Load voltage and current  $V_{line}$  at 90%.

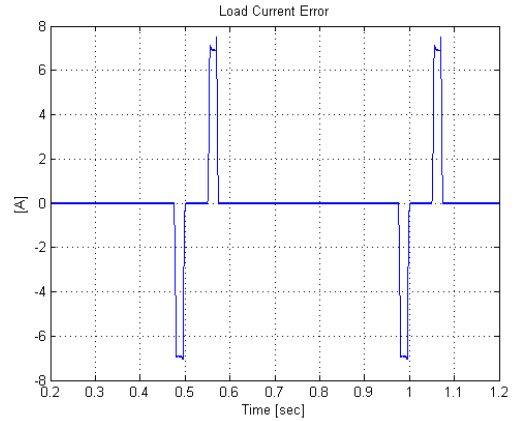


Figure 5: Load current error,  $V_{line}$  at 90%.

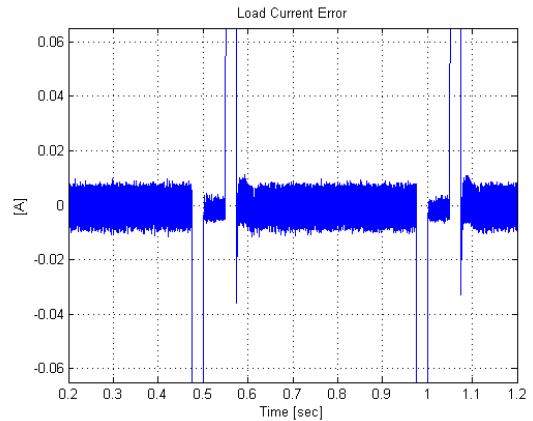


Figure 6: Load current error (zoom),  $V_{line}$  at 90%.

# THE ITALIAN HADRON THERAPY CENTER (CNAO): A REVIEW OF THE POWER SUPPLY SYSTEM FOR CONVENTIONAL MAGNETS

M. Incurvati, C. Sanelli, LNF-INFN, Frascati, Italy, I. De Cesaris, CNAO Foundation, Milan, Italy

F. Burini, S. Carrozza, M. Cavazza, M. Farioli, S. Minisgallo, M. Pretelli, G. Taddia, OCEM, Bologna, Italy

L. Balbo, N. Balbo, A. Tescari, EEI, Vicenza, Italy

## Abstract

A hadron (Carbon/Proton) medical centre based on a synchrotron accelerator dedicated to the cure of deep tumours is under construction in Pavia (Italy) under the joint responsibility of CNAO (Centro Nazionale di Adroterapia Oncologica) and INFN (Istituto Nazionale di Fisica Nucleare). This paper describes the power supply system, made up of nearly 200 units designed by LNF, and whose converters for the synchrotron ring and related low, medium and high energy transfer lines are now under construction by the major Italian companies. The requirements and electrical characteristics of the power supplies will be reported describing the most interesting topologies that satisfy the requested performances together with the main features of each power supply topology.

Synchrotron dipoles, quadrupoles, sextupoles, steering magnets and resonance sextupole power supplies have tight characteristics with respect to precision class (current resolution, residual ripple, short-long term stability, etc.) that range from  $\pm 5$  ppm to  $\pm 1000$  ppm, fast dynamical response with bandwidth up to some hundreds hertz, high power from tens of kW to many MW and output current ranging from hundreds of Amps to 3 kA.

## INTRODUCTION

The CNAO project is a synchrotron accelerator where heavy Carbon ions or Protons are injected at a fixed energy through Low-Energy and Medium-Energy Beam-Transfer lines (LEBT and MEBT); the particle beam is accelerated and then extracted to be driven (by High-Energy-Beam-Transfer line HEBT) to the treatment room where the patient has to be cured. To maximize the number of patients per year the acceleration cycle shape has been optimized allowing the energy variations from injection to extraction in 0.5 sec. Moreover, the relatively low energy of the beam and the stringent requests on the energy level accuracy of the extracted beam, have lead to the design of very unique power supplies (PSs).

A summary of PSs characteristics can be found in Tab.1. The major part of PSs is under construction by two Italian firms: EEI is building the synchrotron quadrupoles and chromaticity sextupoles PSs, and OCEM all the other PSs of the synchrotron and transfer lines. The PSs have been tightly specified by LNF. The specifications have been written out taking into account many requirements:

- Achieving high reliability to increase life time and MTBF by suitable component over-sizing or PSs redundancy.
- Selection of PSs topology and definition of major technical aspects to be followed by the firms.
- Reduction of topologies number to standardize the system and reducing spare parts.
- Detailed description of technical and precision class requirements.
- Advanced local control facilities to be able to perform meaningful tests during maintenance and reducing repairing time of PSs.

A first set of detailed simulations of the most critical PSs have been also carried out by LNF to investigate their feasibility [1]. All the PSs have then been carefully simulated by the firms.

## POWER SUPPLIES REQUIREMENTS

The major characteristics of the PSs can be found in Tab.1. As can be seen the output currents range from 30 A to 3000 A and the output voltage from 15 V to 1600 V. In spite of this relatively wide spread of values the PSs topologies have been reduced to only four as can be seen also in Fig.1.

The most critical PSs are the ones for the synchrotron dipoles [2] and quadrupole magnets. Their requirements in terms of precision class – i.e.: stability, accuracy, output current ripple – and linearity are about a factor ten more stringent than what usually requested for other synchrotron accelerators. Moreover, they are requested to perform in the same way during the fast energy variations of the synchrotron.

To achieve precise regulation and fast dynamic response Switch Mode Power Supply Active Filter (SMPS-AF) have been implemented in the high-power bending dipole PS and in the high-current PSs of the HEBT line.

Quadrupoles PSs are SMPS characterized by a high power density; to fulfil the tight precision requirements they are implemented with a power-mosfets linear regulator system. As reported in Tab.1 all the PSs are bipolar in voltage to discharge the magnet energy in the proper way and in a short time. This requirement has heavily conditioned the design of the PSs.

Description	Voltage [V]	Current [A]	Precision Class [ppm]	Linearity Error [ppm]	Number of PSs	Topology	Circuit Inductance [mH]	Circuit Resistance [mohm]
<b>SYNCHROTRON</b>								
Bending Dipoles	±1600	3000	±5	±5	1	Thyristors+ SMPS-AF	210.29	81.77
Quadrupoles	±160	650	±5	±5	4	SMPS	36.71	152.24
Resonance Sextupole	±130	650	±100	±50	2	Pulsed SMPS	3.27	26.28
Chromaticity Sextupoles	±60	650	±100	±50	3	SMPS	6.54	52.56
Horizontal Correctors	±30	±30	±1000	±250	11	Linear	84.87	462.70
Vertical Correctors	±30	±30	±1000	±250	9	Linear	9.75	92.00
					<b>30</b>			
<b>LEBT</b>								
Dipole 90°	±35	300	±50	±50	3	SMPS	107.00	150.00
Dipole Y 30°	±30	±30	±1000	±250	2	Linear	168.40	441.50
Dipole 75°	±35	300	±50	±50	1	SMPS	6.87	43.22
Correctors (both planes)	±15	±60	±1000	±500	20	Linear	0.08	145.07
Quadrupoles	±35	300	±50	±50	12	SMPS	0.80	22.36
					<b>38</b>			
<b>MEBT</b>								
Dipoles	±35	300	±50	±50	3	SMPS	61.60	65.90
Quadrupoles	±20	150	±50	±25	10	SMPS	23.86	32.30
Correctors	±15	±60	±1000	±500	16	Linear	9.73	73.15
					<b>29</b>			
<b>HEBT</b>								
Dipoles	±110	3000	±25	±25	11	Thyristors+ SMPS-AF	12.37	4.81
Quadrupoles	±65	350	±50	±25	38	SMPS	48.30	51.36
Correctors	±30	±150	±1000	±500	38	Linear	9.40	94.78
					<b>87</b>			
<b>TOTAL NUMBER OF PSs</b>					<b>184</b>			

Tab.1: Power Supplies Characteristics

Another interesting PS typology is the one adopted for the Resonance Sextupole PS [3]. The resonance sextupole is a magnet that allows the extraction of the particles from the synchrotron ring and drives them into the HEBT line. For this purpose it must reach the set current, different for any energy level, in about 25 ms. This PS is an SMPS that does not use large resonant capacitor as in conventional pulsed PSs. The implemented topology achieves fast dynamic response and valuable reduction of size using a relatively small electrolytic capacitor bank providing ideal voltage source for the DC-link and high-power IGBTs H-bridge connected to perform waveform regulation during ramp and DC operation.

Steering magnets PSs have linear regulation to provide optimum zero-crossing and true bipolar output current. They have been built in cabinets having a common part and two to four independent ways each, reaching a relatively high power density. They also have valuable characteristics with respect to dynamics; they must not only track the standard reference cycle but have to reproduce an additional bump during particles injection for beam scraping purposes. Such a function requires a PS with several kHz bandwidth.

The reference current figure of each cycle will be given to the PSs in two different ways:

1. Each Synchrotron PS will be equipped with a National Instruments electronics rack that generates a digital data sequence of the sampled cycle with a frequency varying from 10 kHz to 50 kHz according to the PS requirements, allowing fine tuning and control.
2. Transfer Lines PSs will receive digital words in which the basic parameters for cycle description

are coded; different segments of the cycle will be performed using suitable timing signals (i.e.: start acceleration ramp, start hysteresis cycle,...).

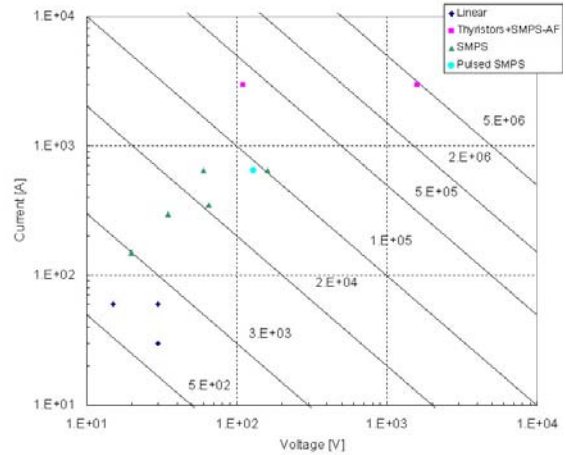


Fig.1: PSs topologies and electrical characteristics

## HOW TO GET HIGH PERFORMANCE

To achieve the high performance formerly described, several expedients have been adopted. All power supplies have been carefully simulated by Matlab/Simulink® and PSIM® software by the firms. This allowed the optimization of control loop parameters taking into account, as far as possible, devices non-linearity (sensors, electronic elements, mains perturbations,...) and circuit parameter uncertainties.

The cycle shape has been optimised with the help of simulations. It has been found that power supply tracking errors can be reduced by building the cycle with linear ramps and polynomial interconnections. The coefficients of the polynomials have been calculated imposing continuity conditions at the extreme points and setting to zero the first and second derivatives. Fifth-order polynomials are sufficient to drastically reduce transient errors.

High precision DCCTs have been adopted for almost all the PSs. In particular the PSs for synchrotron dipoles and quadrupoles and for HEBT dipoles, are equipped with HITEC® DCCTs and burden resistors that exhibit excellent linearity and power coefficient. This is a fundamental parameter since the synchrotron is a cycled machine, and one important problem is the thermal stabilization of the burden resistor. In some applications the dissipated power on this component has been strongly reduced. For example, for the bending dipoles PS the voltage across the burden resistor has been reduced to only 100 mV for 3000 A. In many PSs the burden resistor has been thermally stabilized by water cooling ( $32\pm 2^\circ\text{C}$ ).

An additional winding has been foreseen on the measuring head of many DCCTs to calibrate them and to reduce linearity errors. The synchrotron dipoles PS is equipped with two DCCTs to provide a spare and an out of loop independent measuring point.

All the electronics cabinets will be air conditioned to provide constant temperature and optimal component working point.

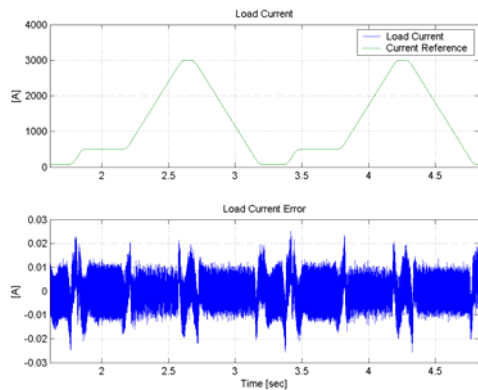


Fig.2: Typical load current shape and error of synchrotron dipoles PS

The layout of the cabinets has been tightly designed in collaboration with the firms with particular attention to proper arrangement of bus-bars, to the symmetry of the component positioning, to the decoupling of AC and DC elements, to the maintenance ease and accessibility, etc.

Fully digital control of PSs has been required. OCEM will adopt the digital control boards developed at PSI (Paul Scherrer Institute) also used in DIAMOND accelerator PSs developing the firmware and implementing the control algorithms; EEI will use

proprietary digital control boards that make use of both DSPs and high-speed FPGA.

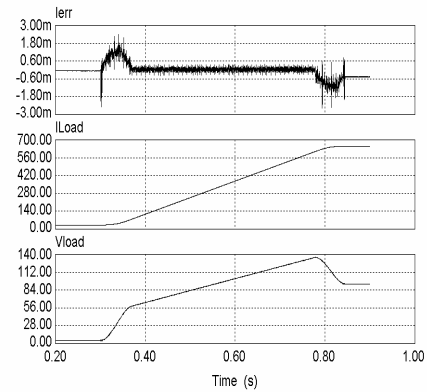


Fig.3: Typical load current shape and error of synchrotron quadrupoles PSs

To increase synchrotron PSs performances the cycle reference points will be provided to the PSs three points in advance to allow suitable calculations to the digital processors.

Typical current reference cycles and tracking errors of the simulations of synchrotron dipoles and quadrupoles PSs are shown in Figs.2-3. It can be seen that within the approximations so far described the specification requirements are fulfilled.

## CONCLUSIONS

The complete PS system of a synchrotron accelerator for medical purposes has been presented in the paper. PSs requirements have been summarized highlighting the most challenging ones. Major technical aspects of the most critical PSs that will determine the achievement of high-performances, have been analysed as well.

The hadrontherapy center is now under construction in Italy at Pavia site and PSs are going to be completed by the firms in a few months. Simulations and preliminary measurements on the first prototypes show promising results.

## REFERENCES

- [1] M.Incurvati, C.Sanelli, I. De Cesaris: “Feasibility Study of High-Precision Power Supply for Ramping Dipoles of a Carbon/Proton Medical Synchrotron”, presented at Magnet Technology, Genova 2005 and to be published on IEEE Trans. On Applied Superconductivity, June 2006
- [2] M.Incurvati, C.Sanelli, I.DeCesaris, M.Pretelli et Alt. of OCEM: “CNAO Storage ring dipole magnet Power Converter 3000A/±1600V”, this conference.
- [3] M.Incurvati, C.Sanelli, I.DeCesaris, M.Farioli et Alt. of OCEM: “CNAO Resonance magnet Power Converters”, this conference.

# ELECTRON BEAM-LASER INTERACTION NEAR THE CATHODE IN A HIGH BRIGHTNESS PHOTOINJECTOR

M. Ferrario, G. Gatti, INFN-LNF, Frascati, Italy; L. Serafini, INFN-Mi, Milano, Italy;  
J. B. Rosenzweig, UCLA, Los Angeles, USA

## Abstract

The production of high charge short bunches in a high brightness photoinjector requires laser pulses driving the cathode with GW range peak power on a mm spot size. The resulting transverse electric field experienced by the electron beam near the cathode is of the order of 200-500 MV/m, well in excess of a typical RF accelerating field of 50-100 MV/m. We present here a preliminary study of the resultant beam dynamics. Simulations including the electron beam-laser interaction have been performed with the code HOMDYN taking into account the superposition of incident and reflected laser pulses as well as space charge fields. Under this conditions the emittance degradation is negligible, as predicted by analytical methods, but a longitudinal charge modulation occurs on the scale of the laser wavelength, in case of oblique incidence, driven by the longitudinal component of the laser field. Charge modulation is transformed into energy modulation via the space charge field, which may produce enhanced microbunching effects when the beam is further compressed in a magnetic chicane.

## INTRODUCTION

Electron beam – laser interaction near the cathode surface could be important in case of short and strong laser pulses, when the involved field becomes high and the electrons have a very low momentum (emission is achieved slightly overcoming the cathode work-function to reduce thermal emittance). We consider in this study the case of a metal photocathode. Other kinds of photocathodes, such as high Quantum Efficiency (QE) Cs<sub>2</sub>Te have no need to be driven at high power, in addition their response is slower (some ps), and the considerations that will be made in this framework require some slight adjustments to fit the alternative case of semiconductor cathodes. A large laser field at the cathode can produce “heating” of the electron beam through the induced wiggling motion. The degree to which the laser field causes emittance growth can be estimated as [1]:

$$\varepsilon_n = a_l \sigma_x \approx \frac{\lambda_l}{2\pi m_e c^2} \sqrt{Z_0 P_l}$$

Here  $a_l$  is the peak normalized vector potential of the laser field,  $P_l$  is the peak laser power and  $\lambda_l$  the laser wavelength (note the independence of the beam size  $\sigma_x$ ). For example a laser pulse 300 fs long with an energy of 0.2 mJ as required by a blow out experiment [1], able to extract 0.33 nC charge from a 10<sup>-5</sup> quantum efficiency cathode, results in a 0.04  $\mu\text{m}$  induced emittance growth.

This effect, while physically interesting, is negligible in this case. A more interesting effect is produced on the longitudinal phase space, as will be discussed in the next sections.

## HOMDYN SIMULATIONS

The fast running code HOMDYN [2] has been modified in order to include the beam interaction with the laser field, here modelled as a simple truncated plane wave, in addition to the RF and space charge fields already implemented in the code, including the important effect of the cathode image charges.

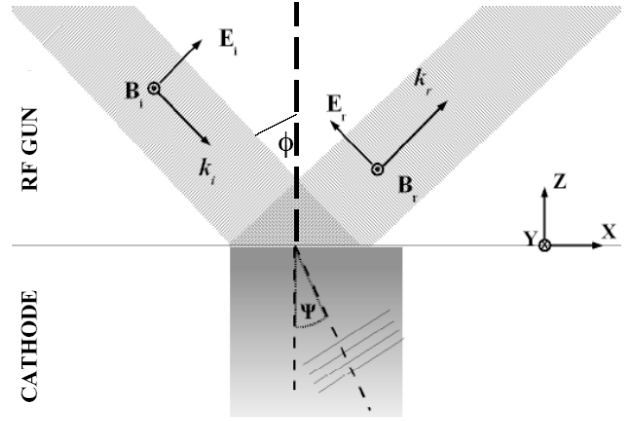


Figure 1: P-polarized plane wave incident on a lossy medium [3].

The expression of the electromagnetic field of a plane wave incident on a lossy medium for a p-polarized wave is the following, see also Fig. 1:

$$B_i = -\hat{y}(E_i / c) \cos(k_i \cdot r - \omega t + \varphi_i)$$

$$E_i = E_i [\hat{x} \cos \vartheta + \hat{z} \sin \vartheta] \cos(k_i \cdot r - \omega t + \varphi_i)$$

$$B_r = -\hat{y} R(E_i / c) \cos(k_r \cdot r - \omega t + \varphi_R)$$

$$E_r = E_i R [-\hat{x} \cos \vartheta + \hat{z} \sin \vartheta] \cos(k_r \cdot r - \omega t + \varphi_R).$$

Assuming a cathode reflection coefficient constant within the laser wavelength spectrum. The previous expressions can be easily extended to the general case of a real laser pulse, without operating integration over the spectrum. It is sufficient to substitute the incoming envelope expression into the amplitude of the incoming field  $E_i$ .

Dealing with lossy media (i.e. radiation must be absorbed to generate photo-electrons) the p-polarization is reflected again as p, but with a phase shift due to the complex index of refraction  $n$ . Photoemitted electrons experience a field that is sum of incoming and reflected

wave. Inside photocathode the field amplitude is attenuated exponentially in direction normal to the surface, and propagates at a slightly different angle, this effect will be include in a future work.

Both normal and oblique laser incidence (at 70 degrees) have been taken in consideration in HOMDYN simulations. A laser field amplitude of 190 MV/m is assumed, the RF field experienced by the electrons injected in the gun with 26 phase degrees is 53 MV/m, (120 MV/m peak field). Laser wavelength was fixed at 266 nm, able to drive Cu and other metal photo-cathodes.

The first case considered here is a 10 ps long laser pulse at normal incidence and a 1 nC e-bunch charge, corresponding to the nominal SPARC parameters [4]. An integration time step of 0.1 fs (corresponding approximately to 10% of the laser central wavelength period) and 1000 slices 40 nm long (about  $\lambda/7$ ) were used. As was expected, each slice experiences the fast varying field of the laser, as a cosequence slice centroids undergoes a fast oscillation in space. The amplitude of the oscillations grows with the time, and so this effect is enhanced in the first emitted slices compared to the last ones as shown in Fig. 2.

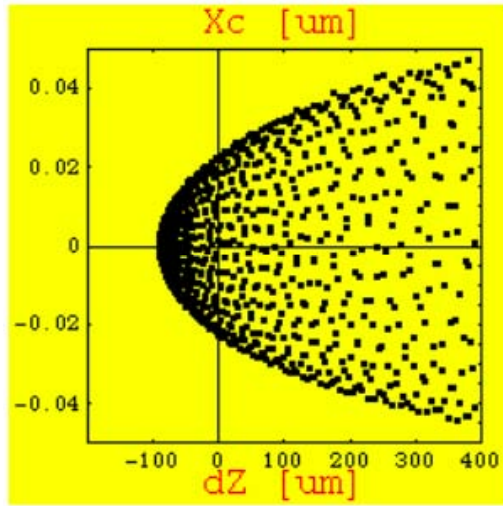


Figure 2: Slice centroids evolution during the interaction with the laser beam. Each dot represents a slice centroid located at a distance dz from the bunch central slice.

This effect occurs on a negligible scale , so that, looking at the macroscopic consequences on the beam, neither envelope, nor emittance or energy spread are affected in such a way to show a noticeable degradation of the beam quality. Emittance on a time scale of 10 ps reaches a value of  $0.05 \mu\text{m}$ .

The case of grazing incidence is more interesting. First of all, the angle introduces an asymmetry on electron trajectories, depending on different field phase which particles experience at different emission times, Fig. 3. Once again, the transverse dynamics is affected by an even weaker effect, than in normal incidence

The computed emittance behaviour for a 1 ps laser pulse, 1 pC charge is shown in Fig. 4. As can be seen in

the plot, after a time of 1 ps the emittance growth due to space charge prevails.

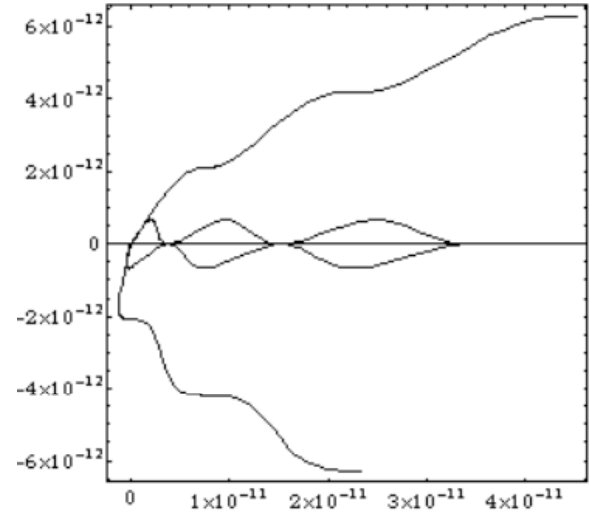


Figure 3: Electron trajectories for different injection phases in a laser field with grazing incidence. (Transverse displacement [m] versus time [s]).

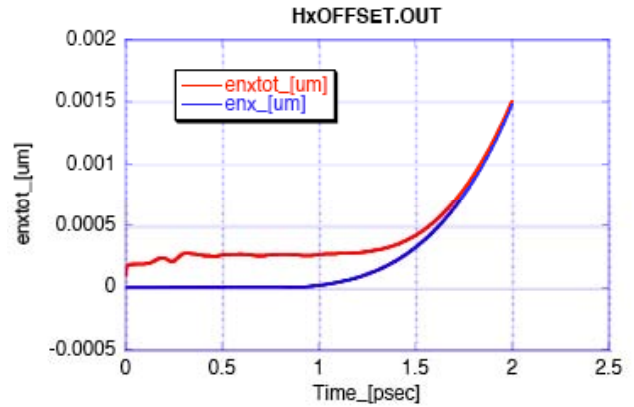


Figure 4: Normalized emittance vs. time for the 1 ps laser, 1 pC case. Blue line: space charge induced emittance Red line: total emittance including laser induced emittance.

On the other hand since laser contribution is now mainly longitudinal, we expect a some effect on the longitudinal motion. Preliminary simulations show that even if the induced energy spread is negligible, a charge modulation on a scale of the laser wavelength occurs. Different groups of slices emitted within different half periods of the laser field will experience in fact accelerating or decelerating laser fields components, while the electron velocity changes from a non-relativistic to a relativistic regime, due to the superimposed RF accelerating field. The initial extraction velocity  $\beta=v/c=0.002$  in this case is enough to prevent backward acceleration. This periodic shrinking and broadening of the slices, that last until the end of the electron-laser interaction, results in a slice current modulation, as shown if Figures 5 and 6. Notice that the current modulation can reach a 40% depth. Downstream the

cathode the beam evolution is dominated by space charge effects and will transform this current modulation in energy modulation [5].

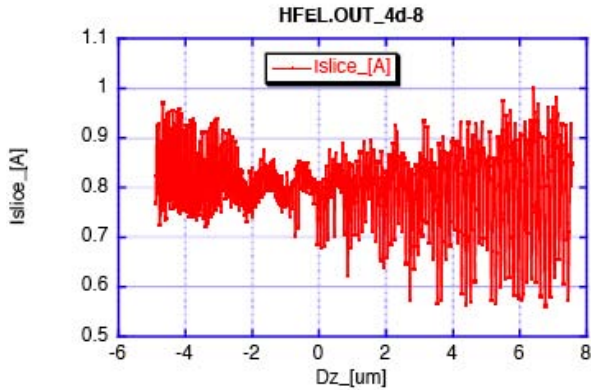


Figure 5: Normalised beam current modulation at the end of the photo-emission process.

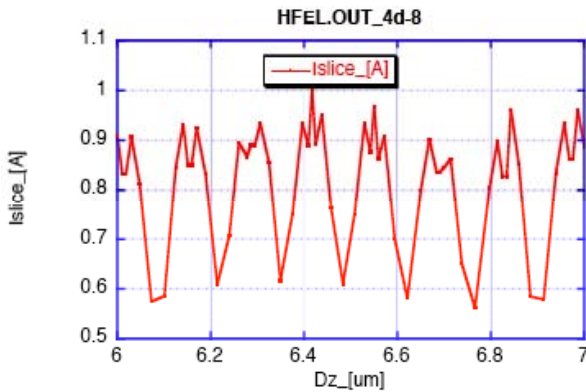


Figure 6: Normalised beam current modulation at the end of the photo-emission process, blow up of Fig. 5. Notice the deep current modulation (40%) on the laser wavelength scale.

This effect could be important when a magnetic compressor is installed in the downstream beam line

because it could produce an enhanced micro-bunching on the scale of the photo-injector laser wavelength [5].

## CONCLUSIONS

Though laser field doesn't affect in a relevant way the electron beam emittance and energy spread, in the case of grazing incidence it generates a current modulation inside the bunch. Current modulation is transformed into energy modulation via the space charge field, which may produce enhanced micro-bunching when the beam is further compressed in a magnetic chicane. On the other hand, as a concluding and wishful remark, one can take profit of such an energy modulation as a possible alternative to laser heating [6]. By means of a high power longer wavelength (I.R.) laser conditioned photo-emission (i.e. illuminating the cathode with an IR laser light in addition to the required UV light), one may think to pre-heating the electron beam by enhancing the current modulation at the cathode. The space charge induced energy spread is then transformed in an uncorrelated energy spread in a downstream chicane with negative  $R_{56}$  [5]. A more detailed study on this subject is under way to assess the amplitude of the achievable energy spread.

## REFERENCES

- [1] J.B. Rosenzweig et al., "Experimental testing of dynamically optimized photoelectron beams", Proc. of the ICFA workshop "The Physics and applications of high brightness electron beams", Erice, 2005.
- [2] M. Ferrario et al., "HOMDYN study for the LCLS photoinjector", SLAC-PUB-8400 (2000).
- [3] T. Plettner, SLAC-PUB-11800 (2006).
- [4] D. Alesini et al., "Status of the SPARC project", these proceedings.
- [5] M. Boscolo et al., "Laser comb: simulations of pre-modulated e- beams at the photocathode of a high brightness rf photoinjector", these proceedings.
- [6] Z. Huang et al., Phys. Rev. STAB 7, 074401 (2004).

# ELECTRON BEAM-LASER INTERACTION NEAR THE CATHODE IN A HIGH BRIGHTNESS PHOTOINJECTOR

M. Ferrario, G. Gatti, INFN-LNF, Frascati, Italy; L. Serafini, INFN-Mi, Milano, Italy;  
J. B. Rosenzweig, UCLA, Los Angeles, USA

## Abstract

The production of high charge short bunches in a high brightness photoinjector requires laser pulses driving the cathode with GW range peak power on a mm spot size. The resulting transverse electric field experienced by the electron beam near the cathode is of the order of 200-500 MV/m, well in excess of a typical RF accelerating field of 50-100 MV/m. We present here a preliminary study of the resultant beam dynamics. Simulations including the electron beam-laser interaction have been performed with the code HOMDYN taking into account the superposition of incident and reflected laser pulses as well as space charge fields. Under this conditions the emittance degradation is negligible, as predicted by analytical methods, but a longitudinal charge modulation occurs on the scale of the laser wavelength, in case of oblique incidence, driven by the longitudinal component of the laser field. Charge modulation is transformed into energy modulation via the space charge field, which may produce enhanced microbunching effects when the beam is further compressed in a magnetic chicane.

## INTRODUCTION

Electron beam – laser interaction near the cathode surface could be important in case of short and strong laser pulses, when the involved field becomes high and the electrons have a very low momentum (emission is achieved slightly overcoming the cathode work-function to reduce thermal emittance). We consider in this study the case of a metal photocathode. Other kinds of photocathodes, such as high Quantum Efficiency (QE) Cs<sub>2</sub>Te have no need to be driven at high power, in addition their response is slower (some ps), and the considerations that will be made in this framework require some slight adjustments to fit the alternative case of semiconductor cathodes. A large laser field at the cathode can produce “heating” of the electron beam through the induced wiggling motion. The degree to which the laser field causes emittance growth can be estimated as [1]:

$$\varepsilon_n = a_l \sigma_x \approx \frac{\lambda_l}{2\pi m_e c^2} \sqrt{Z_0 P_l}$$

Here  $a_l$  is the peak normalized vector potential of the laser field,  $P_l$  is the peak laser power and  $\lambda_l$  the laser wavelength (note the independence of the beam size  $\sigma_x$ ). For example a laser pulse 300 fs long with an energy of 0.2 mJ as required by a blow out experiment [1], able to extract 0.33 nC charge from a 10<sup>-5</sup> quantum efficiency cathode, results in a 0.04  $\mu\text{m}$  induced emittance growth.

This effect, while physically interesting, is negligible in this case. A more interesting effect is produced on the longitudinal phase space, as will be discussed in the next sections.

## HOMDYN SIMULATIONS

The fast running code HOMDYN [2] has been modified in order to include the beam interaction with the laser field, here modelled as a simple truncated plane wave, in addition to the RF and space charge fields already implemented in the code, including the important effect of the cathode image charges.

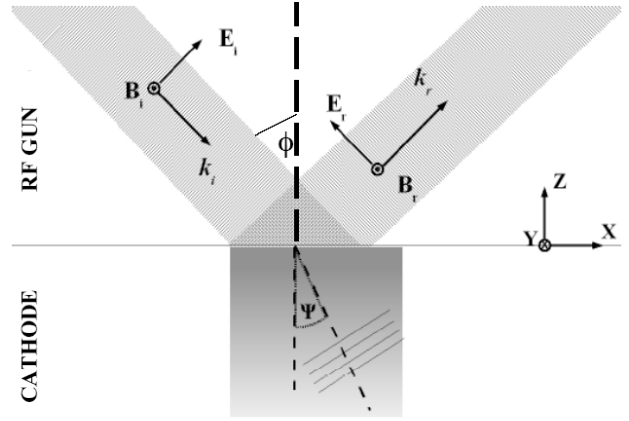


Figure 1: P-polarized plane wave incident on a lossy medium [3].

The expression of the electromagnetic field of a plane wave incident on a lossy medium for a p-polarized wave is the following, see also Fig. 1:

$$B_i = -\hat{y}(E_i / c) \cos(k_i \cdot r - \omega t + \varphi_i)$$

$$E_i = E_i [\hat{x} \cos \vartheta + \hat{z} \sin \vartheta] \cos(k_i \cdot r - \omega t + \varphi_i)$$

$$B_r = -\hat{y} R(E_i / c) \cos(k_r \cdot r - \omega t + \varphi_R)$$

$$E_r = E_i R [-\hat{x} \cos \vartheta + \hat{z} \sin \vartheta] \cos(k_r \cdot r - \omega t + \varphi_R).$$

Assuming a cathode reflection coefficient constant within the laser wavelength spectrum. The previous expressions can be easily extended to the general case of a real laser pulse, without operating integration over the spectrum. It is sufficient to substitute the incoming envelope expression into the amplitude of the incoming field  $E_i$ .

Dealing with lossy media (i.e. radiation must be absorbed to generate photo-electrons) the p-polarization is reflected again as p, but with a phase shift due to the complex index of refraction  $n$ . Photoemitted electrons experience a field that is sum of incoming and reflected

wave. Inside photocathode the field amplitude is attenuated exponentially in direction normal to the surface, and propagates at a slightly different angle, this effect will be include in a future work.

Both normal and oblique laser incidence (at 70 degrees) have been taken in consideration in HOMDYN simulations. A laser field amplitude of 190 MV/m is assumed, the RF field experienced by the electrons injected in the gun with 26 phase degrees is 53 MV/m, (120 MV/m peak field). Laser wavelength was fixed at 266 nm, able to drive Cu and other metal photo-cathodes.

The first case considered here is a 10 ps long laser pulse at normal incidence and a 1 nC e-bunch charge, corresponding to the nominal SPARC parameters [4]. An integration time step of 0.1 fs (corresponding approximately to 10% of the laser central wavelength period) and 1000 slices 40 nm long (about  $\lambda/7$ ) were used. As was expected, each slice experiences the fast varying field of the laser, as a cosequence slice centroids undergoes a fast oscillation in space. The amplitude of the oscillations grows with the time, and so this effect is enhanced in the first emitted slices compared to the last ones as shown in Fig. 2.

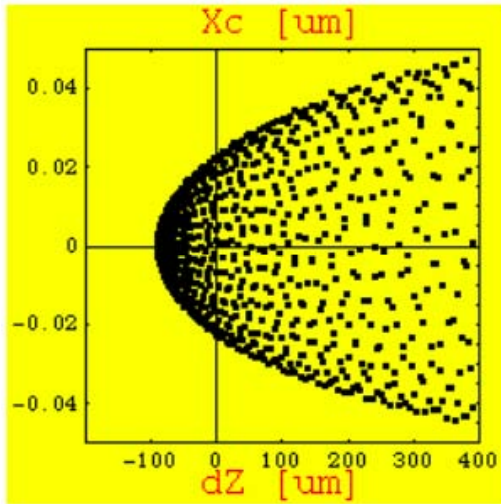


Figure 2: Slice centroids evolution during the interaction with the laser beam. Each dot represents a slice centroid located at a distance dz from the bunch central slice.

This effect occurs on a negligible scale, so that, looking at the macroscopic consequences on the beam, neither envelope, nor emittance or energy spread are affected in such a way to show a noticeable degradation of the beam quality. Emittance on a time scale of 10 ps reaches a value of  $0.05 \mu\text{m}$ .

The case of grazing incidence is more interesting. First of all, the angle introduces an asymmetry on electron trajectories, depending on different field phase which particles experience at different emission times, Fig. 3. Once again, the transverse dynamics is affected by an even weaker effect, than in normal incidence

The computed emittance behaviour for a 1 ps laser pulse, 1 pC charge is shown in Fig. 4. As can be seen in

the plot, after a time of 1 ps the emittance growth due to space charge prevails.

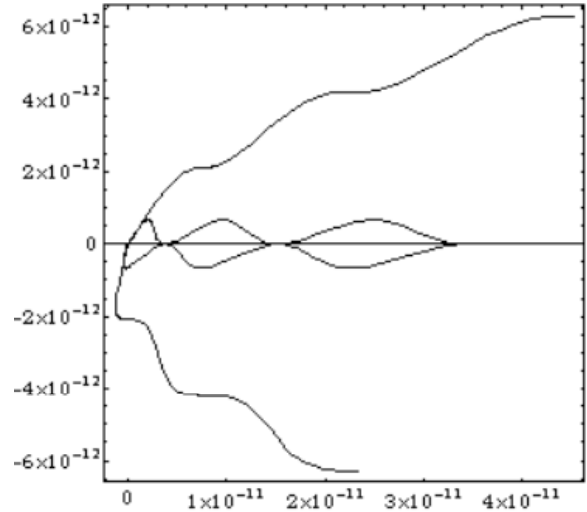


Figure 3: Electron trajectories for different injection phases in a laser field with grazing incidence. (Transverse displacement [m] versus time [s]).

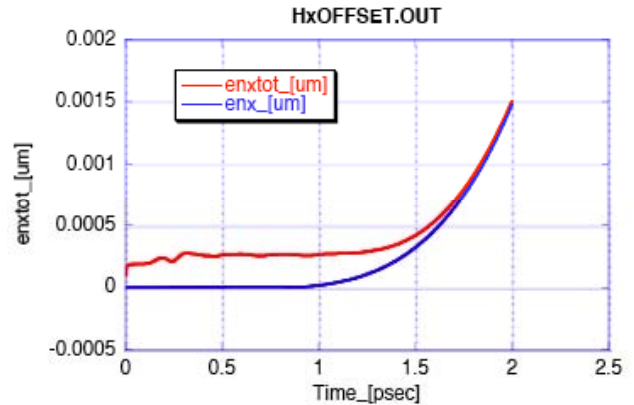


Figure 4: Normalized emittance vs. time for the 1 ps laser, 1 pC case. Blue line: space charge induced emittance Red line: total emittance including laser induced emittance.

On the other hand since laser contribution is now mainly longitudinal, we expect a some effect on the longitudinal motion. Preliminary simulations show that even if the induced energy spread is negligible, a charge modulation on a scale of the laser wavelength occurs. Different groups of slices emitted within different half periods of the laser field will experience in fact accelerating or decelerating laser fields components, while the electron velocity changes from a non-relativistic to a relativistic regime, due to the superimposed RF accelerating field. The initial extraction velocity  $\beta=v/c=0.002$  in this case is enough to prevent backward acceleration. This periodic shrinking and broadening of the slices, that last until the end of the electron-laser interaction, results in a slice current modulation, as shown if Figures 5 and 6. Notice that the current modulation can reach a 40% depth. Downstream the

cathode the beam evolution is dominated by space charge effects and will transform this current modulation in energy modulation [5].

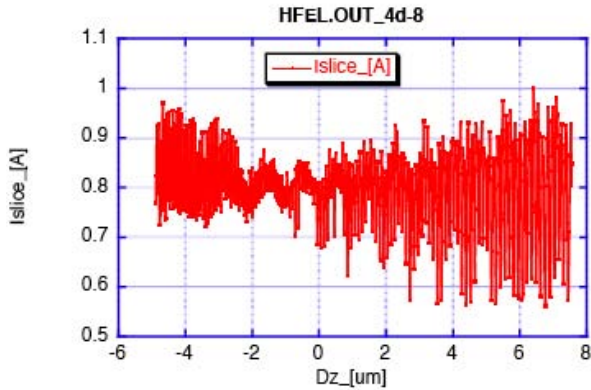


Figure 5: Normalised beam current modulation at the end of the photo-emission process.

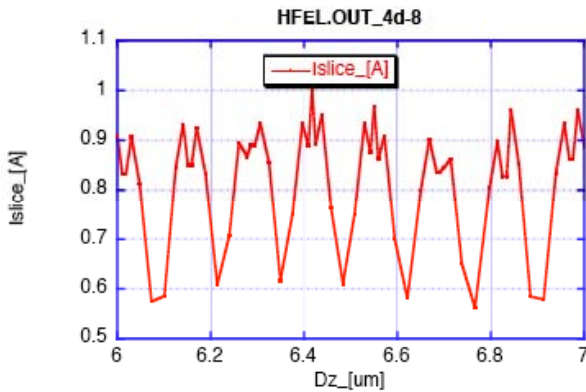


Figure 6: Normalised beam current modulation at the end of the photo-emission process, blow up of Fig. 5. Notice the deep current modulation (40%) on the laser wavelength scale.

This effect could be important when a magnetic compressor is installed in the downstream beam line

because it could produce an enhanced micro-bunching on the scale of the photo-injector laser wavelength [5].

## CONCLUSIONS

Though laser field doesn't affect in a relevant way the electron beam emittance and energy spread, in the case of grazing incidence it generates a current modulation inside the bunch. Current modulation is transformed into energy modulation via the space charge field, which may produce enhanced micro-bunching when the beam is further compressed in a magnetic chicane. On the other hand, as a concluding and wishful remark, one can take profit of such an energy modulation as a possible alternative to laser heating [6]. By means of a high power longer wavelength (I.R.) laser conditioned photo-emission (i.e. illuminating the cathode with an IR laser light in addition to the required UV light), one may think to pre-heating the electron beam by enhancing the current modulation at the cathode. The space charge induced energy spread is then transformed in an uncorrelated energy spread in a downstream chicane with negative  $R_{56}$  [5]. A more detailed study on this subject is under way to assess the amplitude of the achievable energy spread.

## REFERENCES

- [1] J.B. Rosenzweig et al., "Experimental testing of dynamically optimized photoelectron beams", Proc. of the ICFA workshop "The Physics and applications of high brightness electron beams", Erice, 2005.
- [2] M. Ferrario et al., "HOMDYN study for the LCLS photoinjector", SLAC-PUB-8400 (2000).
- [3] T. Plettner, SLAC-PUB-11800 (2006).
- [4] D. Alesini et al., "Status of the SPARC project", these proceedings.
- [5] M. Boscolo et al., "Laser comb: simulations of pre-modulated e- beams at the photocathode of a high brightness rf photoinjector", these proceedings.
- [6] Z. Huang et al., Phys. Rev. STAB 7, 074401 (2004).

# WIRE COMPENSATION OF PARASITIC CROSSINGS IN DAΦNE

C. Milardi, D. Alesini, M.A. Preger, P. Raimondi, M. Zobov, LNF-INFN, Frascati, Italy  
D. Shatilov, BINP, Novosibirsk, Russia

## Abstract

Long-range beam-beam interactions (parasitic crossings) are one of the main luminosity performance limitations for the Frascati  $e^+e^-$   $\Phi$ -factory DAΦNE. In particular, the parasitic crossings lead to a substantial lifetime reduction of both beams in collision. This puts a limit on the maximum storable current and, as a consequence, on the achievable peak and integrated luminosity. In order to alleviate the problem numerical and experimental studies of the parasitic crossings compensation with current-carrying wires have been performed at DAΦNE. Two such wires have been installed at both ends of the KLOE interaction region. Switching on the wires in agreement with the numerical predictions, improvement in the lifetime of the “weak” beam (positrons) has been obtained at the maximum current of the “strong” one (electrons) without luminosity loss. In this paper we describe the parasitic crossings effects in DAΦNE, summarize the results of numerical simulations on their compensation with the wires and discuss the experimental measurements and observations.

## INTRODUCTION

The Frascati  $\Phi$ -factory DAΦNE is an  $e^+e^-$  collider operating at the energy of  $\Phi$ -resonance (1.02 GeV c.m.) [1]. Its best peak luminosity reached so far is  $1.5 \times 10^{32}$   $\text{cm}^{-2}\text{s}^{-1}$  with a maximum daily integrated luminosity of about  $10 \text{ pb}^{-1}$  [2].

In order to obtain such a high luminosity at low energy high current bunched beams are stored in each collider ring. Usually, the number of adjacent filled buckets is in the range 109÷111 out of 120 available. A short gap is needed for ion clearing. It’s worth reminding that in DAΦNE the bunch separation of 2.7 ns is the shortest among all existing colliders and particle factories.

In order to minimize the effect of parasitic crossings (PC) of the closely spaced bunches the beams collide under a crossing angle in the range 10÷20 mrad. However, in spite of the crossing angle, the long-range beam-beam interactions (LRBB) remain one of the most severe limitations to the performance of DAΦNE in terms of luminosity. In fact LRBB interaction leads to a substantial lifetime reduction of both beams, limiting the maximum storable currents and, as a consequence, the maximum achievable peak and integrated luminosity. The latter is strongly influenced by the beam lifetime because in the topping up regime a fraction of the integrated luminosity is lost during the time necessary to switch the injection system from from one beam to the other. The problem of the LRBB interactions is expected to be even more pronounced in future operation for the FINUDA

experiment [3], because the crossing angle is intrinsically lower. The PC effects are foreseen to be also very important for the DAΦNE upgrade options [4], where the number of colliding bunches will be increased by means of higher frequency RF cavities making the bunch separation even shorter than in the present situation.

Looking for a compensation scheme to reduce the impact of LRBB interactions we decided to install two windings (wires) at both ends of the KLOE interaction region (IR). This approach revises an idea originally proposed by J.P.Koutchouk [5] for LHC, and recently tested during single beam operation on SPS [6, 7]. Simulations using LHC compensation devices also predicted a relevant dynamic aperture enlargement for the Tevatron collider [8].

At DAΦNE we have performed an experimental study of the LRBB compensation using purposely built wires obtaining encouraging results, and testing for the very first time the wire compensation scheme in collision.

In this paper we describe our experience and the experimental results.

## PARASITIC CROSSINGS IN DAΦNE

DAΦNE consists of two independent rings sharing two interaction regions: IR1 and IR2. The KLOE detector is installed in IR1. While delivering luminosity to KLOE bunches collide with a crossing angle of 14.5 mrad, and are vertically separated in IR2 by a distance larger than  $200 \sigma_y$ . For this reason, in the following considerations only LRBB interactions in IR1 will be taken into account.

The bunches experience 24 PCs in IR1, 12 before and 12 after the main interaction point (IP), until they are separated by splitter magnets into two different rings.

Table 1 summarizes the main parameters for some PCs: relative position, beta functions, phase advances with respect to the IP and transverse separation in terms of  $\sigma_{x,y}$ .

Table 1: Parameters for the PCs, one every four, in IR1.

PC order	Z-Z <sub>IP</sub> [m]	$\beta_x$ [m]	$\beta_y$ [m]	$\mu_x - \mu_{IP}$	X [ $\sigma_x$ ]	Y [ $\sigma_y$ ]
BB12L	-4.884	8.599	1.210	0.167230	26.9050	26.238
BB8L	-3.256	10.177	6.710	0.140340	22.8540	159.05
BB4L	-1.628	9.819	19.416	0.115570	19.9720	63.176
BB1L	-0.407	1.639	9.426	0.038993	7.5209	3.5649
IP1	0.000	1.709	0.018	0.000000	0.0000	0.0000
BB1S	0.407	1.966	9.381	0.035538	-6.8666	3.5734
BB4S	1.628	14.447	19.404	0.092140	-16.4650	63.196
BB8S	3.256	15.194	6.823	0.108810	-18.7050	157.74
BB12S	4.884	12.647	1.281	0.126920	-22.1880	25.505

There are indications that the LRBB interactions affect the beam dynamics in DAΦNE: in fact, the PCs induce orbit distortion that can be satisfactorily reproduced by the

machine model, based on the MAD [9] code, when the PCs are taken into account. MAD predictions agree with the orbit distortion obtained from the beam-beam simulation code Lifetrack [10], see Fig. 1

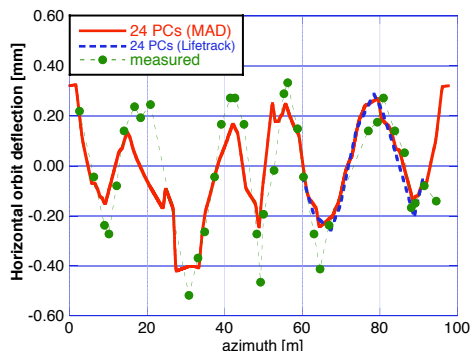


Figure 1: computed orbit deflection due to 24 BBLR interactions for the positron bunch colliding against 10 mA electron bunches.

Moreover, the lifetime of each beam starts decreasing during injection of the opposite beam and remains low soon after injection. Typically, in collision, the electron beam current reaches  $1.8 \div 2.2$  A, while the maximum positron beams is  $1.3 \div 1.4$  A. Exceeding these values the lifetime of the beams drops down to  $700 \div 800$  sec. Presently this behaviour is considered one of the main limitation of the collider performance.

## NUMERICAL SIMULATIONS

The “weak-strong” tracking code LIFETRAC was used to simulate the equilibrium distribution of the positron (‘weak’) beam. The main sources of long beam tails are the 2 PCs nearest to the Main IP, but the other PCs also make some contribution, so we account for all of them. The wires were simulated as additional PCs with variable current (“wire-PC”), so that no special tracking algorithm for wires was used. This approach is justified by the rather large values of the  $\beta_{x,y}$  functions at the wire locations (16.5 and 4 m respectively), much larger than both the bunch and wire length. This allows simulating the interaction with the wire as a single kick, neglecting the effect of movement of the “strong” bunch: the longitudinal coordinate of collision point for the real PC depends on the particle's longitudinal coordinate, while the wire are fixed, but for large betas a shift of few millimeters gives actually no effect. On the other hand, the betas are small enough to have a large separation in units of the transverse beam size ( $\approx 20$ ), so the actual “shape of wire” (i.e. density distribution inside the wire-PC) does not matter: it works like a simple  $1/r$  lens. Some simulation results are shown in Fig. 2. The beam current was chosen to be large enough to have long beam tails due to PCs (a), then the wires were switched on and the tails reduced (b). When the wires are powered with wrong polarity, the tails blow-up becomes even stronger (c).

As a matter of fact, the PCs compensation with a single wire on each side of the interaction region is not perfect

since distances between the beams at PC locations are different in terms of the horizontal sigma and phase advances between PCs and wires are not completely compensated (see Table 1). Indeed, the numerical simulations did not show improvements in luminosity. However, the positive effect of tails reduction and corresponding lifetime increase is very important, because it leads to a larger integrated luminosity.

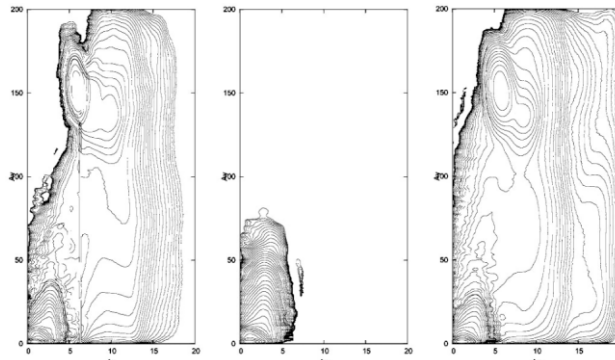


Figure 2: Particle equilibrium density in the normalized transverse phase space, starting from left: wires off (a), wires on (b) and wires powered with wrong polarity (c).

## WIRE DESIGN AND INSTALLATION

The wires have been built and installed in IR1 in November 2005. Each device is made of two windings of rectangular shape, 20 coils each, installed symmetrically with respect to the horizontal plane, see Fig. 3. Our device differs from the LHC one for several aspects: our wires are installed outside the vacuum chamber exploiting a short section in IR1, just before the splitters, where the vacuum pipes are separated to host Lambertson type correctors not essential for operation and therefore removed. The wires carry a tunable DC current, and produce a stationary magnetic field with a shape similar to the one created by the opposite beam.



Figure 3: The wires installed at one end of IR1.

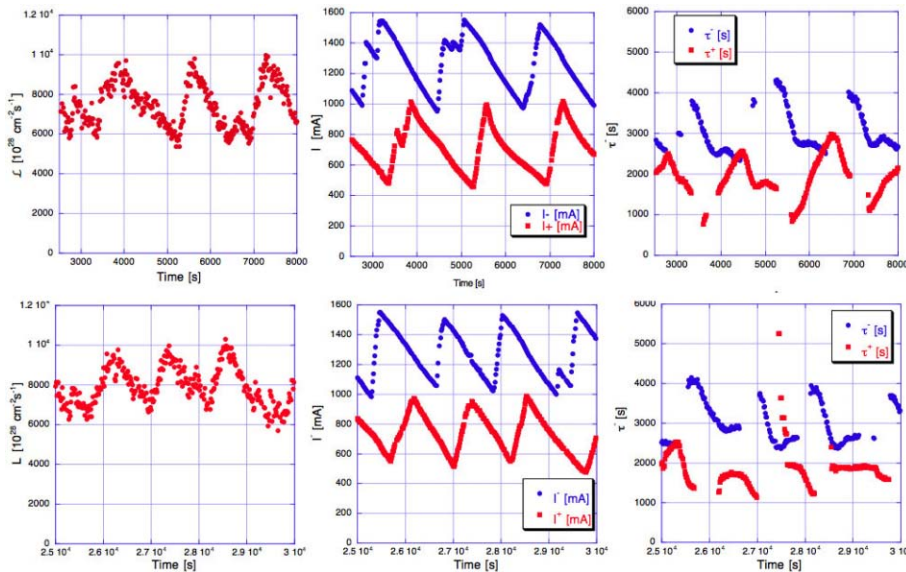


Figure 4: Luminosity, colliding currents and lifetime as a function of time : wires on (upper frames) and wires off (lower frames).

### EXPERIMENTAL RESULTS

A systematic study of the wires in collision has been undertaken during the machine shifts in March 2006.

The wires were powered at 3.6 A to compensate as much as possible the beam lifetime of the positron beam that, due to the limited maximum achievable current, can be considered as the ‘weak’ one.

It has been experimentally verified that the residual orbit distortions with maximum deviations of +0.4 -0.5 mm due to the PCs is very well corrected with wire currents of  $\approx 1$  A. This is a proof that the wires behave as correctors “in phase” with the PCs. It has been also measured that the wires introduce some betatron tunes shifts which should be corrected.

The residual orbit distortion due to the wires at 3.6 A was corrected by the ordinary dipole correctors, while the tune shifts were compensated by means of the quadrupoles in a dispersion free straight section.

Several luminosity runs have been compared by switching the wires on and off to study their impact on the collisions. In the following the two most relevant sets are presented taking into account 2 hours long runs. The results in Fig. 4 show some clear evidences. Switching on and off the wires we obtain the same luminosity while colliding the same beam currents. The positron lifetime is on average higher when wires are on, while the electron one is almost unaffected. The beam blow-up occurring from time to time at the end of beam injection, corresponding to a sharp increase in the beam lifetime, almost disappear.

A further aspect becomes evident when comparing, on the same plot, the positron current and lifetime with and without wires, see Fig. 5. The positron current starts from the same value, then, in the case of wires off the current decreases with a higher derivative than in the case with wires on. The lifetime exhibits a consistent behavior, being higher in the case when wires are on. In this way it

is possible to keep the same integrated luminosity injecting the beam two times only instead of three in the same time integral, or to increase the integrated luminosity by the same factor keeping the same injection rate.

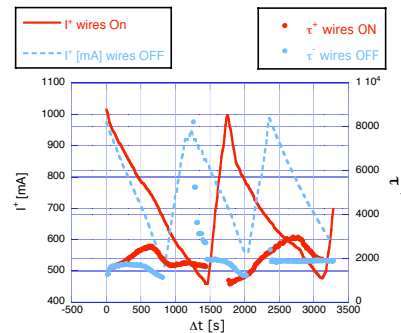


Figure 5: Positron current and lifetime as a function of time: wires on (red) and wires off (cyan).

### CONCLUSIONS AND ACKNOWLEDGMENTS

The wires installed on DAΦNE proved to be effective in reducing the impact of BBLR interactions and improving the lifetime of the positron beam. We are indebted to G. Sensolini, R. Zarlenga and F. Iungo for the technical realization of the device.

### REFERENCES

- [1] G. Vignola, PAC93, p.1993.
- [2] A. Gallo et al., this conference, MOPLS028.
- [3] The FINUDA Collaboration, LNF-93/021 (IR), 1993.
- [4] [http://www.lnf.infn.it/Infadmin/direzione/DANAE\\_LOI.pdf](http://www.lnf.infn.it/Infadmin/direzione/DANAE_LOI.pdf)
- [5] J.P. Koutchouk, LHC Project Note 223 (2000)
- [6] J.P. Koutchouk et al., EPAC2004, p. 1936.
- [7] F. Zimmermann et al., PAC2005, p.686.
- [8] T. Sen, PAC2005, p.2645.
- [9] H. Grate et al., “The MAD Program”.
- [10] D. Shatilov, Particle Accelerator 52:65-93, 1996.

# THE FAST VERTICAL SINGLE-BUNCH INSTABILITY AFTER INJECTION INTO THE CERN SUPER PROTON SYNCHROTRON

E. Métral, G. Arduini, T. Bohl, H. Burkhardt, G. Rumolo, CERN, Geneva, Switzerland  
B. Spataro, INFN/LNF, Frascati, Italy

## Abstract

Since 2003, high-intensity single-bunch proton beams with low longitudinal emittance have been affected by heavy losses after less than one synchrotron period after injection. The effects of the resonance frequency of the responsible impedance, longitudinal emittance and chromaticity on the intensity threshold were already discussed in detail in 2004, comparing analytical predictions with simulation results. In this paper the evolution of the instability between injection and the time of beam loss is our main concern. Measurements are compared with HEADTAIL simulations. A travelling-wave pattern propagating along the bunch, which is the signature of a Beam Break-Up or Transverse Mode Coupling Instability (TMCI), is clearly identified. The oscillating frequency, near  $\sim 1$  GHz, is in good agreement with the usual broad-band impedance model deduced from beam-based measurements like the head-tail growth rate vs. chromaticity.

## INTRODUCTION

The low-frequency longitudinal impedance of the SPS has been reduced by a factor of  $\sim 2.5$  from 1999 to 2001 by modification and shielding of over thousand elements like vacuum ports [1]. The threshold for the longitudinal microwave instability increased even more. However, the transverse impedance has only been reduced by  $\sim 40\%$  [2] and this improvement was since then partially cancelled by the re-installation of the equipment needed for the SPS as LHC injector (5 MKE extraction kickers installed in 2003 and 4 installed for the 2006 start-up).

Measurements have been performed in 2003 in the SPS right after injection at 26 GeV/c, where a fast single-bunch vertical instability develops if the longitudinal emittance of the beam is too small [3]. Figure 1 is an example of what was observed with a high-intensity single bunch ( $\sim 1.2 \times 10^{11}$  p/b) of low longitudinal emittance ( $\sim 0.2$  eV.s). The RF voltage was  $\hat{V}_{RF} \approx 0.6$  MV, which corresponds to the synchrotron period  $T_s = 7.1$  ms. Keeping the chromaticity close to zero, the bunch was stabilized when the intensity was reduced to  $\sim 6 \times 10^{10}$  p/b.

The effects of the resonance frequency of the responsible impedance, longitudinal emittance and chromaticity on the intensity threshold were already discussed in detail in 2004, comparing analytical predictions with simulation results [4]. In this paper the evolution of the instability between injection and the time of beam loss is our main concern.

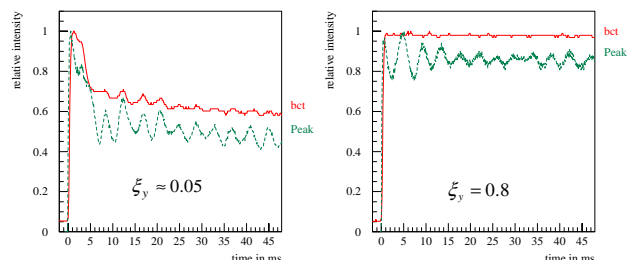


Figure 1: Plot of the measured relative (normalized to the value at injection) bunch intensity vs. time in the SPS machine in 2003. bct stands for beam current transformer and Peak stands for peak intensity. The bunch, which is unstable when  $\xi_y \approx 0.05$  (left) is stabilized by increasing the (relative) chromaticity to  $\xi_y = 0.8$  (right).

## MEASUREMENTS

The evolution of the vertical centroid position along the bunch has been recorded turn by turn using the “Head-Tail” monitor (with a sampling period of 125 ps) [5]. An animation has been produced, clearly revealing a travelling-wave pattern propagating from the head of the bunch to the tail, with a frequency of  $\sim 1$  GHz [6]. As the animation could not be reproduced here, only the picture with 150 traces superimposed is shown in Fig. 2. The oscillation frequency is clearly visible on Fig. 3.

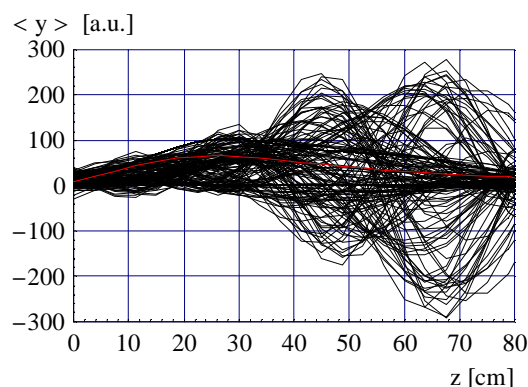


Figure 2: Measured evolution of the vertical centroid position along the bunch  $\langle y \rangle = N(z) \times y_{av}(z)$ , where  $N(z)$  is the longitudinal bunch profile, using the “Head-Tail” monitor (with the traces of all the 150 turns superimposed), for a vertical (relative) chromaticity close to zero (see Fig. 1). The first turn after injection is shown in red. The head of the bunch (truncated at  $\pm 2 \sigma_z$ ) is on the left and the tail on the right.

Increasing the chromaticity above a certain value prevents the instability from developing (see Fig. 4). Here again, it is nicely seen in the animation [6] that the travelling-wave pattern does not succeed to propagate along the bunch. Only the picture with the traces of all the 150 turns superimposed is shown in Fig. 4.

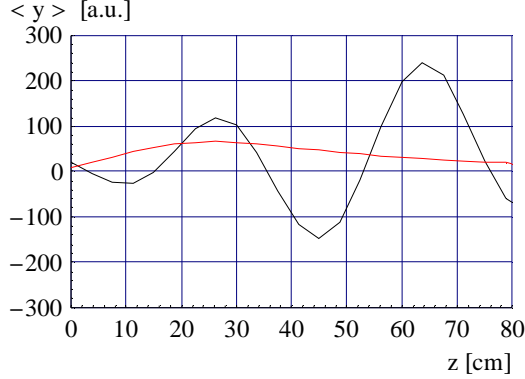


Figure 3: Measured evolution of the vertical centroid position along the bunch using the “Head-Tail” monitor (only the trace of turn 99 is shown), for a vertical (relative) chromaticity close to zero (see Fig. 1).

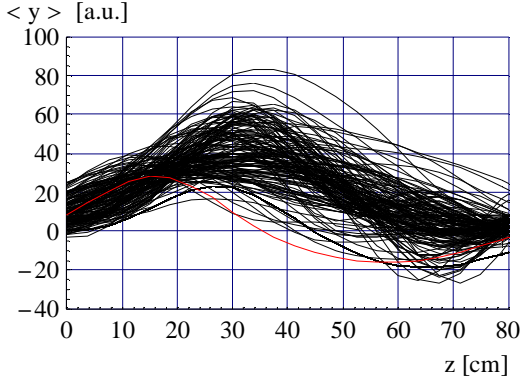


Figure 4: Measured evolution of the vertical centroid position along the bunch using the “Head-Tail” monitor (with the traces of all the 150 turns superimposed), for a vertical (relative) chromaticity of  $\sim 2$ . Note the difference in vertical scale.

## SIMULATIONS

Simulations have been performed using the HEADTAIL code [7], assuming the beam and SPS parameters reported in Table 1. The cases of round and flat geometry (which is the real case in the SPS) have both been simulated, but revealed no significant difference concerning the evolution in time of the instability. The evolution of the vertical centroid position along the bunch has been simulated turn by turn, and an animation has also been produced, clearly revealing a travelling-wave pattern propagating from the head of the bunch to the tail, with a frequency of  $\sim 1$  GHz [6]. The picture with all the traces superimposed is shown in Fig. 5, where the same kind of picture as the measured

Fig. 2 is reproduced from simulation using the “classical” Broad-Band (BB) impedance model deduced from several beam-based measurements.

Table 1: Basic beam and SPS parameters relevant for this simulation study. The BB shunt impedance is given here for a round chamber.

Parameter	Value	Unit
Circumference	6911	m
# of bunches	1	
Relativistic $\gamma$	27.7286	
# of protons per bunch	$1.2 \cdot 10^{11}$	
Vert. tune	26.13	
Vert. relative chromaticity	0	
Rms bunch length	20	cm
Rms long. mom. spread	0.00093	
Synchrotron tune	0.00323	
Cavity harmonic number	4620	
Mom. compaction factor	0.00192	
BB tr. shunt impedance	20	M $\Omega$ /m
BB resonance frequency	1	GHz
BB quality factor	1	

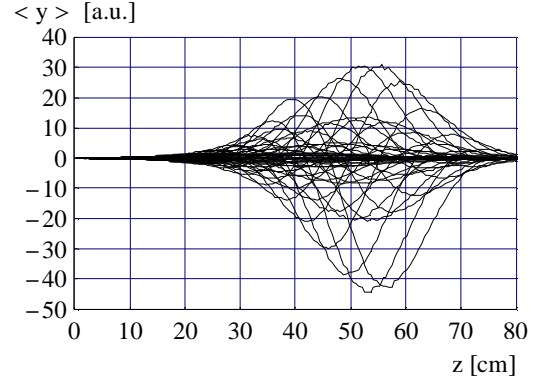


Figure 5: Simulated evolution of the vertical centroid position along the bunch using the HEADTAIL code (with the traces of all the turns superimposed). The head of the bunch (truncated at  $\pm 2\sigma_z$ ) is on the left.

The effects of space charge and RF voltage have also been studied in detail with predictions for the LHC beam, whose longitudinal emittance is  $0.35$  eV.s instead of  $\sim 0.2$  eV.s used here [8]. For the simulations a BB impedance model with a resonance frequency  $f_r = 1.3$  GHz and a quality factor  $Q = 1$  was used. The transverse shunt impedance  $Z_{\perp}$  was scanned to try to fit observed thresholds with different beam parameters. The results are shown in Fig. 6, which reveals that the nominal LHC beam (with the estimated impedance of  $\sim 20$  M $\Omega$ /m) should be close to the instability with matched longitudinal voltage ( $\sim 0.7$  MV). However, capturing the beam in a 2 MV bucket, as normally done in operation, should considerably help.

Space charge seems beneficial since it raises the TMCI

threshold, but it also gives rise to a fast emittance blow-up below TMCI threshold. This effect should be studied in detail in future machine studies as this could considerably degrade the LHC beam quality.

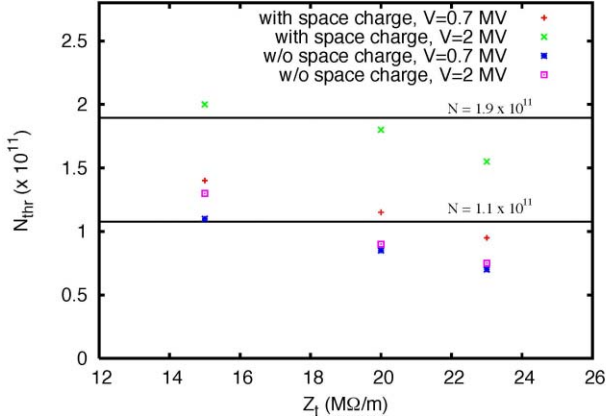


Figure 6: Simulated TMCI intensity threshold for the LHC beam with/without space charge for two different RF voltages, using the HEADTAIL code.

A more precise model of the SPS transverse impedance is under development. For the moment only the transverse impedances of the MKE kicker and the Beam Position Monitors (BPMs) have been computed and/or measured. The results of analytical prediction and measurements using two wires [9] for one MKE kicker are shown in Fig. 7. It is seen that the measurements are close to the theoretical (2D) prediction, which is close to a BB impedance with a resonance frequency near 1.8 GHz, a quality factor  $Q \sim 1$ , and a shunt impedance of  $\sim 0.5 \text{ M}\Omega/\text{m}$ . As there are nine MKE kickers in the SPS, it leads to  $\sim 4.5 \text{ M}\Omega/\text{m}$  in total.

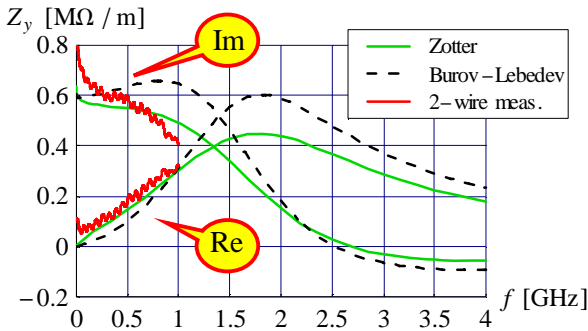


Figure 7: Theoretical predictions of the transverse resistive-wall impedance of one SPS MKE kicker, using both Zotter's [10] and Burov-Lebedev's [11] formalisms.

Concerning the 108 horizontal and 108 vertical BPMs, simulations with MAFIA have been performed, revealing the presence of four potentially dangerous transverse trapped modes (two from the horizontal and two from the vertical BPMs). The basic parameters of these modes are listed in Table 2. HEADTAIL simulations, considering

only the four trapped modes, revealed that the TMCI intensity threshold is one order of magnitude higher than the observed one. Therefore, the BPMs alone cannot explain the observed fast instability.

Table 2: The four most dangerous transverse trapped modes per BPM from MAFIA simulations.

	$\beta_x$ (m)	$\beta_y$ (m)	$f_r$ (GHz)	$R$ (M $\Omega$ /m)	$Q$
BPH	103	21	0.537	4.6	1951
BPH	103	21	1.836	2.35	3367
BPV	22	101	0.786	1.67	2366
BPV	22	101	2.27	2.05	5880

## CONCLUSION

The measured evolution of the vertical centroid position along the bunch can be reasonably reproduced using the “classical” broad-band impedance model deduced from several beam-based measurements. A detailed analysis of this evolution in time will be used in the future to refine our SPS transverse impedance model, which is under development. For the moment only the transverse impedance of the 9 SPS MKE kickers has been computed and measured, and the impedance of the 108 horizontal and 108 vertical BPMs simulated.

The nominal LHC beam in the SPS could be unstable after the installation of the last four MKE kickers before the 2006 start-up. Capturing the beam in a 2 MV bucket, as normally done in operation, should considerably increase the intensity threshold. The TMCI threshold is certainly increased by space charge, however there is an emittance blow-up associated below threshold, which could degrade the beam quality. Another possibility to increase the instability threshold could be the use of linear coupling [12].

## REFERENCES

- [1] T. Bohl et al., Proc. EPAC'02, Paris, France, 2002.
- [2] H. Burkhardt, Proc. 33rd ICFA Advanced Beam Dynamics Workshop, Bensheim, Germany, 2004.
- [3] H. Burkhardt et al., Proc. EPAC'04, Lucerne, Switzerland, 2004.
- [4] E. Métral et al., Proc. 33rd ICFA Advanced Beam Dynamics Workshop, Bensheim, Germany, 2004.
- [5] N. Catalan-Lasheras et al., CERN-AB-2003-058 BDI, 2003.
- [6] E. Métral, (<http://ab-div.web.cern.ch/ab-div/Meetings/APC/Welcome.html>).
- [7] G. Rumolo et al., CERN-SL-Note-2002-036 AP.
- [8] G. Rumolo et al., CERN-AB-2005-088-RF, 2005.
- [9] F. Caspers et al., Private communication (2006).
- [10] E. Métral, CERN-AB-2005-084, 2005.
- [11] A. Burov, LHC Project Note 353 (revised), 2004.
- [12] E. Métral and G. Rumolo, these proceedings.

# DESIGN AND TESTING OF Gproto BUNCH-BY-BUNCH SIGNAL PROCESSOR \*

D. Teytelman<sup>†</sup>, C. Rivetta, D. Van Winkle, R. Akre, J. Fox, A. Krasnykh, SLAC, Stanford, USA  
 A. Drago, LNF-INFN, Frascati, Italy  
 J. Flanagan, T. Naito, M. Tobiyaama, KEK, Tsukuba, Japan

## Abstract

A prototype programmable bunch-by-bunch signal acquisition and processing channel with multiple applications in storage rings has been developed at SLAC. The processing channel supports up to 5120 bunches with bunch spacings as close as 1.9 ns. The prototype has been tested and operated in five storage rings: SPEAR-3, DAΦNE, PEP-II, KEKB, and ATF damping ring. The testing included such applications as transverse and longitudinal coupled-bunch instability control, bunch-by-bunch luminosity monitoring, and injection diagnostic. In this contribution the prototype design will be described and its operation will be illustrated with the data measured at the above-mentioned accelerators.

## INTRODUCTION

Most modern lepton storage rings operate above the dipole coupled-bunch instability thresholds in transverse and longitudinal planes. Digital bunch-by-bunch feedback systems have become in the last 15 years a ubiquitous solution for controlling such instabilities [1, 2].

In this paper we describe a prototype (Gproto) of a highly flexible bunch-by-bunch signal processing channel. The Gproto provides real-time baseband signal processing at the sampling frequencies up to 550 MHz. Flexibility is achieved via the use of a field-programmable gate array (FPGA) for all demultiplexing and signal processing tasks. The Gproto can be configured to support bunch-by-bunch feedback as well as a host of bunch-by-bunch beam and collider diagnostic functions. The Gproto supports reconfiguration of the processing harmonic number to adapt to a particular storage ring. Feedback controller topology can also be modified allowing one to use finite or infinite impulse response (FIR or IIR) filters of different orders. For longitudinal feedback applications which often demand controller impulse response persisting for tens of revolutions, downsampling can be used to more efficiently utilize the computational resources. In the most challenging case of KEKB rings with 509 MHz RF frequency and 5120 bunches the Gproto executes an equivalent of  $4 \times 10^9$  integer multiply/accumulate operations per second.

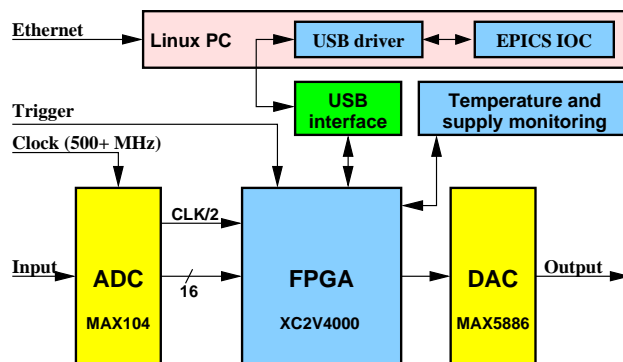


Figure 1: The Gproto block diagram.

## SYSTEM ARCHITECTURE

The block diagram of the prototype is shown in Fig. 1. The heart of the system is a Virtex-II FPGA. The FPGA receives the high-speed digitized data from the 1 GSPS 8-bit analog-to-digital converter (ADC). Feedback output correction is converted to baseband analog signal by 500 MSPS 12-bit digital-to-analog converter (DAC). Both the ADC and the FPGA are mounted on evaluation boards from Maxim Semiconductor and Xilinx respectively. The use of these evaluation boards shortened the development cycle of the prototype to one month. For interconnect between the ADC and the FPGA standard ribbon cable was used to carry fully differential digital data. That interface has been tested to transfer clock rates up to 300 MHz which corresponds to 600 MSPS ADC conversion rate.

In transverse feedback applications the Gproto is combined with a front-end that converts raw BPM signals to baseband bunch positions. A typical back-end set-up consists of two power amplifiers differentially driving a set of striplines. The Gproto provides complementary low-level DAC outputs for simple interfacing. The DAC output structure is optimized for wide bandwidth, achieving 240 ps rise and 360 ps fall times for the full-scale swings.

Any accelerator instrumentation and diagnostic system to be fully usable requires some form of the operator interface. The Gproto utilizes an EPICS softIOC running under a standard Linux distribution. The softIOC communicates with the hardware via USB interface, previously developed for low group-delay woofer application in PEP-II [3].

The Gproto user interface, built using edm display manager, provides operator with control functions for feedback configuration, system and beam diagnostics. Feedback control functions include two selectable sets of FIR

\* Work supported by U.S. Department of Energy contract DE-AC02-76SF00515

<sup>†</sup> dim@slac.stanford.edu

## EXPERIMENTAL RESULTS

Within 6 months of its creation the Gproto has been tested in 5 storage rings: SPEAR-3, DAΦNE, PEP-II, KEKB, and the ATF damping ring. Here selected results of these tests are presented.

### Longitudinal Feedback

The Gproto has been tested in the Accelerator Test Facility (ATF) damping ring as a longitudinal feedback channel. In order to create the 90 degree phase shift at the synchrotron frequency of 10 kHz the feedback controller needs to have impulse response lasting around one period of that frequency, i.e. 100  $\mu$ s corresponding to 216 turns. Since a 216-tap FIR implementation was unfeasible in the Gproto, downsampling by 16 combined with a 16-tap FIR was used for a filter spanning 256 turns.

A comparison between the open and closed-loop quadratically averaged bunch spectra is presented in Fig. 3. Closing the longitudinal feedback loop suppresses the unstable synchrotron motion and reduces the oscillation due to the various noise sources within the ring RF system.

### Transverse Feedback

In Fig. 4 a grow/damp measurement performed in the DAΦNE positron ring is shown. This measurement was performed with a 100-bunch train and a 20-bunch gap. Plot a) shows the bunch oscillation amplitude increasing along the train with all the bunches participating in the exponential growth and, once the feedback loop is closed, damping. In plot b) the bunch motion is shown in the even-fill eigenmode basis showing several dominant low-frequency modes. By fitting a complex exponential to the growing and damping sections of the transient one can estimate the open and closed-loop modal eigenvalues [4].

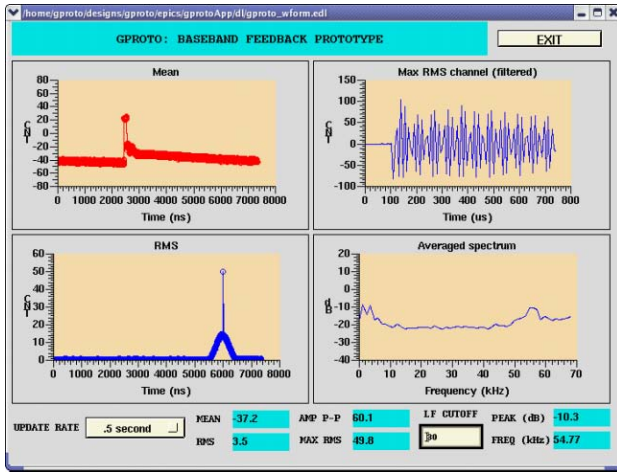


Figure 2: Beam data display for the LER.

filter coefficients, shift gain, and one-turn delay. System diagnostics include RF clock loss and output saturation detectors, supply voltage and component temperature monitoring. The Gproto includes a built-in DAC test pattern generator which allows one to test the performance of the output section and also to properly match the DAC full-scale and the saturation level of the power amplifier.

Integrated beam diagnostics in the Gproto use the internal FPGA memory to acquire 128–240 kB of beam data. The acquired waveform is read out via the USB at an update rate up to 2 Hz. A set of IOC subroutines postprocesses the data in the real-time and provides four concise plots displayed in the waveform panel as shown in Fig. 2. The four plots are: bunch-by-bunch mean and RMS of bunch oscillations, time-domain signal of a bunch with the largest RMS. The last plot is obtained by performing the FFT on each of the bunches and quadratically averaging the resulting spectra. This plot aliases coupled-bunch eigenmodes to a frequency span from DC to  $\omega_{\text{rev}}/2$ . Such a spectrum allows the operator to very quickly check how well the system damps the coupled-bunch motion. The snapshot in Fig. 2 shows the vertical motion in the PEP-II LER acquired on an external trigger synchronized with the injection. The plot clearly shows the large RMS value of the injected bunch as well as the smaller perturbation of the stored beam by the injection kicker bump. The max RMS plot shows the time-domain motion of the injected bunch, while in the spectrum a wideband excitation around the vertical betatron frequency of 56 kHz can be seen.

The postprocessing reduces the two-dimensional matrix of bunch positions versus turns to several one-dimensional vectors. Next, from these vectors we derive a set of six scalar metrics which encapsulate the information about beam stability, excitations, etc. The scalar values are: overall mean and RMS, RMS of the most excited bunch, peak-to-peak amplitude, and, finally, the frequency and the amplitude of the largest spectral peak.

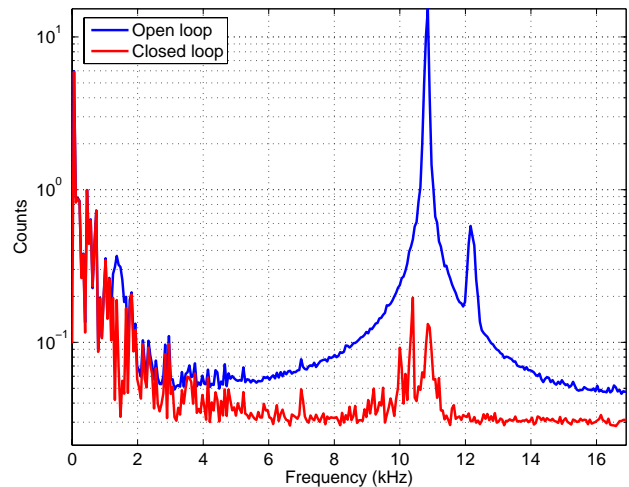
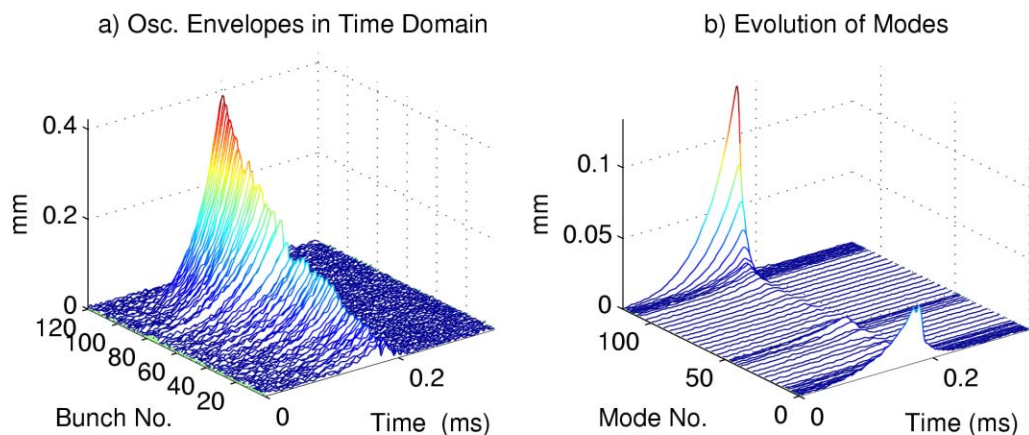


Figure 3: A comparison of open-loop (blue) and closed-loop (red) longitudinal spectra in the ATF damping ring.



DAFNE E+ (Gproto):aug0305/155222: Io= 892.338mA, Dsamp= 1, ShifGain= 2, N bun= 120, At Fs: G1= 11.4717, G2= 0, Ph1= 162.3264, Ph2= 0, Brkpt= 531, Calib= 5.386.

Figure 4: A horizontal grow/damp measurement in DAΦNE positron ring.

### Beam Diagnostic Applications

The integrated real-time beam diagnostics in the Gproto open a large field of applications of the architecture in storage rings. The externally triggered recording capability, illustrated in Fig. 2 has been used in PEP-II HER and LER to optimize timing and amplitudes of the injection kickers, leading to reduced beam perturbation and lower injection backgrounds.

The Gproto has also been tested in PEP-II as a bunch-by-bunch luminosity monitor. In this application the feedback FIR filter was replaced by an IIR turn-by-turn integrator with a 4000 turn time constant. The output of the integrator was stored in the FPGA memory and polled at 2 Hz rate to produce an updating display. Due to parasitic nature of the testing the digitized signal was derived from an output of a discriminator and required multi-turn integration. In Fig. 5 the Gproto luminosity data is shown for section of the PEP-II bunch train. The empty mini-train gaps show zero luminosity, as expected. Note the systematically lower luminosity of the last bunch in each mini-train.

### SUMMARY

A bunch-by-bunch processing channel has been prototyped and tested at five accelerator facilities. During the tests the prototype was used to stabilize horizontal, vertical, and longitudinal coupled-bunch instabilities, to optimize injection, to provide bunch-by-bunch luminosity information. The built-in diagnostic capabilities allow the user to quickly set-up the system and provide a way for routine monitoring of system performance. Two prototype chassis have been built and tested with one unit operating as a horizontal bunch-by-bunch feedback channel in DAΦNE positron ring since October 2005. At this time an integrated processing channel is under development for multiple ap-

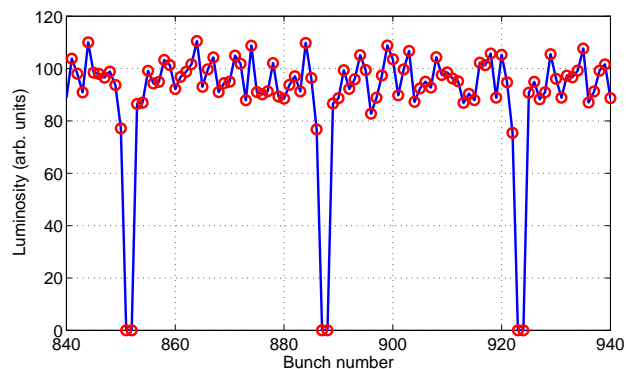


Figure 5: Luminosity information from the Gproto for a section of PEP-II bunch train.

plications in PEP-II and KEKB machines.

### REFERENCES

- [1] M. Tobiyama and E. Kikutani, “Development of a high speed digital signal process system for bunch-by-bunch feedback systems,” *Phys. Rev. ST Accel. Beams*, vol. 3, p. 012801, 2000.
- [2] C. G. M. Lonza, D. Bulfone, “Digital processing electronics for the ELETTRA transverse multi-bunch feedback system,” in *Accelerator and Large Experimental Physics Control Systems*, (Trieste, Italy), pp. 255–257, Comitato Conferenze ELETTRA, 1999.
- [3] D. Teytelman, D. Van Winkle, and J. Fox, “Operating performance of the low group delay woofer channel in PEP-II,” in *Proceedings of the 2005 Particle Accelerator Conference*, (Piscataway, NJ, USA), pp. 1069–1071, IEEE, 2005.
- [4] D. Teytelman, *Architectures and algorithms for control and diagnostics of coupled-bunch instabilities in circular accelerators*. PhD thesis, Stanford University, 2003. SLAC-R-633.

# COMMISSIONING OF THE LASER SYSTEM FOR SPARC PHOTOINJECTOR\*

C. Vicario<sup>†</sup>, M. Bellaveglia, D. Filippetto, A. Gallo, G. Gatti, A. Ghigo,  
INFN-LNF, Frascati, Rome, Italy  
P. Musumeci, M. Petrarca, INFN Rome1, Italy.

## Abstract

In this paper we report the commissioning of the SPARC photoinjector laser system. In the high brightness photoinjector the quality of the electron beam is directly related to the features of the laser pulse. In fact the temporal pulse shape, the temporization and the transverse distribution of the electron beam is determined by the incoming laser pulse. The SPARC laser system is based on an amplified Ti:Sapphire active medium and the pulse shape is imposed by a programmable acousto-optics dispersive filter. The transfer-line has been designed to reduce the angular jitter and to preserve to the cathode the temporal and spatial features of the laser pulse. The laser system has been integrated with the accelerator apparatus. The diagnostics and the control system has been completed. We present the measured performances and the simulations we carried out.

## INTRODUCTION

Specs on SPARC laser system were fixed within the phase of the machine design [1, 2]. The goal is to provide photo-injector (RF-gun) with a proper laser pulse of the order of 10 ps, able to generate an electron beam with a normalized transverse emittance less than 2 mm-mrad and a current of 100 A. We currently use a monocrystalline Cu cathode with a quantum efficiency ( $QE$ ) of  $2 \cdot 10^{-4}$  at 120 MV/m [2] therefore it is required about 50  $\mu J$  to extract 1 nC at the operating phase. Challenging requests are made on laser temporal pulse profile (flat top pulse with 1 ps rise time and ripples limited to 30%) to minimize the e-beam emittance; a pulse shaping activity is in progress and some results have been presented [3, 4]. The SPARC laser is a 10Hz TW system produced by *Coherent*.

The laser system [1] is composed by a Ti:Sa oscillator that generates 100 fs pulses with a repetition rate (r.r.) of 79.3 MHz and an energy of 10 nJ. An acousto-optic programmable dispersive filter called “DAZZLER” [5], used to modify the spectral amplitude and phase is placed between the oscillator and the amplifier to obtain the target temporal profile in the UV. The regenerative and two multipass amplifiers delivers pulses with bandwidth of at 10 nm FWHM  $\lambda = 800$  nm with energy of  $\sim 50$  mJ and divergence less than 1 mrad.

The amplified pulses go to the third harmonic generator (THG) where UV pulses with an energy up to  $\sim 4$  mJ are

produced. The THG is characterized by two type-I BBO (Beta Barium Borate) crystals of 0.5 mm and 0.3 mm thickness used to produce respectively the second and third harmonics. The crystal lengths have been chosen to allocate enough bandwidth to preserve the pulse shape and, at the same time, to guarantee good efficiency. The efficiency of the first conversion is about 50% and the overall conversion efficiency is more than 10%.

After the THG the pulse is sent to a pair of 4300 g/mm UV parallel gratings, that forms a negative group velocity dispersion two passes stretcher. Varying the distance  $L$  between the gratings it is possible to obtain the output pulse length  $\tau[ps] = \tau_0 + 0.44 \cdot L[cm] \cdot \Delta\lambda[nm]$ , where  $\tau_0$  is the UV input pulse duration and  $\Delta\lambda$  is its spectral width. The energy efficiency of the UV stretcher is about 30% producing an energy up to 1.5mJ with an amplitude jitter of 5%<sub>RMS</sub>.

To characterize the pulse time profile a multishot cross-correlator with 200fs resolution was built. The diagnostics uses part of the sub-ps IR pulse to cross-correlate the UV pulse and generating the frequency difference at 400nm. According with the theory and experimental measurements, when a large chirp is imposed, such as for our the UV stretcher, the pulse spectrum allows the direct reconstruction of the time intensity distribution [3]. For the spectral measurements in the UV it has been designed a spectrometer using a UV grating with 4350 g/mm and a converging lens to focus the different wavelength on a ccd camera. This diagnostic proved a the resolution of 0.02 nm.

## OPTICAL TRANSFER LINE TO THE CATHODE

The gun is placed several meters far away the laser room. At the laser exit it is mounted an iris to select the most uniform part of the beam. A 4f imaging system is used to bring the laser to the gun table and to reduce the effect of laser angular jitter, after a telescope is employed to change the laser spot diameter. Before the gun window is placed a reflective diffraction grating to compensate the effects of the grazing incidence on the cathode. The last mirror is motorized to align the beam at the center of the cathode with a resolution of 1  $\mu m$ . Before the gun port a thin beam splitter reflects a small part of the laser beam to a Ce:YAG crystal virtual cathode.

The grating is needed because the gun layout foresees a laser incidence on the cathode at 72° [1]. This layout benefits from the removal of launch optics from the electron beamline and of an enhanced the  $QE$  of the cathode.

\* supported by the EU Commission in the 6<sup>th</sup> FP, contract no. 011935 EUOFEL and contract no. RII3-CT-2003-506395 CARE.

<sup>†</sup> carlo.vicario@lnf.infn.it

However, the grazing incidence also introduces two well-known distortions in the laser pulse: (i) the original circular beam becomes elliptical and (ii) the laser amplitude front is tilted respect to the cathode plane and therefore the photons time of arrival depends of the transverse coordinate. This effects induce a strong distortion on the distribution of emitted electron respect to the ideal cylindrical shape. While for the first distortion the use of an anamorphic can easily yield a pulse the desired ellipticity, the correction of the time-slew is more problematic. The commonly accepted solution of using a grating to "crab" the beam [6] is in practice an open issue, especially when considering the fact that a large bandwidth is needed for the optimal pulse shape. The amount of time of arrival difference  $\Delta t$  across the beam  $x$  can be simply derived using Eq. (2):

$$\Delta t(x) = \frac{x}{2} (\sin(\theta_i) + \sin(\theta_d)) \quad (1)$$

here  $\theta_i$  and  $\theta_d$  are the input and the diffracted angle respectively. The grating acts also as a anamorphic system producing an elliptical diffracted beam given by:

$$e = \frac{a}{b} = \frac{\cos(\theta_d)}{\cos(\theta_i)} \quad (2)$$

where  $a$  is and  $b$  are the input and the output beam dimension. To obtain simultaneously the conditions  $\Delta t(x) = 0$  and a circular beam at the cathode, it was adopted a grating parallel to the cathode with  $3600 \text{grooves/mm}$  which has the characteristics that when  $\theta_i = 0^\circ$ , the diffracted radiation, for  $266 \text{nm}$ , comes out at  $\theta_d = 72^\circ$ . Because the grating is a highly dispersive optical element by design, the unavoidable chromatic dispersion complicates the launch optical set-up. In our case the angular dispersion is quite large:  $\partial\beta/\partial\lambda = 12 \text{ mrad}$ .

To balance the dispersion a lens with focal length  $f_0 = 50 \text{cm}$  is placed at  $2f_0$  after the grating and  $2f_0$  from the cathode. This lens recombines the dispersed wavelengths on the cathode where the circular laser spot is obtained.

To observe the grating induced front tilt, we performed a series of measurements with a streak camera Hamamatsu model 1360, which has  $\sim 2 \text{ ps}$  resolution. Since the available optics of the streak camera are not optimized for UV radiation we analyzed the time slew introduced by a grating across the IR pulse before the THG.

For the measurements we used a  $1200 \text{ lines/mm}$  grating to scale the grooves density to the case of  $800 \text{ nm}$  central wavelength pulse, maintaining unchanged  $\theta_i$  and  $\theta_d$ . We introduced also a lens between the grating and the streak camera slits. In this way we imaged on the camera the grating plane.

The streak images, in the cases of sub-ps and  $5 \text{ ps}$  laser input pulse are shown in Fig. 1. The measurement of the length of the laser pulse when the beam is fully compressed is limited by the streak camera resolution as it was obtained by autocorrelation technique that the pulse length in this case is  $< 200 \text{ fs}$ . In order to decrease the aberrations introduced by the streak camera that occur when the beam

transverse size is large compared to the entrance slit, we selected an horizontal slice of the beam of width  $4 \text{ mm}$ .

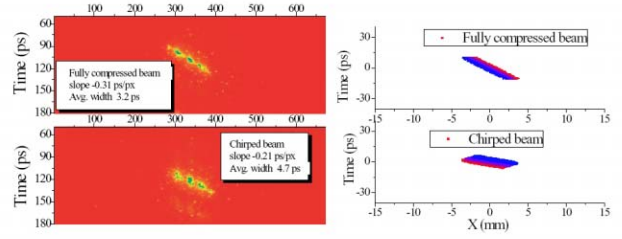


Figure 1: On the right streak images, time of arrival vs transverse position, of a sub-ps (a) and a  $5 \text{ ps}$  (b) IR pulse after the grating. On the right are reported the corresponding results obtained with the ZEMAX simulations.

From the streak images reported it is evident the amplitude front tilt imparted on the beam, especially in the case of the short pulse. To completely understand the measurements we used the optical design simulation code ZEMAX [7]. We developed a macro function that keeps track of the optical path length and by tracing a large number of rays reconstructs the three dimensional distribution of the photons at any given surface, be it the entrance slit of the streak camera. The agreement between measurements and simulations reported in Fig. 1 is quite good. For the proposed optical set up at the photocathode, the simulations indicate a minor time distortion for the different frequencies (less than  $250 \text{ fs}$  for  $\Delta\lambda = 1.4 \text{ nm}$ ).

To prove the effectiveness of the designed optical set-up we used a  $2 \text{ mm}$  diameter, sub-ps laser pulse to illuminate the cathode. The presence of a front tilt would lengthen up to  $4 \text{ ps}$  the effective width of the e-beam. We measured downstream the gun the e-beam duration, using the ps streak camera and a Cerenkov radiator [8]. In the low charge limit, the pulse length turns out to be close to  $2 \text{ ps}$ , that is the resolution of the streak. We can infer therefore that the time slew compensation is achieved in the ps range.

The main drawback of the proposed set-up is that the compensation is achieved only for a well defined position of the lens. Misalignment of about  $1 \text{ cm}$  introduces pulse distortion and significant optical path difference between the wavelengths of  $1.5 \text{ ps}$ . In the set-up proposed, the grating generate two diffracted orders, and therefore only 35% of the input energy is useful to illuminate the cathode. Even though, the laser energy on the cathode is large enough to produce the target beam charge  $1 \text{ nC}$ .

## LASER TO RF SYNCHRONIZATION MEASUREMENTS

A precise synchronization between the photocathode drive laser and the accelerating wave is necessary to have a fixed and stable time-of-arrival of the photons on the cathode with respect of the phase of the  $2856 \text{ MHz}$  RF accelerating field. This condition is very important to guarantee

the stability and the shot-to-shot reproducibility of crucial beam parameters as the beam charge, energy, emittance and energy spread and to ensure a proper matching condition in the accelerator. From beam dynamics simulations [9], a variation over  $\pm 4^\circ$  of RF (about  $\pm 4$  ps) of the laser-to-gun phase, in ideal conditions, increases the output rms projected normalized emittance of about 20%. From these results it has been concluded that a tolerance of  $\pm 2$  ps around the optimal phase is acceptable in order to limit the emittance growth to less than 10%. The issue of timing jitter becomes even more critical when the future experiments planned at the SPARC facility are considered. For example in FEL seeding experiments, Inverse Compton Scattering experiments, or laser acceleration experiments requires sub-ps synchronization. Since the amplification process and the optical launching to the cathode introduce a negligible time jitter the synchronization has to be carried out at the level of the laser oscillator. The oscillator synchronization unit monitors continuously the laser's phase through a 2 GHz photodiode and compare the laser repetition rate and its 9<sup>th</sup> harmonic with the reference signal from the S-band master clock waveform and 1/36<sup>th</sup> divider. The laser frequency lock is achieved using three cavity length actuators in the laser head: a high frequency piezo-electric trasducer, a low frequency galvanometer driven delay line and a DC motor.

We measured the time jitter at oscillator level using well-known technique, by mixing the reference signal and with the laser pulse detected by a 25 GHz photodiode. The IF mixer employed is a custom device from Pulsar Microwave Corporation able to demodulate the signal and to provide in-phase and in-quadrature components from which we can simply calculate amplitude (absolute) and phase (relative to a reference). The observed time jitter that varied from  $650 f_{s_{rms}}$  to  $750 f_{s_{rms}}$ . This value takes into account also the time jitter of the S-band master oscillator and the successive signal down-conversion.

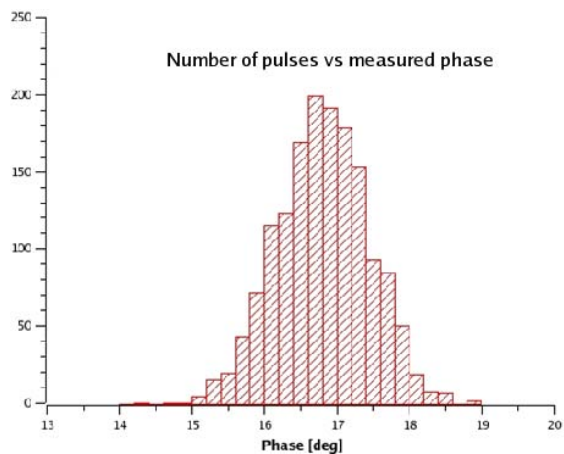


Figure 2: Statistics of the the UV laser pulse to RF reference measured phase noise.

To have information on the phase noise on the single

laser UV pulse near the cathode at 10 Hz, we adopted pulse-to-pulse phase lock feedback. The measured signal comes from a cavity tuned at 2856MHz, fed by a high voltage electric pulse (with a peak of about 100V) coming out a fast photodiode illuminated by the laser pulse. This photodetector is a bi-planar vacuum photodiode with a rise time of 100ps operating at 1.5 kV bias voltage. The cavity grants an exponential decaying pseudo-sinusoidal signal with a duration of about 1.5μs and allows to perform a consistent relative phase measurement using the IF mixer and the a 14-bit DAQ card with sampling rate of 60 Msamples/s. As reported in Fig 2 the time jitter, recorded over few minutes, is about  $630 f_{s_{rms}}$  and in general is limited to 1 ps. The good level of synchronization is confirmed by the stability of the SPARC e-beam parameters.

## CONCLUSION

This paper reports the performances of the SPARC laser system. The laser, the diagnostic and the optical transfer line to the cathode have been presented. The experimental characterization of the front tilt introduced by a reflective diffraction grating has been reported. The results are in good agreement with simulations. The optical scheme to compensate the time slew and the ellipticity associated with the grazing incidence on the cathode have been implemented and shows a successful compensation within 1 ps in time slew. Measurement of the phase noise indicates less than 1 ps time jitter of the UV laser pulse respect to the RF system.

## REFERENCES

- [1] Eds: L. Palumbo and J. B. Rosenzweig. *Technical Design Report for the SPARC Advanced Photo-Injector*, INFN-LNF, 12/01/2004.
- [2] L. Serafini, *Status of the SPARC Project*, to be appear in Proc. Epac06, Edinburgh (2006).
- [3] C. Vicario, S. Cialdi and M. Petrarca, *High power third harmonic flat pulse laser generation*, accepted for publication by Opt. Lett. (2006).
- [4] M. Petrarca et al. *Production of Temporally Flat Top UV laser pulses for SPARC Photoinjector*, to be appear in Proc. Epac06, Edinburgh (2006).
- [5] F. Verluise et al. *J. Opt. Soc. Am. B*, **17**, 138 (2000).
- [6] P. R. Bolton *LCLS-TN-05-18* (2005).
- [7] [http : \www.zemax.com](http://www.zemax.com).
- [8] J. Rosenzweig et al. *Optimum Beam Creation in Photoinjectors Using Space-charge Expansion*, to be appear in Proc. Epac06, Edinburgh (2006).
- [9] C. Ronsivalle et al., *Study of tolerances and sensitivity to erros in the SPARC high brightness photo-injector*, SPARC-BD-03/008 (2003).

# PRODUCTION OF TEMPORALLY FLAT TOP UV LASER PULSES FOR SPARC PHOTOINJECTOR\*

M. Petrarca<sup>†</sup>, P. Musumeci, M. C. Mattioli, Univ. “La Sapienza” INFN sez. Rome 1, Rome, Italy  
 C. Vicario, G. Gatti, A. Ghigo, INFN-LNF, Frascati, Rome, Italy  
 S. Cialdi, I. Boscolo, INFN sez. Milan, Milan, Italy

## Abstract

In the SPARC photoinjector, the amplified Ti:Sa laser system is conceived to produce an UV flat top pulse profile required to reduce the beam emittance by minimizing the non-linear space charge effects in the photoelectrons pulse. Beam dynamic simulations indicate that the optimal pulse distribution must be flat top in space and time with 10 ps FWHM duration, 1 ps of rise and fall time and a limited ripple on the plateau. In a previous work [1] it was demonstrated the possibility to use a programmable dispersive acousto-optics (AO) filter to achieve pulse profile close to the optimal one. In this paper we report the characterization of the effects of harmonics conversion on the pulse temporal profile. A technique to overcome the harmonics conversion distortions on the laser pulses at the fundamental wavelength in order to obtain the target pulse profile is explained too. Measurements and simulations in the temporal and spectral domain at the fundamental laser wavelength and at the second and third harmonics are presented in order to validate our work. It is also described a time diagnostic device for the UV pulses.

## INTRODUCTION

The SPARC project (Sorgente Pulsata Autoamplificata di Radiazione Coerente) is a 150 MeV advanced photoinjector designed to drive a SASE-FEL in the visible ( $\sim 300 - 500$  nm) [4]. The photoinjector, that is being developed at LNF, is conceived to explore the emittance correction technique and high current production with the preservation of the transverse emittance in order to obtain high brightness electron beam. This is an important requirement for the good development of the SPARC SASE FEL and in particular for its future upgrade to reach the soft x-ray. The accelerator consists of a Ti:Sa laser to illuminate a metal photocathode, an rf-gun and 3 SLAC s-band accelerating sections. As it has been demonstrated [3, 4], the generation of high energy laser pulses with a few picoseconds time width, center wavelength at 266 nm, flat top temporal profile with fast rise and fall time, is required to start the photo-emission process from metal cathodes in order to achieve electron bunches characterized by low transverse emittance  $\sim 1$  mm-mrad and high current. In order to manipulate the Gaussian natural shape of the usual laser

pulses and transform it into a uniform profile as required by SPARC, the following Ti:Sa laser chain has been chosen [4, 5]. A Ti:Sa oscillator generates 100 fs pulses with a repetition rate (r.r.) of 79.3 MHz. An acousto-optic programmable dispersive filter called “DAZZLER” [6], used to modify the spectral amplitude and phase function is placed between the oscillator and the amplifier to obtain the target temporal profile. The amplifier is based on the well known “chirp pulse amplification” (CPA) process [7] and it is composed by a regenerative and a multipass amplifier. It delivers pulses at  $\lambda = 800$  nm with energy of  $\sim 50$  mJ and r.r. of 10 Hz. The pulses get into the harmonic conversion box (HGCB) where UV pulses with an energy up to  $\sim 4$  mJ are produced. The HGCB is characterized by two type-I BBO (Beta Barium Borate) crystals of 0.5 mm and 0.3 mm used to produce respectively the second harmonic generation signal (SHG) and the third harmonic generation signal.

At the end of the laser chain there is a grating stretcher used to broaden temporally the pulses up to (8 – 12) ps. In this paper we present some pulse shape measurements going through the evolution from the fundamental towards the third harmonic generation and we show how to operate to obtain the target pulse shape. At the end we show how the UV pulse shape is retrieved.

## PULSE SHAPING

In the previous work [8], we showed that by using the DAZZLER to introduce a proper spectral phase and amplitude modulation in the initial IR pulses, it is possible to manipulate their natural Gaussian shape to obtain the flat top profile with the right features required from SPARC. The obtained pulses profile is no more maintained as soon as the pulses go into the SHG and THG crystals to produce UV light. The reasons for these are fully explained in [9, 10] and briefly reported in the following for the simplest case of Type-I SH generation. In the situation of “non depletion” condition [11] and perfect phase-matching, the SH signal is given by:

$$\tilde{I}_2 \propto \text{sinc}^2(\beta\omega d) d^2 \left| \left[ \tilde{A}_1 \otimes \tilde{A}_1 \right] \right|^2 \quad (1)$$

where:  $\beta$  is a factor that takes into account the group velocities of the pulses inside the crystal,  $d$  is the crystal length and the dispersion factor is neglected due to the short crystal length (500  $\mu$ m). Being the signal proportional to the convolution product of the power spectrum  $\tilde{A}_1(\omega)$ , it

\* Supported by: EU Commission in the FP6 program, CARE contract No. RII3-CT-2003-506395 and EUROFEL contract No. SSA - 011935.

<sup>†</sup> massimo.petrarca@roma1.infn.it

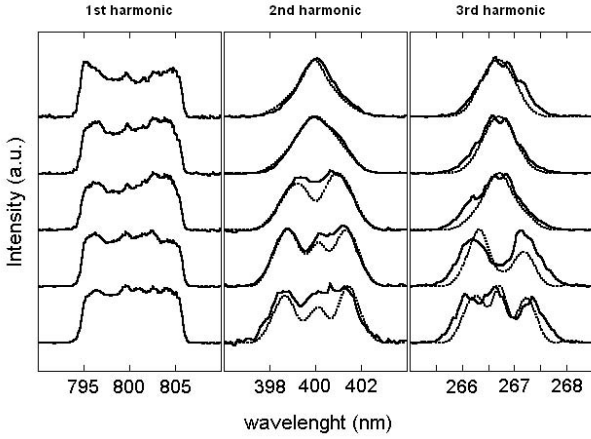


Figure 1: From the left to the right: measured IR, BLUE and UV spectra are reported in solid line; simulated spectra for second and third harmonic, (dashed line) are also shown. The chirp increases from the top to the bottom.

is clear that it is not possible to obtain a SH rectangular spectrum starting by just a first harmonic rectangular one, in fact the convolution product will yield a triangle. On the contrary by introducing a chirp into the fundamental signal, the initial rectangular shape can be preserved. In fact, considering  $A_1(\omega) = S(\omega)e^{i\phi(\omega)}$  with  $S(\omega)$  real and  $\phi(\omega) = \alpha\omega^2/2$ , where the  $\alpha$  parameter is the chirp strength introduced by the DAZZLER, we obtain:

$$\tilde{A}_1 \otimes \tilde{A}_1(\omega) = \int S(\omega - \Omega)S(\Omega)e^{i(\phi(\omega-\Omega)+\phi(\Omega))} d\Omega \quad (2)$$

Since in the phase factor,  $\phi(\omega - \Omega) + \phi(\Omega)$  is a parabolic function centered at  $\Omega = \omega/2$ , the dominant contribution comes for  $\Omega$  close to  $\omega/2$  when enough chirp is applied. Thus we can write:

$$\int S(\omega - \Omega)S(\Omega)e^{i(\phi(\omega-\Omega)+\phi(\Omega))} d\Omega \sim S^2(\omega/2)e^{2i\phi(\omega/2)} \quad (3)$$

Therefore in the fundamental beam, the leading behavior of the SH spectral intensity is given by the square of the fundamental with twice the spectral width and the SH spectrum changes its shape from triangular to rectangular. Moreover, being the SH spectrum proportional to the square of the initial one, the increasing of the ripple in the higher harmonic is explained too. The above considerations can be extended to the third harmonic generation. The results of this discussion is that it is necessary to introduce a large enough chirp factor on the 800nm pulse in order to produce a UV rectangular spectrum. The amount of this chirp has to be determined accurately because a large value can reduce too much the conversion efficiency. These considerations are in good agreement with the experimental data reported in Fig. (1).

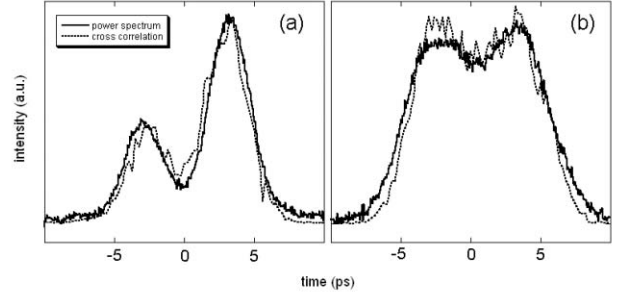


Figure 2: Comparison between the spectral, solid line, and temporal profile, dashed line, in two cases.

### SPECTRUM TRANSFERRED IN TIME

In the previous section we demonstrate that by using the Dazzler to introduce proper spectral phase and amplitude modulation in the fundamental beam, it is possible to produce flat top UV spectra. Now we show that it is possible to have the same produced spectra profiles but in the time domain. In this way, once the correct flat top spectrum profile is obtained for the TH signal, the desired temporal shape is almost obtained too [10]. This is achieved by introducing enough temporal linear chirp into the TH signal by sending the pulse trough the UV stretcher. In Fig. (2) two examples are shown: we compare the spectral profile, solid line, and the time profile, dashed line. In both cases we obtained a good superposition between the spectrum and the temporal profile. These two profiles, have been produced by introducing with the Dazzler a proper phase and amplitude modulations in the fundamental. In Fig. (2), the spectral x-axis has been converted in the time coordinate using the relation  $\Delta t = a \cdot \Delta\omega$  (in our case  $a = 0.3 \text{ ps}^2$ ) between angular frequencies and time delay which is introduced by the stretcher and that will be discussed later on. In these two cases we have a strong pulse stretching, in fact the UV pulse length before the stretcher is about 300 fs while the final pulse length is about 10 ps. The temporal profile has been traced by a UV-IR cross correlator that has been built, studied and characterized [12, 13] and briefly described later on. For completeness we report here the relation between the time profile and its spectrum. Let us consider a pulse with complex amplitude  $A(\omega)$  and a quadratic phase function given by  $\exp[i \cdot a\omega^2/2]$ ; the  $a$  parameter takes into account the chirp introduced by the stretcher. The time intensity profile, given by the square modulus of the inverse Fourier transform, turns out to be:

$$I(t) = \left| \int A(\omega)e^{i(\frac{a\omega^2}{2}-\omega t)} d\omega \right|^2 \sim \mathcal{I}(\omega = t/a) \quad (4)$$

where  $\mathcal{I}(\omega) = |A(\omega)|^2$  is the power spectrum. In fact, since the phase function is a parabola centered at  $\omega = t/a$ , when the stretched pulse has a temporal width much longer than the input one, the leading contribution to the integral

comes from the angular frequencies near the minimum of the phase. Therefore the spectral profile can be used as a time profile diagnostic. Moreover the temporal coordinate can be obtained by the relation  $\Delta t = a \cdot \Delta \omega$ .

## TIME DIAGNOSTIC

To measure the UV time pulse length a cross-correlator device based on the difference frequency generation (DFG) process is made using a BBO crystal by mixing a part of the IR pulses at frequency  $\omega$  with the UV pulses at frequency  $3\omega$  [12, 13]. Since the IR pulses of intensity  $I_{IR}$  have a temporal width much shorter  $\sim 100fs$  (thus are called reference pulses) than the UV pulses  $\sim 10ps$  of intensity  $I_{UV}$ , the signal produced at frequency  $3\omega - \omega$  is proportional to the cross correlation function of the UV pulses:

$$I(3\omega - \omega, \tau) \propto \int I_{UV}(3\omega, t) I_{IR}(\omega, t - \tau) dt \quad (5)$$

The device is capable to measure  $\sim 100fs$  UV full width half maximum pulses. A complete and more detailed description of the device and of the physics behind it, is reported in [12, 13] where it is analyzed and discussed the presence of the spatial chirp in the UV beam and it is pointed out the importance of the crystal angle alignment. In fact changing the crystal phase matching angle, the temporal shape of the harmonic signal generated as well as its efficiency changes. The changes of the temporal shape due to the crystal angle mismatching have been observed. To overcome this problem the following procedure has been adopted: we first generated a two peaks spectrum profile and then we aligned the crystal angle in order to have the same shape in the time domain. This is possible once again because in our case the spectrum shape is transferred in the time domain.

## CONCLUSION

In this paper we have presented a technique to produce the desired UV flat top laser pulses required from the SPARC project to achieve high brightness electron beam through the photoemission process from a metal photocathode. The whole technique is based on the Dazzler. Using this device it is possible to introduce the proper spectral phase and amplitude modulation in the initial IR pulses in order to manipulate their spectral shape and to obtain the target UV spectrum profile. A way to eliminate the distortions introduced by the SH and TH crystals is explained. This is done by introducing through the Dazzler a chirp factor in the fundamental beam. We also showed that the UV spectrum shape can be transferred to time profile by introducing a large enough chirp factor in the UV beam. So that once the desired UV spectrum is achieved, the temporal shape is obtained too. As it is shown in Fig. (2), the desired rise and fall time of the pulses are longer ( $\sim 2.5 ps$ ) than the required one  $< 1 ps$ . This will be the subject of further studies.

A time diagnostic device necessary to study the time profile of UV pulses has been presented: the UV-IR cross correlator.

We acknowledge the supports of the EU Commission in the FP6 program, CARE contract No. RII3-CT-2003-506395 and EUROFEL contract No. SSA - 011935.

## REFERENCES

- [1] H. Loos et al. "Temporal E-Beam Shaping in an S-Band Accelerator", Proc. Particle Accelerator Conference, p.642, 2005, Knoxville, TN, USA.
- [2] M. Ferrario, M. Boscolo, V. Fusco, C. Vaccarezza, C. Roncisvalle, J. B. Rosenzweig, L. Serafini, in ICFA Workshop "The physics and applications of high brightness electron beams" (Chia Laguna, Sardinia, Italy, July 2002)
- [3] J. Yang, F. Sakai, T. Yanagida, M. Yorozu, Y. Okada, K. Takasago, A. Endo, A. Yada, M. Washio, J. Appl. Phys. **92**, 1608 (2002)
- [4] Eds: L. Palumbo, J. Rosenzweig. Autori: D. Alesini et al. (INFN/LNF), F. Alessandria et al. (INFN/Milano), D. Levi, M. Mattioli, G. Medici (INFN/Roma1), L. Catani et al. (INFN/Roma2), G. Dattoli et al. (ENEA/FIS), S. Reiche, J. Rosenzweig, G. Travish (UCLA), D. Dowell et al. (SLAC), *Technical Design Report for the SPARC Advanced Photo-Injector*, Preprint INFN National Laboratories of Frascati, 12/01/2004
- [5] C. Vicario et al., *Commissioning of the laser system for SPARC photoinjector* Proceedings of EPAC 2006 (Edinburgh, Scotland)
- [6] F. Verluise, V. Launde, J. P. Huignard, P. Tournois, A. Migus, J. Opt. Soc. Am. B, **17**, 138 (2000)
- [7] P. Maine, D. Strickland, P. Bado, M. Pessot, G. Mourou, *IEEE J. Quantum Electronics*, **24**, 398, (1988).
- [8] C. Vicario, M. Petrarca, A. Ghigo, *Laser temporal pulse shaping experiment for SPARC photoinjector*, Proceedings of EPAC 2004 (Lucerne, Switzerland)
- [9] S.Cialdi, F. Castelli, I. Boscolo, Appl. Phys. B, **3**, (2006), 383-389.
- [10] C. Vicario, M. Petrarca, S. Cialdi *High power third harmonic flat pulse laser generation* Accepted for publication by Optics Letters
- [11] A. Yariv, *Quantum Electronics*, (Wiley, New York, 1989, 3rd ed.).
- [12] M.Petrarca, C. Vicario, S. Cialdi et al. *UV-IR Cross Correlator*, Report INFN-SPARC/LS-06/002 (2006).
- [13] M. Petrarca, C. Vicario, S. Cialdi, in preparation

# Nb-Pb SUPERCONDUCTING RF-GUN<sup>1</sup>

J. Sekutowicz, J. Iversen, D. Klinke, D. Kostin, W.-D. Möller, DESY, Hamburg, Germany  
 I. Ben-Zvi, A. Burrill, J. Smedley, T. Rao, BNL, Upton, NY 11973, USA  
 J. Langner, P. Strzyżewski, A. Soltan INS, Swierk/Otwock, Poland  
 P. Kneisel, TJNAF, Newport News, VA 23606, USA  
 R. Lefferts, A. Lipski, SUNY, Stony Brook, 11794-3800 NY, USA  
 K. Szałowski, Institute of Physics, University of Łódź, Łódź, Poland  
 K. Ko, L. Xiao, SLAC, Menlo Park, CA 94025, USA  
 M. Ferrario, INFN, Frascati, Italy  
 J. B. Rosenzweig, UCLA, Los Angeles, CA 90095, USA

## Abstract

We report on the status of an electron RF-gun made of two superconductors: niobium and lead [1]. The presented design combines the advantages of the RF performance of bulk niobium superconducting cavities and the reasonably high quantum efficiency (QE) of lead, as compared to other superconducting metals. The concept follows the approach of all niobium superconducting RF-gun as it has been proposed by the BNL group. Measured values of quantum efficiency for lead at various photon energies, results of analysis of recombination time of photon-broken Cooper pairs for lead and niobium, and preliminary cold test results are presented in this paper

## INTRODUCTION

One of the most demanding components of a cw injector is a cw operating RF-gun generating low emittance ( $\leq 1 \mu\text{rad}$ ) bunches with  $\sim 1 \text{ nC}$  charge. Present room temperature designs face several difficulties in meeting these requirements. The first one is the limited life time of high quantum efficiency cathodes. A load lock system where the cathode is fabricated external to the cavity, transported under ultra high vacuum, and inserted into the RF gun has been used to address this issue. This exchange mechanism is usually complicated and causes nonlinearities in the electric field pattern in the vicinity of the inserted cathode. The nonlinear fields, together with space charge force, dilute the emittance of photo-emitted bunches. The second difficulty in some designs is that the RF-contacts around the insert enhance emission of the dark current resulting in an uncontrolled additional source of heat and radiation in an accelerator. Finally, RF-guns, both normal- and superconducting, generating highly populated bunches have to be operated at high accelerating gradients to suppress space charge effects. Normal conducting guns dissipate many kilowatts of power fulfilling this condition even when they operate at low pulse repetition rate (low duty factor). It is a technical challenge to increase significantly the duty factor of normal conducting RF-guns while having sufficient cooling and keeping them thermally stable

during operation. Superconducting RF-guns dissipate orders of magnitude less power but the challenge here is integrating a typical, non superconducting photo cathode material, with a superconducting cavity. An electron RF-gun made of superconducting niobium cavity with superconducting lead deposited for photoemission combines the advantages of the RF performance of bulk niobium superconducting cavities and the reasonably high quantum efficiency of lead.

## RF-GUN DESIGN

### General Layout

The design is based on 1.6-cell bulk niobium cavity. In this design, a small spot of lead, approximately 4 mm in diameter ( $D$ ) used as a photo-cathode is located in the centre of the cavity back wall. Lead has QE superior to niobium and is a commonly used superconductor. Its critical temperature ( $T_c$ ) is 7.2 K, not very different from niobium (9.2 K). The emitting spot can be formed either by a coating technique or by pressing a small lead button into a recess in the niobium wall. The mechanical difficulty is that niobium and lead contract very differently. Their expansion coefficients are  $7 \cdot 10^{-6} \text{ 1/K}$  and  $3 \cdot 10^{-5} \text{ 1/K}$  for niobium and lead respectively. In the event of the lead layer peeling off, which to our current knowledge should not happen when the film thickness is less than  $10 \mu\text{m}$ , we will pursue the alternative way of pressing lead button into niobium.

A preliminary design of the superconducting RF-gun is shown in Fig. 1. The superconducting cavity is surrounded by the helium vessel and shielded with  $\mu$ -metal to reduce the exposure of the superconducting wall to solenoid field. In the design shown here the solenoid is

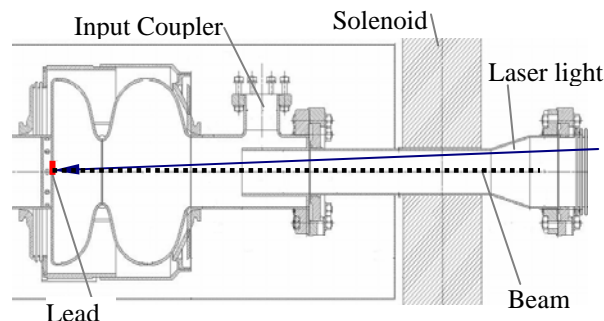


Figure 1. Nb-Pb RF-gun.

<sup>\*</sup> Work This work has been partially supported by the EU Commission, contract no. 011935 EUROFEL-DS5, US DOE under contract number DE-AC02-98CH10886.

normal conducting but the alternate option of a superconducting solenoid placed in the cryostat is technically possible. Modelling of the solenoid showed a small residual field of 1 Gauss at the beam tube iris when only one  $\mu$ -metal layer is applied for the shielding. In practice, the solenoid will be switched on after the cavity reaches its superconducting state, thus no intrinsic  $Q_0$  degradation is expected due to the Meissner effect. The input coupler is placed in isolation in vacuum (not in helium bath). For the final beam energy of  $\sim 6$  MeV and the nominal current of 1 mA (1nC/bunch, 1 MHz repetition frequency) the input coupler will transfer about 6 kW of RF power to the generated beam. This is within the TTF type III coaxial coupler capability with marginally improved cooling.

### Cavity Design

The geometry of the RF-gun cavity is based on the Low Loss shape (LL). The cavity, as shown in Fig. 2, was modelled, first in 2D for the cell shape optimization, and then in 3D [2] with the coaxial input coupler and two HOM couplers attached. The result of 3D modelling of

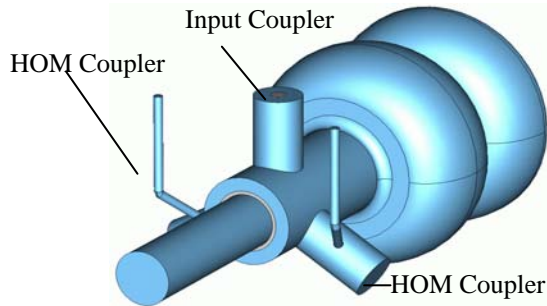


Figure 2. 1.6-cell Nb-Pb RF-gun

the external coupling ( $Q_{ext}$ ) for the fundamental mode as a function of the penetration depth of the input coupler inner conductor showed that nominal  $Q_{ext}=3.5 \cdot 10^7$  (for the 1 mA and 6 MeV beam) is obtained when the inner conductor marginally penetrates the beam tube. Data of the fundamental mode passband and the nominal operation data are listed in Table 1. The modelling also estimated the asymmetry in the accelerating field caused by the couplers to be of order  $10^{-3}$ . Finally, the frequencies, (R/Q)s and damping of the monopole and dipole passbands were also computed with the 3D code. The computed data of parasitic modes is shown in Table 2 and in Fig. 3.

Table 1. Parameters of RF-gun cavity

Parameter	Unit	
$\pi$ -mode frequency	[MHz]	1300
0-mode frequency	[MHz]	1286.5
Cell-to-cell coupling	-	0.015
Nominal $E_{cath}$ at cathode	[MV/m]	60
Energy stored at nominal $E_{cath}$	[J]	20
Nominal beam energy	[MeV]	6

Table 2. Parameters of parasitic modes

Mode	f [MHz]	(R/Q)
Monopole: Beam Tube	793.9	57.9 [ $\Omega$ ]
Dipole: TE111-1H	1641.8	1.85 [ $\Omega/cm^2$ ]
Dipole: TE111-1V	1644.9	1.30 [ $\Omega/cm^2$ ]
Dipole: Beam Tube-H	1686.3	3.33 [ $\Omega/cm^2$ ]
Dipole: Beam Tube-V	1754.7	5.13 [ $\Omega/cm^2$ ]
Dipole: TM110-1H	1883.5	10.1 [ $\Omega/cm^2$ ]
Dipole: TM110-1V	1884.0	9.99 [ $\Omega/cm^2$ ]
Dipole: TM110-2H	1957.0	3.90 [ $\Omega/cm^2$ ]
Dipole: TM110-2V	1957.1	3.85 [ $\Omega/cm^2$ ]
Monopole: TM011	2176.5	43.2 [ $\Omega$ ]

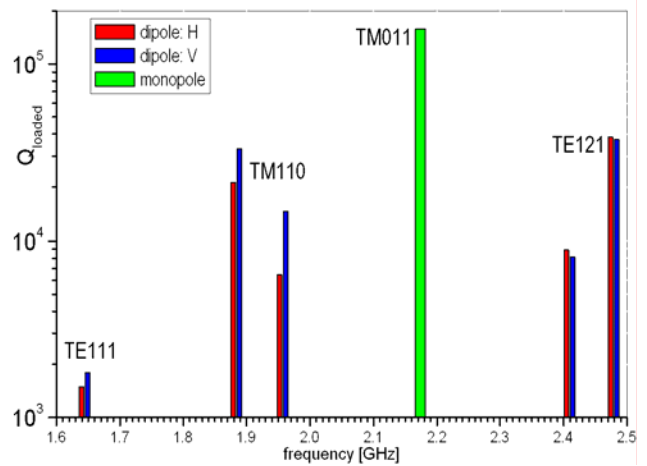


Figure 3. HOMs damping ( $Q_{ext}$ ).

## Pb QUANTUM EFFICIENCY

We used an existing room temperature setup at BNL for the QE measurements of various lead samples [3]. The samples were illuminated with KrF Excimer, ArF Excimer, Nd:YAG (4<sup>th</sup> harmonic) lasers and with a

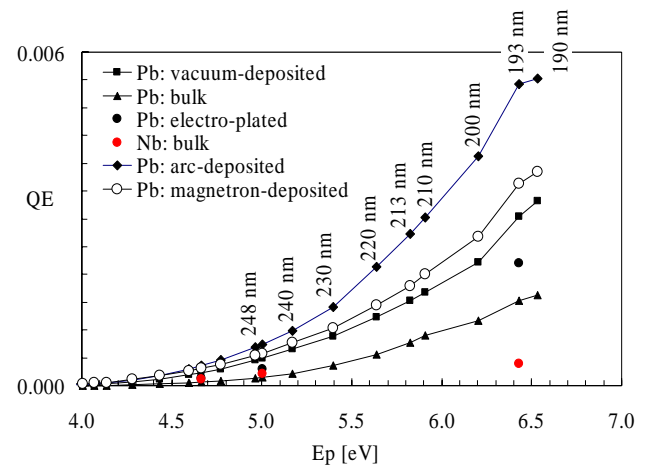


Figure 4. Measured QE of lead deposited with various coating methods as function of photon energy. Bulk Pb and Nb data are displayed for comparison.

deuterium light source fiber-coupled to a monochromator (output bandwidth 2 nm). The QE data for the lead samples is summarized in Fig. 4. The Pb surfaces were cleaned with pulsed laser beam of 248 nm wavelength and 10 ns duration time to improve the QE. A single pulse energy density of  $\sim 0.2$  mJ/mm<sup>2</sup> with a total of  $10^4$  pulses was found to provide the maximum QE with minimal change to the surface morphology. Arc-deposited lead demonstrated both the best QE and the best surface quality.

### COLD TESTS

Two half-cell cavities, 1.3 GHz at DESY and 1.42 GHz at JLab, have been built for QE measurements at 2 K and RF performance tests with lead spot located at centre of the endplate (Fig. 5). For the DESY cavity lead was arc-deposited. For the JLab cavity lead was electroplated on the Nb plug. The cavities have been tested preliminary for the RF performance. No QE test at 2K has been conducted up to now. Results of the RF tests, without and with lead, are shown in Fig. 6 and 7. In both cases performance is to be improved with a better cleaning before and after the deposition (DESY cavity) and a better plug cooling (JLab cavity).

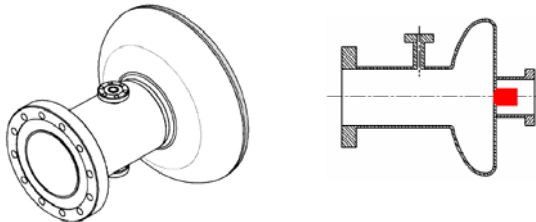


Figure 5: Test cavities; (left) DESY option with closed endplate, (right) JLab option with hole in the endplate and plug (marked in red).

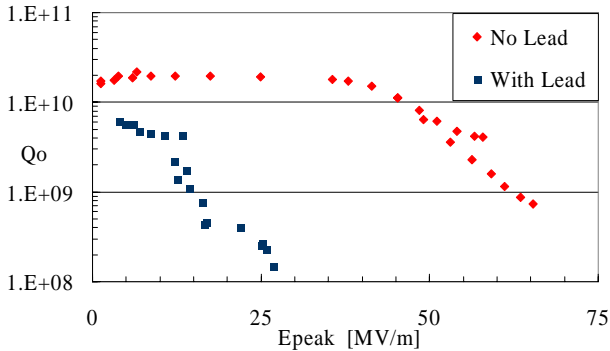


Figure 6: 2K test: DESY half-cell with and without lead.

### TWO QUESTIONS TO BE ANSWERED

In near future, two questions we need to answer experimentally with a prototype of the SRF gun as it is shown in Fig. 1. At first, we have to verify the estimated relaxation time  $\tau_r$  of quasi-particles generated during the irradiation process in the  $\sim 10$  nm thin layer of the emitting spot. The layer absorbing almost whole photons energy will lose its superconducting state since all Cooper

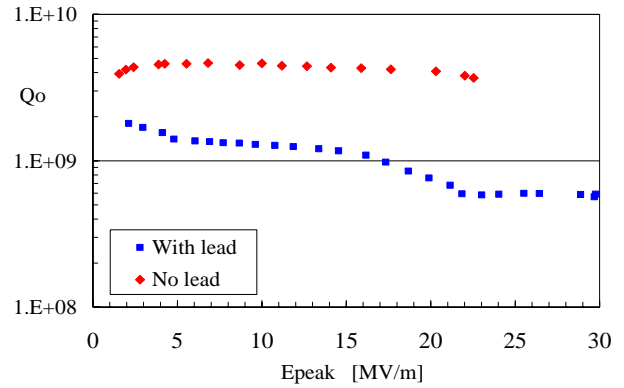


Figure 7: 2K test: JLab half-cell with and without lead.

pairs will be broken by the laser pulse. They will form an excess of quasi-particles as compared to their density due to the thermal equilibrium. Their recombination time, to form back the Cooper pairs, depends on temperature (see Fig. 8). By irradiation of the emitting spot with intense laser light when cavity has very high intrinsic quality factor we should be able to benchmark our theoretical estimation of  $\tau_r$ .

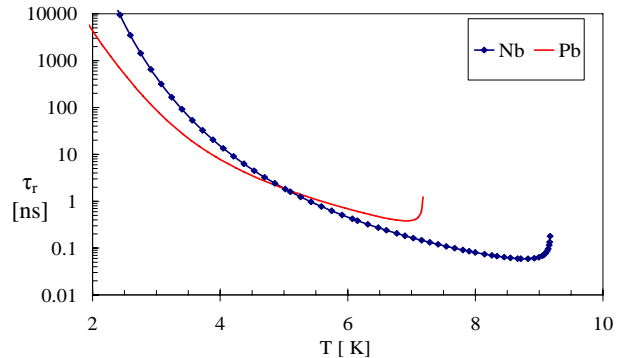


Figure 8: Relaxation time in lead and niobium vs.  $T$ .

The second question is the thermal emittance. To keep the laser power as low as possible, one needs to irradiate the lead cathode with wavelength close to 200 nm. At this wavelength, assuming 4.25 eV work function of lead, 1mm radius of the spot and 60 MV/m electric field on the cathode, thermal emittance can be estimated to be 1.25  $\mu$ rad. This value is above our spec and if confirmed experimentally will force us to operate the gun with lower charge ( $\sim 0.4$  nC) generated from the spot of smaller  $\sim 0.7$ mm radius.

### REFERENCES

- [1] J. Sekutowicz et al., “Nb-Pb superconducting RF-gun”, TESLA-FEL Report 2005-09, DESY, Hamburg, December 2005.
- [2] Z. Li et al., “X-Band Linear Collider R&D in Accelerating Structures Through Advanced Computing”, EPAC04, Lucerne, Swiss, 2004.
- [3] J. Smedley et al., “Photoemission Properties of Lead”, EPAC04, Lucerne, Swiss, 2004.

# CHARACTERIZATION OF THE SPARC PHOTO-INJECTOR WITH THE MOVABLE EMITTANCE METER\*

A. Cianchi<sup>†</sup>, L. Catani, E. Chiadroni, INFN-Tor Vergata, Roma, Italy  
 P. Musumeci, INFN-RM, Roma, Italy

M. Boscolo, M. Castellano, G. Di Pirro, M. Ferrario, D. Filippetto,  
 L. Palumbo, V. Fusco, C. Vaccarezza, INFN-LNF, Frascati, Roma, Italy

## Abstract

As a first stage of the commissioning of SPARC accelerator a complete characterization of the photo-injector is planned. The objective is the optimization of the RF-gun setting that best matches the design working point and, generally, a detailed study of the emittance compensation process providing the optimal value of emittance at the end of the linac. For this purpose a novel beam diagnostic, the emittance-meter, consisting of a movable emittance measurement system, was conceived and built. This paper presents the results of the first measurements with the emittance-meter showing the characteristics and the performance at the SPARC photo-injector.

## INTRODUCTION

The aim of the SPARC [1] project is to promote R&D towards high brightness photo-injectors to drive a SASE-FEL experiment. The 150 MeV SPARC photo-injector consists of a 1.6 cell RF gun operated at S-band (2.856 GHz, of the BNL/UCLA/SLAC type) and high-peak field on the cathode incorporated metallic photo-cathode of 120 MV/m, generating a 5.6 MeV, 100 A (1 nC, 10 ps) beam.

The beam is then focused and matched into 3 SLAC-type accelerating sections, which boost its energy to 150-200 MeV. The first phase of the SPARC Project was dedicated to the beam RMS emittance measure along the drift space following the RF gun, where the emittance compensation process occurs.

The complete characterization of the beam parameters at different distances from the cathode is important to find the injector settings optimizing emittance compensation and for code validation. For this measurement, a dedicated moveable (in  $z$ ,  $z$  being the distance from the cathode, measured along the accelerator axis) emittance measurement device (emittance-meter) is used allowing to measure the RMS emittance in the range from about  $z=86$  cm to  $z=210$  cm. More than a simple improvement over conventional, though non-trivial, beam diagnostic tools this device defines a new strategy for the characterization of novel high performance photo-injectors, providing a tool for detailed analysis of the beam dynamics and the phase space.

The technique to measure the beam emittance and the phase space, in both the horizontal and vertical planes,

makes use of a double system of horizontal and vertical slit masks [2]. Each mask consists of a slit array (7 slits, 50  $\mu\text{m}$  width spaced of 500  $\mu\text{m}$ , 2 mm thick) and two single slits, 50 and 100  $\mu\text{m}$  width. The slits are realized by photo-chemical etching providing, compared to mechanical machining, higher precision and improved smoothness of slits edges. The multislits are used for single shot measurements, provided the beam size is large enough for an adequate beam sampling by the slit array. Alternatively, a single slit can be moved across the beam spot. In this case the accuracy of transverse sampling can be freely chosen adjusting the step between the different positions of the slit. This measurement is an integration over many pulses.

Linear actuators with stepper motors are used to control the insertion of the slits masks into the beamline. A differential encoder and a reference end switch guarantee reproducibility and accuracy of the movement to better than 2  $\mu\text{m}$ , required for single-slit multi-shots measurements.

The projected cross-section of beamlets emerging from the slit-mask are measured by means of a downstream Ce:YAG radiator [3]. Because beam size and divergence depend on the device longitudinal position, the slit to screen distance must be properly adjusted in order to optimize the accuracy of the beamlet profiles measurement. A bellow is therefore interposed between the slit mask and the screen, allowing their relative distance to be changed from 22 to 42 cm, to optimize the drift in order to fit several scenarios (converging beam, diverging beam, single or multi-slits). Refer to Fig.1 for a schematic drawing of the emittance meter.

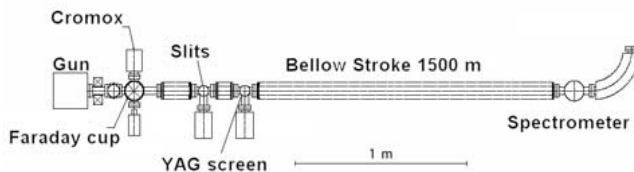


Figure 1: Schematic drawing of the e-meter

Radiation emitted in the forward direction from the Ce:YAG crystal is collected by a 45 degrees mirror downstream from the radiator. The back face of the transparent crystal radiator is observed, thus minimizing degradation of the spatial resolution due to the depth of field of the optics.

Images are acquired using digital CCD cameras (Basler 311f) equipped with simple 105mm "macro" type objective

\* This work has been partially supported by the EU Commission in the sixth framework program, contract no. 011935 EUROFEL-DS1.

<sup>†</sup> cianchi@roma2.infn.it

from SIGMA. The magnification of 0.66 gives a calibration of  $15.4 \mu\text{m}$  per pixel.

Such cameras offer the advantage that the signal is digitalized directly by on-board electronic so that there is no need for a frame grabber and the output signal, being digital, is less sensitive to environmental noise. Furthermore, the IEEE1394 (firewire) link allows simpler cabling topology because it carries both pixels readout and commands to the camera. Charge is measured by means of a Faraday cup, placed in a cross together with a cromox screen to image the beam at 60 cm from the cathode. This screen is also used to monitor the position of the laser spot on the cathode. The emittance-meter is followed by a magnetic spectrometer measuring the beam energy and energy spread

## TRANSVERSE PLANE MEASURE

We performed a detailed characterization of the photo-injector, studying the beam dynamics as function of relevant parameters such as the solenoid field, the beam charge and size, the laser pulse length and its shape. Refer to [4] for more details.

### *Beam Envelope measure*

Evolution of the bunch transverse size along the photo-injector is a important, although simple, measurement we performed with the emittance-meter. It takes less than 5 minutes to complete the measurement that consists of continuously changing the z-position of the movable part between the upper and lower ends, grabbing beam images at every position. These images are on-line processed to filter out the background noise and to calculate the RMS value of the beam size. In Fig.2 are shown results of measurements of the RMS beam size vs z for different values of the solenoid field.

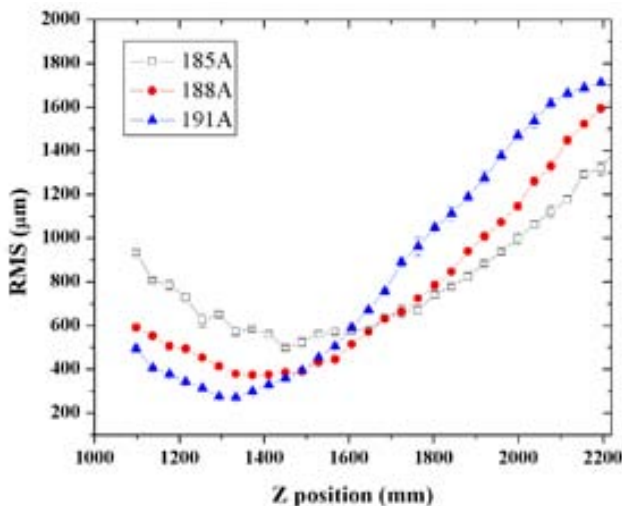


Figure 2: Envelope of the beam with different solenoid currents

The different curves show that the position of the beam envelope waist and its value are changed as consequence of the different solenoid currents. With this system we can easily identify the solenoid value that gives the waist in the expected z position.

### *Emittance measurements*

The emittance is measured, for both x and y both planes, at different positions along the emittance-meter. As consequence of emittance compensation process, the beam size and divergence change along the photo-injector: the beam is converging at the beginning of the emittance-meter and diverging in the second half. The transverse dimension depends on several factors but, usually, we obtained a beam with RMS size ranging from 1.5 mm down to  $200 \mu\text{m}$ .

### *Single vs multi-slits*

Usually, when the beam is close to the waist and the beam size is small the multi-slits mask is not convenient because it produces a limited number of beamlets. The multi-slits mask is not used also in the region close to the end of the emittance-meter where the beam size is larger than the part of the mask covered by the slit-array. In all of the others conditions the multi-slits mask provides fast single-shot measurements, while we use the single-slit for accurate analysis.

It's worth to mention that results produced by single-slit or multi-slit measurement, with the same beam conditions, have always been fully consistent. In addition we compare the RMS beam size at the slit-mask (measured by moving the screen at the slits position) against the value of beam size estimated by the algorithm we use to calculate the emittance. We always obtained an excellent agreement between the results. While for the multislits the sampling rate is fixed by the slits distance ( $500 \mu\text{m}$ ) with a single slit we can change it depending of the beam size. Typical values of the sampling distance between the slit positions ranges from  $110 \mu\text{m}$  to  $380 \mu\text{m}$ . At least nine beamlets are always collected with the single slit.

### *Emittance calculation and phase space tracing*

With the emittance meter is possible to follow the emittance evolution, and tuning the machine parameters. Fig. 3 shows an emittance behaviour at  $200 \text{ pC}$ , measured before the laser cleaning of the cathode, when the quantum efficiency at the cathode was not uniform.

A typical emittance measurement with the single-slit mask consists of collecting 15 beam images for each slit position. The center of mass and RMS size of beamlets are then calculated for each image and averaged. We verified that a larger statistic doesn't significantly improve the accuracy of results. From the beamlets images we calculate the projection on the axis, subtract the baseline, try a gaussian fit to find the best position for the distribution center, reduce the number of the relevant points skipping these

that are outside the 3 standard deviation from the centre and only on the remaining points we calculate the RMS parameters.

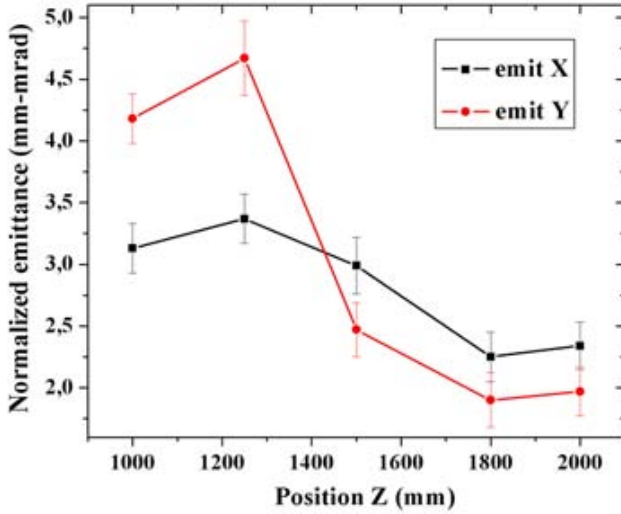


Figure 3: Emittance measurements along the e-meter

The use of big magnification, an high efficiency YAG and a CCD with a gain remotely controlled give a good signal to noise ratio and large number of sampling point for every beamlet in all the conditions.

The 1-D pepper pot technique allows not only to measure the beam and the Twiss parameters, but also to reconstruct the phase space [5]. Here in Fig.4 the phase space reconstruction in different positions, measured at low charge, 100 pC.

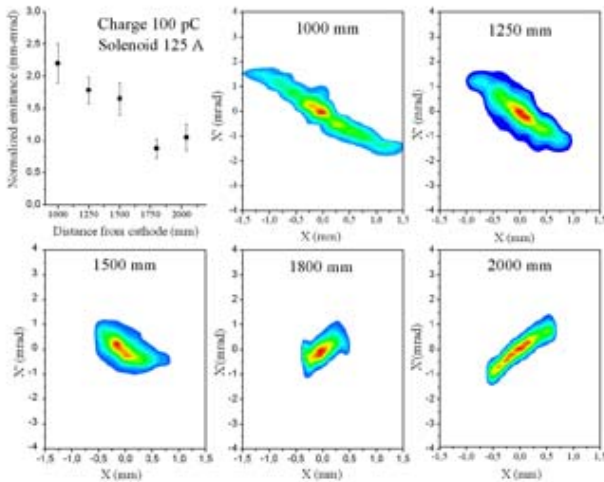


Figure 4: Phase space measure along the e-meter

## LONGITUDINAL PLANE MEASURE

The e-meter gives also the possibility to investigate the longitudinal dynamics.

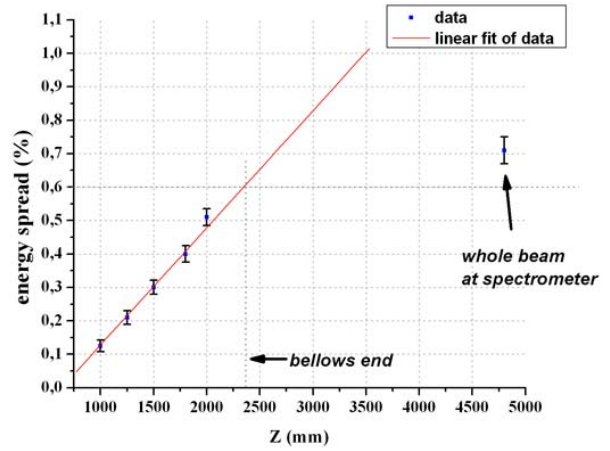


Figure 5: Energy spread vs longitudinal position

Moving the slit over the beam and measuring the energy and the energy spread in the spectrometer gives information of possible correlation between position and energy. Also centering the slit on the beam and moving along the emittance meter allows the measure of the energy spread in different longitudinal positions. The energy spread is frozen at the point where the beam is cut. Measuring it at the spectrometer, moving that position, gives the graph in Fig 5.

While the contribution at the energy spread from the longitudinal space charge is always present, the wake fields of the bellow affects the spread only till its end.

## CONCLUSION

The SPARC emittance meter gives the possibility to measure the beam parameters a different distances from the cathode, giving information on the transversal and longitudinal phase space. The improvement on the laser parameters, the change in the solenoids field, the modification in the solenoids alignment can be easily and fast checked. Also the possibility to have several measures along the beam line gives a better understanding of the dynamics and easier comparison with the simulations.

## REFERENCES

- [1] D. Alesini et al., Nucl. Instr. & Meth. In Phys. Res. A 507 (2003) 345-349C.
- [2] M. Zhang "Emittance Formula for Slits and Pepper-pot measurement", FERMILAB-TM-1998A.
- [3] L.Catani and al. "Commissioning of the SPARC movable emittance meter and its first operation at PITZ", Proc. FEL 2005.
- [4] L.Serafini "Status of the SPARC project", these Proceedings.
- [5] S. G. Anderson et al. "Space-charge effects in high brightness electron beam emittance measurements", Phys. Rev. ST Accel. Beams 5, 014201 (2002).